UAB
Universitat Autònoma de Barcelona

DELOS Nanovesicles for the Subcutaneous and Oral Delivery of Challenging-to-Formulate Compounds

Carla Castellar Álvarez

ADVERTIMENT. L'accés als continguts d'aquesta tesi doctoral i la seva utilització ha de respectar els drets de la persona autora. Pot ser utilitzada per a consulta o estudi personal, així com en activitats o materials d'investigació i docència en els termes establerts a l'art. 32 del Text Refós de la Llei de Propietat Intel·lectual (RDL 1/1996). Per altres utilitzacions es requereix l'autorització prèvia i expressa de la persona autora. En qualsevol cas, en la utilització dels seus continguts caldrà indicar de forma clara el nom i cognoms de la persona autora i el títol de la tesi doctoral. No s'autoritza la seva reproducció o altres formes d'explotació efectuades amb finalitats de lucre ni la seva comunicació pública des d'un lloc aliè al servei TDX. Tampoc s'autoritza la presentació del seu contingut en una finestra o marc aliè a TDX (framing). Aquesta reserva de drets afecta tant als continguts de la tesi com als seus resums i índexs.

ADVERTENCIA. El acceso a los contenidos de esta tesis doctoral y su utilización debe respetar los derechos de la persona autora. Puede ser utilizada para consulta o estudio personal, así como en actividades o materiales de investigación y docencia en los términos establecidos en el art. 32 del Texto Refundido de la Ley de Propiedad Intelectual (RDL 1/1996). Para otros usos se requiere la autorización previa y expresa de la persona autora. En cualquier caso, en la utilización de sus contenidos se deberá indicar de forma clara el nombre y apellidos de la persona autora y el título de la tesis doctoral. No se autoriza su reproducción u otras formas de explotación efectuadas con fines lucrativos ni su comunicación pública desde un sitio ajeno al servicio TDR. Tampoco se autoriza la presentación de su contenido en una ventana o marco ajeno a TDR (framing). Esta reserva de derechos afecta tanto al contenido de la tesis como a sus resúmenes e índices.

WARNING. The access to the contents of this doctoral thesis and its use must respect the rights of the author. It can be used for reference or private study, as well as research and learning activities or materials in the terms established by the 32nd article of the Spanish Consolidated Copyright Act (RDL 1/1996). Express and previous authorization of the author is required for any other uses. In any case, when using its content, full name of the author and title of the thesis must be clearly indicated. Reproduction or other forms of for profit use or public communication from outside TDX service is not allowed. Presentation of its content in a window or frame external to TDX (framing) is not authorized either. These rights affect both the content of the thesis and its abstracts and indexes.

Universitat Autònoma de Barcelona

DELOS Nanovesicles for the Subcutaneous and Oral Delivery of Challenging-to-Formulate Compounds

Carla Castellar Álvarez

Tesi Doctoral

Programa de Doctorat de Química

Directores

Dr. Lidia Priscila Ferrer Tasies

Dr. Elisabet González Mira

Tutora

Prof. Nora Ventosa Rull

Departament de Química

Facultat de Ciències

2024

La present memòria es presenta per aspirar al Grau de Doctor per:

Carla Castellar Álvarez

Vist i plau:

Dr. Lidia Priscila Ferrer Tasies,

Dr. Elisabet González Mira

Prof. Nora Ventosa Rull

Bellaterra, setembre 2024

Lidia Priscila Ferrer Tasies, R&D Director of Nanomol Technologies S.L. and **Elisabet González Mira**, Researcher of the Spanish National Research Council at the Institute of Materials Science of Barcelona (ICMAB-CSIC)

CERTIFY:

That Carla Castellar Álvarez, Master's Degree in Molecular Biotechnology and Bachelor's Degree in Biomedical Sciences, has performed, under their management, the research work entitled "**DELOS Nanovesicles for the Subcutaneous and Oral Delivery of Challenging-to-Formulate Compounds**". This work has been performed under the frame of the Chemistry PhD program of the Physics and Chemistry Department of the Autonomous University of Barcelona.

And in witness whereof this is signed by

Directors

Dr. Lidia Priscila Ferrer Tasies

Dr. Elisabet González Mira

Bellaterra, August 2024

Preamble

Some parts of this Ph.D. thesis include experiments performed within the framework of collaborative projects. Accordingly, besides the results obtained by the author, some results obtained through the collaborative efforts of other researchers have been included to complement and reinforce the findings presented in this thesis.

Agraïments

Aquestes línies marquen l'inici del final d'una etapa. Una etapa de quasi quatre anys carregada d'experiències, d'aprenentatges, però sobretot, de persones. Persones que, de moltes maneres diferents, han contribuït a fer que aquest projecte es faci realitat.

Per això vull acabar aquesta etapa donant les gràcies a totes aquestes persones que m'han acompanyat.

No podria començar d'altra manera que agraint a les meves directores de tesi, la Dra. Lidia Ferrer i la Dra. Elisabet González, per tot el suport que m'han donat durant el transcurs de la tesi. He tingut la sort de ser acompanyada per unes grans professionals, amb un fort esperit crític i amb una forta responsabilitat pel rigor científic, que han impactat directament a la qualitat d'aquesta tesi. Però sobretot, unes magnífiques persones que m'han aplanat el camí en els moments més difícils, i que han estat disponibles sempre que les he necessitat. Gràcies, Lidia, ja són molts anys aprenent de tu, i a mesura que passa el temps vaig sumant raons per sentir-me agraïda. Gràcies, Eli, ha sigut un plaer haver fet aquest projecte sota la teva supervisió. Treballar amb tu és fàcil i t'estic molt agraïda. No tinc paraules per expressar quant afortunada em sento d'haver comptat amb el vostre suport per realitzar aquesta tesi.

Voldria continuar agraint a la Prof. Nora Ventosa, tutora de la tesi i IP del grup Nanomol-Bio, per permetre'm fer aquest treball al seu grup. És un plaer haver format part d'un grup tan potent, i on es respira un ambient de companyonia i germanor. A més, comptar amb tot el teu coneixement i experiència pel desenvolupament d'aquesta tesi ha sigut de gran valor. També voldria agrair al Dr. Santi Sala, per l'oportunitat de realitzar el Doctorat Industrial a Nanomol Technologies S.L., però sobretot per haver impulsat el meu creixement professional des que vaig entrar a l'empresa. Gràcies, Santi per la teva confiança. I a la Dra. Alba Córdoba, per la seva ajuda i assessoria en tot el procés d'avaluació de resultats i sol·licitud de patents.

També vull expressar el meu agraïment a les diferents entitats que han finançat la realització d'aquesta tesi. Voldria agrair a l'AGAUR el finançament rebut a través de l'ajuda de Doctorat Industrial. També voldria agrair el finançament rebut a través dels projectes *Armonia* (PID2022-

137332OB-I00), finançat per MCIN/AEI/10.13039/501100011033/FEDER (UE), i el finançament rebut a través del projecte *Mol4Bio* (PID2019-105622RB-I00I) finançat per AEI/10.13039/501100011033. Igualment, vull agrair a la Unió Europea per impulsar la recerca i innovació a través del programa *Horizon 2020*, especialment per mitjà del projecte *Nano-Oligomed* (778133) per promoure col·laboracions científiques, i a través de la convocatòria *TamaTA-INNOV* (101007804) per permetre'm utilitzar la línia de llum BL11-NCD-SWEET del sincrotró ALBA per a realitzar mesures de SAXS.

In the frame of the *Nano-Oligomed* project, I had the opportunity to do a secondment at Prof. Alessandro Porchetta's group, in Rome. Hence, I would like to express my most sincere gratitude to Alessandro Porchetta. Thank you for welcoming me into your group and allowing me to learn from your expertise with oligonucleotides. Also, many thanks to all the members of the group for their warm welcome, and especially, to Elisa Paialunga and Andrea Di Pede for showing me all the laboratory techniques and how to work with oligonucleotides, and for contributing to the obtainment of some results. Grazie Mille!

Gracias a la convocatoria *TamaTA-INNOV*, tuve la oportunidad de realizar medidas en el sincrotrón ALBA, con la valiosísima ayuda del Dr. Cristián Huck. Muchas gracias por realizarnos las medidas de SAXS y por el tiempo dedicado al análisis de resultados. Also, I would like to express my gratitude to Prof. Jan Skov Pedersen, who contributed to all the SAXS analysis. Thank you very much to both of you for your support on this matter.

Por supuesto, también quiero agradecer a la Dra. Lyda Hallbaut, de la Universidad de Barcelona, por su ayuda altruista con el uso del reómetro. Muchas gracias Lyda por compartirnos tu conocimiento, aprendimos mucho de tu mano.

Y también quiero dar las gracias al Dr. Juan Sabín, por todo el tiempo dedicado a ayudarme con el análisis de datos de ITC con el programa Affinimeter. Sin tu ayuda habría sido imposible lograr los buenos ajustes conseguidos. ¡Muchas gracias!

Durant tota la tesi he tingut l'oportunitat de fer ús dels diferents serveis de la UAB, i això m'ha permès aprendre moltes tècniques diferents i ha enriquit el contingut del treball amb una gran varietat de caracteritzacions.

Voldria agrair al Servei d'Anàlisi Química de la UAB per les anàlisis realitzades. També, al Laboratori de Luminescència i Espectroscòpia de Biomolècules, i en especial a Salvador Bartolomé, per l'ajuda amb l'espectrofluorímetre.

A més a més, voldria agrair el Servei de Microscòpia i Difracció de Raig X, sobretot a Martí de Cabo, un gran expert amb el Cryo-TEM, capaç de treure les millors fotografies, fins i tot de les mostres més complicades, i a la Dra. Helena Montón i la Dra. Meritxell Vendrell, per tot el suport amb el confocal.

I finalment, dels serveis de la UAB, voldria donar les gràcies al Servei de Cultius Cel·lulars, Producció d'Anticossos i Citometria. Moltes gràcies, Dra. Francisca García, Francisco Cortés i Dr. Antoni Iborra, per tot el suport brindat durant els assajos en cèl·lules i posteriors caracteritzacions. Fran, a tu també vull agrair-te totes les hores de formació que van fer que perdés la por a treballar amb cultius cel·lulars.

Voldria continuar agraint a la Yolanda Ronda i l'Aniol Gimó tota la contribució que van fer en aquesta tesi durant la seva estança de pràctiques a Nanomol Technologies. Sou uns grans treballadors (no tothom treu un 10 al TFM!) i vau ser de moltíssima ajuda. Us estic profundament agraïda.

Per altra banda, també vull mostrar el meu agraïment cap als professionals de l'ICMAB que m'han ajudat amb tota la part més burocràtica de la tesi. Gràcies, Arnau Jaumandreu, Carme Gimeno, Maria Àngels Vilella i Soraya Hernandez.

I de l'ICMAB també vull agrair a tots els companys, pels moments viscuts dins i fora del laboratori. Ha passat moltíssima gent per l'ICMAB i pel grup Nanomol-Bio d'ençà que vaig arribar i tothom ha deixat la seva empremta. Breument, voldria agrair al Carles Llavina i al Ramón Gonzalez, vosaltres sabeu la il·lusió que em feia fer aquest doctorat. També al Guillem Vargas, al David Piña i a la Judit Tomsen, companys de feina que s'han convertit en amics i a qui aprecio moltíssim. I a la resta de companys, presents i passats, Francesc, Edu, Albert R, Albert G, Mario, Marc, Nerea, Xavi, Sara R, Sara G, Adri, Aida, Alejandro, Amable, Ángel, Fabião, Inés, Jose, Lamia, Mariana, Miquel, Nathaly, Paula, Solène, Sílvia, Adriana, Simona, Toni, Rubén, Núria, Laia, Júlia, Elba, Angelica, Giovanni, Ehsan i Nicolas, gràcies. És una sort haver compartit aquests anys amb vosaltres.

A Nanomol Technologies també he coincidit amb gent molt especial. Gràcies, Estela Álvarez, Yolanda Ronda i Sara Astasio, sou l'alegria del laboratori, ni totes les normes GMP del món podrien eclipsar el bon rotllo de treballar amb vosaltres. Gràcies, Arnau Güell, per les anàlisis d'HPLC, però sobretot per ser un amic amb qui es pot parlar de tot. Gràcies, Josep pel teu suport incondicional amb la planta, per tenir sempre una bona solució, i per cuidar-nos amb dolços. I gràcies, Marta, per ser la millor companya de doctorat que es pot tenir, aquesta experiència no hauria sigut igual de maca sense algú amb qui compartir els viatges, els nervis previs a les presentacions, i les llargues jornades d'escriptura de la tesi.

També voldria agrair a la Teresa i a l'Òscar, les dues primeres persones que vaig conèixer a l'empresa i que em van formar en les tècniques de caracterització de partícules, i a la Lidia B, a la Ivana, a la Laura G, al Xavi, a la Laura P, a la Sandra, a la Jana i a la Marta V per ser uns companys de feina increïbles. Només tinc paraules d'agraïment per vosaltres.

I per acabar voldria dedicar unes curtes paraules a aquelles persones que no formen part de l'àmbit laboral, però que també m'han acompanyat durant aquests quatre anys.

A les meves amigues de (quasi) tota la vida, el meu *Comando*. Judith, Ona, Sara, Carla, Blanca, sabeu que sou un suport inigualable. Als meus amics de la uni, els *Tikis*. Gemma, Alberto, Aina i Alba sou el millor que m'emporto dels quatre anys de carrera. I als amics de la salsa, que han arribat més tard, però espero que es quedin molts anys. Gràcies!

I per acabar, vull agrair a la meva meravellosa família.

A la meva germana Ester, el meu referent des de petita. Sempre m'has ajudat a prendre bones decisions. Al meu cunyat Víctor, i als meu nebots Leo i Jan, sou un clar exemple de perseverança i esforç. Gràcies!

A la meva parella, Cristian, per estar sempre. Per la paciència. Has aguantat al meu costat durant mooolts anys d'estudiant... màster, doctorat... No puc prometre que s'hagi acabat però de moment vindran uns mesos de descans per recuperar el temps perdut.

Als meus pares, Ángela i Manolo, per donar-ho tot i més perquè pugui complir els meus somnis. Per confiar cegament en mi. Per estimar tant i estimar tan bé.

Gràcies a tots. Aquesta tesi també és vostra.

Al meu pare i a la meva mare.

Abstract

The ongoing shift from traditional orally bioavailable small molecules to novel drug modalities requires more sophisticated and innovative drug delivery strategies. These advanced strategies aim to improve the solubility and stability of challenging-to-formulate drugs while ensuring selective delivery with predictable rates and mechanisms to specific organs, tissues, or cells.

In this context, DELOS nanovesicles, also known as Quatsomes, offer a promising solution to address the complexities associated with novel, challenging-to-formulate drugs. DELOS nanovesicles are a unique class of nanocarriers composed of sterols and ionic surfactants. They are produced using the DELOS technology (Depressurization of an Expanded Liquid Organic Solution), an eco-efficient, scalable, one-step method based on compressed CO_2 for producing colloidal systems.

DELOS nanovesicles have shown potential to deliver a variety of drug modalities, ranging from small molecules to biologics, via intravenous and topical administration routes. However, their application for other administration routes remains unexplored, limiting their versatility.

This thesis aims to investigate the potential of DELOS nanovesicles as drug delivery systems specifically formulated for subcutaneous and oral administration routes.

In pursuit of this goal, a systematic design of experiments was conducted to refine DELOS nanovesicles composition, using exclusively excipients listed in the United States Food and Drug Administration (FDA) Inactive Ingredients Database, to pursue the development of a biocompatible and regulatory-oriented formulation for the intended administration routes.

Considering the subcutaneous route, a hybrid *in situ*-forming subcutaneous depot was developed based on the optimized DELOS nanovesicles and a thermoreversible hydrogel. Different concentrations of the thermoreversible Poloxamer 407 were tested in combination with the DELOS nanovesicles. Through rheological characterization of the obtained hydrogels, the 17% w/w Poloxamer 407 was identified as optimal for subcutaneous administration, being injectable at 22 °C and forming a cohesive *in situ* depot at 37 °C. *In vitro* tests showed a consistent release pattern of

the DELOS-NV over an 8-hour period, following zero-order kinetics. Additionally, a highly hydrophobic compound, as challenging-to-formulate “beyond the Rule of Five” (bRo5) molecule, was entrapped into the DELOS-NV based thermoreversible hydrogel. This compound was successfully loaded into the DELOS nanovesicles with high entrapment efficiency, and the nanoconjugates demonstrated long-term stability under storage conditions (5 ± 3 °C) and at 40 ± 3 °C. When integrated into the 17% w/w Poloxamer 407 hydrogel, a 10-hour zero-order *in vitro* release profile of the nanoconjugate was achieved, highlighting the potential of the developed hybrid system for extended subcutaneous drug delivery.

To explore the feasibility of using the DELOS nanovesicles for the oral administration route, the impact of these nanovesicles on the intestinal epithelium was assessed using Caco-2 *in vitro* models. A nanoconjugate containing a model protein (bovine serum albumin) was prepared, and isothermal titration microcalorimetry characterization confirmed strong hydrophobic binding of the protein to the DELOS nanovesicles, suggesting no premature release of the protein before or during *in vitro* permeation assays. Besides, two additional model molecules, a small molecule (lucifer yellow) and another protein (insulin), were evaluated by loading them into the DELOS nanovesicles. Permeation assays in Caco-2 monolayers demonstrated that DELOS-NV significantly enhanced the permeation of lucifer yellow, while both proteins (bovine serum albumin and insulin) did not permeate the Caco-2 barrier. These results suggest that DELOS-NV have potential for either systemic or local delivery in the gastrointestinal tract, depending on the integrated molecule.

To further harness their potential for gastrointestinal applications, DELOS-NV were developed into a biosensor incorporating an oligonucleotide as a sensing biomolecule, capable of detecting miR21, a microRNA overexpressed in colorectal cancers. The biosensor exhibited very high sensitivity and specificity, highlighting the potential of DELOS-NV for dual purposes in therapy and diagnosis.

Contents

PREAMBLE 7

AGRAÏMENTS 9

ABSTRACT 17

LIST OF ABBREVIATIONS 31

1. INTRODUCTION 37

1.1. An overview on drug discovery evolution 37

1.2. Nanoparticles as drug delivery systems 39

1.2.1. Self-assembled lipid nanovesicles as drug delivery systems 40

1.2.2. DELOS nanovesicles: A novel class of non-liposomal lipid nanovesicles 42

1.3. Technologies to prepare nanovesicles 45

1.3.1. Conventional methods for nanovesicles production 45

1.3.2. Novel methods for nanovesicles production 46

1.3.2.1. Supercritical fluid-based technologies to produce nanovesicles 47

1.3.2.1.1. The DELOS technology to produce nanovesicles 50

1.4. Routes for drug administration 52
1.4.1. The subcutaneous administration route 53
1.4.1.1. Anatomy of the subcutaneous tissue and its impact on drug delivery 54
1.4.2. The oral administration route 56
1.4.2.1. Anatomy of the gastrointestinal system and its impact on drug delivery 56

1.5. References 59

2. OBJECTIVES 67

3. DESIGN AND DEVELOPMENT OF BIOCOMPATIBLE DELOS-NV FOR THERAGNOSTIC PURPOSES 71

3.1. Introduction 71
3.1.1. Market- and -regulatory oriented DELOS-NV 71
3.1.1.1. The membrane components of the DELOS-NV 72
3.1.1.2. The buffer selection 72
3.1.2. The design of experiments to speed up research 73

3.2. Definition of the critical quality attributes of DELOS-NV 75

3.3. Novel DELOS-NV with CPC and BKC surfactants 76

3.4. Optimization of DELOS-NV with CPC using histidine buffer to ensure biocompatibility 84

3.5. Summary of the chapter and perspectives 92

3.6. References 93

4. DEVELOPMENT OF A HYBRID SYSTEM COMPOSED OF DELOS-NV AND POLOXAMER 407 AS AN IN SITU SUBCUTANEOUS DEPOT 97

4.1. Introduction 97
4.1.1. Subcutaneous long-acting formulations 97
4.1.2. Poloxamer 407 as thermoreversible hydrogel 99

4.2. Formulation of DELOS-NV into Poloxamer 407 thermoreversible hydrogels 101

4.2.1. Production of the DELOS-NV for the subcutaneous administration route 101

4.3. Preparation and characterization of the DELOS-NV-loaded Poloxamer 407 hydrogels 105

4.3.1. Preparation of TFF-Chol:CPC DELOS NV-loaded Poloxamer 407 hydrogels 105

4.3.2. Macroscopical and microscopical observation of the Poloxamer 407 hydrogels 106

4.3.3. Small-angle X-ray scattering characterization of the Poloxamer 407 hydrogels 108

4.3.4. Evaluation of the DELOS-NV integrity within the Poloxamer 407 hydrogels by cryogenic transmission electron microscopy 110

4.3.5. Evaluation of the DELOS-NV integrity within the Poloxamer 407 hydrogels by Förster resonance energy transfer analysis 111

4.3.6. Rheological behavior of TFF-Chol:CPC DELOS-NV-loaded Poloxamer 407 hydrogels 117

4.3.7. In vitro injectability of the DiD-Chol:CPC DELOS-NV-loaded 17% w/w Poloxamer 407 hydrogel through a 25 G needle 122

4.3.8. Gelation time of the TFF-Chol:CPC DELOS-NV-loaded Poloxamer 407 hydrogels 122

4.3.9. In vitro DiD-Chol:CPC DELOS-NV release from Plx407 hydrogels 123

4.4. Alternative polymers for subcutaneous *in situ* depots 127

4.5. Summary of the chapter and perspectives 130

4.6. References 132

5. FORMULATION OF BEYOND THE RULE OF 5 MOLECULES INTO DELOS-NV-LOADED THERMOREVERSIBLE HYDROGELS AS SUBCUTANEOUS DEPOT 139

5.1. Introduction 139

5.1.1. Lipinski's rule of 5 139

5.1.2. Beyond the rule of 5 (bRo5) compounds 140

5.2. Selection of the Beyond rule of 5 compounds and production of the preliminary prototypes by DELOS method 141

5.3. Advancement of the bRo5.1- and bRo5.2-DELOS-NV nanoconjugates and physicochemical characterization 144

5.3.1. Diafiltration and concentration of the bRo5.1- and bRo5.2-DELOS-NV nanoconjugates. Quantification of the entrapment efficiency and the final bRo5 concentration 144

5.3.2. Characterization of the average hydrodynamic diameter, size PdI and apparent Z-potential in the concentrated bRo5.1- and bRo5.2-DELOS-NV 146
5.3.3. Cryogenic transmission electron microscopy images of the concentrated bRo5.1- and bRo5.2-DELOS-NV 148
5.3.4. Stability at 40 °C of the concentrated bRo5.1- and bRo5.2-DELOS-NV 150
5.3.5. Reproducibility of the concentrated bRo5.1- and bRo5.2-DELOS-NV formulations 151

5.4. Scaling up the production of bRo5.1-DELOS-NV and estimating the maximum achievable bRo5.1 concentration 154

5.5. Formulation of bRo5.1-DELOS-NV into Poloxamer 407 hydrogels 157
5.5.1. In vitro degradation and release test with the bRo5.1-DELOS-NV-loaded 17% w/w Plx407 hydrogel 158

5.6. Summary of the chapter and perspectives 160

5.7. References 162

6. DELOS-NV AS THERAGNOSTIC CARRIERS FOR THE ORAL ADMINISTRATION ROUTE 165

6.1. Introduction 165
6.1.1. The physiological barriers of the gastrointestinal tract 165
6.1.2. Gastrointestinal models for drug permeation evaluation 167
6.1.2.1. In vitro Caco-2 cell model 168

6.2. Obtainment of the optimum nanoconjugate prototype of DELOS-NV loaded with FITC-BSA using DoE 170

6.3. Physicochemical characterization of nanoconjugates based on FITC-BSA integrated in DELOS-NV. Binding thermodynamics by isothermal titration microcalorimetry (ITC) 179
6.3.1. Setting up the procedure to determine binding thermodynamics between proteins and DELOS-NV by isothermal titration microcalorimetry 180
6.3.2. Determining the FITC-BSA and Chol:CPC DELOS-NV binding thermodynamics by isothermal titration microcalorimetry 187

6.4. Biological characterization of nanoconjugates based on FITC-BSA integrated in DELOS-NV. Permeation assays in a Caco-2 intestinal model. 191

6.4.1. Permeation assays in Caco-2 cells grown in transwells 191
6.4.1.1. Production and characterization of the formulations for the *in vitro* permeation studies 191
6.4.1.2. Viability assays in Caco-2 cells with the 4 prepared nanoconjugates based on FITC-BSA integrated in DELOS-NV 195
6.4.1.3. Caco-2 cells differentiation and quality checks to perform permeation assays 199
6.4.1.4. Caco-2 permeation assays and quantification of the permeability 201
6.4.2. Permeation assays in CacoReady models 204
6.4.2.1. Production and physicochemical characterization of nanoconjugates based on insulin integrated in DELOS-NV 205
6.4.2.2. Production and physicochemical characterization of nanoconjugates based on lucifer yellow integrated in DELOS-NV 207
6.4.2.3. Viability assays in Caco-2 cells with the Ins-DELOS-NV and the LY-DELOS-NV 210
6.4.2.4. CacoReady permeation assays and quantification of the permeability 211

6.5. Summary of the chapter and perspectives 215

6.6. References 217

7. DNA-GRAFTED DELOS-NV AS A POTENTIAL BIOSENSOR 223

7.1. Introduction 223
7.1.1. Oligonucleotides in biomedicine 224
7.1.2. The intricacies of gene expression 225
7.1.3. Overexpression of miR21 in gastrointestinal cancers 227
7.1.4. Design of a novel DNA-grafted DELOS-NV biosensor for miR21 detection 228

7.2. Production and characterization of the DELOS-NV for the development of the DNA-grafted DELOS-NV biosensor 230

7.3. Design of the oligonucleotide sequences for the development of the DNA-grafted DELOS-NV biosensor 231

7.4. Development and optimization of the DNA-grafted DELOS-NV biosensor for miR21 detection 232
7.4.1. Preliminary test to establish the most relevant conditions to develop the DNA-grafted DELOS-NV biosensor 232

7.4.1.1. Evaluation of the designed DNA sequences and selection of the optimal ratio for the pre-hybridized sequences 232
7.4.1.2. Evaluation of the Anti-miR21 fluorescence in different scenarios as controls 234
7.4.1.3. Confirmation of the adequacy of ratio 20:30 nM Anti-miR21:OligoQ in presence of the DELOS-NV 236
7.4.1.4. Impact of the DELOS-NV concentration in the miR21 recognition 238
7.4.2. DNA-grafted DELOS-NV biosensor production and miR21 binding assay 239
7.4.3. Determination of the binding specificity for the developed DNA-grafted DELOS-NV biosensor 243

7.5. Summary of the chapter and perspectives 244

7.6. References 246

8. GENERAL CONCLUSIONS 249

9. EXPERIMENTAL METHODS 253

9.1. Materials 253
9.1.1. Components employed in the DELOS-NV formulation preparation 253
9.1.2. Model molecules and fluorophores 253
9.1.3. Hydrogelling agents 254
9.1.4. Buffers, media, and reagents 254
9.1.5. Other materials and reagents 254

9.2. Preparation and post-process of DELOS nanovesicles 255
9.2.1. Production of DELOS nanovesicles by DELOS technology 255
9.2.1.1. Description of the technology and the equipment 255
9.2.1.2. Procedure for DELOS-NV obtainment by DELOS technology 257
9.2.2. Tangential flow filtration of the DELOS-NV suspension 258
9.2.3. Formulation of DELOS-NV into polymer matrix 262

9.3. DELOS-NV suspensions and hydrogels physicochemical characterization 263
9.3.1. Particle hydrodynamic diameter, size polydispersity index and apparent zeta potential assessment 263
9.3.2. pH measurements of DELOS-NV 264
9.3.3. Quantification of the DELOS-NV membrane components by HPLC 264

9.3.4. Morphological characterization by cryogenic transmission electron microscopy 265
9.3.5. Small-angle X-ray scattering 266
9.3.6. Loading and entrapment efficiency of actives and model molecules in DELOS-NV 268
9.3.7. Ultraviolet-visible spectroscopy 270
9.3.8. Fluorescence spectroscopy 270
9.3.9. Stability of DELOS-NV in Poloxamer 407 hydrogels by Förster resonance energy transfer efficiency evaluation 270
9.3.10. Stability tests at 40 °C 271
9.3.11. Isothermal titration microcalorimetry 271
9.3.12. Rheological characterization of the hydrogels 273
9.3.12.1. Shear Viscosity Measurements 273
9.3.12.2. Oscillatory Measurements 273
9.3.13. Determination of the gelation time 274
9.3.14. Optical microscopy of DELOS-NV in hydrogel dosage form 274

9.4. *In vitro* assays 274

9.4.1. In vitro injectability and thixotropy of DELOS-NV-loaded hydrogel 274
9.4.2. In vitro hydrogel dissolution test 274
9.4.3. In vitro DELOS-NV release from hydrogels 275
9.4.4. In vitro viability assays in Caco-2 cells 276
9.4.5. In vitro permeation assays in Caco-2 cells 277
9.4.5.1. Caco-2 monolayer culture and differentiation 277
9.4.5.2. Quality tests of the monolayer integrity 277
9.4.5.3. Permeation assays in Caco-2 cells 278
9.4.5.4. Staining and confocal imaging 278
9.4.5.5. FITC-BSA quantification by fluorescence in a spectrofluorometer 279
9.4.5.6. Lucifer yellow quantification by fluorescence in a multiwell plate reader 279
9.4.5.7. Enzyme-linked immunosorbent assay (ELISA) quantification of the insulin 280
9.4.6. In vitro DNA assays 281
9.4.6.1. DNA stock solutions and determination of the DNA concentration 281
9.4.6.2. Titration of the DNA sequences free in medium, without DELOS-NV 281
9.4.6.3. Titration experiment to evaluate the Anti-miR21 fluorescence in different scenarios 282
9.4.6.4. Titration experiment to test the impact of the Anti-miR21 and OligoQ molar ratio in presence of DELOS-NV 282
9.4.6.5. Kinetic assay: Impact of the DELOS-NV concentration in the miR21 recognition 283

9.4.6.6. Binding assay miR21 to the DNA-grafted DELOS-NV biosensor 283
9.4.6.7. Binding assay of non-specific miRNA to the DNA-grafted DELOS-NV biosensor 284

9.5. Design of experiments and statistical analysis 284

9.6. References 285

SCIENTIFIC CONTRIBUTIONS 287

List of Abbreviations

A	Abs	Absorbance
	ADME	Absorption, distribution, metabolism, and excretion
	AEMPS	Agencia Española de Medicamentos y Productos Sanitarios
B	BHQ	Black hole quencher 1
	BKC	Benzalkonium chloride
	bRo5	Beyond rule of 5
C	CD	Circular dichroism
	Chol	Cholesterol
	CIGB	Centro de Ingeniería Genética y Biotecnología
	CMC	Critical micellar concentration
	CO_2	Carbon Dioxide
	CPC	Cetylpyridinium chloride
	CQA	Critical quality attributes
	Cryo-TEM	Cryogenic transmission electron microscope
	CSIC	Consejo Superior de Investigaciones Científicas
	CTAB	Cetyltrimethylammonium bromide
D	DC-Chol	DC-Cholesterol; Cholesteryl N-(2-dimethylaminoethyl)carbamate
	DELOS	Depressurization of an expanded liquid organic solution
	DELOS-NV	DELOS nanovesicles
	DiD	1,1'-dioctadecyl-3,3,3',3'-tetramethyl-indodicarbocyanine perchlorate
	DiI	1,1'-dioctadecyl- 3,3,3',3'-tetramethyl-indocarbocyanine perchlorate
	DLS	Dynamic light scattering
	DMSO	Dimethyl sulfoxide

	DNA	Deoxyribonucleic acid
	DoE	Design of experiments
	dPBS	Dulbecco's phosphate-buffered saline
E	ECACC	European Collection of Authenticated Cell Cultures
	EE%	Entrapment efficiency (%)
	ELISA	Enzyme-linked immunosorbent assay
	ELS	Electrophoretic light scattering
	EMA	European Medicines Agency
	EtOH	Ethanol
F	FBS	Fetal bovine serum
	FDA	US Food and Drug Administration
	FITC-BSA	Fluorescein isothiocyanate bovine serum albumin
	FRET	Förster resonance energy transfer
G	G'	Storage (or elastic) modulus
	G''	Loss (or viscous) modulus
	GMP	Good Manufacturing Practices
	GRAS	Generally recognized as safe
	GUV	Giant unilamellar vesicles
H	HBSS	Hanks' balanced salt solution
	HEPES	4-(2-hydroxyethyl)-1-piperazineethanesulfonic acid
	HPLC	High-performance liquid chromatography
I	ICH	International Council for Harmonization
	ICMAB	Institute of Materials Science of Barcelona
	IID	Inactive ingredients database
	ITC	Isothermal Titration Microcalorimetry
K	KCl	Potassium chloride
	lncRNA	Long non-coding ribonucleic acid
L	LoD	Limit of detection
	LoQ	Limit of quantification
	LUV	Large unilamellar vesicles
M	MALS	Multiangle Light Scattering
	MEM	Minimum essential medium
	min	Minutes
	miR21	Micro ribonucleic acid 21
	miRNA	Micro ribonucleic acid
	MKC	Miristalkonium chloride

	MLR	Multiple Linear Regression
	MLV	Multilamellar vesicles
	mRNA	Messenger ribonucleic acid
	MTS	3-(4,5-dimethylthiazol-2-yl)-5-(3-carboxymethoxyphenyl)-2-(4-sulfophenyl)-2H-tetrazolium
	MVV	Multi-vesicular vesicles
	MW	Molecular weight
N	n	Sample size; number of replicates
	N_2	Nitrogen
	Na_2HPO_4	Sodium hydrogen phosphate
	NaCl	Sodium chloride
	$NaH_2PO_4 \cdot 2H_2O$	Sodium phosphate monobasic dihydrate
	$NaHCO_3$	Sodium bicarbonate
O	OD_{260}	Optical Density at 260 nm
	OFAT	One factor at a time
P	P	Pressure
	P_{app}	Apparent permeability coefficient
	PdI	Polydispersity index
	PEG	Polyethylene glycol
	PEO	Polyethylene oxide blocks
	PES	Polyethersulfone
	PEST	Penicillin/streptomycin solution
	PI	Isoelectric point
	PLGA-PEG-PLGA	Poly(lactide-co-glycolide)-block-poly(ethylene glycol)-block-poly(lactide-co-glycolide)
	Plx407	Poloxamer 407
	PPO	Polypropylene oxide block
	Pre-mRNA	Pre messenger RNA
Q	q	Modulus of scattering vector in SAXS
R	rhEGF	Recombinant human epidermal growth factor
	RNA	Ribonucleic acid
	rRNA	Ribosomal ribonucleic acid
	RSM	Response surface methodology
S	SAS	Supercritical anti-solvent
	SAXS	Small angle X-ray scattering
	SC	Subcutaneous
	SCF	Super Critical Fluid
	SC-RPE	Supercritical reverse-phase evaporation

	SD	Standard deviation
	siRNA	Small interfering ribonucleic acid
	S-MLS	Static multiple light scattering
	snRNA	Small nuclear ribonucleic acid
	Sol-gel	Solution to gelation
	SUV	Small unilamellar vesicles
T	T	Temperature
	t	Time
	TEER	Transepithelial electrical resistance
	TFF	Tangential flow filtration
	tRNA	Transporter ribonucleic acid
	$T_{sol\text{-}gel}$	Transition temperature from solution to gelation
U	UAB	Universitat Autònoma de Barcelona
	US	United States
	UV	Ultraviolet
	UV-Vis	Ultraviolet-visible
W	WHO	World Health Organization
Z	Z-potential	Zeta potential
Other	δ	Phase angle
	λ	Wavelength

1 Introduction

1.1. An overview on drug discovery evolution

Drugs have been used since the beginning of civilization. The word "drug" comes from the French "Drogue" which means "dry herb"[1]. In Mesopotamia, around 2600 BC, the first reports of drugs were written on clay tablets. They used substances derived from the plants for the treatment of different diseases such as coughs and parasite infections. First Egyptian medicines also date back to those years, although the best well-known report, the "Ebers Papyrus", dates from 1500 BC. This report described mostly drugs obtained from plants, but also from animal organs and minerals. The first Chinese record dates from about 1100 BC[2] and they also employed herbs as medicinal products.

In the following centuries, these plant-derived compounds led to the development of "pure" substances. A good example is morphine, which was isolated from opium extracts by Sertüner in 1815[3]. This evolved into the first natural pure commercial product by E. Merck in 1826. The first semi-synthetic commercial product was the aspirin, sold by Bayer in 1899[2]. By this date, some essential fundamentals of chemistry had been settled, such as Avogadro's atomic theory, the establishment of the periodic table, the theory of acids and bases, and the theory of the structure of aromatic organic molecules (Benzene theory). The Benzene theory boosted the research on co-altar derivatives, especially dyes. The selective affinity of certain dyes for specific tissues made Paul Ehrlich postulate the existence of chemoreceptors. He argued that those chemoreceptors were different between species and also in cancer cells and that they could be targeted for disease treatment[3,4]. All these advances, by the beginning of the 20th century, paved the way for the development of the first rational-designed synthetic drugs, such as arsphenamine. During the beginning of the 20th century, also penicillin was discovered by Alexander Fleming (1928)[3]. However, at this time, the technologies available for drug discovery were very limited.

The middle years of the 20th century were distinguished by the use of *in vivo* testing to evaluate the pharmacokinetics of drugs[3]. It was not until the 1800s that novel design and screening technologies were developed, such as the nuclear magnetic resonance spectrometer and the high throughput screening method. All these technological advances contributed to the quick obtainment of large

libraries of drugs. In addition, not only the discovery, but also the optimization of drug compounds was expedited, and gained importance in the drug development process[3,4]. Genetic engineering also gained importance by the end of the 20th century. Hence, insulin, which was first introduced in 1922 for the treatment of diabetes[5], was reintroduced in 1982 as a product of DNA recombinant technology. Since then, numerous proteins have been developed for therapeutic use[3].

By that time, advances in molecular biology, coupled with the completion of the Human Genome Project, resulted not only in a better understanding of critical disease-relevant targets but also in increasing interest in addressing these targets. Over the past decades, there has been a slow but steady transition from traditional small molecules and proteins to novel drug modalities (e.g., beyond the rule of 5 (bRo5) compounds, oligonucleotides, antibody-drug conjugates...) designed to modulate complex biological targets once considered "undruggable". As the pharmaceutical landscape broadens with an expanding variety of drug modalities, there arises a parallel need for more creative drug delivery approaches driven by the inherent challenges of novel modalities, such as poor stability and permeability under physiological conditions[6–8].

The first modern drug delivery systems were designed in the middle of the 20th century. However, until 1989, most of them consisted of oral and transdermal formulations of small molecules designed for extended release of up to 24 h. They were mostly composed of microparticles. In 1989, the commercialization of Lupron Depot® opened the door for long-acting injectables, extending the drug release period to up to several months. The liposomes were first discovered by Alec Bangham in 1964[9,10]. However, they were not commercialized until 1995, with the approval of the pegylated liposome formulation Doxil® for the delivery of the doxorubicin. The approval of Doxil® together with the launch of the National Nanotechnology Initiative by the U.S. government in the year 2000 promoted the research in nanomedicine. Nanomedicine is the study of nanotechnology applied to the drug discovery and delivery field. The onset of the nanomedicine revolution transformed the field of drug delivery systems. Nanometric drug delivery systems emerged as a creative alternative for delivering challenging-to-formulate drugs, and research in the area of nanomedicine gained force. Actually, the extensive research in nanomedicine resulted in the development of the well-known lipid nanoparticle formulations for COVID-19 vaccine delivery in 2020. The rapid development of these vaccines would have not been possible without the extensive knowledge generated in nanomedicine over the last two decades[9].

Summarizing, drug development has evolved from early serendipitous discoveries to the rational design of molecules based on existing compounds, and now to the identification of diseases and their related biochemical pathways as starting points. This evolution in drug discovery has been propelled by novel technologies and an increased understanding of the human genome and molecular pathways. Consequently, the complexity of drug discovery has increased, requiring a flexible and divergent approach. Biotechnological industries have emerged as 'discovery' industries, composed of scientists from various disciplines (e.g., chemists, pharmacists, biologists, geneticists) to advance drug discovery[4]. In this complex framework, alongside the evolution of drugs, drug delivery systems, particularly those utilizing nanoparticles, have gained critical importance. These advanced delivery systems are essential for addressing the challenges associated with novel drug modalities, thereby playing a pivotal role in the future of drug discovery.

1.2. Nanoparticles as drug delivery systems

As mentioned previously, the launch of the National Nanotechnology Initiative by the U.S. government in the 2000 expelled the research in nanomedicine. This initiative was then followed by other countries, contributing to the nanotechnology and nanomedicine advancement[9].

Nanomedicine encompasses several fields of research, with drug delivery accounting for approximately 50% of the research[11]. Nanoparticles are being explored for their potential as nanometric drug delivery systems, able to carry and release drugs into specific tissues or organs in the body. Nanoparticles are defined by the International Organization for Standardization (ISO) as a nano-object with all the external dimensions in the nanoscale[12].

Nanoparticles can be designed to accumulate in certain organs through passive or active mechanisms. Passive targeting refers to the accumulations of particles in damaged tissues such as tumors and inflamed tissues by the enhanced permeability and retention (EPR) effect[11,13–15]. Damaged tissues are characterized by presenting tight junction gaps between 100 and 800 nm[14]. Thus, the nanovesicles tend to passively accumulate on them, reducing cytotoxicity to healthy tissues. Active targeting is achieved by attaching cell-specific ligands, which are overexpressed in damaged tissues, to the nanoparticles, such as antibodies, peptides and vitamins[11,15,16]. In addition, nanoparticles can be designed to release the cargo in a specific way. They can release their cargo gradually, avoiding peaks of concentration and the associated toxicity. An example is the Doxil®, a liposomal formulation designed to reduce the cytotoxicity of the doxorubicin anticancer drug[14]. Nanoparticles can also be designed to release the cargo in response to an external stimulus such as the pH-responsive nanovesicles developed in Nanomol-Bio (Institute of Materials Science of Barcelona, ICMAB-CSIC)[17]. These nanovesicles contain the ionizable sterol derivative cholesteryl N-(2-dimethylaminoethyl) carbamate (DC-Chol), which deprotonates inside tumoral cells due to their higher pH (7.6) compared to the bloodstream pH (7.4). This change in surface charge causes the negatively charged miRNA cargo, attached to the nanovesicles through electrostatic forces, to be released from the nanovesicles[17]. COVID-19 vaccine lipid nanoparticles (LNP) are also an example of stimuli-responsive nanoparticles. These LNPs contain ionizable lipids that protonate in the acidic environment of the endosomes. This protonation enables them to interact with the negatively charged phospholipids of the endosomal bilayer, releasing the mRNA cargo and aiding its escape from the endosomes[18,19].

Initially, nanoparticles were specially investigated for tumor-targeted drug delivery, to leverage the EPR effect and reduce the side effects commonly associated with anticancer drugs[9]. However, their potential goes beyond this disease, as demonstrated with the COVID-19 vaccine. Apart from reducing the side effects, nanoparticles are also a creative approach to deliver molecules with poor drug-like properties, such as molecules highly hydrophobic, molecules with low permeability through cellular membranes, and/or even labile molecules with a tendency to degrade. As an example, Nanomol-Bio and Nanomol Technologies have employed nanoparticles to deliver labile biomolecules on several occasions, demonstrating their protective capabilities against enzymes[17,20–22].

There are different nanoparticles that can be classified according to their composition and nature (**Figure 1.1**). The simplest classification would be into organic and inorganic nanoparticles[23]. This

simplistic classification would include several families of nanoparticles in each group. The organic nanoparticles include polymeric-based nanoparticles (polymeric nanoparticles, polymeric micelles, nanogels and dendrimers); lipid-nanoparticles (lipid nanovesicles such as liposomes, lipid micelles, lipid nanoparticles); protein-based nanoparticles (virus-like nanoparticles, protein complexes); among others. Inorganic nanoparticles include carbon-based nanoparticles, which are composed exclusively of carbon atoms (Fullerenes, carbon quantum dots); metal nanoparticles (gold nanoparticles); ceramic nanoparticles and semiconductor nanoparticles among others[13,15].

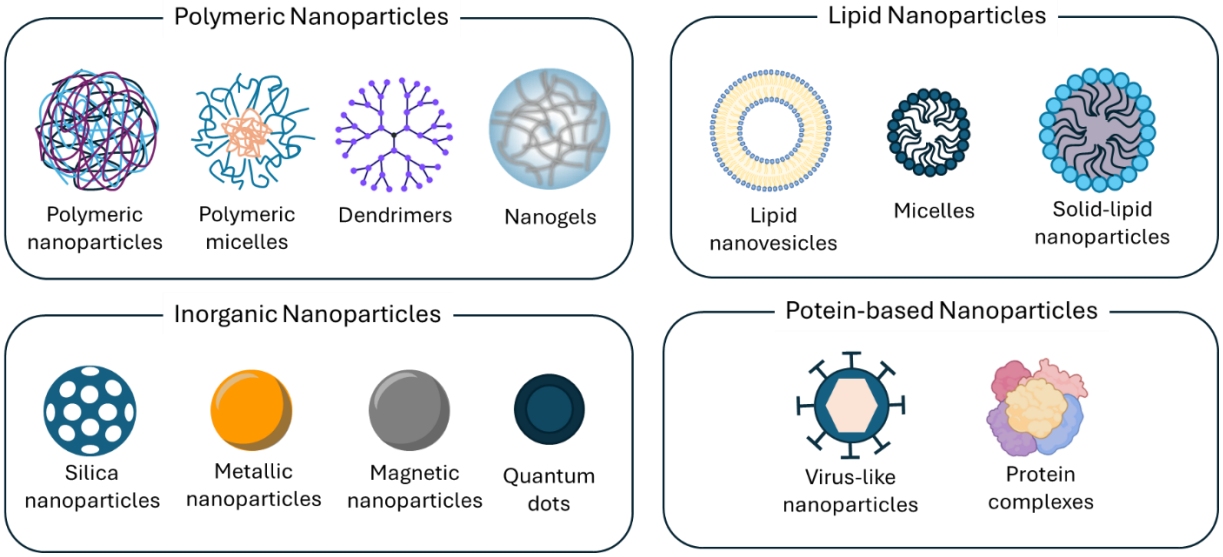


Figure 1.1. *Classification of nanoparticles based on their composition and different examples of each category. Adapted from Z. Gu, et. al.*[15].

1.2.1. Self-assembled lipid nanovesicles as drug delivery systems

Nanovesicles are nanometric sphere-shaped bilayered vesicles. They are composed of amphiphilic molecules that in aqueous media self-organize into enclosed bilayers, delimiting an internal hydrophilic core. Their structure makes them highly versatile drug delivery systems, as they can integrate hydrophilic molecules into their core or attach them to their surface, and accommodate hydrophobic molecules within the hydrophobic bilayer[24]. Most of them are lipid-based, although there are also nanovesicles formed by other components such as proteins[25].

Self-assembled nanovesicles are built spontaneously. Self-assembly is a process by which atoms, molecules, or functional building blocks are joined into well-organized hierarchical structures through non-covalent interactions such as hydrophobic, ionic, π– π stacking, and hydrogen bonding. Self-assembly occurs naturally in the environment, where building blocks such as proteins, carbohydrates, lipids, and nucleic acids organize into functional supramolecular structures[26,27]. The low-energy binding in self-assembled supramolecular structures can confer stimuli-responsive behavior to them. The organization of supramolecular structures can change in response to environmental conditions, a very necessary attribute for biological organisms. Small molecular amphiphiles have been extensively explored as self-assembling molecules. They possess both

hydrophilic (water affinity) and lipophilic (water-repellent) properties[26]. Thus, their self-assembly is led by hydrophobic forces in aqueous media aiming to achieve a state of minimum free energy and maximum stability[26,28]. In addition, intermolecular polar interactions, such as electrostatics and hydrogen bonding, can also occur and contribute to defining the structure[28].

The organization of the supramolecular structure formed by the amphiphilic molecules in water depends mostly on the geometry of the amphiphiles (**Figure 1.2**). The simplest approximation determines the geometry of an amphiphile with the packing parameter "p", defined in **Equation 1.1**. Based on this packing parameter, the preferred curvature of the aggregates can be predicted, and thus, the final supramolecular structure that will self-assemble in water: p<1/3 spherical micelles; 1/3<p<1/2 cylindrical micelles; 1/2<p<1 vesicles; p=1 planar bilayers; p>1 reverse micelles (**Figure 1.2**)[28].

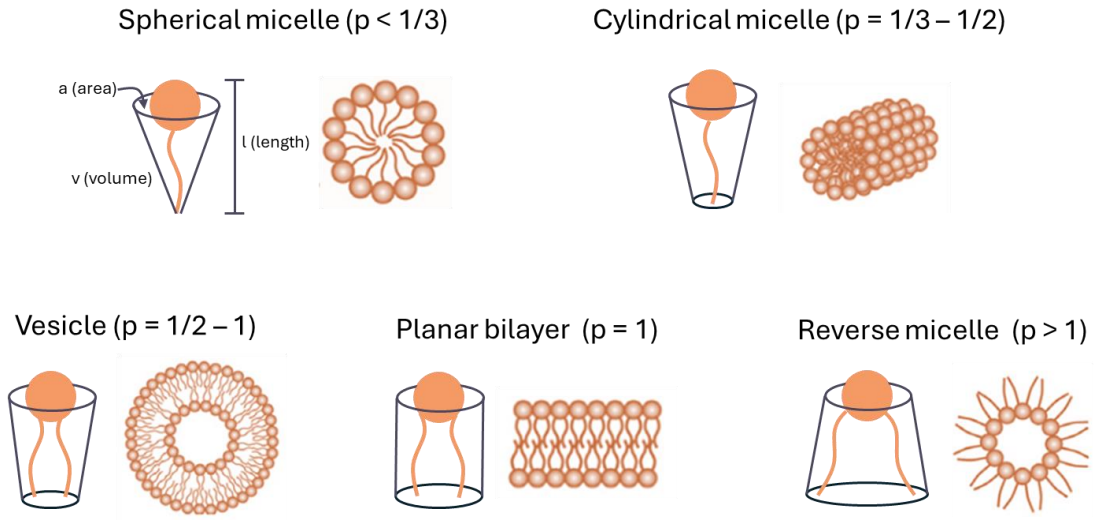


Figure 1.2. *Relationship between the packing parameter "p" and the self-assembled morphology of amphiphilic molecules in aqueous conditions. Figure obtained from E. Elizondo et. al.* [28].

$$p = \frac{v}{al}$$

Equation 1.1. *Packing parameter "p", where "v" refers to the volume of the hydrophobic tail, "a" to the area of the hydrophilic head and "l" to the length of the hydrophobic tail.*

Therefore, nanovesicles are self-assembled in water by amphiphilic molecules with a packing parameter 1/2<p<1. Apart from the packing parameter, the external environment in which the process occurs also impacts the morphology of the self-assembled structures. As an example, the temperature or the concentration of amphiphilic molecules can affect the final structure organization. Therefore, predicting the supramolecular structure is challenging due to the spatial complexity and the relative weakness of the intermolecular interactions[29].

Based on the geometry of the amphiphiles, the external environment, and the methodology used for their production, nanovesicles with different sizes and lamellarity (i.e., number of bilayers) can be obtained. Usually, they are broadly classified into small unilamellar vesicles or nanovesicles (SUV; <200 nm and a single bilayer), large unilamellar vesicles (LUV; 200-1000 nm and a single bilayer),

giant unilamellar vesicles (GUV; >1000 nm and a single bilayer), multilamellar vesicles (several concentric bilayers) and multivesicular vesicles (small vesicles entrapped in a larger vesicle) (**Figure 1.3**)[24].

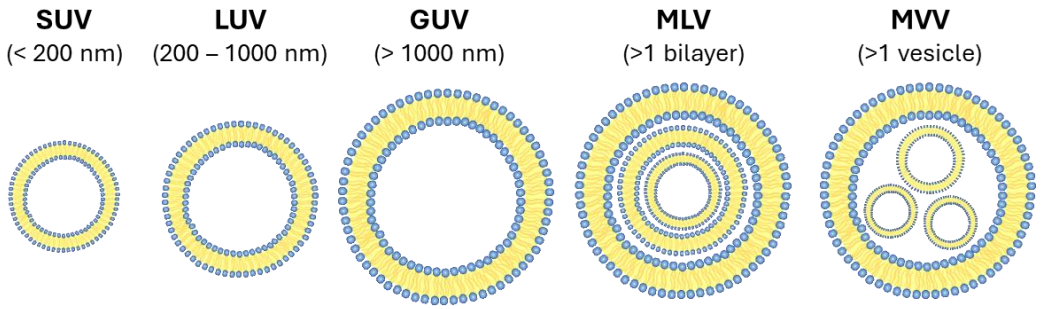


Figure 1.3. *Classification of self-assembled nanovesicles based on their size and lamellarity: small unilamellar vesicle (SUV); large unilamellar vesicle (LUV); giant unilamellar vesicle (GUV), multilamellar vesicle (MLV) and multivesicular vesicle (MVV).*

Among the different types of vesicles, small unilamellar vesicles (SUV) are preferred as drug delivery systems. They are large enough to avoid rapid clearance by the kidneys but not so large to be extensively taken up by the mononuclear phagocytic system, thus increasing their residence time in the blood. Their small size also enables the EPR effect in tumors and damaged tissues, facilitating their accumulation in these areas. In addition, in comparison to MLV and MVV, SUV allow a more accessible and homogeneous membrane functionalization which results in a more homogeneous and sharp response to stimulus[24].

The most well-known SUV are the liposomes. As mentioned in **Section 1.1**, they were discovered by Alec Bangham in 1964[9,10] although it took 30 years to commercialize Doxil®, the first drug based on liposomes[9]. Since their discovery, they have been extensively studied as drug delivery systems due to their ability to stabilize and protect compounds within the body, deliver them to target tissues, provide high biocompatibility and degradability, and excellent membrane permeation. However, liposomes also have several drawbacks, including poor colloidal stability, short shelf-life, which highly depends on the final pharmaceutical form, and limited and expensive scalability, basically because of the price of phospholipids, their fundamental constituents[24]. In consequence, alternative self-assembled lipid nanovesicles, non-liposomal, are being studied to overcome some of the liposomes' limitations.

1.2.2. DELOS nanovesicles: A novel class of non-liposomal lipid nanovesicles

To try to leverage the potential of lipid-based nanovesicles while overcoming the limitations of liposomes, different types of non-liposomal lipid nanovesicles are being studied. Non-liposomal lipid nanovesicles contain at least a natural and/or a synthetic lipid as a fundamental component of the bilayer[24]. The **Table 1.1** summarizes different examples of non-liposomal lipid nanovesicles and compares their properties to liposomes.

Table 1.1. *Examples of non-liposomal lipid nanovesicles, their main composition, and benefits (labeled with **+**) and drawbacks (labeled with **-**)*[21,24,30].

Lipid nanovesicles	*Main composition*	*Benefits (+) and drawbacks (-)*
Niosomes	*Cholesterol* *Non-ionic surfactants*	**+** *Non-ionic surfactants as cheaper and more stable alternatives to phospholipids.* **-** *Short stability.*
Transfersomes	*Phospholipids* *Surfactants*	**+** *Highly deformable nanovesicles and enhanced permeability through skin in comparison to liposomes.* **-** *Low Chemical stability due to oxidation. Lack of purity of natural phospholipids.*
Ethosomes	*Phospholipids* *Alcohol*	**+** *Nanovesicles with enhanced skin permeation lead by the alcohol effect, which can affect the intercellular regions of the stratum corneum.* **-** *Short stability.*
Sphingosomes	*Cholesterol* *Sphingolipids*	**+** *Enhanced resistance to hydrolysis and better drug retention in comparison to liposomes. Stable for several months.* **-** *High cost of sphingolipids and low entrapment efficiency.*
Ufasomes	*Fatty acids*	**+** *Improved stability and better entrapment efficiency in comparison to liposomes.* **-** *Short stability and low entrapment efficiency of hydrophilic compounds. Risk of skin toxicity.*
Pharmacosomes	*Phospholipids* *Drugs*	**+** *Drugs are covalently linked, increasing the entrapment efficiency and avoiding leakage.* **-** *Short stability.*
Virosomes	*Phospholipids* *Viral envelope proteins*	**+** *The viral proteins confer on the virosomes enhanced cellular permeation and endosomal scape.* **-** *Short stability. Risk of immunogenicity.*
DELOS nanovesicles (Quatsomes)	*Cholesterol* *Cationic surfactants*	**+** *Highly stable nanovesicles (over years), with intrinsic antimicrobial activity. Cationic surfactants as cheaper and more stable alternatives to phospholipids.* **-** *Risk of cytotoxicity.*

As shown in the table, different strategies can be employed to address some of the liposomes' limitations. Depending on the objective, some lipid nanovesicles may be more suitable than others. Among these alternatives, DELOS nanovesicles (DELOS-NV), also known as Quatsomes, are an outstanding drug delivery system due to their extremely high stability, even upon dilution or temperature changes, their in-built antimicrobial activity[31–35], and their membrane components, which are inexpensive and accessible in pharmaceutical-grade[24].

These nanovesicles were discovered serendipitously by the Nanomol-Bio group about fifteen years ago[36]. In aqueous media, the cholesterol (Chol) is insoluble and forms crystals, while the cetyltrimethylammonium bromide (CTAB) surfactant, due to its geometry, self-assembles into micelles. They found that an equimolar mixture of Chol and CTAB in water formed nanovesicles (**Figure 1.4**). Molecular dynamics showed that these two components in aqueous media self-assemble forming stable amphiphilic bimolecular building blocks with the appropriate geometry and packing parameter to form SUV[37]. These nanovesicles can be found in the literature as Quatsomes (inspired by the QUATernary ammonium surfactant used for their production), although Nanomol Technologies refers to them as DELOS-NV, in honor to the technology used for their production, and explained in detail in **Section 1.3.2.1.1**.

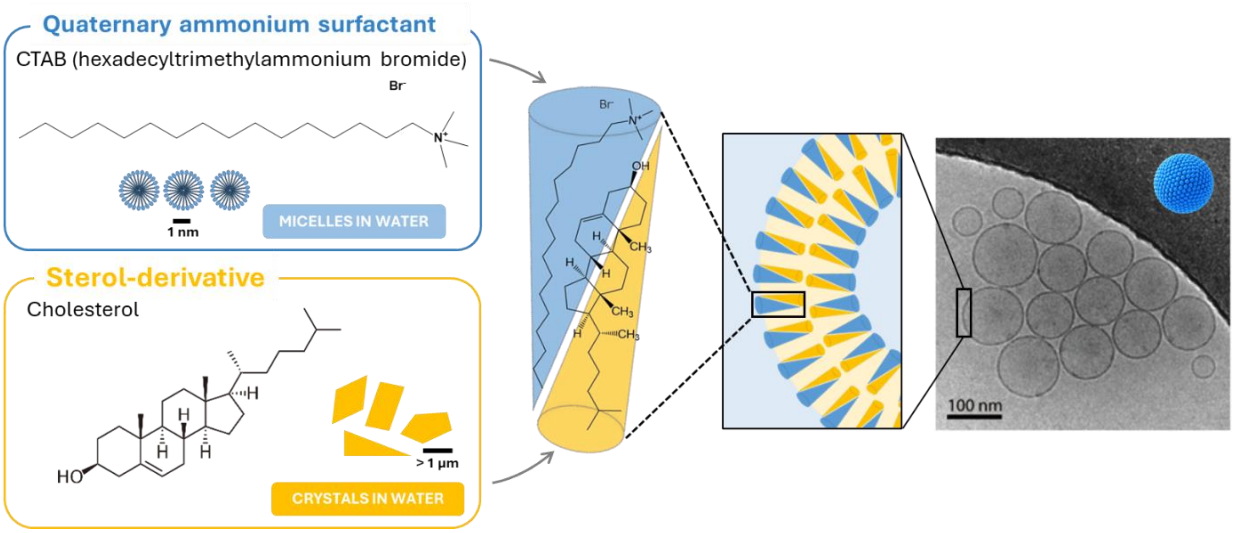


Figure 1.4. Schematic representation of DELOS-NV composed by CTAB and Chol. Both components self-assemble in an equimolar ratio to form a structure that behaves as an amphiphilic molecule, which in turn is organized forming the membrane bilayer of a nanovesicle. Adapted from Ferrer-Tasies et al.[37].

Since their discovery, different quaternary ammonium surfactants (e.g. myristyl trimethyl ammonium bromide (cetrimide)[37] and myristalkonium Chloride (MKC)[38]) and sterol derivatives (e.g. β-sitosterol[37] and cholesteryl N-(2-dimethylaminoethyl)carbamate (DC-Chol)[17]) have been tested for the DELOS-NV production with success. The DELOS-NV have demonstrated their potential as drug delivery systems of nucleic acids[17], proteins[21,39] and small molecules[40,41], and also as fluorescent probes[30,38,42–44] for diagnostic purposes. In addition, they are small, unilamellar and highly homogeneous in terms of size and morphology, which makes them ideal candidates to be functionalized and provide a sharp and homogeneous response. For example, the poly(ethylene glycol) (PEG) polymer has been efficiently anchored to their surface, reducing their opsonization and increasing their circulation time in blood-stream[39].

Therefore, these versatile DELOS-NV, capable of entrapping a wide range of substances—from small molecules to biologics, both hydrophilic and hydrophobic— and with demonstrated thermodynamic stability over time, are a promising theragnostic system for application in nanomedicine.

1.3. Technologies to prepare nanovesicles

There are different technologies that can be employed to prepare nanovesicles. They have been extensively reviewed in the bibliography[28,45,46]. The quality of nanovesicles—including their size, morphology, lamellarity, and homogeneity—is influenced not only by their composition but also by the production method. Therefore, the choice of preparation method significantly impacts the characteristics of the resulting nanovesicles and must be carefully considered. Additionally, the scalability of the method and its compliance with Good Manufacturing Practices (GMP) regulations are crucial factors in the development of pharmaceutical products for clinical use. This is particularly important because most conventional preparation methods involve organic solvents, which must be limited to concentrations within the guidelines established by the regulatory agencies for pharmaceutical products[47,48]. In this **Section**, the different methods used for nanovesicles production will be disclosed, with special emphasis on those that can be scaled up for the industrial production of pharmaceutical products.

1.3.1. Conventional methods for nanovesicles production

Conventional methods mostly involve the solubilization of the lipid membrane components in an organic solvent followed by the drying of the solvent and hydration of the dried lipids to obtain nanovesicles. The drying and hydration step order is inverted in some methods[45]. By these methods, the nanovesicles obtained tend to present large size and polydispersity, as well as multilamellarity. Commonly, these conventional methods require a downsizing and homogenization step to transform the obtained GUV, MLV and MVV vesicles into SUV and LUV nanovesicles[28,45,46]. Requiring several production steps results in time-consuming processes with lower reproducibility. Mainly for this reason, these methods are difficult to scale up in a cost-effective and reproducible way. In addition, these methods usually require large quantities of organic solvents that are difficult to remove to comply with pharmaceutical limitations. Despite all these drawbacks, they also have some benefits, specifically for laboratory production of nanovesicles, which are the simplicity of the process and the low requirement of technology in most cases. The most common example of conventional methods is the *Thin film hydration* method, where the membrane components are dissolved in an organic solvent that is subsequently removed through evaporation, forming a thin film of dried lipids. This film is then hydrated with aqueous media, resulting in the formation of nanovesicles. Other common examples are the *Ethanol/ether injection method*, the *Reverse phase evaporation method,* and the *Detergent depletion method*. In the *Ethanol/ether injection method,* the lipids are dissolved in an organic solvent and injected into an aqueous phase where liposomes are formed at high temperatures or low pressure. In the *Reverse phase evaporation method,* lipids are dissolved in an organic solvent and water is added to the mixture. The lipids rearrange at the interface water-oil microemulsion in inverted micelles. Upon removal of the organic solvent, some inverted micelles break, and the free phospholipids reorganize over the remaining micelles forming nanovesicles. In the *Detergent depletion method,* the lipids are solubilized in a detergent solution and form mixed micelles (detergent/lipid). Then, the mixed micelles are further diluted in buffer, and their size increases until the spontaneous formation of nanovesicles[28,45,46].

There are other methods, but those aforementioned are a good example of conventional methods. As commented before, these methods commonly require a downsizing and post-formation processing to obtain the desired nanovesicles quality (**Figure 1.5**). The most common post-processes are the *Sonication method*, the *Extrusion method,* and the *High-pressure homogenization method*. All these down-sizing and homogenization methods require high mechanical energies to disrupt the GUV, MLV and MVV into small membrane patches that can afterwards self-assemble into SUV. However, the use of these high mechanical energies can damage labile molecules, thus reducing the versatility of compounds that can be effectively entrapped in the nanovesicles prepared by conventional methods[28].

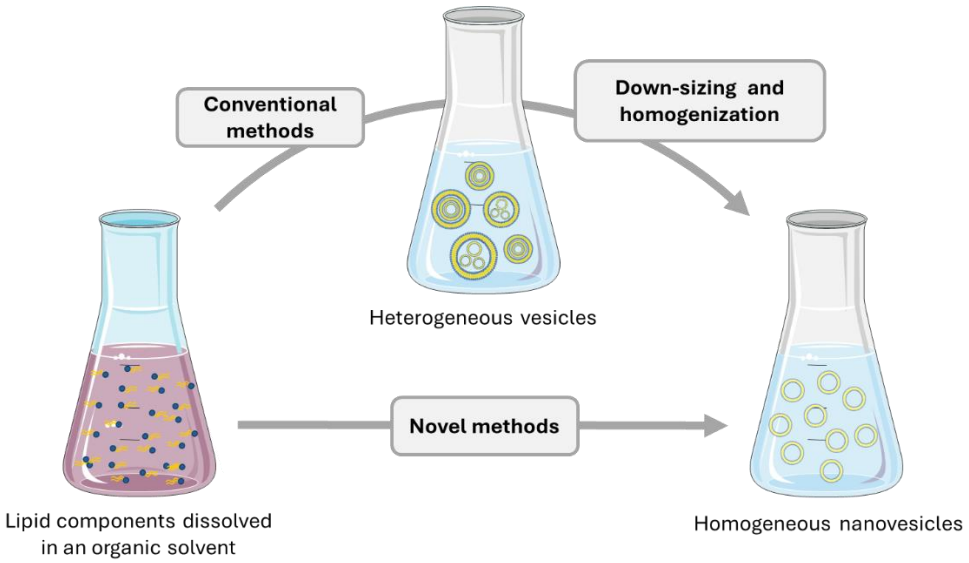


Figure 1.5. *Different methods to achieve homogenous vesicles starting from their membrane components dissolved in an organic solvent.*

1.3.2. Novel methods for nanovesicles production

Conventional methods are characterized by low scalability, poor entrapment efficiencies, and limited capacity for processing labile molecules (such as biomolecules) due to exposure to organic solvents, detergents, and high mechanical forces. These challenges motivated the research into novel technologies capable of producing nanovesicles in a single step. The most relevant novel technologies will be disclosed in the present section.

An example of novel technology for nanovesicles production is the *Lyophilization method*. Lyophilization is a common procedure in pharmaceutical development that consists of sublimating (i.e., the phase change from solid to gas) water of pharmaceutical products to improve their shelf stability. Lyophilization has been used also for nanovesicles production by dissolving the lipids in alcohol at 45 °C and cryo-preserving in water at 45 °C. Then, the solutions are mixed and lyophilized. The obtained lyophilizate will convert into liposomes upon rehydration with aqueous media. This technology is scalable; however, it is time and energy-consuming, increasing the production costs[45,46].

Microfluidics is also a recent technology employed for nanovesicles production. In microfluidics, a solution of the lipids in alcohol is hydrodynamically focused between two aqueous streams in a microfluidic channel (5–500-µm cross-section) with an accurate design, enabling a controlled diffusive mixing at the two liquid interfaces where the lipids self-assemble into vesicles. By modifying the flow, the size and polydispersity of nanovesicles can be adjusted[28,45,46]. This technique, although allows a high control of the nanovesicles morphology and is highly reproducible, is not easy to scale up. The main scalability challenge would be the cleaning of the several micro-channels that conform the system to comply with the regulatory agencies' cleanliness requirements. In addition, the shear forces intrinsic to the method could prevent the processing of labile compounds[28].

In the *Dual asymmetric centrifugation method,* vials are rotated in the main rotational axis and also in their own axis. The main rotation pushes the sample outward, while rotation around its own center pushes the sample material in the opposite direction. This induces the formation of nanovesicles through mechanical turbulence and cavitation. This method is scalable and allows obtaining small nanovesicles with high control over size. However, it only permits batch-scale production[46].

Apart from these three examples of novel technologies, there is also a group of methods which benefit from compressed fluids for the production of nanovesicles.

1.3.2.1. Supercritical fluid-based technologies to produce nanovesicles

Supercritical fluid (SCF)-based technologies emerged in the early 1990s as an alternative to conventional technologies employing liquid solvents[28,49]. They were mostly utilized for the processing of nanoparticulate solids, although they are currently being used also for nanovesicles production.

A SCF (or dense gas) is a substance that exists as a gas under normal environmental conditions of pressure and temperature (**Figure 1.6**), but above its critical pressure and temperature (i.e., at the point where the line between liquid and gas state disappears), it exhibits mass transport properties similar to gases and dissolution properties similar to liquids[28,45]. SCF-based technologies are advantageous with respect to conventional technologies because they permit to obtain liposomes in a single step. In addition, the use of SCF permits to reduce or even completely suppress the use of organic solvents. Moreover, these technologies increase the control over the physicochemical properties of the nanovesicles[50].

CO_2 is the most widely employed SCF, because it is non-toxic, non-flammable, non-reactive, economical, and non-polluting. In addition, it is recognized as safe by the Food and Drug Administration (FDA) from the United States (US) in pharmaceutical processing and it can be operated at mild conditions (31.1 °C and 74.8 bar)[28,50,51].

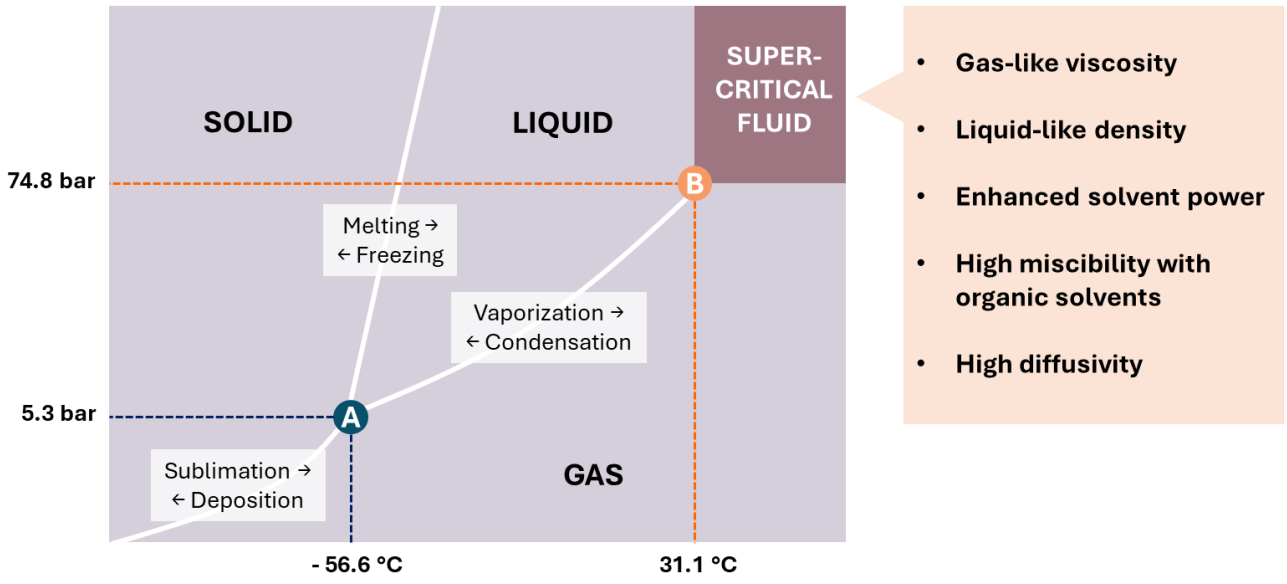


Figure 1.6. *Phase diagram of carbon dioxide (CO_2) and list of its properties in supercritical conditions. The triple point (A) and the critical point (B) are each defined by a specific temperature (T) and pressure (P). Adapted from William, B, et. al.*[50].

There are several SCF-based technologies, which can be classified according to the role that the SCF plays in the technology. It can act as a solvent (i.e., Supercritical Reverse-Phase Evaporation (SC-RPE) method), co-solvent (i.e., Depressurization of an Expanded Liquid Organic Solution (DELOS) method) or even antisolvent (i.e., Supercritical Anti-Solvent (SAS) method). When SCF act as a solvent, the lipid components are dissolved in the SCF or in a mixture SCF/organic solvent, while when acting as a co-solvent, the lipids are preliminary dissolved in an organic solvent and subsequently, the solution is expanded with the SCF. When using the SCF as a solvent, the organic solvents can be completely eliminated from the production process, however, phospholipids have low solubility on SCF-CO_2 due to their amphiphilic nature. Because of this, it is necessary to work at very high pressures when using the CO_2 as a solvent. Oppositely, when using the CO_2 as a co-solvent, the solubility problems at mild temperature and pressure conditions are solved[50]. Thus, it can be worth it to assume a residual amount of organic solvent in the formulation to work at mild conditions of pressure and temperature. This approach can permit the processing of heat-labile compounds, and reduce the capital cost of a high-pressure plant when scaling the technology[28]. SCF can also work as an antisolvent. In these methods, the SCF is mixed with an organic solution of lipids and causes the precipitation of lipids and the formation of nanovesicles' precursors. The rehydration of these nanovesicles' precursors will finally form the nanovesicles[50]. Methods based on SCF as antisolvent also work at mild conditions of pressure and temperature, and are specifically appropriate for molecules with poor solubility in SCF[51].

The Depressurization of an Expanded Liquid Organic Solution (DELOS) method is especially interesting among SCF-based technologies because it can operate at mild conditions of pressure and temperature using the CO_2 as co-solvent, and results in yielding small and homogeneous nanovesicles in terms of size and morphology. Both, hydrophilic and hydrophobic molecules can be processed with this technology, incorporating them to the aqueous phase (at environmental pressure and temperature conditions), or to the SCF/organic phase (at mild temperature and

pressure conditions), being a very versatile technology for the processing of hydrophilic, lipophilic, small and large and labile molecules. In addition, it is scalable, and thanks to the mild pressure conditions, the scalation capital cost is lower than other SCF-based technologies. Moreover, it can operate in batch-scale production or in continuous.

The following **Table 1.2** compares the different methodologies for nanovesicles production, paying special attention to those properties that differentiate them as appropriate technologies for market-production of pharmaceutical products.

Table 1.2. *Comparison between different nanovesicles' production methods based on their use of organic solvents, scalability, and compatibility with labile molecules. Color code: drawbacks in red and benefits in green.*

Method	***Organic solvent use***	***Scalability***	***Labile-molecules compatibility***
Conventional Methods			
Thin film hydration	*Large organic solvent*	*Very difficult*	*Low compatibility*
Ethanol/Ether injection	*Large organic solvent*	*Very difficult*	*Low compatibility*
Reverse phase evaporation	*Large organic solvent*	*Very difficult*	*Low compatibility*
Detergent depletion	*Large organic solvent*	*Very difficult*	*Low compatibility*
Novel Methods			
Lyophilization	*Low organic solvent*	*Scalable* *Time & energy-consuming* *Only batch-scale production*	*High compatibility*
Microfluidics	*Large organic solvent*	*Very difficult*	*Low compatibility*
Dual asymmetric centrifugation method	*Low organic solvent*	*Scalable* *Only batch-scale production*	*High compatibility*
Supercritical reverse-phase evaporation (SC-RPE)	*No organic solvent*	*Scalable* *High capital cost*	*Low compatibility*
Supercritical anti-solvent (SAS)	*Low organic solvent*	*Scalable* *High capital cost*	*High compatibility*
Depressurization of an expanded liquid organic solution (DELOS)	*Low organic solvent*	*Scalable* *Batch and continuous production*	*High compatibility*

1.3.2.1.1. The DELOS technology to produce nanovesicles

The DELOS technology was developed and patented by the Nanomol-Bio group in 2005[52]. The patent was afterwards acquired by Nanomol Technologies for its commercial use.

Initially, the DELOS technology was mostly used to produce solid particulate dispersions. Its crystallization capacity was compared to other SCF-based crystallization technologies, and the results were equivalent or even better. Since in most of the SCF-based crystallization technologies the SCF acts as an anti-solvent, while in the DELOS technology it acts as a co-solvent, it was suggested that the novel technology could be adequate for compounds with high solubility in organic solvent/SCF mixtures[53–55]. The DELOS technology for particle crystallization involved (I) the initial solubilization of the compounds of interest in an organic solvent (e.g., ethanol); (II) The expansion of the solution with SCF-CO_2 at specific pressure and temperature. At this point, it is important that SCF-CO_2 acts as a co-solvent (i.e., the compounds dissolved are below the saturation limit in the expanded solution); (III) Depressurization of the expanded solution from the working conditions to the atmospheric pressure through a valve. During depressurization, a fast, large and extremely homogeneous temperature decrease occurs, which results in the supersaturation of the compounds of interest and their very homogeneous crystallization[53,54].

Later, the DELOS technology was optimized to produce colloidal suspensions/dispersions by depressurizing lipids and/or membrane constituents over an aqueous phase[39,49,55]. This method enabled the creation of nanovesicles with very uniform size and morphology, and high reproducibility between batches. The promising physicochemical properties of these colloidal dispersions are likely due to the abrupt cooling of the solution during depressurization. The rapid temperature decrease leads to the homogeneous precipitation of dissolved membrane constituents, which self-assemble into colloidal systems upon contact with water.

Apart from offering high control over the physicochemical properties of colloidal dispersions, the novel technology provides several other benefits, which were briefly mentioned in the previous **Section 1.3.2.1**. These benefits include:

- **Eco-Friendly**: The technology uses a minimal amount of organic solvents and employs CO_2 as SCF. Additionally, CO_2 can be recirculated and reused.
- **Scalable**: It is a scalable technology with lower capital cost than most SCF-based technologies due to the mild pressure conditions required for its operation.
- **Flexible Production**: The technology permits both batch and continuous scale production, making it adaptable to market requirements.
- **Gentle Processing Conditions**: It allows the processing of labile molecules due to the mild temperature and pressure conditions required, and the low volume of organic solvents used.
- **Versatile**: It can process both, lipophilic and hydrophilic molecules, by dissolving them in the organic solvent/SCF-CO_2 mixture or in the aqueous phase.

The one-step preparation of multifunctional cholesterol-rich nanovesicles such as liposomes (phospholipid-based vesicles) and DELOS nanovesicles, as well as nanovesicle-(bio)active conjugates involves the following steps (**Figure 1.7**):

A) Addition: An organic solution of the membrane components and hydrophobic payloads -when applicable-, is added into a high-pressure vessel, at atmospheric pressure, previously pre-warmed at working T > 31.1 ºC (**Figure 1.7A**).

B) Expansion: Liquid compressed CO_2 is introduced into the reactor at working P > 74.8 bar and working T > 31.1 ºC. A homogeneous membrane components/organic solvent/SCF-CO_2 expanded solution is achieved inside the reactor. The system is let for several minutes to attain equilibration (**Figure 1.7B**).

C) Depressurization: The expanded solution is depressurized over an aqueous phase containing, if applicable, the hydrophilic payloads. A flow of N_2 at P > working P is used to plunge the CO_2-expanded solution from the reactor, maintaining a constant pressure inside the vessel during depressurization (**Figure 1.7C**).

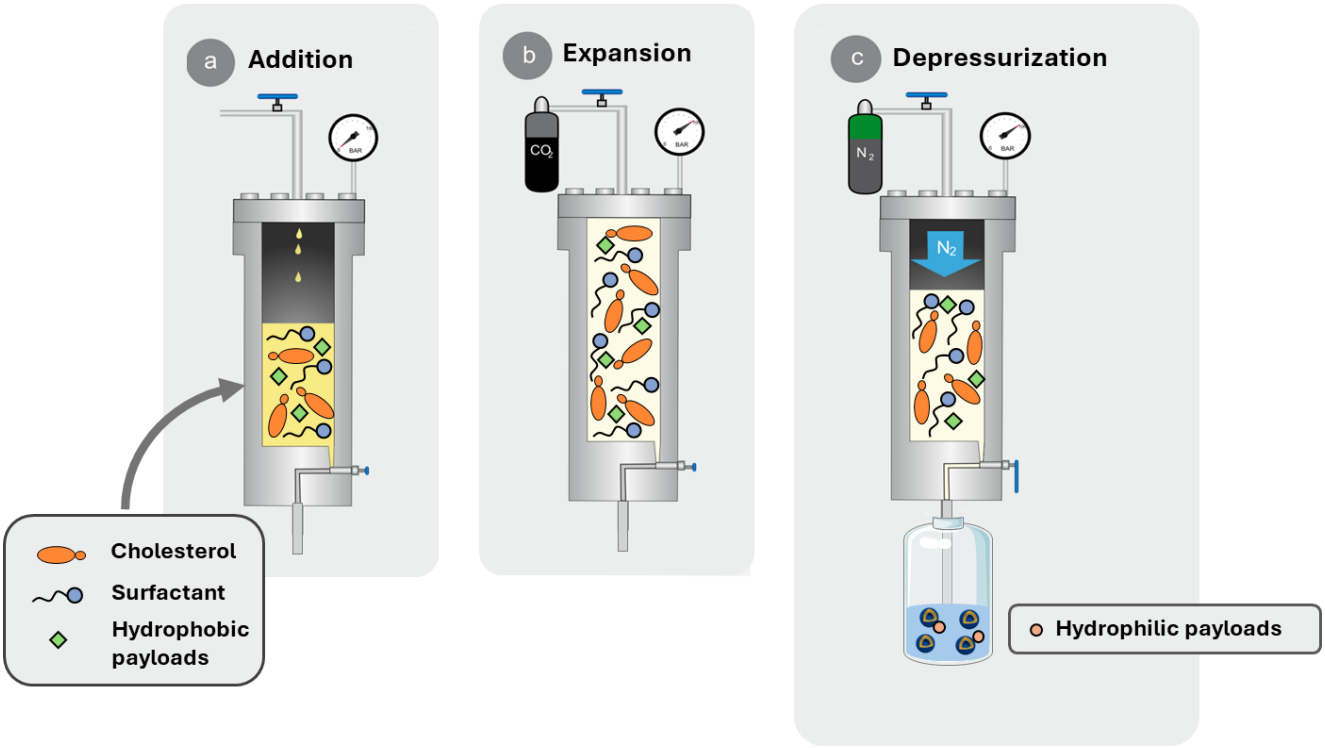


Figure 1.7. Schematic procedure of the preparation of nanovesicles by DELOS technology, including: (A) addition of the membrane components dissolved in an organic solvent, (B) expansion of the solution by the addition of compressed CO_2 acting as co-solvent, and (C) depressurization of the CO_2-expanded solution over an aqueous solution, which can contain hydrophilic (bio)molecules. More detailed explanations of DELOS technology can be found in ***Chapter 9, Section 9.2.1****.*

Since its optimization for the preparation of colloidal systems, the DELOS technology has been widely used by Nanomol-Bio and Nanomol Technologies to obtain liposomes[22,39,56], and DELOS-NV[20,42,44] nanoconjugates with various active molecules for different indications and administration routes. For instance, DELOS-NV loaded with a small hydrophobic carbocyanine (1,1'-dioctadecyl-3,3,3',3'-tetramethylindotricarbocyanine iodide, DiR) were successfully produced by DELOS method for bioimaging applications via parenteral administration[38]. Additionally, liposomes containing the enzyme α-galactosidase A were produced using the DELOS method as an intravenous treatment for

Fabry disease[22]. DELOS-NV loaded with another protein, the recombinant human epidermal growth factor, were also produced by this method as a topical treatment for complex wounds[21,57]. Beyond proteins, other biomolecules have been processed using the DELOS method, including oligonucleotides. For example, miR323a-5p was loaded into pH-responsive DELOS-NV as an intravenous treatment for neuroblastoma[17].

Hence, this technology has proven to be a powerful tool for producing nanovesicles with high structural homogeneity and controlled process parameters for different administration routes, allowing the potential translation of these new nanomedicine candidates.

1.4. Routes for drug administration

A medication administration route is understood as the body location where a drug is applied, such as oral or intravenous[58]. The selection of the most appropriate administration route depends on several factors:

- **The therapeutical objective:** The administration route directly impacts the pharmacokinetics of the drug (ADME cycle). The ADME drug cycle is composed of 4 steps: Absorption (i.e., travel from administration site to blood circulation); Distribution (i.e., drug spread over the body); Metabolism (i.e., Breakdown of drug) and Excretion (i.e., Drug elimination)[59]. It is evident that the administration route can impact ADME in several ways. As an example, absorption is instantaneous and complete for intravenous administration; the intravenous route involves injecting the drug directly into the bloodstream, providing 100% bioavailability. Therefore, for urgent treatments intravenous administration would be preferable, allowing for a rapid therapeutic effect[58].
- **The drug physicochemical properties:** The physicochemical properties of a drug candidate will impact the administration route selection[60]. For example, the efficient oral administration of a drug depends on its resistance to degradation by gastric enzymes and its capability to permeate the intestinal epithelia to reach circulation. Some of the drug's physicochemical properties to be considered are its solubility in water, lipophilicity -typically expressed as the partition coefficient (log P) between octanol and water-, molecular weight (MW) and pKa[60]. High water solubility generally improves absorption and bioavailability, especially for oral medications, because it facilitates the drug's transport across aqueous environments in the body. Lipophilic drugs tend to cross cell membranes more readily and may accumulate in fatty tissues, affecting distribution and duration of action. However, very high lipophilicity can lead to poor solubility in water and challenges in formulation and delivery. The MW also impacts since small molecules generally diffuse more easily across membranes, influencing absorption and distribution. Finally, regarding the pKa, non-ionized (uncharged) forms of drugs typically cross cell membranes more easily. Thus, understanding the pKa helps predict the drug's behavior in different body compartments with varying pH levels, such as the stomach (acidic) and intestines (neutral to basic).
- **The patient:** The patient can impact the selection of the administration route in different ways. The first thing to evaluate will be the patient's clinical state. If the patient is unable to swallow, such as an unconscious patient or a patient vomiting, the oral administration route will be

contraindicated. The same would occur with a patient with active rectal bleeding or diarrhea and the rectal administration route[58]. Patient preferences must also be considered. Nonadherence to drug therapy is one of the biggest causes of unsuccessful medical care[61]. The oral route is generally the patients' preferred route for drug delivery[61]; although many patients would prefer a weekly subcutaneous injection over daily oral medication[62]. Considering patient preferences contributes to increase adherence to a treatment and, therefore, to the success of a drug therapy[61].

- **Practical considerations:** Beyond the factors mentioned above, various practical considerations play a crucial role in selecting the appropriate administration route. These include the costs associated with each route and the dependence on healthcare professionals for administration. The COVID-19 vaccines highlighted these challenges vividly. The pandemic underscored the necessity of utilizing parenteral routes in decentralized healthcare settings to alleviate pressure on the healthcare system and manage associated costs effectively[63,64].

Entrapment of drugs in nanovesicles can also affect the administration route selection, since nanovesicles can modify the physicochemical properties of drugs, (i.e., stabilizing lipophilic drugs in water[30,44]), and alter their pharmacokinetics (i.e., increasing the blood circulation time[28,39]).

At Nanomol-Bio and Nanomol Technologies, there is extensive experience working with the DELOS-NV, produced through the DELOS technology, as novel nanocarriers for the intravenous[17,22,38] and the topical[21,57] route. However, there is a lack of experience with other administration routes, reducing the versatility of this promising drug delivery system. For this reason, the present thesis investigates the potential of formulating DELOS-NV for drug delivery via two alternative administration routes: subcutaneous and oral.

1.4.1. The subcutaneous administration route

In the subcutaneous (SC) administration, drugs are injected through a needle into the SC tissue, which is the tissue located between the skin (epidermis and dermis) and the deep fascia surrounding the muscle[63].

Although experimentation with drug administration into SC tissue began in the 19th century, it was not until 1853 that Alexander Wood coined the term "SC administration" for this procedure. Wood developed a glass syringe with a needle by combining previous inventions, which allowed him to effectively deliver morphine into SC tissue. He erroneously believed that the injection had to be in the affected area[63]. It was Charles Hunter, 5 years later, who discovered that the effect of SC administration was systemic, revolutionizing the field of medical administration[63,65].

Since then, the SC administration route has evolved considerably. In 1922, the successful SC administration of insulin promoted this administration route on an enormous scale[63]. Most of the current knowledge is based on the experience with insulin. The rise of biopharmaceuticals is also pushing the SC administration route in detriment of the intravenous route. There has been an increasing trend to deliver monoclonal antibodies subcutaneously versus intravenously[66]. In addition, currently the vast majority of peptide candidates are being developed as SC formulations[62]. Despite the oral administration route is still the preferred for patients, it might not be appropriate to all drugs. Oral administration can lead to challenges such as low bioavailability, where a significant

drug amount is lost before reaching systemic circulation. This loss can occur due to factors like degradation by stomach acid, poor absorption in the gastrointestinal tract, and first-pass metabolism in the liver. As a result, some drugs may require alternative administration routes, such as intravenous or subcutaneous, to ensure effective delivery and therapeutic outcomes[67]. In that framework, the SC administration route provides several benefits in comparison to other parenteral routes, such as convenience, lower risk of infection, ease of use, and possible self-administration at home, reducing the pressure and cost to the healthcare system[62,63,67–69]. These benefits can be specially advantageous in chronic diseases[62,66], and also in response to pandemic crisis[63,64].

1.4.1.1. Anatomy of the subcutaneous tissue and its impact on drug delivery

The subcutaneous tissue is composed of collagen, elastin, fibronectin, and proteoglycans, such as hyaluronic acid, which conform the viscoelastic extracellular matrix[63]. At physiological pH most of these components are negatively charged, resulting in faster transport of negatively charged drugs through the extracellular matrix[66]. Depending on the physicochemical properties of the drugs, they can reach systemic circulation through blood or lymph vessels. The blood uptake is mainly limited by the drug size. Only smaller size compounds (MW <16 kDa) can penetrate into blood vessels. One exception is the monoclonal antibodies, whose trans-cellular transport into blood vessels is mediated by the FcRn receptors. Oppositely, bigger-size compounds (MW >16 kDa) are mainly absorbed by the lymphatic system[62,66,69]. The lymphatic absorption results in a subsequent systemic bioavailability. Therefore, both, charge and size of the compounds can directly impact the pharmacokinetics of subcutaneously administered drugs.

The extracellular matrix also contains several enzymes which can degrade biological compounds before they reach the systemic circulation. To avoid the maximum this pre-systemic catabolism, there are several approaches that can be implemented, such as co-injecting protease inhibitors together with the medications[66], or protect the compounds with drug delivery systems, such as nanovesicles.

Apart from the mentioned factors that can affect the pharmacokinetics of drugs administered subcutaneously, other factors can also impact the absorption velocity, such as the anatomical location of the injection[66], unintentional compression of SC tissue with clothes and/or the post-injection application of heat or ice[63].

The anatomy of the subcutaneous tissue also has relevance in the volume that can be administered. The SC injection volume accepted as well-tolerated is around 1.5 mL[69,70]. However, there are medications approved that require larger volumes. In fact, some monoclonal antibodies require up to 15 mL injections. An approach to reach this high volume reducing the pain sensation is to employ hyaluronidase, an enzyme that temporarily degrades the hyaluronic acid present in the extracellular matrix[63]. The volume of medication that can be administered subcutaneously can be considered one of the major challenges of this administration route and must be addressed, especially when re-formulating medications that were previously administered intravenously. Extensive work has been focused on developing high-concentrated formulations that permit to reduce the volume administered[68].

The subcutaneous route is also gaining importance thanks to the possibility of using long-acting injectable formulations. Long-acting injectable formulations can achieve extended drug release, which results in less frequent dosing requirements leading to higher patient adherence and more optimal therapeutic outcomes[71]. Indeed, as mentioned previously, many patients would prefer a weekly SC injection over daily oral medication, making the SC route an effective approach for chronic diseases[62].

As it can be observed, the subcutaneous administration route offers several benefits, highlighting it as a promising administration route for some medications. However, it also has some drawbacks that must be considered and addressed when possible. Below are summarized the principal attributes of the subcutaneous administration route, especially in comparison to the intravenous route, the most widely studied route with DELOS-NV, and the oral route, the alternative administration route studied in this thesis**:**

- **Long-acting formulations:** The subcutaneous administration route allows for the development of long-acting formulations, such as *in situ* implants or depots, to reduce the frequency of administration[71]. Although it is possible to modify the release kinetics for oral and intravenous administration routes, very long extended-release formulations are uncommon for these routes.
- **Ease of administration:** The subcutaneous route is easier for drug administration than other parenteral routes and can be self-administered at home, reducing pressure on the healthcare system[62,63,67–69].
- **Safety:** The subcutaneous route presents low risk of infection. Additionally, if an infection occurs, it will be local rather than systemic, as could happen with the intravenous route[69,70].
- **Avoidance of liver first-pass metabolism:** Unlike the oral route, the subcutaneous route bypasses the liver upon entry into the body, reducing first-pass metabolism. First-pass metabolism is the process by which a drug is metabolized before reaching its site of action, thus diminishing the active drug in the target tissue. It is mostly associated with the liver, the principal organ of drug metabolism[72]. Although subcutaneous administration avoids the liver, it is known that there are enzymes in the subcutaneous tissue that can metabolize the medication before it reaches the systemic circulation, reducing its concentration in the target tissue[66]. The intravenous route does not suffer from this pre-systemic catabolism.
- **Invasive route**: As with all parenteral routes, subcutaneous administration requires injection with a subcutaneous needle. In comparison, the oral administration route is preferred by patients because it is non-invasive and well-known[67].
- **Slower effect**: As explained before, medication injected subcutaneously needs to travel through the extracellular matrix to the blood or lymphatic vessels. Thus, compared to the intravenous administration route, the medication takes longer to reach the systemic circulation, delaying the onset of the medication's effect.

Based on these points, the subcutaneous administration route can be particularly interesting for chronic diseases (e.g., diabetes), especially through the use of subcutaneous long-acting injectable formulations of drugs with low oral bioavailability. In contrast, the intravenous route is preferred for urgent situations since it is directly injected into the systemic circulation and provides a very quick effect (e.g., acute myocardial infarction).

1.4.2. The oral administration route

In the oral administration route, drugs are taken by mouth. This route is considered the most user-friendly and well-known[73,74], as it is the same route used for feeding in healthy individuals.

The ancient civilizations employed the oral route with administration forms named lohochs, linctuses, electuaries, conserves, confections and others. These administration forms evolved with time, and in the 19th century, the most common oral dosage forms were pills and powders, solutions, tinctures and spirits[75]. During that century, there was significant interest in improving oral dosage forms to enhance their appearance, make them more palatable and easier to swallow, and to increase control over dosage. In that context, different administration forms were developed, such as "dosimetric granules" by Abbott Laboratories, based on the idea that medications should consist of chemically pure, stable, and precise doses. By the end of that century, in 1884, Dr. Paul G. Unna introduced a novel pill coating that was stable in the gastric environment but dissolved in the presence of intestinal fluids, as a novel form of extended-release. He introduced the idea that the "form" was also equally important as the "dose" and that could impact the outcome of the medication. His discovery propelled the investigation of novel enteric coatings during the beginning of the 20th century. It was also by those dates that pharmacokinetics was born, and the concepts learned on this area could be translated into novel oral dosage forms. In addition, the success of injectable medications increased the interest in developing oral dosage forms that could perform functions beyond merely retarding the dissolution of the capsules[75]. In that context, Spansule® was marketed in 1952 as a novel 12 hours sustained-release capsule technology, settling the beginning of modern drug delivery technology[9,75]. At present, nanomedicines are considered the most promising systems for oral delivery. They aim to overcome some limitations of conventional drugs such as low site-specific accumulation of drugs, unfavorable body distribution and adverse side effects. The interests and focus are also centered on increasing the oral bioavailability of labile compounds[73]. Biopharmaceuticals are gaining significant interest due to their specific challenges in oral administration, such as poor permeability across gastrointestinal barriers and the destructive effect of enzymes in the gastrointestinal tract[74].

Apart from its potential systemic effect, the oral is also the most direct route for treating local diseases in the gastrointestinal tract[76], such as the inflammatory bowel disease (IBD)[77] or the colorectal cancer[78]. Digestive diseases and cancers have significantly increased since 2000 in Europe. Digestive cancers are the leading cause of cancer death in Europe[79]. In the United States, colorectal cancer is the second most common cause of death, and its burden is shifting to younger individuals[80]. This data evidence the necessity of developing medications with local effects on the gastrointestinal tract.

1.4.2.1. Anatomy of the gastrointestinal system and its impact on drug delivery

The oral administration route involves the gastrointestinal system, which is more complex than a single tissue, such as SC tissue. In orally administered drugs, the medication is taken by mouth and travels through the pharynx (throat) and esophagus into the stomach. The stomach has the most acidic pH in the gastrointestinal tract (1.5-2.2) and contains several digestive enzymes, such as pepsin. After the stomach, the medication moves to the small intestine, where most nutrient

absorption occurs due to the large surface area created by villi and microvilli. The small intestine has a higher pH (5.9-7.8) and different digestive enzymes. Following the small intestine is the colon, where some nutrient absorption also takes place. The colon has a pH between 6 and 6.7 and a lower proportion of digestive enzymes, primarily produced by the colon microbiota. The higher residence time and lower enzyme levels make the colon an interesting target for drug delivery. Additionally, targeting the colon allows for the local treatment of IBD and/or colorectal cancers. However, individual variations in gastric emptying and gut microflora present significant challenges to the efficacy of colon-targeted drug delivery. Finally, the process leads to the rectum and anus, which eliminate non-absorbed compounds[73,74,81].

During the transition through the gastrointestinal tract, the medication encounters different pH, the presence of digestive enzymes, and a mucus barrier which covers all the lumen surface preventing the medication from contacting the gastrointestinal epithelia. In addition, gastrointestinal epithelia are composed of cells tightly attached through tight junctions, challenging the permeation of molecules and the reaching of the systemic circulation[73,74]. This quick overview of the gastrointestinal barriers, which will be further developed in **Chapter 6**, explains the low bioavailability of the oral administration of biopharmaceuticals.

In addition, the challenges of oral efficacy are not limited to the gastrointestinal barriers but also include hepatic first-pass metabolism, which typically metabolizes a significant portion of the medication before it reaches the target tissue. Most orally administered drugs reach systemic circulation by passing directly from the enterocytes of the gastrointestinal epithelium into the mesenteric blood capillaries, and then to the portal vein. The portal vein transports the drug directly to the liver, where hepatic metabolism occurs.

A small proportion of drugs binds to fats and is secreted into the lymphatic circulation, allowing entering the systemic circulation via the post-portal bloodstream, and thus avoiding hepatic first-pass metabolism; however, these are a minority[82].

Therefore, the oral administration route presents several challenges that must be overcome, particularly related to the bioavailability of drugs. However, it is preferred by patients and can increase patient adherence to treatments, and, in addition, it is especially useful for treating local gastrointestinal diseases, which are very prevalent nowadays due to lifestyle changes[79]. Below the key points of the oral administration route are summarized**:**

- **Patient convenience:** Patients prefer oral medication to invasive routes such as parenteral administration routes. Therefore, the oral route can increase the patient's adherence to treatment and, subsequently, its outcome[73,74].
- **Ease of administration:** In comparison to the intravenous route, it can be self-administered and has no risk of infection. This increases the patient’s adherence as well as decreases costs associated with administration.
- **Potential for local effect:** The oral route is especially interesting for the treatment of local diseases in the gastrointestinal tract[76]. Since the prevalence of these diseases is increasing[79,80], there will be also a medical need for novel treatments for these diseases with low risk of systemic effects.

- **Slower effect:** In comparison to the intravenous route, which directly administers the drug into the systemic circulation, the onset effect of the oral administration route is slower. This more controlled and gradual onset of effects can reduce the likelihood of acute toxicity.
- **Variable pharmacokinetics:** The individual differences in gastrointestinal emptying time, microflora, pH and composition of gastrointestinal fluid[73], as well as in diet and drug consumption[83], can affect the absorbance of the drug, resulting in different pharmacokinetics and bioavailability between individuals.
- **Lower bioavailability and hepatic first-pass metabolism**: Drugs must overcome several barriers to reach the systemic circulation, which often results in lower bioavailability[73,74]. In addition, those drugs that reach the systemic circulation through the portal vein (most orally administered drugs), are primarily transported to the liver where a significant proportion is metabolized before reaching the target organ[82]. This can lead to the necessity of higher oral doses compared to other administration routes.

From all these key points, it can be concluded that the oral administration route is especially interesting for the treatment of chronic diseases which require a friendly and easy treatment for the patient to improve adherence, as well as for the local treatment of digestive diseases. In contrast, the oral route may not be the most appropriate for urgent treatments, where intravenous administration is often preferred for its rapid onset. In addition, large biopharmaceuticals may face significant challenges with oral administration due to their very low bioavailability through this route.

Hence, different diseases may benefit from different administration routes, as each route optimizes drug effectiveness, bioavailability, and targeted delivery according to the specific characteristics of the disease and the drug. **Figure 1.8** below highlights the key differences between the two administration routes proposed for DELOS-NV, which will be further explored in this thesis.

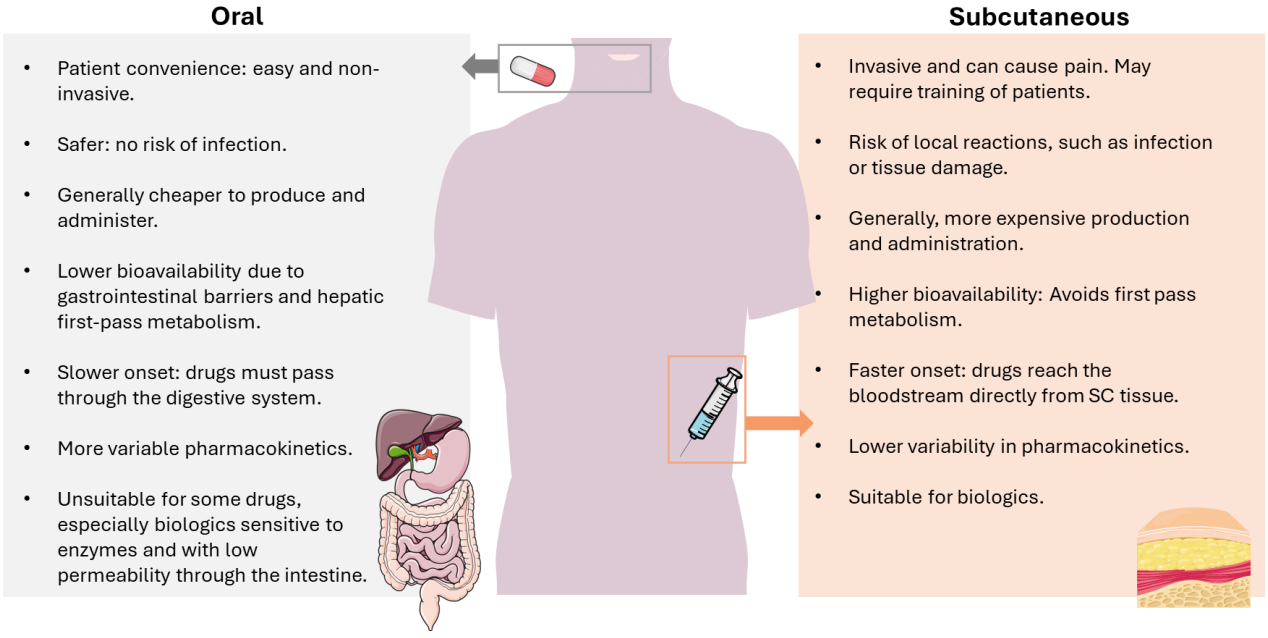


Figure 1.8. Comparison between the two alternative administration routes proposed for the DELOS-NV in the present thesis.

1.5. References

1. A. Wabdul, P. Prasad, M. Rao, A. Narayana. Evolution of drug: a historical perspective. *Bull Indian Inst Hist Med Hyderabad* **2007**, 37 (1), 69–80.
2. D.J. Newman, G.M. Cragg, K.M. Snader. The influence of natural products upon drug discovery. *Nat. Prod. Rep.* **2000**, 17 (3), 215–234.
3. A. Sofia Pina, A. Hussain, A.C.A. Roque. An historical overview of drug discovery. In *Ligand-macromolecular interaction in drug discovery*; **2015**; Vol. 572, pp 3–12.
4. J. Drews. Drug discovery: A historical perspective. *Science.* **2000**, 287 (5460), 1960–1964.
5. Leader B, Baca Q J, Golan D E. Protein therapeutics: a summary and pharmacological classification. *Nat. Rev. Drug Discov.* **2008**, 7 (1), 21–39.
6. E. Valeur, S.M. Guéret, H. Adihou, et al. New modalities for challenging targets in drug discovery. *Angew. Chemie - Int. Ed.* **2017**, 56 (35), 10294–10323.
7. M.J. Blanco, K.M. Gardinier, M.N. Namchuk. Advancing new chemical modalities into clinical studies. *ACS Med. Chem. Lett.* **2022**, 13 (11), 1691–1698.
8. M.J. Blanco, K.M. Gardinier. New chemical modalities and strategic thinking in early drug discovery. *ACS Med. Chem. Lett.* **2020**, 11 (3), 228–231.
9. H. Park, A. Otte, K. Park. Evolution of drug delivery systems: From 1950 to 2020 and beyond. *J. Control. Release* **2022**, 342, 53–65.
10. Y. Ren, L. Nie, S. Zhu, X. Zhang. Nanovesicles-mediated drug delivery for oral bioavailability enhancement. *Int. J. Nanomedicine* **2022**, 17, 4861–4877.
11. C. Zhang, L. Yan, X. Wang, et al. Progress, challenges, and future of nanomedicine. *Nano Today* **2020**, 35, 101008.
12. International organization for standarization. ISO 80004-1:2023(en) Nanotechnologies; **2023**.
13. A.Z. Wilczewska, K. Niemirowicz, K.H. Markiewicz, H. Car2. Nanoparticles as drug delivery systems. *Pharmacol. Reports* **2012**, 64, 1020–1037.
14. A. Yusuf, A.R.Z. Almotairy, H. Henidi, O.Y. Alshehri, M.S. Aldughaim. Nanoparticles as drug delivery systems: A review of the implication of nanoparticles' physicochemical properties on responses in biological systems. *Polymers (Basel).* **2023**, 15 (7).
15. Z. Gu, A. Biswas, M. Zhao, Y. Tang. Tailoring nanocarriers for intracellular protein delivery. *Chem. Soc. Rev.* **2011**, 40 (7), 3638–3655.
16. C.L. Ventola, D.J. Bharali, S.A. Mousa. The nanomedicine revolution: Part 1: Emerging concepts. Pharmacy and Therapeutics. *Pharmacol. Ther.* **2010**, 128 (9), 512–525.
17. A. Boloix, N. Feiner-Gracia, M. Köber, et al. Engineering pH-sensitive stable nanovesicles for delivery of microRNA therapeutics. *Small* **2022**, 18 (3), 2101959.
18. X. Zhang, Y. Li, Z. Zhou. Lipid nanoparticle-based delivery system–a competing place for mRNA vaccines. *ACS Omega* **2024**, 9, 6219–6234.

19. D. Sun, Z.R. Lu. Structure and function of cationic and ionizable lipids for nucleic acid delivery. *Pharm. Res.* **2023**, 40 (1), 27–46.

20. M. Rossetti, L. Stella, J. Morlà-Folch, et al. Engineering dna-grafted quatsomes as stable nucleic acid-responsive fluorescent nanovesicles. *Adv. Funct. Mater.* **2021**, 31 (46), 1–9.

21. L. Ferrer-Tasies, H. Santana, I. Cabrera-Puig, et al. Recombinant human epidermal growth factor/Quatsome nanoconjugates: A robust topical delivery system for complex wound healing. *Adv. Ther.* **2021**, 4 (6), 2000260.

22. J. Tomsen-Melero, S. Passemard, N. García-Aranda, et al. Impact of chemical composition on the nanostructure and biological activity of α-galactosidase-loaded nanovesicles for Fabry disease treatment. *ACS Appl. Mater. Interfaces* **2021**, 13 (7), 7825–7838.

23. N. Joudeh, D. Linke. Nanoparticle classification, physicochemical properties, characterization, and applications: a comprehensive review for biologists. *J. Nanobiotechnology* **2022**, 20 (1), 1–29.

24. N. Grimaldi, F. Andrade, N. Segovia, et al. Lipid-based nanovesicles for nanomedicine. *Chem. Soc. Rev.* **2016**, 45 (23), 6520–6545.

25. P. Moitra, K. Kumar, P. Kondaiah, S. Bhattacharya. Efficacious anticancer drug delivery mediated by a pH-sensitive self-assembly of a conserved tripeptide derived from tyrosine kinase NGF receptor. *Angew. Chemie - Int. Ed.* **2014**, 53 (4), 1113–1117.

26. B. Parshad, S. Prasad, S. Bhatia, et al. Non-ionic small amphiphile based nanostructures for biomedical applications. *RSC Adv.* **2020**, 10 (69), 42098–42115.

27. G.M. Whitesides, M. Boncheva. Beyond molecules: Self-assembly of mesoscopic and macroscopic components. *Proc. Natl. Acad. Sci. U. S. A.* **2002**, 99 (8), 4769–4774.

28. E. Elizondo, E. Moreno, I. Cabrera, et al. Liposomes and other vesicular systems: Structural characteristics, methods of preparation, and use in nanomedicine. In *Progress in Molecular Biology and Translational Science*; **2011**; Vol. 104, pp 1–52.

29. J.H. Ryu, D.J. Hong, M. Lee. Aqueous self-assembly of aromatic rod building blocks. *Chem. Commun.* **2008**, No. 9, 1043–1054.

30. X. Liu, A. Ardizzone, B. Sui, et al. Fluorenyl-loaded Quatsome nanostructured fluorescent probes. *ACS Omega* **2017**, 2 (8), 4112–4122.

31. H.J. Santana Milián, L. Ventosa Rull, E. Martínez Díaz, et al. Vesicle comprising epidermal growth factor and compositions thereof. WO2014/O19555, 2014.

32. N. Thomas, D. Dong, K. Richter, et al. Quatsomes for the treatment of Staphylococcus aureus biofilm. *J. Mater. Chem. B* **2015**, 3 (14), 2770–2777.

33. D. Dong, N. Thomas, M. Ramezanpour, et al. Inhibition of Staphylococcus aureus and Pseudomonas aeruginosa biofilms by quatsomes in low concentrations. *Exp. Biol. Med.* **2020**, 245 (1), 34–41.

34. Y. Zhang, J. Zhou, J.L. Wu, et al. Intrinsic antibacterial and osteoinductive sterosomes promote infected bone healing. *J. Control. Release* **2023**, 354, 713–725.

35. C. Du, S. Woolcott, A.S. Wahba, et al. Evaluation of Quatsome morphology, composition, and stability for pseudomonas aeruginosa biofilm eradication. *Langmuir* **2024**, 40 (3), 1623–1632.

36. M. Cano-Sarabia, N. Ventosa, S. Sala, et al. Preparation of uniform rich cholesterol unilamellar nanovesicles using CO2-expanded solvents. *Langmuir* **2008**, 24 (6), 2433–2437.

37. L. Ferrer-Tasies, E. Moreno-Calvo, M. Cano-Sarabia, et al. Quatsomes: Vesicles formed by self-assembly of sterols and quaternary ammonium surfactants. *Langmuir* **2013**, 29 (22), 6519–6528.

38. G. Vargas-Nadal, M. Muñoz-Ubeda, P. Alamo, et al. MKC-Quatsomes: a stable nanovesicle platform for bio-imaging and drug-delivery applications. *Nanomedicine Nanotechnology, Biol. Med.* **2020**, 24, 102136.

39. I. Cabrera, E. Elizondo, O. Esteban, et al. Multifunctional nanovesicle-bioactive conjugates prepared by a one-step scalable method using CO2-expanded solvents. *Nanoletters* **2013**, 13, 3766–3774.

40. A. Kassem, H. Refai, M.A. El-Nabarawi, M.M. Abdellatif. Formulation and evaluation of prednisolone sodium metazoate-loaded mucoadhesive Quatsomal Gel for Local Treatment of Recurrent Aphthous Ulcers: Optimization, in vitro, ex vivo, and in vivo studies. *Pharmaceutics* **2023**, 15 (7).

41. E. Elizondo Sáez de Vicuña. New molecule based nanostructured drug carriers prepared using compressed fluids. *Doctoral Dissertation, Universitat Autonoma de Barcelona,* **2010**.

42. J. Morla-Folch, G. Vargas-Nadal, T. Zhao, et al. dye-loaded quatsomes exhibiting fret as nanoprobes for bioimaging. *ACS Appl. Mater. Interfaces* **2020**, 12 (18), 20253–20262.

43. A. Ardizzone, D. Blasi, D. Vona, et al. Highly stable and red-emitting nanovesicles incorporating lipophilic diketopyrrolopyrroles for cell imaging. *Chem. - A Eur. J.* **2018**, 24 (44), 11386–11392.

44. A. Ardizzone, S. Kurhuzenkau, S. Illa-Tuset, et al. Nanostructuring lipophilic dyes in water using stable vesicles, quatsomes, as scaffolds and their use as probes for bioimaging. *Small* **2018**, 14 (16), e1703851.

45. D. Lombardo, M.A. Kiselev. Methods of liposomes preparation: Formation and control factors of versatile nanocarriers for biomedical and nanomedicine application. *Pharmaceutics* **2022**, 14 (3).

46. V.V.S.N.L. Andra, S.V.N. Pammi, L.V.K.P. Bhatraju, L.K. Ruddaraju. A comprehensive review on novel liposomal methodologies, commercial formulations, clinical trials and patents. *Bionanoscience* **2022**, 12 (1), 274–291.

47. FDA. Guidance for Industry Q3C Impurities : Residual Solvents; **2021**.

48. EMA. ICH guideline Q3C (R6) on impurities: Guideline for Residual Solvents; **2019**.

49. E. Elizondo, J. Veciana, N. Ventosa. Nanostructuring molecular materials as particles and vesicles for drug delivery, using compressed and supercritical fluids. *Nanomedicine* **2012**, 7 (9), 1391–1408.

50. B. William, P. Noémie, E. Brigitte, P. Géraldine. Supercritical fluid methods: An alternative to

conventional methods to prepare liposomes. *Chem. Eng. J.* **2020**, 383, 123106.

51. R. Kumar Kankala, Y. Shrike Zhang, S.-B. Wang, C.-H. Lee, A.-Z. Chen. Supercritical fluid technology: An emphasis on Drug Delivery and Related Biomedical Applications. *Adv. Healthc. Mater.* **2017**, 6 (16), 1700433.

52. N. Ventosa, J. Venciana, S. Santiago, M. Cano. Method for obtaining micro- and nano-disperse systems. WO2006079889A1, 2005.

53. N. Ventosa, S. Sala, J. Veciana. DELOS process: A crystallization technique using compressed fluids - 1. Comparison to the GAS crystallization method. *J. Supercrit. Fluids* **2003**, 26 (1), 33–45.

54. N. Ventosa, S. Sala, J. Venciana, J. Torres, J. Llibre. Despressurization of an expanded liquid organic solution (DELOS): A new procedure for obtaining submicron- or micron-sized crystalline particles. *Cryst. growth Des.* **2001**, 1 (4), 299–303.

55. E. Elizondo, J. Larsen, N.S. Hatzakis, et al. Influence of the preparation route on the supramolecular organization of lipids in a vesicular system. *J. Am. Chem. Soc.* **2012**, 134 (4), 1918–1921.

56. J. Merlo-Mas, J. Tomsen-Melero, J.L. Corchero, et al. Application of Quality by Design to the robust preparation of a liposomal GLA formulation by DELOS-susp method. *J. Supercrit. Fluids* **2021**, 173, 105204.

57. L. Ballell-Hosa, E. González-Mira, H. Santana, et al. DELOS nanovesicles-based hydrogels: An advanced formulation for topical use. *Pharmaceutics* **2022**, 14 (1), 1–20.

58. J. Kim, O. De Jesus. Medication Routes of Administration. In *StatPearls*; Treasure Island (FL): StatPearls, **2023**.

59. K. Ernstmeyer, E. Christman. Pharmacokinetics & Pharmacodynamics. In *Open resources for nursing (Open RN)*; **2023**; p 965.

60. S.Q. Pantaleão, P.O. Fernandes, J.E. Gonçalves, V.G. Maltarollo, K.M. Honorio. Recent advances in the prediction of pharmacokinetics properties in drug design studies: A review. *ChemMedChem* **2022**, 17 (1).

61. A. Shahiwala. Formulation approaches in enhancement of patient compliance to oral drug therapy. *Expert Opin. Drug Deliv.* **2011**, 8 (11), 1521–1529.

62. A.N. Ganesh, C. Heusser, S. Garad, M.V. Sánchez-Félix. Patient-centric design for peptide delivery: Trends in routes of administration and advancement in drug delivery technologies. *Med. Drug Discov.* **2021**, 9, 100079.

63. S. Eisenberg. Subcutaneous administration. Evolution, challenges, and the role of hyaluronidase. *Clin. J. Oncol. Nurs.* **2021**, 25 (6), 663–671.

64. E.K. McCreary, J.R. Bariola, R.J. Wadas, et al. Association of subcutaneous or intravenous administration of casirivimab and imdevimab monoclonal antibodies with clinical outcomes in adults with COVID-19. *JAMA Netw. Open* **2022**, 5 (4), E226920.

65. R. Harris. Origins of hypodermic medication. *Aust. Dent. J.* **1971**, 16 (5), 323–324.

66. P. Zou, F. Wang, J. Wang, et al. Impact of injection sites on clinical pharmacokinetics of subcutaneously administered peptides and proteins. *J. Control. Release* **2021**, 336, 310–321.

67. C.H. Ridyard, D.M.M. Dawoud, L. V. Tuersley, D.A. Hughes. A systematic review of patients' perspectives on the subcutaneous route of medication administration. *Patient* **2016**, 9 (4), 281–292.

68. B. Bittner, W. Richter, J. Schmidt. Subcutaneous administration of biotherapeutics: An overview of current challenges and opportunities. *BioDrugs* **2018**, 32 (5), 425–440.

69. A.M. Fathallah, S. V Balu-lyer. Anatomical, physiological and experimental factors affecting the bioavailability of sc administered large biotherapeutics. *J. Pharm. Sci.* **2015**, 104 (2), 301–306.

70. I. Usach, R. Martinez, T. Festini, J.E. Peris. Subcutaneous injection of drugs: Literature review of factors influencing pain sensation at the injection Site. *Adv. Ther.* **2019**, 36 (11), 2986–2996.

71. A. Bauer, P. Berben, S.S. Chakravarthi, et al. Current state and opportunities with long-acting injectables: Industry perspectives from the Innovation and Quality Consortium "Long-Acting Injectables" working group. *Pharm. Res.* **2023**, 40 (7), 1601–1631.

72. J.J. Milligan, S. Saha. A Nanoparticle ' s Journey to the Tumor : Strategies to overcome first-pass metabolism and their limitations. *Cancers (Basel).* **2022**, 14 (1741), 1–17.

73. J. Lou, H. Duan, Q. Qin, et al. Advances in oral drug delivery systems : challenges and opportunities. *Pharmaceutics* **2023**, 15 (484), 1–22.

74. B. Homayun, X. Lin, H.J. Choi. Challenges and recent progress in oral drug delivery systems for biopharmaceuticals. *Pharmaceutics* **2019**, 11 (129), 1–29.

75. W.H. Helfand, D.L. Cowen. Evolution of pharmaceutical oral dosage forms. *Pharm. Hist.* **1983**, 25 (1), 7–18.

76. M. Naeem, U.A. Awan, F. Subhan, et al. Advances in colon-targeted nano-drug delivery systems: challenges and solutions. *Arch. Pharm. Res.* **2020**, 43 (1), 153–169.

77. T. Nunes, M. Barreiro-de Acosta, I. Marin-Jiménez, P. Nos, M. Sans. Oral locally active steroids in inflammatory bowel disease. *J. Crohn's Colitis* **2013**, 7 (3), 183–191.

78. Y.S.R. Krishnaiah, M.A. Khan. Strategies of targeting oral drug delivery systems to the colon and their potential use for the treatment of colorectal cancer. *Pharm. Dev. Technol.* **2012**, 17 (5), 521–540.

79. United european gastroenterology. Burden, economic impact and research gaps: Key findings from the Pan-European study on digestive diseases and cancers; **2023**.

80. R.L. Siegel, N.S. Wagle, A. Cercek, R.A. Smith, A. Jemal. Colorectal cancer statistics, 2023. *CA. Cancer J. Clin.* **2023**, 73 (3), 233–254.

81. National Cancer Institute. NCI dictionary of cancer terms https://www.cancer.gov/publications/dictionaries/cancer-terms/def/gastrointestinal-system.

82. D.R. Brocks, N.M. Davies. Lymphatic drug absorption via the enterocytes: Pharmacokinetic

simulation, modeling, and considerations for optimal drug development. *J. Pharm. Pharm. Sci.* **2018**, 21 (1S), 254s-270s.

83. D. Fleisher, C. Li, Y. Zhou, L.H. Pao, A. Karim. Drug, meal and formulation interactions influencing drug absorption after oral administration. Clinical implications. *Clin. Pharmacokinet.* **1999**, 36 (3), 233–254.



2 Objectives

The incredible potential of DELOS-NV as drug delivery system has been extensively demonstrated by Nanomol-Bio group and Nanomol Technologies S.L. However, their application versatility has been limited so far due to the limited range of administration routes explored for these promising systems.

The main objective of the present thesis has been to evaluate the DELOS-NV as potential theragnostic nanocarriers for two new administration routes not previously explored by the group and the company: the subcutaneous and the oral administration routes. With this major objective in mind, the following specific objectives have been pursued:

1 **Rational optimization of the DELOS-NV composition through Design of Experiments to pursue biocompatible, patient, and regulatory-oriented nanocarriers** with appropriate physicochemical properties to ensure quality, exclusively employing excipients found in FDA-approved drugs.

2 Use of these optimized DELOS-NV for the design of formulations for the subcutaneous administration route:

- 2.1. Development of an advanced **hybrid drug delivery platform based on the biocompatible DELOS-NV embedded in a thermoreversible hydrogel**, specifically designed **as an *in situ*-forming subcutaneous depot** for the extended release of therapeutic compounds. Exhaustive characterization of the rheological properties of the system, the DELOS-NV integrity and stability within the hydrogel matrix, and the injectability and release profile *in vitro*.
- 2.2. **Integration of a highly hydrophobic compound**, as challenging-to-formulate "beyond the Rule of Five" (bRo5) molecule, into the DELOS-NV based thermoreversible hydrogel. Physicochemical characterization, including entrapment efficiency, and evaluation of the *in vitro* release profile.

3 Explore the feasibility of using the **DELOS-NV for the oral administration route**:

3.1. **Evaluation of the effect of the DELOS-NV on the intestinal epithelium using an *in vitro* model** by loading model payloads in these biocompatible nanocarriers: local *vs* systemic effects.

3.2. **Design a potential biosensor based on the biocompatible DELOS-NV** and oligonucleotides **for the diagnosis of cancers in the gastrointestinal tract**. *In vitro* evaluation of its sensitivity and specificity.

Each of these specific objectives has been addressed in a dedicated **Chapter** within the five results' **Chapters** of this thesis. Below, **Figure 2.1** schematizes the relationship between the five **Chapters** and the experimental approaches employed to accomplish the above objectives. Besides, in **Chapter 9** the reader can find the specific methodologies employed to fulfill this work, explained in depth detail.

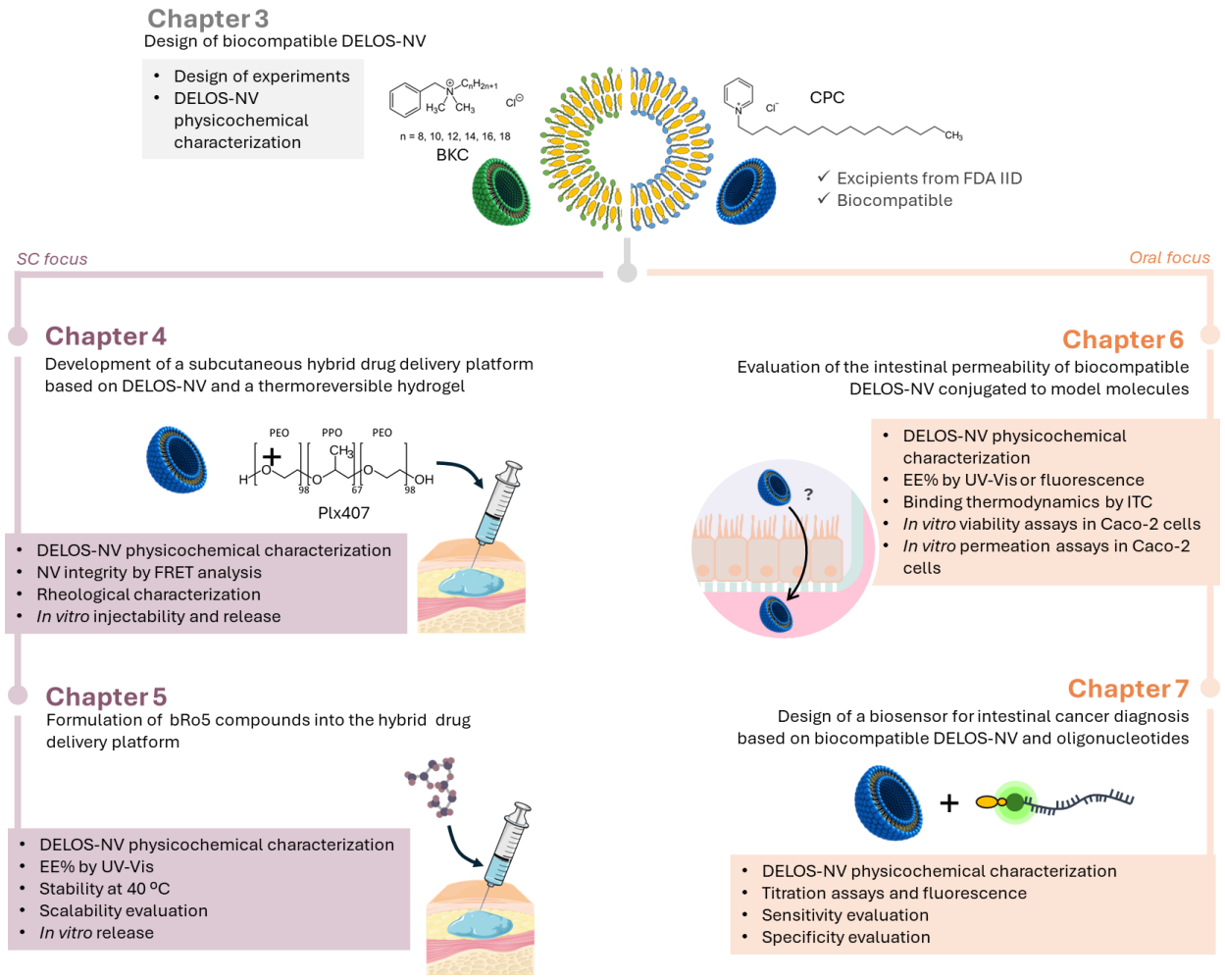


Figure 2.1. *Schematic representation of the thesis objectives (organized by Chapters) and methodological approach employed to accomplish them. Abbreviations employed in the figure: DELOS nanovesicles (DELOS-NV); United States Food and Drug Administration Inactive Ingredients Database (FDA IID); Cetylpiridinium chloride (CPC); Benzalkonium chloride (BKC); Poloxamer 407 (Plx407); Förster resonance energy transfer (FRET); Beyond the rule of 5 compounds (bRo5); Entrapment efficiency% (EE%); Ultraviolet visible (UV-Vis); Isothermal titration microcalorimetry (ITC).*

3

Design and development of biocompatible DELOS-NV for theragnostic purposes

3

3.1. Introduction

3.1.1. Market- and regulatory-oriented DELOS-NV

Nanomol Technologies S.L. and Nanomol-Bio group conduct applied research in biomedicine. This means that their research is designed to solve practical problems, with the objective of accelerating the transfer of knowledge generated at the bench to clinical practice, thereby producing benefits for the community. Consequently, they adopt a market-oriented design thinking approach during the R&D process. They consider the challenges of the drug journey from laboratory to market from the beginning, thus accelerating their path to the clinics.

One of these challenges that must be considered is the scale-up of the formulation. The technologies used to produce the drug product must be scalable in terms of safety and efficacy. DELOS-NV are produced with the DELOS technology (see **Section 1.3.2.1.1** in **Chapter 1** and **Section 9.2.1** in **Chapter 9**), which is scalable. In fact, Nanomol Technologies is setting up a pilot plant for the production of nanovesicles and particulate materials. It is also common to employ Tangential Flow Filtration (TFF) technology as a post-process in DELOS-NV production to remove the organic solvents, purify the sample and/or concentrate the nanovesicles (see **Section 9.2.2** in **Chapter 9** for details), which is also scalable[1]. In addition to technology, it is important to ensure that the components used in the formulation can be purchased in the required quantity and quality, i.e. pharmaceutical grade (meeting pharmacopeia requirements) and/or manufactured under Good Manufacturing Practices (GMP)[2]. Note that GMP is a set of regulations and standards that ensures that the products are manufactured consistently and to a high quality. GMP are applied to products that are developed for use by human beings. The World Health Organization (WHO) has established detailed guidelines to lead GMP, and many countries have formulated their own requirements based on these guidelines.

A significant challenge is to receive the authorization of the regulatory agencies for clinical testing in humans. To do so, the formulations' physicochemical and biological properties are evaluated in detail, to assure their quality, efficacy, and safety. Hence, the selection of the excipients for the formulations is critical. Choosing excipients already present in approved drugs mitigates safety risks. It can also speed up formulation approval by the regulatory agencies since fewer safety pharmacology tests are required[3,4,5].

The present thesis aims to optimize DELOS-NV for two administration routes that have never been addressed with this drug delivery system before. To do so, in this **Chapter**, the DELOS-NV composition will be optimized for the intended new administration routes by employing excipients listed in the FDA's Inactive Ingredients Database (IID)[6].

3.1.1.1. The membrane components of the DELOS-NV

The most widely studied DELOS-NV are composed of Chol and CTAB[7–11] (see **Section 1.2.2** in **Chapter 1**). Chol is a common excipient in LNP[12] such as those employed in the COVID vaccines, and is listed in the FDA's IID[6]. However, the quaternary ammonium surfactant CTAB is not present as an excipient in that list.

To develop market- and regulatory-oriented DELOS-NV two alternative quaternary ammonium surfactants that are present as excipients in the FDA's IID were tested: the benzalkonium chloride (BKC) (used for the intramuscular, intralesional, intra-articular, respiratory, ophthalmic, topical, and other routes) and the cetylpyridinium chloride (CPC) (used for the ophthalmic, oral and respiratory routes). Both cationic surfactants are chlorine-based quaternary ammonium compounds with a polar hydrophilic head and a non-polar lipophilic hydrocarbon radical. The main difference is that BKC corresponds to a mixture of different alkylbenzyldimethylammonium chlorides, in which the alkyl group has various alkyl chain lengths (**Figure 3.1)**.

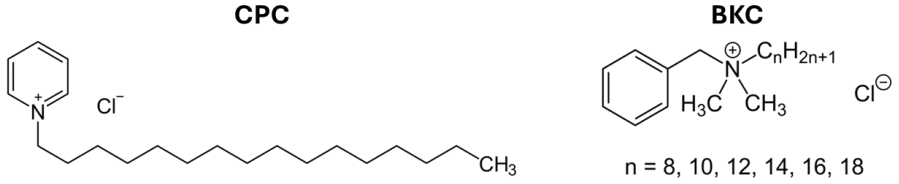


Figure 3.1. *The chemical structure of cetylpyridinium chloride (CPC) and benzalkonium chloride (BKC).*

3.1.1.2. The buffer selection

In addition to the membrane components, buffers are also excipients, and their selection can also impact the progress of the drug formulation. Buffers are used to regulate the pH of the formulations, which can be tailored according to the administration route to match the physiological pH. Buffers can also contribute to preserving the physical and chemical stability of biopharmaceuticals, such as proteins[13].

Considering the most commonly used buffers in pharmaceutical development[14–16], and previous experience with DELOS-NV production, the formulation of this novel DELOS-NV was tested in both water and histidine buffer.

3.1.2. The design of experiments to speed up research

A design of experiments (DoE) is a statistical systematic approach to study simultaneously the relationship between multiple input variables (also known as independent variables or experimental factors) and key output variables (also known as dependent variables or responses). It is especially useful when more than one factor needs to be studied since it can speed up the research process[17–20].

The most common and well-known approach to conduct research is "one factor at a time" (OFAT)[19]. In OFAT, factors are tested individually rather than simultaneously. Initially, factor 1 is adjusted while holding factor 2 constant to observe its effect on the outcome. Then, factor 1 is optimized and fixed, and factor 2 is adjusted to see its effect on the outcome. However, this approach requires multiple experiments for accurate results and fails to account for interactions between factors or to identify an optimal combination for the desired outcome[18]. DoE, by choosing an appropriate model and running statistical analysis, allows researchers to gain a more accurate knowledge of the full combinations of factors while running fewer experiments[18–20]. Next **Figure 3.2** schematizes the comparison between OFAT and DoE.

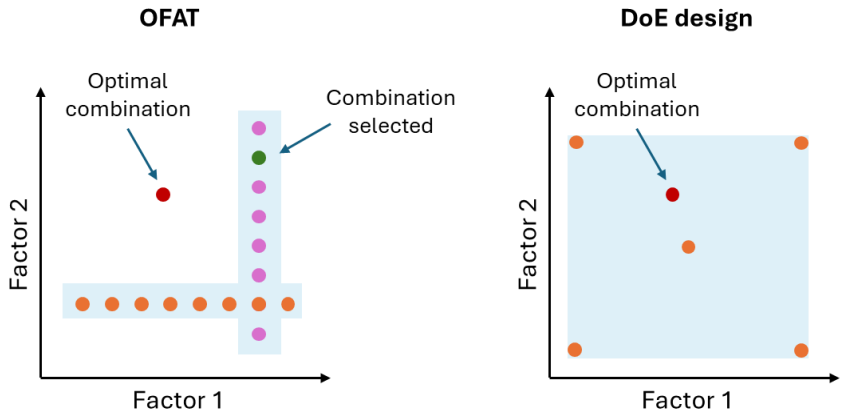


Figure 3.2. *Parameter space exploration when comparing a typical OFAT optimization (left) with a DoE design (right), where each point represents an experiment. The blue area represents the space studied in each approximation. The red point is the optimal combination of factors. The DoE shown represents a full factorial two-level design with one center point. Note that an OFAT optimization does not require a predetermined number of experiments and therefore may or may not exceed the number of experiments in a given DoE design.*

Different DoE models can be employed to fit the data. The selection of the model should be consistent with the goal of the experiment and decided in advance to collect the appropriate data. At the scoping stage of research, when there is very little knowledge of the system, space-filling designs can be adequate. They contribute to gaining a general understanding of the system and to discern in which ranges should be framed the research. Once determined the ranges, for the screening and optimization of a preliminary formulation, factorial designs are the most welcome.

Finally, for advanced formulations, when the objective is to optimize the formulation and study its robustness, response surface methodology (RSM) designs are the best[19]. There are more designs, however, these three are the most popular ones and are schematized in **Figure 3.3**.

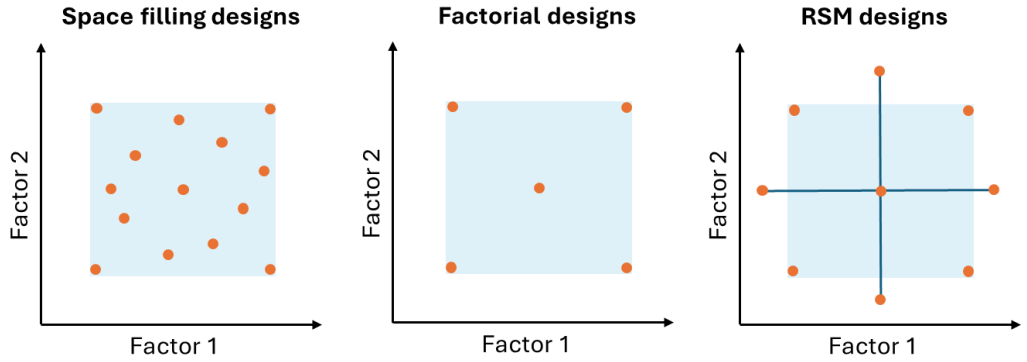


Figure 3.3. Common types of DoE designs. The one in the middle corresponds to the full factorial two-level design with one center point.

Considering all the available previous knowledge related to DELOS-NV, and the objective of screening and optimizing a novel formulation with BKC and CPC surfactants, a factorial design was employed (**Figure 3.4**). Specifically, the model selected was a full factorial two-level design. This model is a very intuitive one that includes all possible experimental factor combinations at two different levels (typically, the maximum and the minimum of the range evaluated for each factor). The addition of a center point in such designs is interesting to identify when the responses are not linear[19].

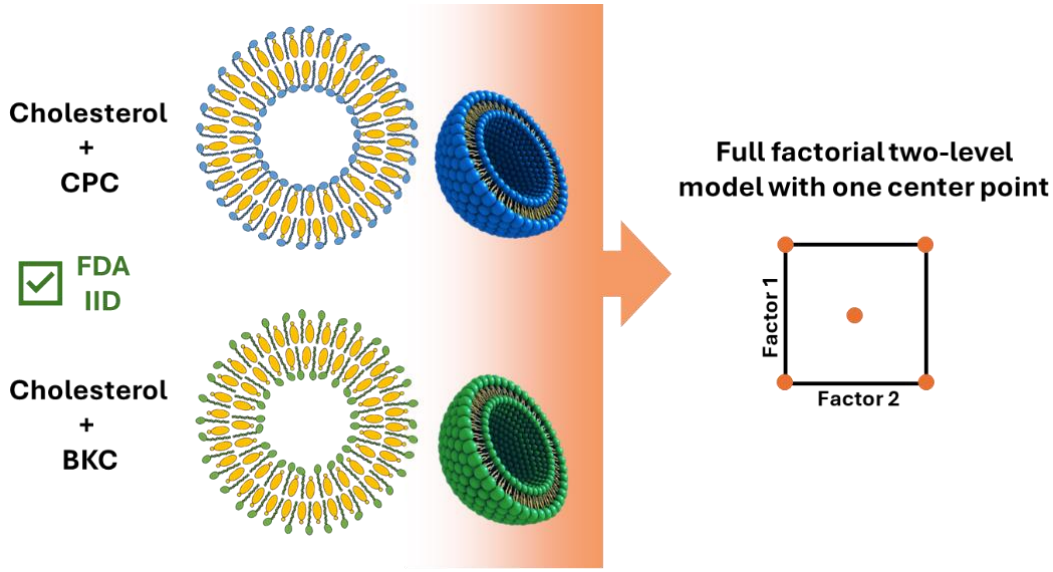


Figure 3.4. Market- and regulatory-oriented DELOS-NV with membrane components selected from the FDA's IID. The screening of parameters affecting the novel formulations will be conducted by a full factorial two-level design with one center point.

3.2. Definition of the critical quality attributes of DELOS-NV

When conducting a DoE, it is important to determine which factors and responses will be evaluated. In this formulation development, the selected responses are the critical quality attributes (CQA) defined for the DELOS-NV colloidal dispersions.

According to the International Council for Harmonization (ICH) Guideline for Pharmaceutical Development, CQA are "physical, chemical, biological or microbiological properties or characteristics that should be within an appropriate limit, range or distribution to ensure desired product quality"[21]. These parameters are crucial for ensuring the consistency and reproducibility of the drug, and consequently, for ensuring safety and efficacy. Typically, these parameters are defined early in the drug development stage and are evaluated throughout the drug life cycle.

The selection of the CQA for the novel DELOS-NV was based on the ICH Q8 recommendations, as well as relevant Chemistry, Manufacturing, and Control guidelines from the FDA[21,22] for liposomes and other nanodrug delivery systems. The selected CQA are as follows:

- **Macroscopic appearance**: The macroscopic appearance allows for a qualitative evaluation of the colloidal suspension. An initial indication of nanovesicle formation would be the observation of the Tyndall effect, which is the scattering of light by fine particles in a colloidal suspension. In addition, macroscopical appearance permits identifying destabilization phenomena. The target is to obtain an aqueous dispersion with a homogeneous, opalescent macroscopical appearance, free of sedimentation.
- **Mean particle size:** Particle size is a major CQA for nanomaterials. It plays a crucial role in drug delivery systems because it directly influences their cellular uptake, transportation, and accumulation behavior. As an example, smaller particles, of 20–30 nm, are eliminated by kidneys, while larger particles, of up to 300 nm, are taken up by the reticuloendothelial system[17]. Importantly, having particles below 220 nm would allow for final sterile filtration, which is a common goal in nanovesicles development[23]. In this specific case, an appropriate limit range for the DELOS-NV would be between 20 and 220 nm. This limit ensures the feasibility of sterilization by filtration using sterile 220 nm filters. In addition, particles wouldn't be excessively small, preventing rapid solubilization in body fluids. In this thesis, the mean particle size is calculated as the mean hydrodynamic diameter by the dynamic light scattering (DLS) technique (see **Section 9.3.1**).
- **Size polydispersity index (PdI):** The size PdI reflects the grade of homogeneity in the particle size distribution of the nanovesicles. The target is to have the lowest value, which would correspond with the narrowest distribution. Typically a size PdI below 0.5 is considered appropriate for liposomal formulations[17]. In the case of DELOS-NV, due to their thermodynamic stability at certain conditions (i.e., DELOS-NV with 1:1 CTAB:Chol molar ratio and 5.3 mg/mL membrane components)[9,24], the size PdI limit can be reduced to 0.40. In this thesis, the size PdI is calculated by DLS technique as explained in **Section 9.3.1**.
- **Apparent zeta potential (Z-potential):** Apparent Z-potential is indicative of the surface charge of the nanovesicles. It is a very relevant parameter to control since it impacts the colloidal stability of the system. The higher the absolute value of the apparent Z-potential,

the more the nanovesicles repeal each other avoiding aggregation and consequently, destabilization phenomena. Values above 30 mV in absolute value are considered enough to sustain the colloidal stability[25]. The apparent Z-potential of the formulations is calculated by Electrophoretic Light scattering (ELS) in a Zetasizer Ultra (see **Section 9.3.1**).

At this first stage of the research, the focus was set on the physical CQA. However, other CQA that were not considered in this study are usually identified in nanovesicular systems: chemical composition and purity, such as drug content and degradation products (chemical CQA); *in vivo* stability and drug release to investigate how the drug behaves in biological systems (biological CQA); and sterility (microbiological CQA for nanovesicular systems intended for parenteral administration)[17].

3.3. Novel DELOS-NV with CPC and BKC surfactants

The aim of this work was to explore whether two alternative quaternary ammonium surfactants, the CPC and BKC, which share similar chemical structure characteristics to CTAB, were able to yield DELOS-NV with appropriate physicochemical properties. There was no previous experience working with these surfactants either at Nanomol Technologies or Nanomol-Bio group. For this purpose, a screening study using a full factorial two-level DoE was conducted. In this specific case, no center point was included since it was only a feasibility test aimed at evaluating the potential to acquire nanovesicles using these new surfactants.

The main factors to be evaluated in the present DoE were the impact of using CPC or BKC on the DELOS-NV production, and the impact of varying molar ratios and concentrations of DELOS-NV membrane components on the physicochemical properties of the nanovesicles. Based on the previous knowledge, these factors were expected to be the ones with a stronger impact on the nanovesicles formulation. For each factor, the lower and higher values of the lower and upper levels were represented by a (−1) and a (+1) sign, respectively, as summarized in **Table 3.1**.

Table 3.1. *The initial full factorial two-level model employed in the design of experiments (DoE), providing the lower (-1) and upper (+1) level values for each factor (independent variables).*

Factors (Independent variables)	*Type*	*Levels*	
		Lower level (-1)	*Higher level (+1)*
Surfactant	*Categorical*	*CPC*	*BKC*
Concentration of membrane components (Chol + Surf) (mg/mL)	*Numeric*	*3*	*6*
Surfactant:Chol molar ratio	*Numeric*	*1:1*	*2:1*

Next, the response variables were defined according to the aforementioned CQA and are listed in **Table 3.2**.

Table 3.2. *The critical quality attributes (CQA) of DELOS-NV introduced in the design of experiments (DoE) as response variables, and the established specifications.*

Critical quality attributes (CQA)	*Criterium*	*Lower limit*	*Higher limit*
Mean hydrodynamic diameter	*Minimize*	*20 nm*	*220 nm*
Size polydispersity Index (PdI)	*Minimize*	*0.01*	*0.4*
Apparent zeta potential (Z-potential)	*Maximize*	*±30 mV*	*±150 mV*

Based on the defined experimental factors and response variables, the DoE was performed. All the experiments were produced following the DELOS method as explained in **Section 9.2.1**. Since it was the first time working with these surfactants, replicates of each experimental run were carried out to check for reproducibility, requiring a total of 16 experiments. For this first proof concept, water was used as a dispersant medium. Accordingly, the nanovesicles produced for the present DoE were named **W-CPC:Chol** or **W-BKC:Chol DELOS-NV** (W refers to the water medium employed in the production, Chol refers to the cholesterol and CPC/BKC to the surfactant employed in the production). **Figure 3.5** shows the 16 experiments conducted for the DoE, identified by their production run order number and the combination of factors employed in each case.

Additionally, the macroscopic appearance of the DELOS-NV was evaluated but not included in the statistical analysis of the DoE because of its qualitative nature. **Figure 3.5** shows the macroscopical appearance of the different formulations on the day of production. The images show homogeneous samples without the presence of sedimentation. W-BKC:Chol DELOS-NV are less translucent than W-CPC:Chol DELOS-NV, regardless of the membrane components concentration in the formulation. Among the W-CPC:Chol DELOS-NV, those with higher concentrations of membrane components are also less translucent than those with lower concentrations of membrane components. Turbidity in colloidal samples is influenced by both the concentration and size of the particles, as larger particles scatter more light. Therefore, the macroscopical appearance suggests that W-BKC:Chol DELOS-NV are bigger in size (i.e., in hydrodynamic diameter).

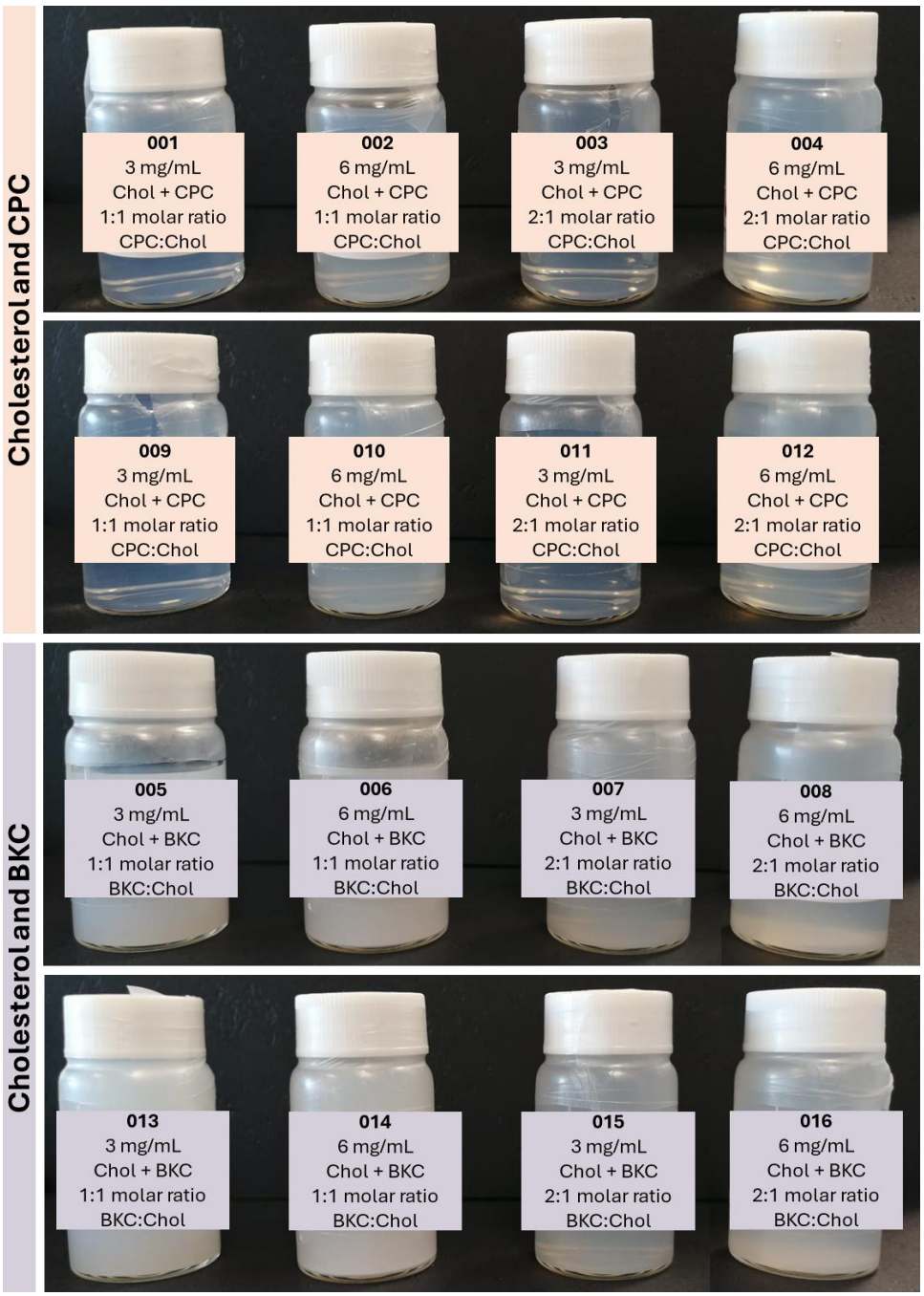


Figure 3.5. *Macroscopic appearance at time 0 of the different DELOS-NV produced for the DoE with water as the dispersant medium. The mg/mL refers to the total membrane components concentration, and the molar ratio between membrane components is expressed as surfactant:Chol. The run number considers the order of performance of the experiments.*

DELOS-NV are thermodynamically stable at specific conditions and it is known that they require a maturation time to reach their lowest energy equilibrium[8]. The selected CQA of the DELOS-NV were measured at different time points by DLS and ELS (see **Section 9.3.1**) over 6 months. The maturation time for the prepared formulations was determined from the stability graphics obtained from the periodical measurements of the CQA (**Figure 3.6**).

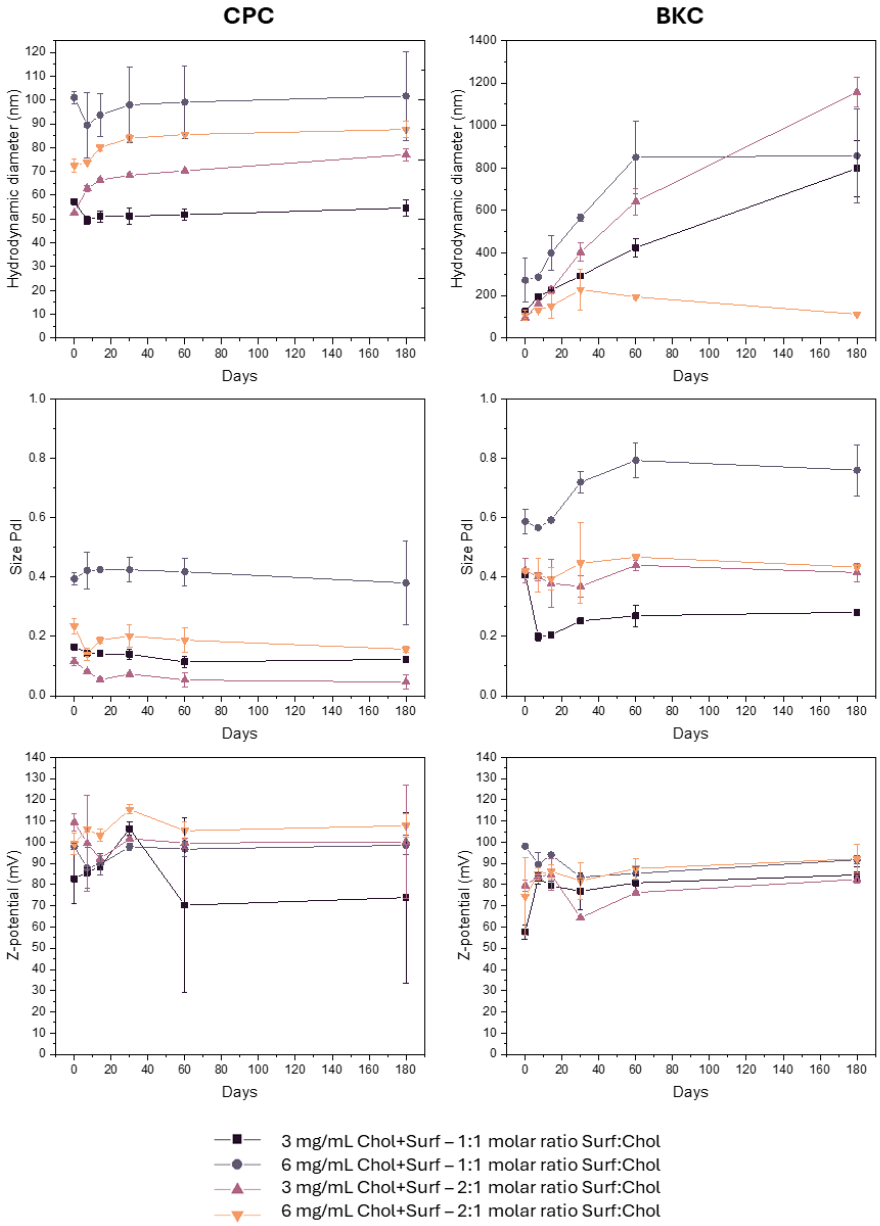


Figure 3.6. *6 months evolution of the selected CQA (mean hydrodynamic diameter, size PdI and apparent Z-potential) of the investigated formulations, i.e., W-CPC:Chol (left) and W-BKC:Chol (right) DELOS-NV in water. The results correspond to the average of the two replicates produced for the DoE (mean ± SD, n = 2).*

Based on the obtained results, it was determined that maturation is achieved 14 days after the DELOS-NV production. Even though stabilization in terms of mean hydrodynamic diameter was not achieved for the W-BKC:Chol DELOS-NV, even after 2 months of production, the other graphics show stabilization of the mean hydrodynamic diameter, size PdI and apparent Z-potential around the 14 days. These results at this aging time were the ones employed for the statistical analysis and are shown in **Table 3.3** and **Figure 3.7**.

Table 3.3. *Matrix of the full factorial two-level design (independent variables or factors: surfactant:Chol molar ratio and nanovesicles membrane components concentration (Chol+surfactant, mg/mL); dependent variables or responses at t = 14 days: hydrodynamic diameter, size PdI and apparent Z-potential (mean ± SD, n = 3)). The run number reflects the order in which the experiments were performed.*

Runs	*Formulation DELOS-NV*	*Membrane components concentration (mg/mL)*	*Surfactant: Chol molar ratio*	*Hydrodynamic diameter (nm)*	*Size PdI*	*Apparent Z -potential (mV)*
01	W-CPC:Chol	3	1	52.8 ± 0.3	0.139 ± 0.012	89 ± 5
09	W-CPC:Chol	3	1	49.41 ± 0.17	0.144 ± 0.011	88 ± 7
02	W-CPC:Chol	6	1	87.4 ± 0.6	0.426 ± 0.007	86 ± 7
10	W-CPC:Chol	6	1	100.1 ± 1.7	0.423 ± 0.012	93 ± 3
03	W-CPC:Chol	3	2	65.99 ± 0.06	0.06 ± 0.03	90 ± 10
11	W-CPC:Chol	3	2	66.8 ± 0.4	0.049 ± 0.018	91.1 ± 2.0
04	W-CPC:Chol	6	2	79.2 ± 0.3	0.18 ± 0.04	101.1 ± 2.2
12	W-CPC:Chol	6	2	80.9 ± 0.7	0.20 ± 0.03	105 ± 7
05	W-BKC:Chol	3	1	228.3 ± 2.3	0.199 ± 0.015	77.9 ± 0.7
13	W-BKC:Chol	3	1	224.4 ± 2.9	0.212 ± 0.013	81 ± 4
06	W-BKC:Chol	6	1	340 ± 70	0.59 ± 0.11	94 ± 4
14	W-BKC:Chol	6	1	457 ± 25	0.59 ± 0.06	94 ± 5
07	W-BKC:Chol	3	2	250 ± 8	0.44 ± 0.05	80 ± 5
15	W-BKC:Chol	3	2	226.2 ± 1.5	0.320 ± 0.019	90 ± 4
08	W-BKC:Chol	6	2	190 ± 80	0.37 ± 0.03	83.8 ± 2.6
16	W-BKC:Chol	6	2	109 ± 7	0.42 0.06	88.6 ± 2.0

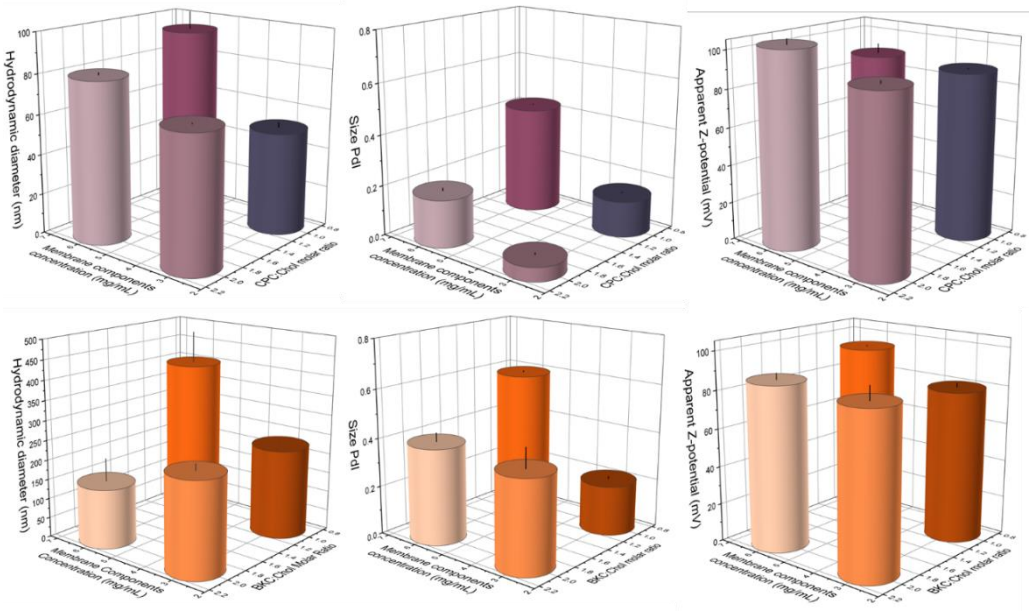


Figure 3.7. *W-CPC:Chol DELOS-NV (above, purple) and W-BKC:Chol DELOS-NV (below, orange) 3D plot for the effect of the studied factors (Independent variables: surfactant:Chol molar ratio and DELOS-NV membrane components concentration (Chol+surfactant, mg/mL)) on the responses (mean ± SD, n = 2). From left to right: hydrodynamic diameter, size PdI and apparent Z-potential.*

The graphics in **Figure 3.7** reveal that the factor with the strongest impact on the CQA of the DELOS-NV is the surfactant used for their production. W-BKC:Chol DELOS-NV are bigger in mean hydrodynamic diameter and present higher size PdI values than W-CPC:Chol DELOS-NV. The apparent Z-potential results of both formulations, with CPC and with BKC, are similar.

Next, the experimental data was fitted to a multiple linear regression (MLR) model employing the Modde software (see **Section 9.5**), and the acceptance for each response variable was evaluated by means of the statistical parameters R2, Q2 model validity, and model reproducibility. R2 represents the percentage of the variation of the response explained by the model, that is, how well the model fits the data. Q2 is the percentage of the variation of the response predicted by the model according to cross-validation, and it gives information about how well the model predicts new data. The hydrodynamic diameter and size PdI responses presented R2 and Q2 values above 0.85 (Hydrodynamic diameter: R2 = 0.96 and Q2 = 0.86; Size PdI: R2 = 0.95 and Q2 = 0.88) indicating a reliable fitting of the model. However, the apparent Z-potential had low values of R2 (0.67) and Q2 (0.3) indicating a bad correlation, and thus, a poor predictive ability of the model. Therefore, the apparent Z-potential response could not be fitted. Nevertheless, **Figure 3.7** shows that all the formulations have apparent Z-potential values widely above 30 mV, which was the limit defined for this CQA.

The influence of the studied factors (surfactant, molar ratio between membrane components, and membrane components concentration) on the hydrodynamic diameter and the size PdI could be statistically analyzed. The results are shown as coefficients of the regression equation plot in **Figure 3.8**. A positive coefficient (represented as a green column) indicates that as the value of the factor increases, the mean of the dependent response (hydrodynamic diameter and size PdI) also tends to increase. A negative coefficient suggests that as the studied factor decreases, the dependent response tends to decrease. The statistical significance for each coefficient is represented by the intervals in black. If they fall within the columns, the coefficient is statistically significant; otherwise, it is not. The correlation between the concentration of membrane components and the surfactant is omitted from the size PdI response because it falls significantly short of statistical significance.

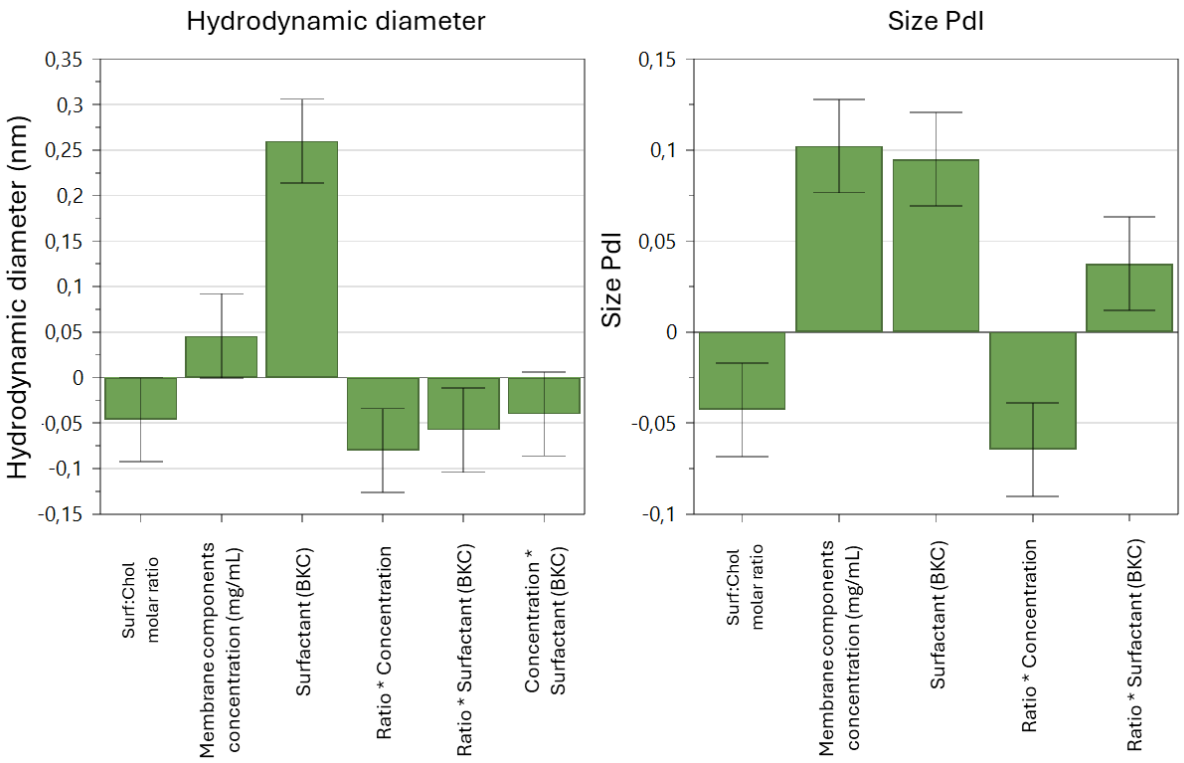


Figure 3.8. *Scaled and centered coefficients of the regression equations describing the influence of formulation parameters (surfactant:Chol molar ratio, membrane components concentration (Chol + surfactant), and their interaction), on the DELOS nanovesicles (DELOS-NV) mean hydrodynamic diameter and size PdI.*

Figure 3.8 shows that the surfactant used in the nanovesicle production has the strongest effect on the hydrodynamic diameter, resulting in larger DELOS-NV with the BKC surfactant. The size PdI response is strongly affected by the surfactant and, also, the membrane components concentration. W-BKC:Chol DELOS-NV present a higher size PdI, and increasing the concentration of membrane components further increases the size PdI of the nanovesicles. Conversely, the surfactant:Chol molar ratio (regardless of the surfactant type) is inversely proportional to both the hydrodynamic diameter and the size PdI. As the surfactant:Chol molar ratio increases, both the hydrodynamic diameter and size PdI decrease. This is likely because, DELOS-NV with a 2:1 surfactant:Chol molar ratio present an excess of surfactant (CPC or BKC) not integrated into the nanovesicle membranes, which contributes to colloidal stabilization. **Figure 3.9** shows the predicted response as a function of the combination of the different studied factors and aligns with the information provided by **Figure 3.8**. The black dotted line indicates the established limit for each CQA (**Table 3.2**).

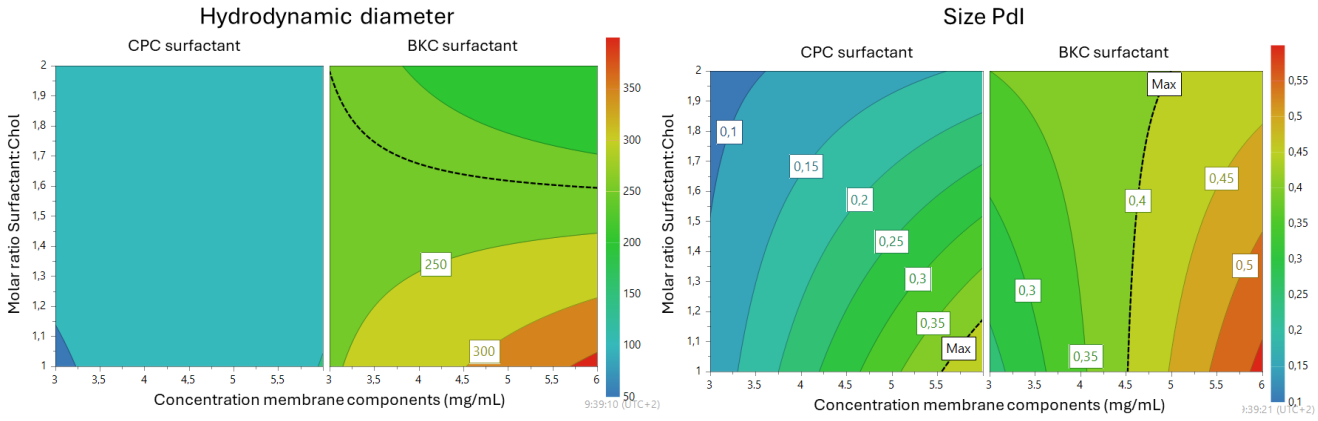


Figure 3.9. Contour plots for the CQA hydrodynamic diameter (left) and size PdI (right).

A design space was explored to evaluate the probability of obtaining DELOS-NV that comply with CQA limits (**Table 3.2**) based on the various combinations of factors analyzed in **Table 3.3**. The resulting design space is shown in **Figure 3.10**. The green region of the design space represents the combinations of factors for which the W-CPC:Chol DELOS-NV will meet the specifications in terms of CQA, with a probability of failure of less than 5%.

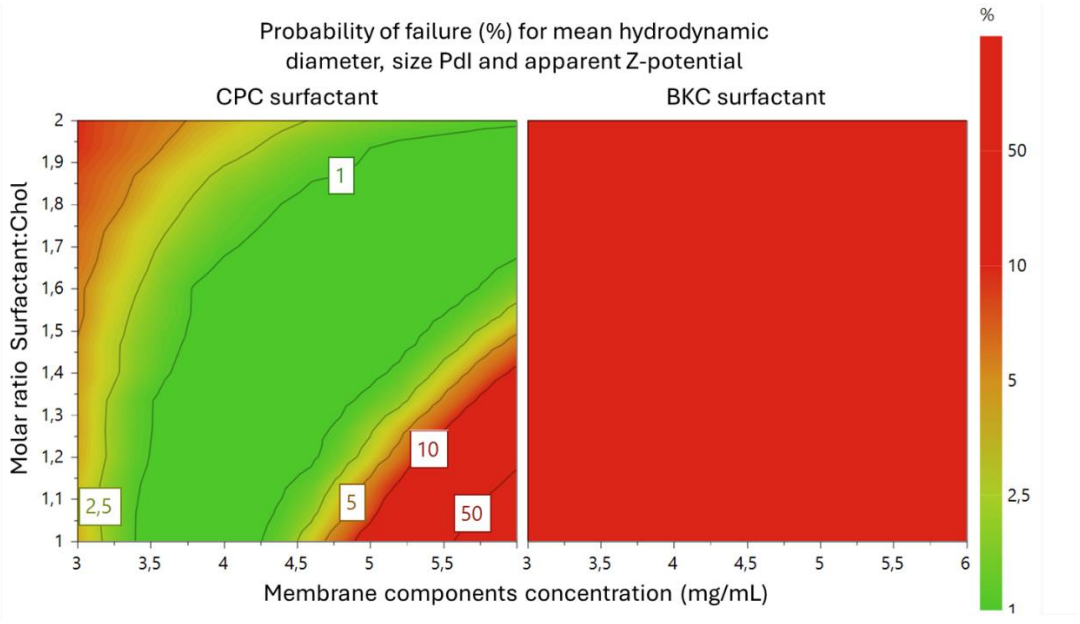


Figure 3.10. The design space for the novel DELOS-NV according to the surfactant employed, the surfactant:Chol molar ratio and the membrane components concentration (mg/mL), expressed as the probability of failure (%). CQA limits defined: mean hydrodynamic diameter 20 to 220 nm, Size PdI 0.01 to 0.4 and apparent Z- potential 30 to 150 mV.

The green region of the design space indicates the factor combinations where DELOS-NV conform to the specified CQA with a failure probability of less than 5%. Through the design space analysis, it is evident that when using the BKC surfactant, no combination of membrane component concentrations and molar ratios of BKC to Chol within the tested ranges reliably yields DELOS-NV

that meet CQA limits with 95% confidence. Conversely, with the W-CPC:Chol DELOS-NV, certain factor combinations exhibit over a 95% likelihood of meeting CQA specifications.

Therefore, the results suggest that only the CPC surfactant can be used to prepare DELOS-NV. Probably, the presence of different alkyl chain lengths in BKC surfactant results in more polydisperse nanovesicles. In addition, the graphs that show the stability (**Figure 3.6**) showed that the W-BKC:Chol DELOS-NV tend to increase the hydrodynamic diameter over time. Formulations with fluctuations in the CQA over time are not attractive for pharmaceutical development since the quality of the product cannot be warranted over time.

To summarize this section, using the CPC surfactant, several combinations of membrane component concentrations and CPC:Chol molar ratios in water can yield DELOS-NV that meet CQA limits with 95% confidence. Conversely, with BKC, no combination of factors offers a high probability of achieving DELOS-NV with the desired CQA in a water dispersant medium. Therefore, CPC outperforms BKC in producing nanovesicles for the pharmaceutical industry. Additionally, stability for at least six months has been demonstrated for all W-Chol:CPC DELOS-NV produced.

3.4. Optimization of DELOS-NV with CPC using histidine buffer to ensure biocompatibility

In **Section 3.3** the possibility of obtaining novel DELOS-NV with CPC and BKC surfactants was demonstrated. The nanovesicles prepared with CPC surfactant appeared more robust, with higher quality, as evidenced by the larger green region -indicating a 95% confidence level of yielding DELOS-NV that meet the defined CQA limits or specifications-. With the goal of optimizing the DELOS-NV and enhancing their biocompatibility for the intended administration routes (e.g. subcutaneous), the CPC was selected as the most suitable surfactant. Besides, the plain water was substituted by histidine buffer as a dispersant medium. While water is inherently biocompatible as a solvent, it lacks the buffering capacity needed for maintaining stability; histidine buffer provides a more controlled environment that closely mimics physiological conditions, making it a superior choice for ensuring the stability of biopharmaceutical formulations. Additionally, histidine buffer is frequently used in parenteral formulations[15], and in a study that compared two commercially available solutions for subcutaneous administration, it caused the lowest sensation of pain[26].

Therefore, the impact of the histidine buffer on the nanovesicles with CPC was evaluated in this section.

Accordingly, a new full factorial two-level DoE adding a central point was conducted with the CPC surfactant in histidine buffer. This is a more advanced DoE, which is better suited for exploring response surfaces and identifying optimal conditions. Including one central point permits to evaluate if the relationship between the factors and the response variables are linear or nonlinear. These novel formulations are named as H-CPC:Chol DELOS-NV. As in the previous section, H refers to the medium (histidine), and CPC:Chol to the combination of membrane components used in the DELOS-NV production.

The factors or independent variables evaluated in the present DoE were the same as previously, except the surfactant type: the concentration of membrane components and the CPC:Chol molar ratio (**Table 3.4**). The aim was to study how these factors -and their interaction- impact on the defined response variables (or CQA) (**Table 3.2**). Moreover, replicates of each experiment were run to assess the reproducibility of the system.

Table 3.4. *Full factorial two-level + one center point model employed in the DoE in histidine 5 mM, providing the lower (-1) and upper (+1) level values for each factor (independent variables).*

Factors (Independent variables)	*Type*	*Levels*	
		Lower level (-1)	*Higher level (+1)*
Concentration of membrane components (Chol + CPC) (mg/mL)	*Numeric*	*1*	*6*
CPC:Chol molar ratio	*Numeric*	*1:1*	*2:1*

According to the different combinations of factors to study and the replicates performed, 10 experiments were required. **Figure 3.11** shows the different experiments conducted for the DoE, identified by their production run order number and the combination of factors used in each case. The 5 mM histidine buffer at pH 7 was prepared as described in **Section 9.1**. The different DELOS-NV were afterward produced by DELOS method employing the histidine buffer in the aqueous phase (see DELOS method in **Section 9.2.1**).

The particles' hydrodynamic diameter, size PdI, and apparent Z-potential of the different formulations were determined as described in **Section 9.3.1**. **Figure 3.11** shows the images of the different formulations prepared for the current DoE. This figure shows homogeneous colloidal dispersions in all cases. It can also be appreciated an opacity increase in the formulations with higher concentrations of membrane components.

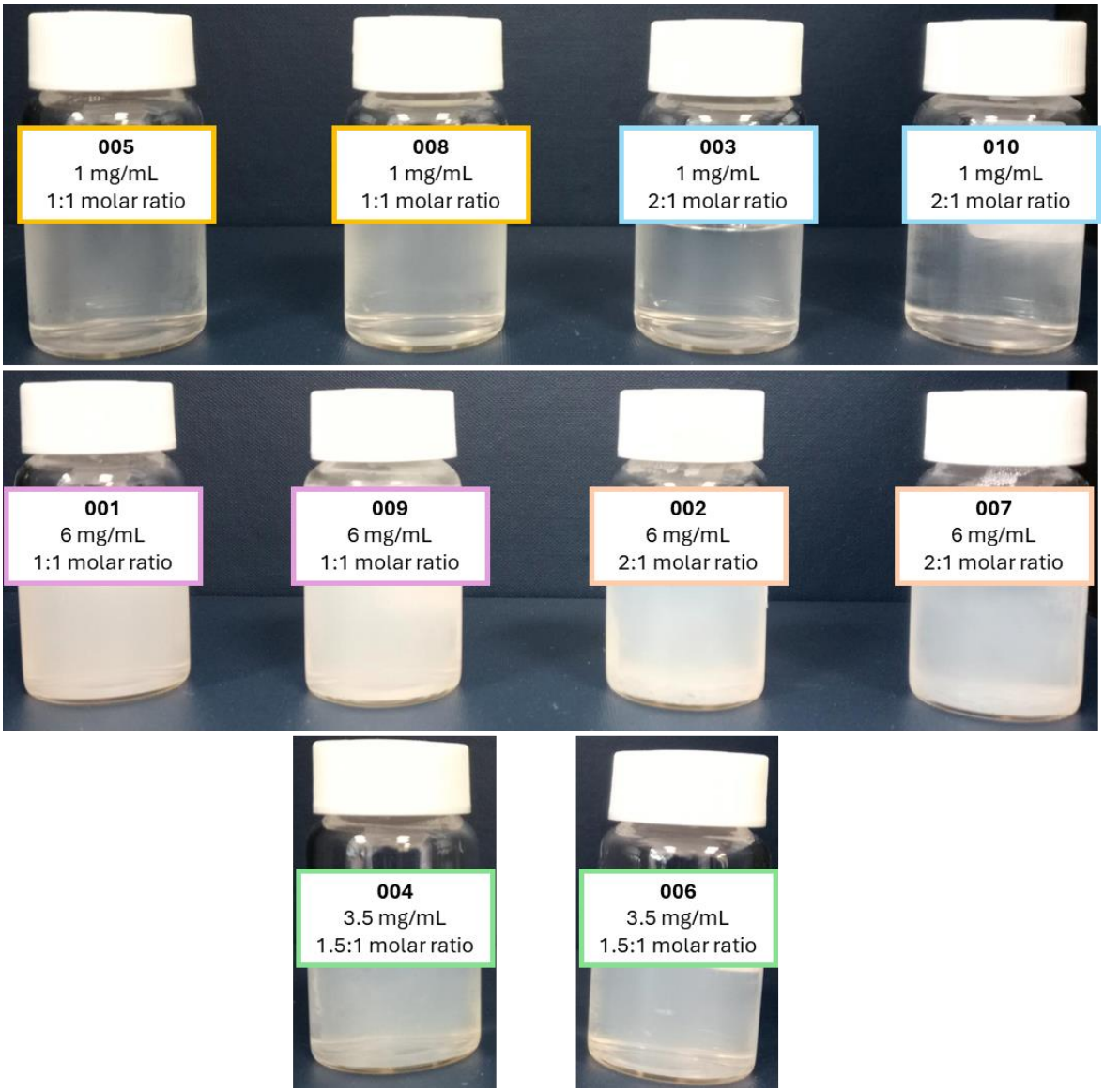


Figure 3.11. *Macroscopical images at time 0 of the different DELOS-NV produced for the DoE in histidine 5 mM pH 7. The mg/mL refers to the total membrane components concentration, and the molar ratio between membrane components is expressed as CPC:Chol. The run number considers the randomized order of performance of the experiments.*

To determine the maturation time required by the H-CPC:Chol DELOS-NV and to assess the long-term stability, the physicochemical properties of these DELOS-NV were measured over 1 year. The stability graphs are shown in **Figure 3.12,** and show that maturation is achieved after 14 days, as was also observed with the W-CPC:Chol DELOS-NV in **Section 3.3**. In addition, the H-Chol:CPC DELOS-NV physicochemical properties were stable for a year. Such high stability is uncommon in nanovesicular systems and aligns with the thermodynamic stability of certain DELOS-NV formulations, which is particularly valuable for pharmaceutical applications.

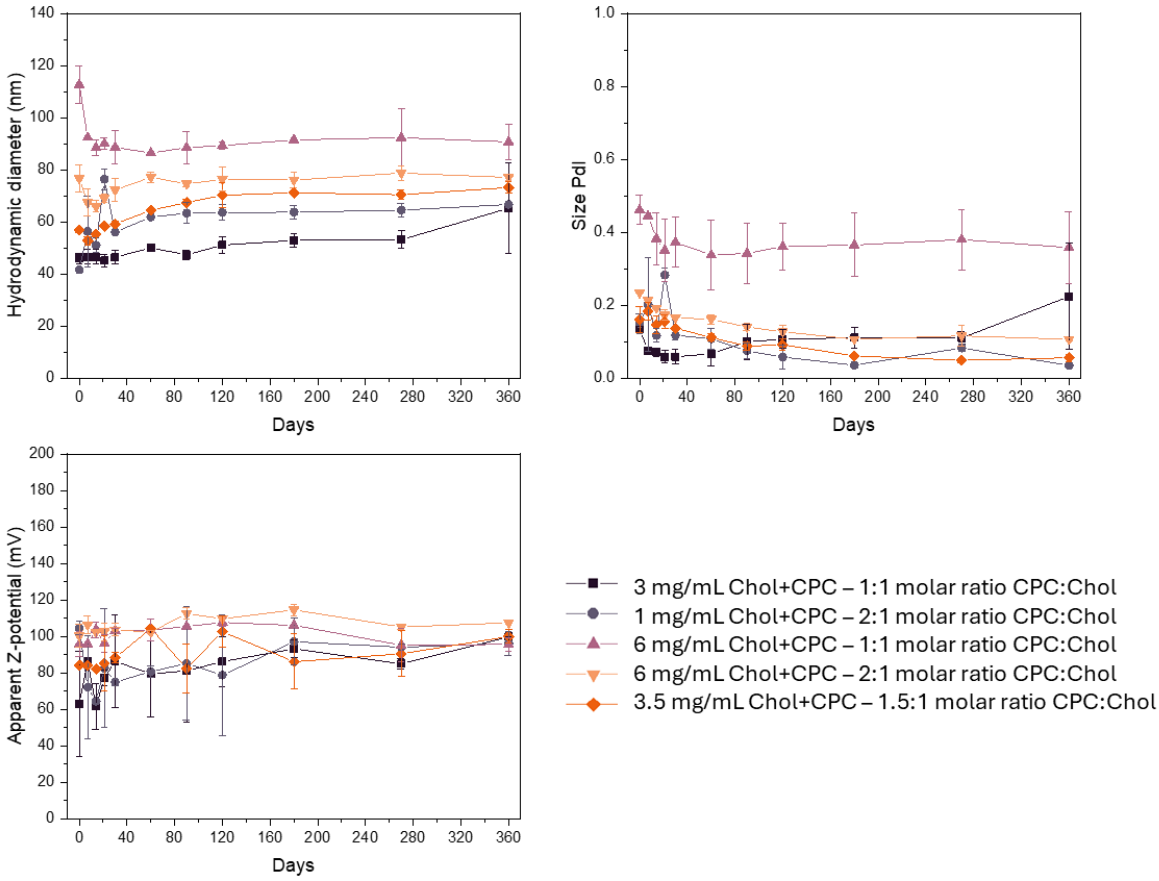


Figure 3.12. *1-year evolution of the CQA (mean hydrodynamic diameter, size PdI, and apparent Z- potential) of the investigated formulations of H-CPC:Chol DELOS-NV in histidine 5 mM pH 7. The results correspond to the average of the two replicates produced for the DoE (mean ± SD, n = 2).*

Once confirmed the maturation time of 14 days, these results were used for the DoE statistical analysis. The **Table 3.5** shows the matrix of experiments, i.e. the different factor combinations, and the results of the response variables obtained 14 days post-production. **Figure 3.13** plots the impact of the studied factors on the response variables. It shows that the formulations produced with the higher concentration of membrane components and lower CPC:Chol molar ratio result in DELOS-NV with larger hydrodynamic diameter and higher size PdI. The Z-potential values are similar to the ones obtained in water and are widely above the limit established for this attribute.

Table 3.5. *Matrix of the full factorial two-level design + 1 center point (independent variables: CPC:Chol molar ratio and DELOS-NV membrane components concentration (Chol+CPC, mg/mL); dependent variables at t = 14 days: hydrodynamic diameter, size PdI and apparent Z- potential (mean ± SD, n = 3)). The run number reflects the randomized order in which the experiments were performed.*

Randomized Run	*DELOS-NV code*	*Membrane components concentration (mg/mL)*	*CPC:Chol molar ratio*	*Hydrodynamic diameter (nm)*	*Size PdI*	*Apparent Z - potential (mV)*
05	H-CPC:Chol	1	1	46.5 ± 1.6	0.0639 ± 0.0021	53 ± 3
08	H-CPC:Chol	1	1	44.6 ± 1.9	0.080 ± 0.012	71 ± 4
01	H-CPC:Chol	6	1	86.3 ± 1.5	0.3327 ± 0.0018	101 ± 4
09	H-CPC:Chol	6	1	91 ± 3	0.433 ± 0.010	107 ± 7
03	H-CPC:Chol	1	2	49.3 ± 1.2	0.104 ± 0.012	65 ± 3
10	H-CPC:Chol	1	2	53.0 ± 1.3	0.131 ± 0.005	76 ± 8
02	H-CPC:Chol	6	2	64.33 ± 0.15	0.191 ± 0.015	102 ± 3
07	H-CPC:Chol	6	2	67.4 ± 1.2	0.1948 ± 0.010	102 ± 6
04	H-CPC:Chol	3.5	1.5	59 ± 3	0.163 ± 0.003	83 ± 5
06	H-CPC:Chol	3.5	1.5	52.1 ± 1.0	0.130 ± 0.013	82 ± 3

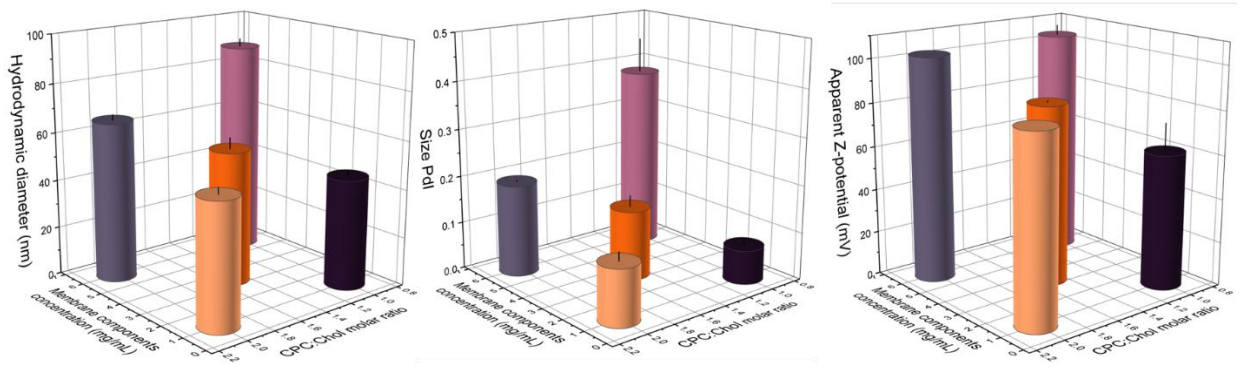


Figure 3.13. *H-CPC:Chol DELOS-NV 3D plot for the effect of the studied factors (Independent variables: CPC:Chol molar ratio and DELOS-NV membrane components concentration (Chol+CPC, mg/mL)) on the responses (mean ± SD, n = 2). From left to right: hydrodynamic diameter, size PdI and apparent Z- potential.*

In addition to these CQA, macro and nanoscopic appearance (i.e. destabilization processes, particle morphology) were analyzed; however, these additional two CQA were not included in the DoE because of their qualitative nature. Representative nanoscopic images of each combination of factors were obtained with Cryo-TEM[a] (**Figure 3.14**) as explained in **Section 9.3.4**. This information, although has not been included in the DoE, provides valuable knowledge regarding the lamellarity and the morphology of the nanovesicles. The images show spherical and unilamellar nanovesicles. All images reveal small homogeneous nanovesicles, except the formulation with 6 mg/mL of

[a]*Cryo-TEM mages were obtained in the Microscopy and X-ray Diffraction Service from the Universitat Autònoma de Barcelona (UAB) by Martí de Cabo, Advanced Technician from the service.*

membrane components and 1:1 CPC:Chol molar ratio, which presents higher size PdI. This qualitative finding is aligned with the quantitative results obtained by DLS and shown in **Table 3.5** and **Figure 3.13**.

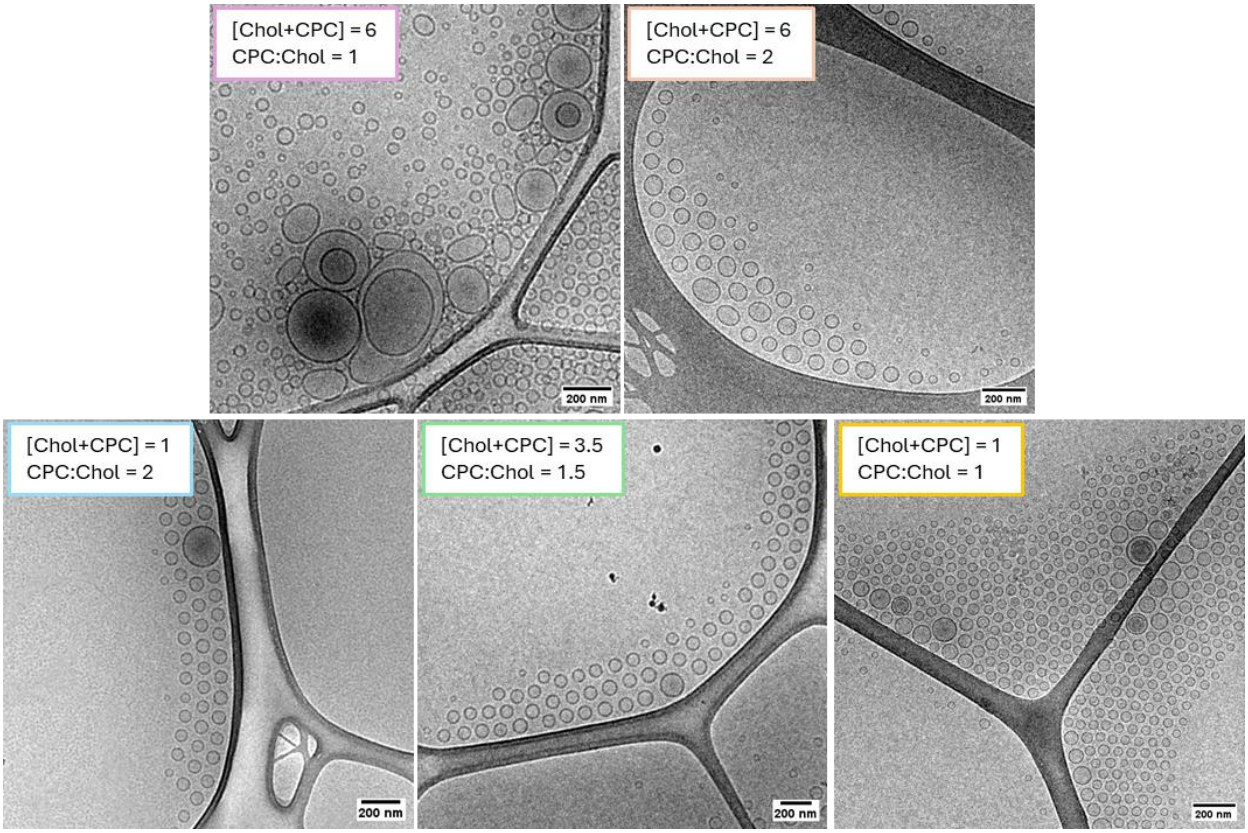


Figure 3.14. *Representative Cryo-TEM images of one replicate of each combination of factors evaluated in the DoE ([Chol+CPC] indicates the concentration of membrane components and CPC:Chol refers to the molar ratio between the membrane components). These results were not included in the statistical analysis of the DoE due to their qualitative nature.*

The fitting of the experimental data shown in **Table 3.5** and the calculation of statistical parameters were performed by MLR model. The R2 and Q2 values were higher than 0.80 for all the responses (R2= 0.94, 0.96, 0.89 and Q2= 0.89, 0.89, 0.82 for hydrodynamic diameter, size PdI and apparent Z-potential, respectively), indicating a reliable fitting of the model.

The statistical impact of the studied factors on the different response variables is shown as coefficients of the regression equation plot in **Figure 3.15**. From the fitting, it could be determined that the concentration of membrane components has the strongest impact on the three response variables. According to the plots in **Figure 3.15**, increasing the concentration of membrane components results in a larger hydrodynamic diameter, size PdI and apparent Z-potential of the DELOS-NV. The CPC:Chol molar ratio had only a statistical effect on the hydrodynamic diameter, lowering it at increasing ratios, while the combination of both formulation factors (concentration of membrane components and CPC:Chol molar ratio) statistically impacts on the hydrodynamic diameter and the size PdI. Surprisingly, the apparent Z-potential was not statistically affected by the CPC:Chol ratio, but only by the concentration of membrane components. The most plausible

explanation for this outcome is that the Z-potential is mainly influenced by the final amount of CPC in the sample. In fact, samples containing 6 mg/mL of membrane components present higher amounts of CPC compared to samples with only 1 mg/mL of membrane components, regardless of the CPC:Chol molar ratio used in the formulation.

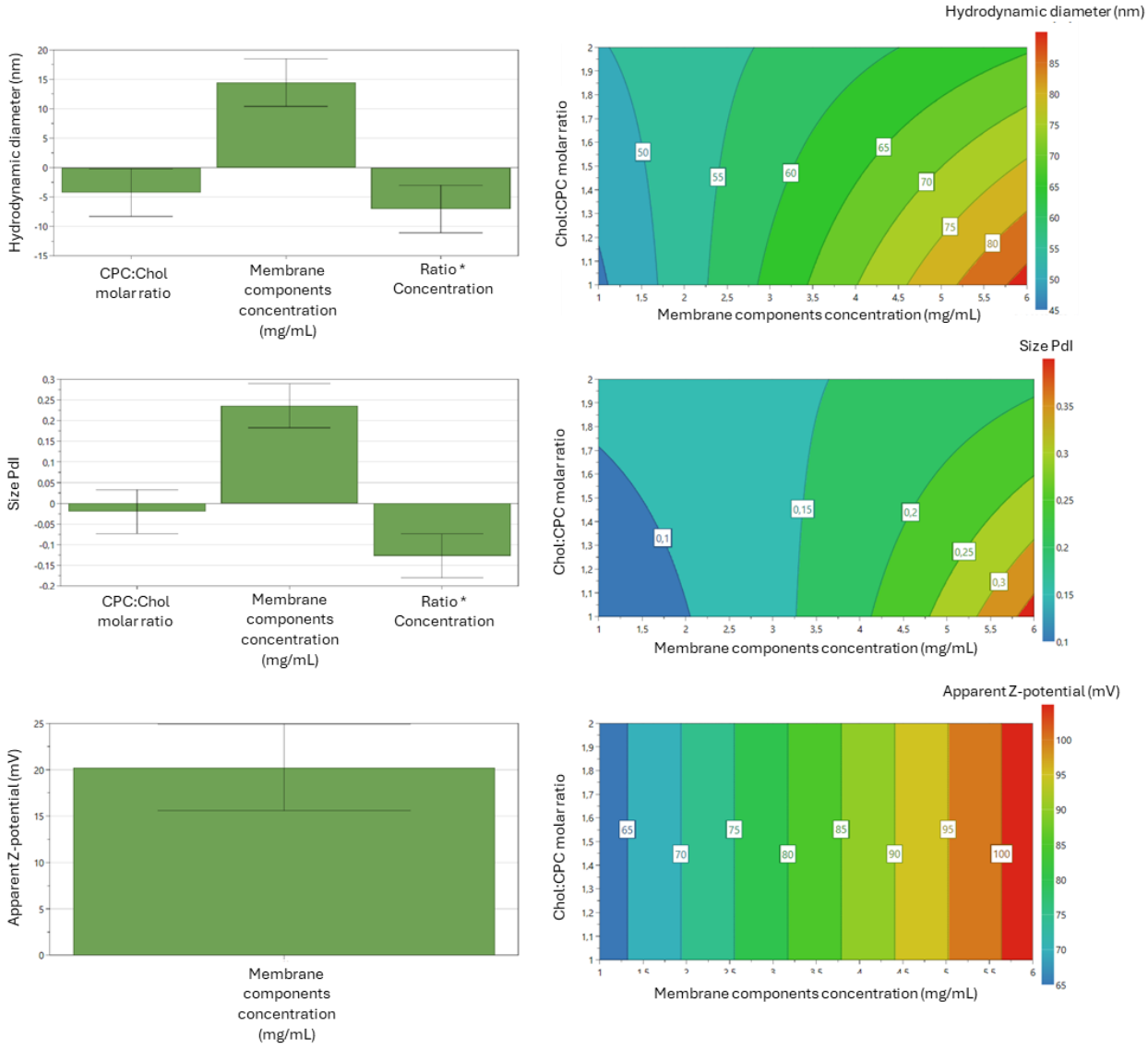


Figure 3.15. *Left side: scaled and centered coefficients of the regression equations describing the influence of formulation parameters (concentration of membrane components, molar ratio CPC:Chol and their interaction), on the DELOS-NV CQA: mean hydrodynamic diameter, size PdI and apparent Z- potential. Right side: contour plots for the same CQA of the DELOS-NV dispersion.*

Besides, a design space for the novel H-CPC:Chol DELOS-NV was constructed, which shows the probability of meeting nanovesicle CQA limits or specifications as a function of the combination of factors studied. This design space is shown in **Figure 3.16**.

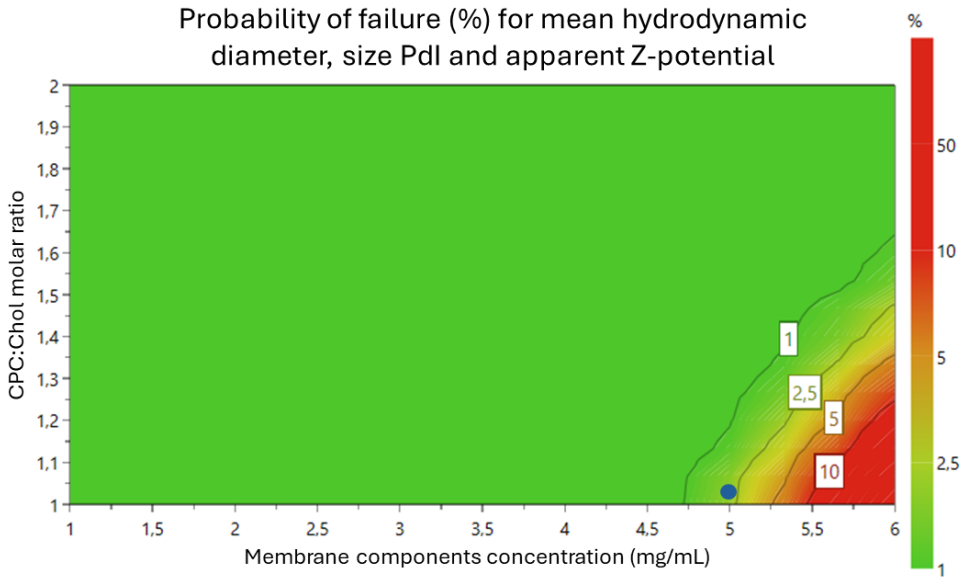


Figure 3.16. *The design space for the H-CPC:Chol DELOS-NV according to the CPC:Chol molar ratio and the membrane components concentration (mg/mL), expressed as the probability of failure (%). CQA limits defined: mean hydrodynamic diameter 20 to 220 nm, Size PdI 0.01 to 0.35 and apparent Z- potential 30 to 150 mV.*

Any combination of factors within the green region has more than a 95% probability of yielding CPC:Chol DELOS-NV with appropriate mean hydrodynamic diameter, size PdI, and apparent Z-potential.

An optimized formulation, that will be further developed into a potential subcutaneous drug delivery system as reported in the next **Chapter 4**, was selected on the basis of the factorial design results. Knowing the impact of the different formulation variables on the CQA of the resulting nanovesicles, the following composition was defined:

- CPC:Chol 1:1 molar ratio, in order to avoid an excess of non-integrated CPC as free surfactant in the formulation, which probably would form micelles/monomers. Although having free surfactant could improve the stability of the colloidal formulation, it is known that it could also induce irritation[27].
- Highest concentration of nanovesicles' membrane components within the design space green region (5 mg/mL) to enhance the entrapment efficiency of potential actives creating a more effective delivery system.

Therefore, the combination inside the design space (**Figure 3.16**), which is pointed out by the blue dot, shows the optimized combination for DELOS-NV with CPC in histidine buffer.

3.5. Summary of the chapter and perspectives

This **Chapter** explains the development of novel DELOS-NV composed exclusively of excipients listed in the FDA IID. Two different quaternary ammonium surfactants have been evaluated in this context, BKC and CPC. The CQA of the DELOS-NV, and their limits or specifications, have been defined, and the probability of obtaining DELOS-NV that meet these CQA limits has been assessed through a DoE. Two DoE have been conducted:

- A full factorial 2-level DoE as first screening study using water as dispersant medium. In water, significant differences between the nanovesicles with CPC and BKC were detected. By adjusting the concentration of membrane components and the CPC:Chol molar ratio, nanovesicles could be obtained with CPC surfactant, meeting the CQA limits with 95% confidence. In contrast, with the BKC surfactant, there was no combination of factors that resulted in nanovesicles compliant with the defined CQA limits with 95% probability. Moreover, the nanovesicles with BKC were unstable and tended to increase in size (i.e. hydrodynamic diameter) over time. This first DoE suggested that nanovesicles can be formed with both surfactants; however, only the CPC surfactant provided a warrantee of appropriate physical characteristics and stability of the nanovesicles.

- A full-factorial 2-level DoE with a center point to optimize the DELOS-NV with CPC and using histidine buffer 5 mM pH 7 as dispersant medium. From this DoE, a design space was obtained which allowed the selection of the optimal formulation. From the combinations of factors that provided more than 95% probability of meeting the CQA specifications, the combination that maximized the membrane components concentration and had the lower CPC:Chol ratio was selected. Having more concentration of membrane components might allow the integration of a higher concentration of actives, thus resulting in a more efficient drug delivery system. In addition, an excess of free surfactant was avoided, since it could have toxicological concerns. Therefore, the optimal formulation consists of nanovesicles with Chol and CPC, with 5 mg/mL of membrane components and 1:1 CPC:Chol molar ratio in histidine 5 mM pH 7.

In conclusion, this chapter has proven the efficacy of implementing DoE approaches to accelerate the research. By using a DoE, a design space enabled the selection of a DELOS-NV composition that will be further developed into a subcutaneous drug delivery system in the following **Chapter 4**.

3.6. References

1. john C. Kraft, J.P. Freeling, Z. Wang, R. Ho. Emerging research and clinical development trends of liposome and lipid nanoparticle drug delivery systems. *J. Pharm. Sci.* **2014**, 103 (1), 29–52.
2. World Health Organization. Good manufacturing practices: supplementary guidelines for the manufacture of pharmaceutical excipients. *Technical Report Series*. 1999, pp 50–71.
3. R.E. Osterberg, C.C. DeMerlis, D.W. Hobson, T.J. McGovern. Trends in excipient safety evaluation. *Int. J. Toxicol.* **2011**, 30 (6), 600–610.
4. FDA. Nonclinical studies for the safety evaluation of pharmaceutical excipients; **2005.**
5. EMA. Guideline on excipients in the dossier for application for marketing authorisation of a medicinal product; **2008**.
6. FDA. FDA inactive ingredient database https://www.accessdata.fda.gov/scripts/cder/iig/index.cfm.
7. L. Ferrer-Tasies, H. Santana, I. Cabrera-Puig, et al. Recombinant human epidermal growth factor/quatsome nanoconjugates: A robust topical delivery system for complex wound healing. *Adv. Ther.* **2021**, 4 (6), 1–14.
8. L. Ballell-Hosa, E. González-Mira, H. Santana, et al. DELOS nanovesicles-based hydrogels: An advanced formulation for topical use. *Pharmaceutics* **2022**, 14 (1), 1–20.
9. L. Ferrer-Tasies, E. Moreno-Calvo, M. Cano-Sarabia, et al. Quatsomes: Vesicles formed by self-assembly of sterols and quaternary ammonium surfactants. *Langmuir* **2013**, 29 (22), 6519–6528.
10. I. Cabrera, E. Elizondo, O. Esteban, et al. Multifunctional nanovesicle-bioactive conjugates prepared by a one-step scalable method using CO2-expanded solvents. *Nanoletters* **2013**, 13, 3766–3774.
11. A. Ardizzone, S. Kurhuzenkau, S. Illa-Tuset, et al. Nanostructuring lipophilic dyes in water using stable vesicles, quatsomes, as scaffolds and their use as probes for bioimaging. *Small* **2018**, 14 (16), 1–6.
12. T.T.H. Thi, E.J.A. Suys, J.S. Lee, et al. Lipid-based nanoparticles in the clinic and clinical trials: From cancer nanomedicine to COVID-19 vaccines. *Vaccines* **2021**, 9 (4), 1–29.
13. L. Jorgensen, S. Hostrup, E.H. Moeller, H. Grohganz. Recent trends in stabilising peptides and proteins in pharmaceutical formulation - Considerations in the choice of excipients. *Expert Opin. Drug Deliv.* **2009**, 6 (11), 1219–1230.
14. S. Pramanick, D. Singodia, V. Chandel. Excipient selection in parenteral formulation development. *Pharma Times* **2013**, 45 (3), 65–77.
15. I. Usach, R. Martinez, T. Festini, J.E. Peris. Subcutaneous injection of drugs: literature review of factors influencing pain sensation at the injection site. *Adv. Ther.* **2019**, 36 (11), 2986–2996.
16. B. Taghizadeh, M.R. Jaafari, N. Zarghami. New insight into the importance of formulation variables on parenteral growth hormone preparations: potential effect on the injection-site

pain. *Front. Endocrinol. (Lausanne)*. **2022**, 13, 1–15.

17. A. Porfire, M. Achim, C. Barbalata, et al. Pharmaceutical development of liposomes using the QbD approach. In *IntechOpen*; **2019**; Vol. 11, p 13.

18. A.G. Mahr, F.R. Lourenço, P. Borman, J. Weitzel, J.-M. Roussel. Introduction to quality by design in pharmaceutical manufacturing and analytical development; Breitkreitz, M. C., Goicoechea, H. C., Eds.; Springer, **2023**.

19. S.N. Politis, P. Colombo, G. Colombo, D.M. Rekkas. Design of experiments (DoE) in pharmaceutical development. *Drug Dev. Ind. Pharm.* **2017**, 43 (6), 889–901.

20. M. Tavares Luiz, J. Santos Rosa Viegas, J. Palma Abriata, et al. Design of experiments (DoE) to develop and to optimize nanoparticles as drug delivery systems. *Eur. J. Pharm. Biopharm.* **2021**, 165 (April), 127–148.

21. EMA. Note for guidance on pharmaceutical development; **2017**.

22. FDA. Introduction to the guidance for industry on liposome drug products: chemistry, manufacturing, and controls; human pharmacokinetics and bioavailability; and labeling documentation; **2018**.

23. X. Xu, M.A. Khan, D.J. Burgess. A quality by design (QbD) case study on liposomes containing hydrophilic API: I. Formulation, processing design and risk assessment. *Int. J. Pharm.* **2011**, 419 (1–2), 52–59.

24. M. Köber, S. Illa-Tuset, L. Ferrer-Tasies, et al. Stable nanovesicles formed by intrinsically planar bilayers. *J. Colloid Interface Sci.* **2023**, 631, 202–211.

25. Z. Fatfat, M. Karam, B. Maatouk, D. Fahs, H. Gali-Muhtasib. Nanoliposomes as safe and efficient drug delivery nanovesicles. In *Advanced and Modern approaches for Drug Delivery*; Kumar Nayak, A., Laha, B., Hasnain, M. S., Maiti, S., Eds.; Elsevier, **2023**; pp 159–197.

26. T. Laursen, B. Hansen, S. Fisker. Pain perception after subcutaneous injections of media containing different buffers. *Basic Clin. Pharmacol. Toxicol.* **2006**, 98 (2), 218–221.

27. J. Tomsen-Melero, S. Passemard, N. García-Aranda, et al. Impact of chemical composition on the nanostructure and biological activity of α-galactosidase-loaded nanovesicles for Fabry disease treatment. *ACS Appl. Mater. Interfaces* **2021**, 13 (7), 7825–7838.

4

4 Development of a hybrid system composed of DELOS-NV and Poloxamer 407 as an *in situ* subcutaneous depot

4.1. Introduction

As mentioned in the **Introduction**, DELOS-NV have previously demonstrated their potential for the delivery of a variety of chemical modalities, from small molecules to biologics, by means of different administration routes such as the intravenous[1,2] and the topical administration routes[3,4]. However, the SC administration route has not yet been addressed with the DELOS-NV, despite its huge potential.

In the present **Chapter,** the biocompatible and regulatory-oriented DELOS-NV optimized in previous **Chapter 3** have been formulated for the SC administration route.

The SC route has many advantages, such as the possibility of being self-administered at home, however, it is an invasive route that requires injections. In chronic diseases, daily injections would result in poor compliance of patients. To overcome this limitation, developing long-acting formulations to reduce the administration frequency is a beneficial approach.

4.1.1. Subcutaneous long-acting formulations

Long-acting formulations are those that extend the half-life of therapeutics for a period of days, weeks, or even months. Therefore, these formulations present reduced toxicity, dosage, and frequency of administration, thus increasing patients' compliance and overall improving the therapeutic efficacy of the drug[5,6].

Several approaches can be considered to prolong the release of subcutaneously administered drugs. These strategies can be classified into two different groups: those that rely on manipulation of the *in vivo* clearance and those that rely on the manipulation of the *in vivo* drug release[6].

The most straightforward approximation to reduce the clearance of drugs is their binding to biomolecules. An example would be binding the active molecule to the human serum albumin. This protein is an ideal candidate due to its long half-life (approximately 19 days) and high abundance[7,8]. Conjugating the active to these proteins prolongs the drug effect by decreasing the clearance of the active. Another common approach with a similar purpose is PEGylation of the active molecule. The covalent attachment of polyethylene glycol (PEG) to therapeutics has been employed for more than 50 years with different finalities such as improving the drug's solubility, reducing immunogenicity and also, extending the drug's circulation time[9]. However, despite being recognized as GRAS (generally recognized as safe) by the FDA, PEG is immunogenic and non-degradable[10,11]. Therefore, developing alternative polymers to PEG to decrease the elimination of drugs is interesting for the development of long-acting formulations[12,13]. It must be noted that PEGylation is also a common optimization in drug delivery systems such as nanovesicles. It acts as the "protein corona", thus avoiding the fast clearance of drug delivery systems by opsonization and increasing the blood circulation time[2,14].

Although these strategies hold promise for clinical translation, especially for those drugs with rapid clearance, it is essential to note that they imply covalent bonding to the active molecule, and it could affect its bioactivity.

A different approach for extending the activity of drugs *in vivo* consists of the immobilization of drugs. This approach instead of reducing the clearance of the drug, focuses on reducing the release rate. As an example, the conjugation of drugs with natural or synthetic macromolecules (polymers or peptides) can result in largely sized depots that release the drug gradually[15]. Another common immobilization strategy lies in the inorganic-organic hybrid generation (e.g. Biomineralization[16]). When the protein or peptide contains adequate acidic amino acid residues, it may easily chelate calcium ions from supersaturated metastable solutions resulting in nucleation which subsequently results in tiny crystals that further orderly assemble into macromolecule-biomineral complexes[6,17]. However, all these strategies still require modifications of the original drug to a certain extent, which may lead to an unpredictable change in its pharmacological activity.

A popular alternative very studied for the obtainment of subcutaneous long-acting formulations is the incorporation of drugs into semi-solid dosage forms, such as hydrogels. Hydrogels can immobilize drugs and release them over time[18]. They are recognized as biocompatible due to their high similarity to the extracellular matrix and are widely employed as drug delivery systems but also for tissue engineering. In comparison to the previous strategies proposed, hydrogels do not require covalent bonding to the active molecule and, therefore, the drug's bioactivity should not be reduced.

Hydrogels are typically formed by biologic or synthetic polymers, which form three-dimensional networks with high content in water. There are three different types of hydrogels according to the crosslinking forces leading the matrix formation: chemical hydrogels involving covalent bonding between the polymer chains, physical hydrogels involving non-covalent bonding, or hybrids (when physical and chemical crosslinking occurs simultaneously)[19]. Among these hydrogels, the physical hydrogels are remarkably interesting for subcutaneous administration. Due to their weak bonding interactions, they show a reversible response (solution to gelation; sol-gel transition) to stimulus. When properly formulated, these hydrogels allow the obtainment of *in situ* subcutaneous depots that behave as free-flowing polymer solutions at injection conditions and transform into viscoelastic gels in the subcutaneous tissue.

Different stimuli can trigger the sol-gel transition of hydrogels[20]: pH changes[21,22], ionic strength changes[23], exposure to ultraviolet (UV) radiation[24] or temperature changes[25–27], thus being a viscous solution during the injection and forming a solid-like depot once in the appropriate tissue. Among these hydrogels, thermoreversible hydrogels (e.g. cellulose derivatives, chitosan) are widely employed, since their gelation can be triggered by the temperature increase when injected subcutaneously[25]. Specifically, the thermoreversible hydrogel Poloxamer 407 (Plx407), also known by the trademark Pluronic® F127 and Synperonic F127, has been widely investigated as a SC depot due to its solubilizing capacity, low toxicity, drug release characteristics, and compatibility with numerous biomolecules and excipients[28].

4.1.2. Poloxamer 407 as thermoreversible hydrogel

The Plx407 is a linear triblock polymer consisting of a hydrophobic polypropylene oxide block (PPO), flanked by two hydrophilic polyethylene oxide blocks (PEO) (**Figure 4.1**). In an aqueous media, and as a function of the concentration and the temperature, the polymer self-assembles into micelles whereby cores of PPO are surrounded by coronas of PEO. At lower concentrations and/or temperature, these micelles are found in a disordered liquid state, and upon increasing temperature or concentration, gelation occurs, which is attributed to the dehydration of the micellar cores resulting in an entropic change of state into a partly ordered cubic liquid crystalline gel state[29]. By modifying the concentration of Plx407, a thermoreversible hydrogel that behaves as an injectable viscous material at room temperatures and gellifies at 37 °C in the SC tissue can be obtained (**Figure 4.1**).

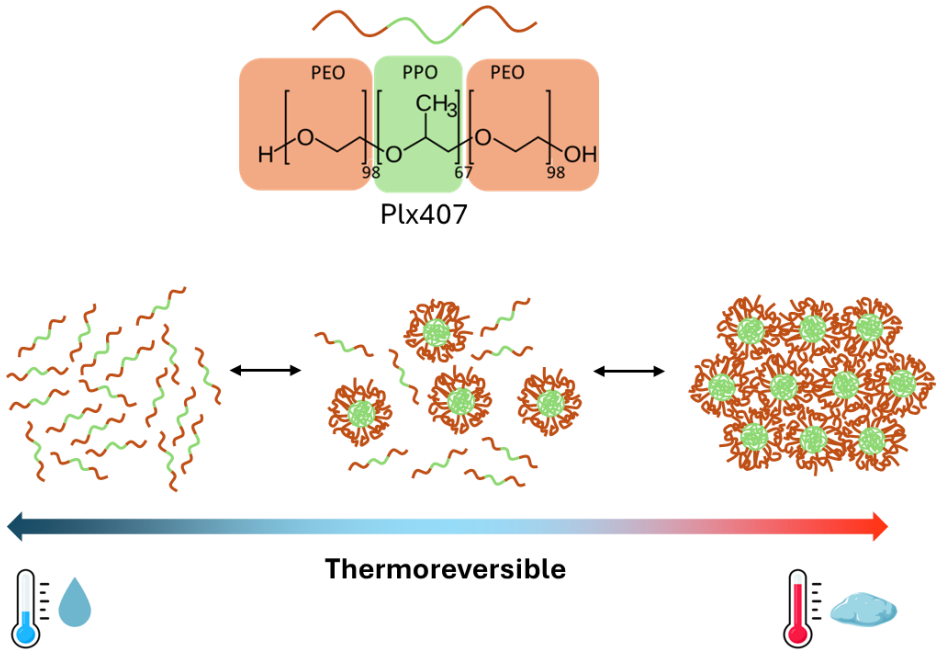


Figure 4.1. *Schematic representation of the Plx407 behavior in response to temperature.*

This Plx407 polymer is included in the FDA IID[30], and there are several medications in the market that contain this component (e. g. Neurontin® from Pfizer and Multaq from Sanofi-Aventis). In 2022, a

clinical trial demonstrated that a single injection of an *in situ* Plx407-based ropivacaine depot provided equal pain relief as a continuous thoracic paravertebral block using On-Q PainBuster (On-Q; B. Braun Medical) in postoperative pain after thoracoscopic pulmonary resection. The trial suggests that Plx407-based ropivacaine hydrogels are a simpler and safer alternative to On-Q, with equal efficacy in pain management[31].

Despite its many advantageous properties, the formulation of drugs into Plx407 hydrogels presents some substantial challenges such as the quantity and homogeneity of drug loading that can be achieved, particularly in the case of hydrophobic drugs, which typically can be loaded only in small amounts due to the predominance of water in the hydrogel[28]. In addition, this high water content, coupled with the large pore sizes within the micelle matrix, often results in relatively rapid drug release rates for hydrophilic drugs when they are directly loaded into the hydrogel[32].

A possible approximation to solve these limitations is to incorporate drug-loaded nanocarriers into the Plx407 hydrogel. Nanocarriers could enhance the drug-loading capacity and drug homogeneity of hydrophobic molecules in the hydrogel matrix[28]. In addition, they could also reduce the burst release of hydrophilic molecules as has been demonstrated with other thermoreversible hydrogels[33]. There are several nanocarriers that have been combined with Plx407 (e. g. liposomes[34], cubosomes[35]) with promising results, however, DELOS-NV have not yet been tested in combination with Plx407.

As presented in the **Introduction** of this thesis, DELOS-NV are a novel class of nanovesicles thermodynamically stable and very homogeneous in terms of size and lamellarity[36,37]. They are produced with a green scalable technology, thus simplifying their progress to the market. DELOS-NV can confer several advantages to drugs, such as enhancing bioavailability, increasing stability, and improving organ targeting[38–41]. Therefore, they are a good candidate to be integrated into the Plx407 hydrogel. In addition, they can also be tailored by modifying their size and decorating their membrane (e.g. PEGylation[2]) to reduce their clearance and circulate for longer periods *in vivo*, thus contributing to the extended-release of drugs. However, it must be highlighted that extended-release achieved with unilamellar and multilamellar nanovesicles typically does not exceed a few days[42], therefore they cannot be considered long-acting formulations by themselves.

Based on this, designing a hybrid formulation combining DELOS-NV and Plx407 was considered a promising approach to enhance the solubility and stability of challenging-to-formulate drugs. DELOS-NV could improve the drug loading of hydrophobic molecules and control the burst release of hydrophilic molecules in the hydrogel, while Plx407 could provide long-acting properties to the formulation (**Figure 4.2**).

The present **Chapter** describes the development of this *in situ*-forming subcutaneous formulation based on DELOS-NV and Plx407. This hybrid system pretends to work as an advanced delivery platform for the subcutaneous administration of challenging-to-formulate chemical modalities.

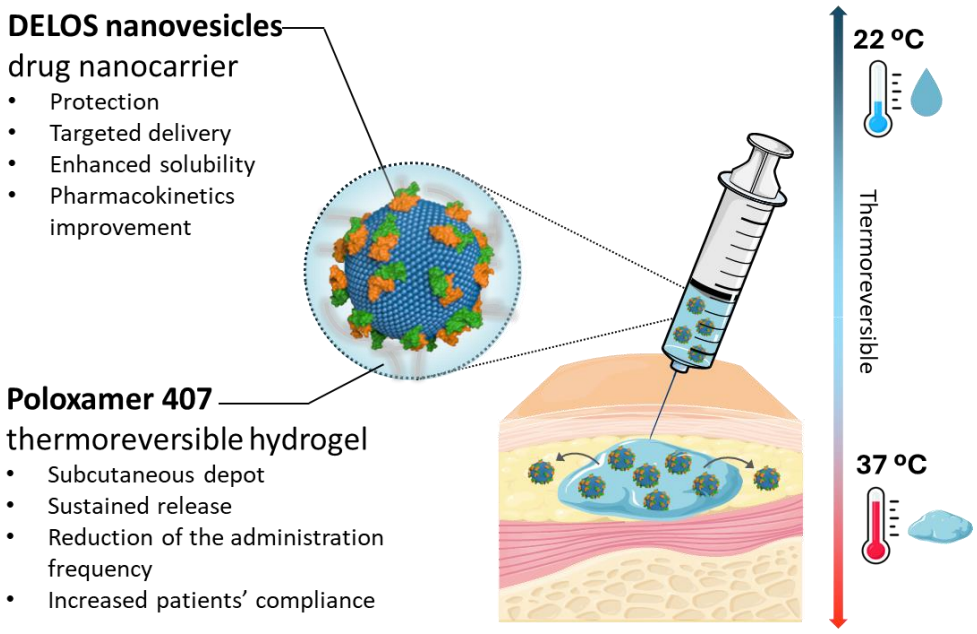


Figure 4.2. *Schematic representation of the hybrid system based on DELOS-NV and Plx407 as an in situ-forming subcutaneous depot for the extended release of challenging-to-formulate drugs.*

4.2. Formulation of DELOS-NV into Poloxamer 407 thermoreversible hydrogels

4.2.1. Production of the DELOS-NV for the subcutaneous administration route

The Chol:CPC DELOS-NV optimized by a DoE in **Section 3.4** in **Chapter 3** were selected to develop the hybrid system with Plx407 polymer. These nanovesicles were specifically designed by employing membrane components listed in the FDA IID[30]. In addition, the histidine buffer employed for their production is a common buffer in parenteral preparations[43]. The optimized DELOS-NV formulation consisted of 5 mg/mL of Cholesterol and CPC membrane components at an equimolar ratio in histidine 5 mM pH 7. The present section describes the production of DELOS-NV with this optimized formulation, their physicochemical characterization, and the further post-process required to evolve them into the final formulation that will be incorporated into the hydrogels.

Hence, DELOS-NV with the optimized formulation were produced by DELOS technology (see **Section 9.2.1**) and were called SC-Chol:CPC DELOS-NV (SC for Subcutaneous; see **Table 9.1** for details on their composition).

As determined previously in **Section 3.4** in **Chapter 3,** 14 days of maturation time is the minimum time required by these nanovesicles to stabilize the CQA. Accordingly, after this time the CQA of this sample were characterized by DLS and ELS (see **Section 9.3.1**). The physicochemical characterization is shown in **Figure 4.3** and demonstrates that the SC-Chol:CPC DELOS-NV produced comply with the CQA limits defined in **Table 3.2** in **Chapter 3**. These good results highlight

the potential of executing a DoE and obtaining a design space when starting a formulation development.

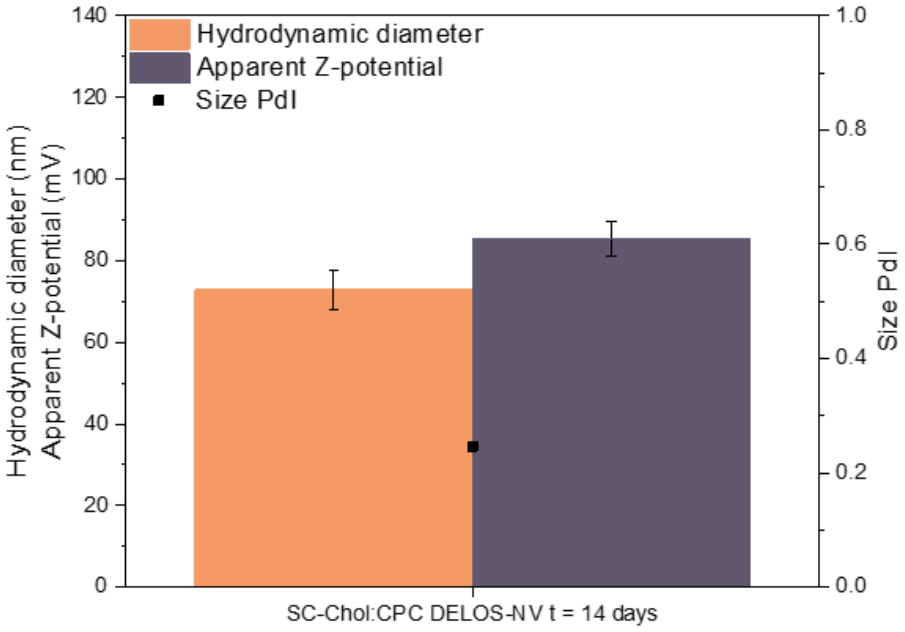


Figure 4.3. *Mean hydrodynamic diameter (nm), size PdI and apparent Z-Potential (mV) of the SC-Chol:CPC DELOS-NV formulated with a membrane concentration of lipids of 5 mg/mL and molar ratio Chol:CPC 1:1.*

On the other hand, as explained in the **Introduction** of this thesis, all the formulations prepared by the DELOS method present a small percentage of organic solvent derived from the production process. In this particular case, the prepared SC-Chol:CPC DELOS-NV have 10% EtOH (v/v) in their media. Even if low percentages of EtOH as an excipient are acceptable in SC administration[44], it is not required in the developed formulation and it was removed by tangential flow filtration (TFF) with a 100 kDa cut-off hollow fiber column (see **Section 9.2.2**). Furthermore, it must be noted that TFF is a post-processing step frequently utilized to purify samples and remove non-integrated molecules when loading cargoes into DELOS-NV (see **Section 9.2.2)**. Consequently, TFF will play a crucial role in the development of future formulations incorporating payloads, making it a convenient approach to assessing its impact in advance.

The SC-Chol:CPC DELOS-NV diafiltrated by TFF were named TFF-Chol:CPC DELOS-NV (see **Table 9.1**).

This post-processed sample was also characterized by DLS and ELS 14 days after its TFF process (see **Section 9.3.1**). As shown in **Table 4.1,** there is almost no impact of the removal of the EtOH in the colloidal suspension CQA. The TFF-Chol:CPC DELOS-NV are stable and present an equivalent mean hydrodynamic diameter, size PdI, and apparent Z-potential to the SC-Chol:CPC DELOS-NV non-diafiltrated by TFF.

Furthermore, by HPLC was quantified the Chol and the CPC concentration in the SC-Chol:CPC DELOS-NV and the TFF-Chol:CPC DELOS-NV in order to control if membrane components were maintained after the TFF process (see **Section 9.3.3**). **Table 4.1** also shows the quantified

concentration of membrane components in the different formulations and the recoveries, calculated with **Equation 4.1.** The recoveries show that there is a slight loss (~ 10-15%) of the membrane components after the DELOS preparation with respect to the theoretical concentration. It is known that this loss is reduced when working with larger reactors. The TFF process also has a minimal impact on the concentration of membrane components. Some Chol and CPC molecules are likely eliminated through the TFF hollow fiber pores because they are not integrated into the DELOS-NV. Instead, they may be solubilized in the EtOH portion of the suspensions or, in the case of CPC, solubilized in the aqueous portion or forming smaller micelles than DELOS-NV.

$$\boldsymbol{Recovery}(\%) = \frac{[\boldsymbol{C}]_{\boldsymbol{HPLC}}}{[\boldsymbol{C}]_{\boldsymbol{Theoretical}}}\ \boldsymbol{x100}$$

Equation 4.1. *Recovery (%) of the membrane components concentration of DELOS-NV. $[C]_{HPLC}$ refers to the concentration of Chol or CPC measured by HPLC after each process (after the DELOS method in one case and after the DELOS method and TFF in the other case), and $[C]_{Theoretical}$ refers to the initial concentration weighted and added inside the reactor during DELOS method.*

Table 4.1. *Physicochemical comparison between the SC-Chol:CPC DELOS-NV non-diafiltrated and the TFF-Chol:CPC DELOS-NV diafiltrated by TFF at t = 14 days.*

Sample ID	*Media*	*Hydro. diameter (nm)*	*PdI*	*Apparent Z-potential (mV)*	*Chol Conc. (mg/mL)*	*Recov. Chol (%)*	*CPC Conc. (mg/mL)*	*Recov. CPC (%)*
SC-Chol:CPC DELOS-NV	*Hist. 5 mM pH 7 + 10% EtOH*	*73 ± 5*	*0.246 ± 0.003*	*85 ± 4*	*2.36 ± 0.04*	*86.4 ± 1.6[1]*	*2.115 ± 0.024*	*88 ± 1[1]*
TFF- Chol:CPC DELOS NV	*Hist. 5 mM pH 7*	*70.3 ± 0.5*	*0.269 ± 0.008*	*78.0 ± 0.1*	*2.21 ± 0.05*	*80.8 ± 1.7[2]*	*1.67 ± 0.04*	*70 ± 2[2]*

[1] Recovery of Chol or CPC after the DELOS method, concerning the theoretical concentration that was weighed and added into the reactor. [2] Recovery of the Chol or CPC after the DELOS method and TFF concerning the theoretical concentration weighted and added into the reactor.

To further demonstrate the elevated stability of this diafiltrated TFF-Chol:CPC DELOS-NV prototype that will be eventually incorporated into the hydrogels, DLS and ELS characterization (see **Section 9.3.1**) was also performed after 1 year of production. The results showed almost no changes in the mean hydrodynamic diameter (70.0 ± 0.4 nm), Size PdI (0.23 ± 0.01) and apparent Z-Potential (85 ± 4 mV) (**Figure 4.4A**). Moreover, Cryo-TEM images of this optimized prototype (see **Section 9.3.4**) depict the presence of spherical, homogeneous, and unilamellar vesicles (**Figure 4.4B**).

In addition to these characterizations, small-angle X-ray scattering (SAXS) measurements were also performed to study the homogeneity of the DELOS-NV sample. This technique can provide unique structural information with the advantage of measuring the average properties of the bulk samples that can be otherwise obviated by using only microscopic techniques such as Cryo-TEM. Measurements and data fitting were conducted as detailed in **Section 9.3.5**[b]**.** As shown in **Figure 4.4C**, the formulation showed small, short-period oscillations on the SAXS profile, demonstrating

[b] *SAXS measurements were conducted by Dr. Cristián Huck Iriart from the ALBA Synchrotron Light Source (Cerdanyola del Vallès, Barcelona, Spain). The data fitting was done by Dr. Cristián Huck Iriart and Prof. Jan Skov Pedersen from Department of Chemistry and Interdisciplinary Nanoscience Center (iNANO), Aarhus University (Aarhus, Denmark).*

high homogeneity of the colloidal sample in terms of size. These oscillations are uncommon in nanovesicular systems which typically exhibit higher polydispersity, and are indicative of the thermodynamic stability of these DELOS-NV[36,37]. The Gaussian-based excess electron density profiles yielded a bilayer thickness of approximately 5.5 nm, with an asymmetric contrast between the inner part (lower values) and the outer shell (higher values). Additionally, the external diameter of the TFF-Chol:CPC DELOS-NV was determined to be 55.4 ± 0.1 nm, with a polydispersity of 3%. The observed differences between techniques (DLS/SAXS) in particle size are caused by the different approaches employed by each technique. Nevertheless, they confirm that the obtained DELOS-NV size is widely below the limit defined for this CQA in previous **Chapter 3**, which was 220 nm (see **Table 3.2**). It is noteworthy that the values obtained by SAXS are more robust than those obtained from DLS as the former directly measures the interference phenomena of the X-rays for the individual vesicles, whereas the latter relies on indirect determination through particle diffusion and cumulant method.

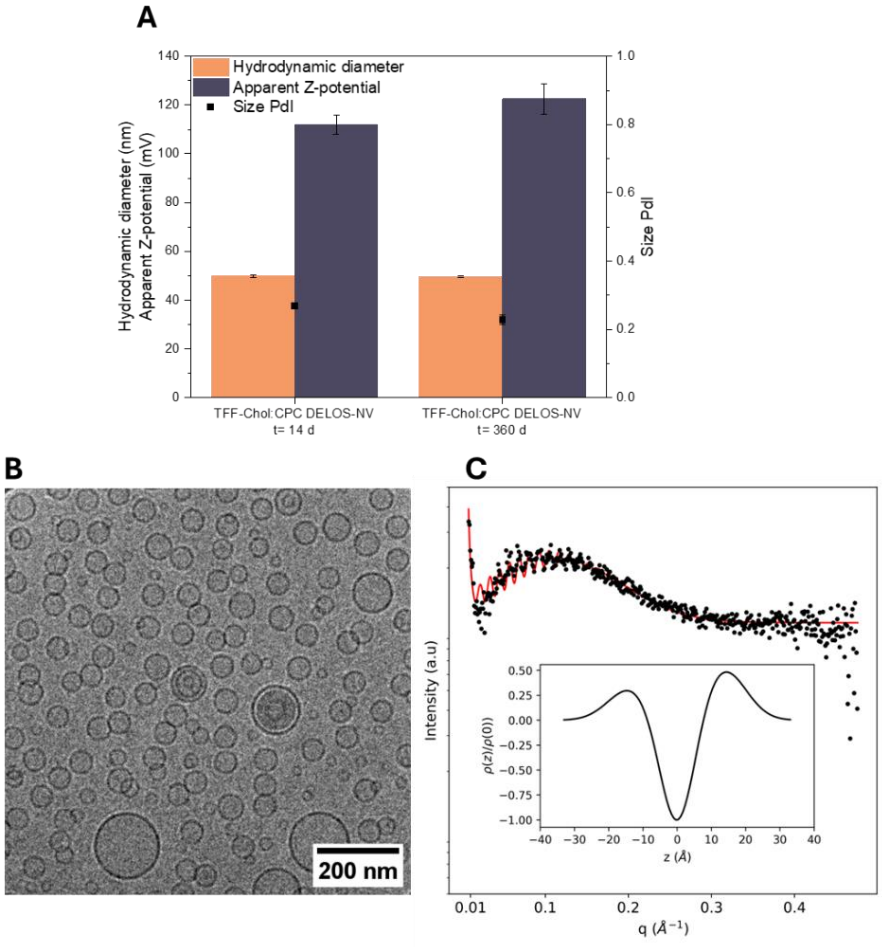


Figure 4.4. Characterization of the optimized TFF-Chol:CPC DELOS-NV after their diafiltration by TFF. A) Mean hydrodynamic diameter, size PdI, and apparent Z-potential obtained by DLS and ELS at t = 14 days and t = 360 days. B) Cryo-TEM image at t = 360 days. C) SAXS data at t = 360 days, in the inset the electron density profile obtained from the bilayer modeling. The model fit including the instrument smearing effects is shown as the red curve.

All characterizations demonstrated that the obtained DELOS-NV possess suitable physicochemical properties to be used as drug delivery systems. Additionally, they exhibit excellent stability over time. Consequently, these DELOS-NV will be further developed into a subcutaneous depot for extended therapeutic molecule administration through gelation with Plx407 polymer.

4.3. Preparation and characterization of the DELOS-NV-loaded Poloxamer 407 hydrogels

4.3.1. Preparation of TFF-Chol:CPC DELOS NV-loaded Poloxamer 407 hydrogels

Plx407 was chosen due to being a non-ionic gelling agent since the compatibility of DELOS-NV with non-ionic polymers has previously been demonstrated[3]. In addition, this polymer is considered a GRAS (generally recognized as safe) substance accepted and listed in the US and European Pharmacopeia[25,28,44].

The optimized prototype of TFF-Chol:CPC DELOS-NV (see formulations details in **Table 9.1**), composed of 5 mg/mL of Chol and CPC at an equimolar ratio in histidine 5 mM buffer, pH 7, and diafiltrated by TFF, was gelled by adding the Plx407 polymer as powder (see method in **Section 9.2.3**).

As mentioned in **Section 4.1.2**, Plx407 hydrogels are thermoreversible, they change their structuration in response to the temperature. But this transition is also concentration-dependent. At the same temperature, higher concentrations of Plx407 are more organized than lower concentrations of Plx407 (**Figure 4.1**). Therefore, modulating the concentration of Plx407, the hydrogels' transition temperature from solution to gelation ($T_{sol\text{-}gel}$) can be adjusted. This temperature is also known as the low critical solution temperature and is highly relevant as it indicates the temperature at which the hydrogel transitions from behaving primarily as a liquid to behaving predominantly as a solid.

Different concentrations of Plx407 were tested based on the literature[27,35,45–47] (15%, 17%, 20%, and 23% w/w) to find the most appropriate concentration for SC delivery of DELOS-NV, as a function of the $T_{sol\text{-}gel}$ and solid character. Blank hydrogels with the same Plx407 concentration were also produced as controls considering the same media as DELOS-NV but without nanovesicles. Next **Table 4.2** describes the different hydrogels prepared to evaluate the impact of Plx407 concentration on the formulations.

Table 4.2. *Hydrogels prepared with the different concentrations of Plx407 tested.*

Sample ID	***Poloxamer 407 concentration (% w/w)***	***DELOS-NV incorporation***
Blank 15% w/w Plx407	*15*	*NA*
Blank 17% w/w Plx407	*17*	*NA*
Blank 20% w/w Plx407	*20*	*NA*
Blank 23% w/w Plx407	*23*	*NA*
TFF-Chol:CPC DELOS-NV-loaded 15% w/w Plx407	*15*	*TFF- Chol:CPC DELOS-NV*
TFF-Chol:CPC DELOS-NV-loaded 17% w/w Plx407	*17*	*TFF- Chol:CPC DELOS-NV*
TFF-Chol:CPC DELOS-NV-loaded 20% w/w Plx407	*20*	*TFF- Chol:CPC DELOS-NV*
TFF-Chol:CPC DELOS-NV-loaded 23% w/w Plx407	*23*	*TFF- Chol:CPC DELOS-NV*

4.3.2. Macroscopical and microscopical observation of the Poloxamer 407 hydrogels

Once prepared, the hydrogels were macroscopically examined. Colorless blank Plx407 hydrogels and whitish TFF-Chol:CPC DELOS-NV-loaded Plx407 hydrogels, very homogeneous in appearance, were obtained, exhibiting excellent organoleptic properties. **Figure 4.5** presents images of the hydrogels at 4 °C, 22 °C, and 37 °C, illustrating the viscosity change according to temperature for the four concentrations of Plx407 tested. While all samples are liquid at 4 °C (the hydrogel flows from the base of the vial to the cap of the vial when inverted), at 22 °C, each hydrogel concentration displays a different behavior. The 15% and 17% w/w Plx407 hydrogels still behave as liquids, whereas the 20% w/w hydrogel shows an increase in viscosity and some resistance to flow, and the 23% w/w hydrogel does not flow at all, behaving as a solid. At 37 °C, again, blank and NV-loaded hydrogels behave similarly, becoming solid and remaining at the base of the vial despite gravitational force.

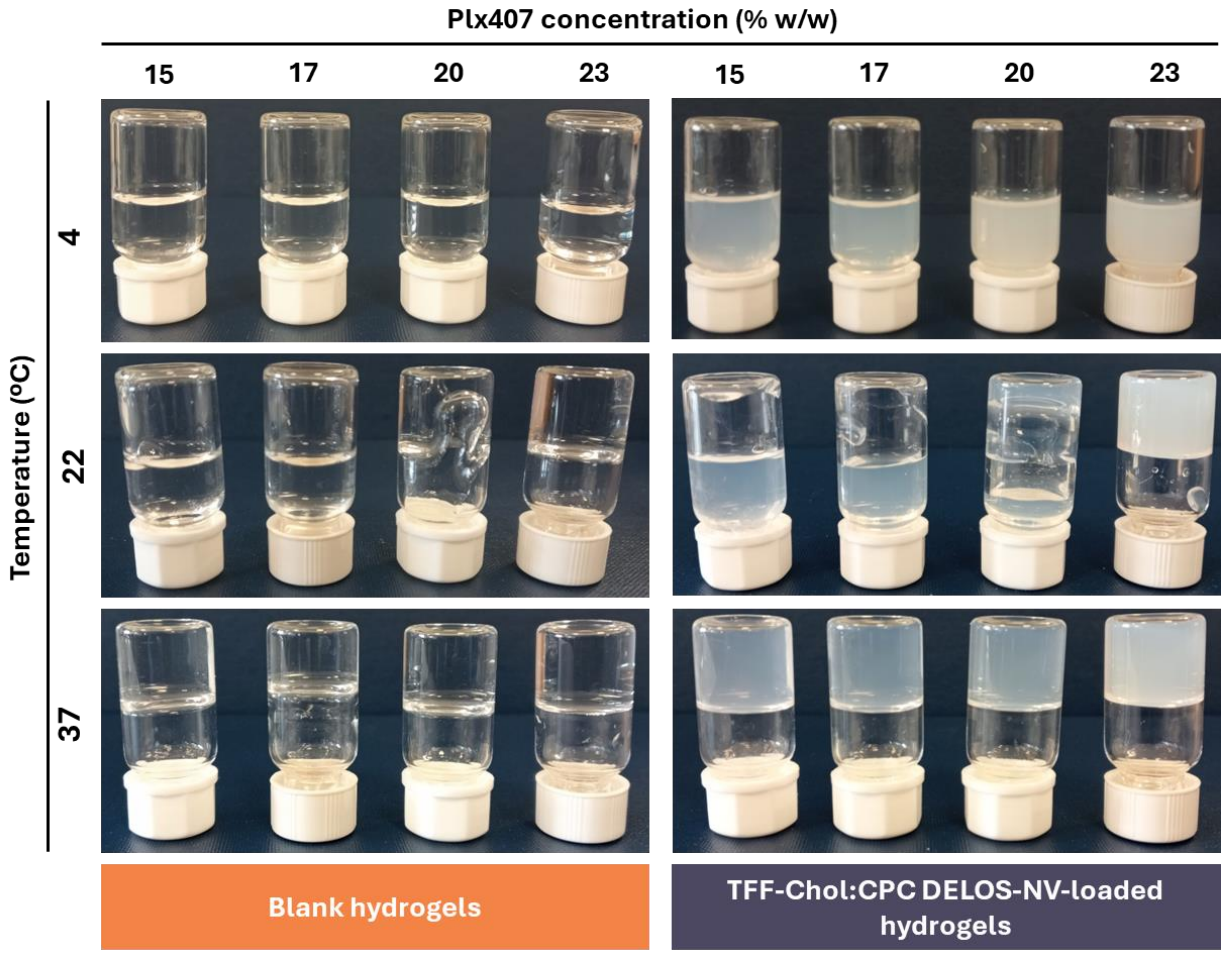


Figure 4.5. *Macroscopical images of inverted vials containing the different concentrations of Plx407 at 4 °C, 22 °C, and 37 °C. Images were obtained after 30 minutes of temperature stabilization.*

The hydrogels were microscopically examined with an optical microscope coupled to a camera (see **Section 9.3.14**) in search of aggregates or microscopic precipitation. Several areas of each hydrogel were screened. The hydrogels exhibited a homogeneous structural composition (**Figure 4.6**). Only a few isolated particles were detected at a concentration that appeared insignificant. These particles likely represented small air bubbles entrapped within the hydrogel matrix rather than any form of precipitate. Therefore, concluding that the hydrogel samples are free from precipitated material.

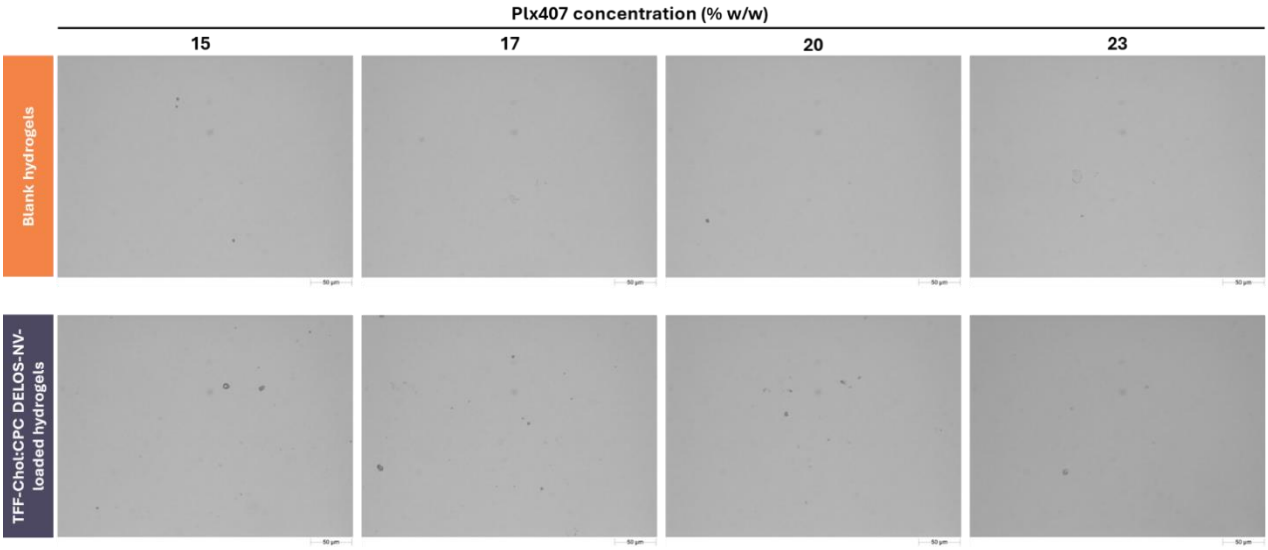


Figure 4.6. *Representative optical microscope images at 20x magnifications of the microscopical appearance of the Poloxamer 407 (Plx407) hydrogels.*

4.3.3. Small-angle X-ray scattering characterization of the Poloxamer 407 hydrogels

In this section, the TFF-Chol:CPC DELOS-NV-loaded Plx407 hydrogels (15%, 17%, 20%, and 23% w/w Plx407) were analyzed by SAXS at 22 °C to understand their structurization at room temperature. Different concentrations of Plx407 polymer are expected to exhibit varying structurization at this temperature. This information is relevant since, as explained at the beginning of **Section 4.2**, the objective of this **Chapter** is to develop an injectable hydrogel at 22 °C that forms an *in situ* depot at SC temperature.

The SAXS analysis of the hydrogels were also conducted at the ALBA Synchrotron. The fundaments of the SAXS technique and the parameters employed for the analysis are described in **Section 9.3.5**, and the SAXS profiles of the hydrogels studied are shown in **Figure 4.7.**

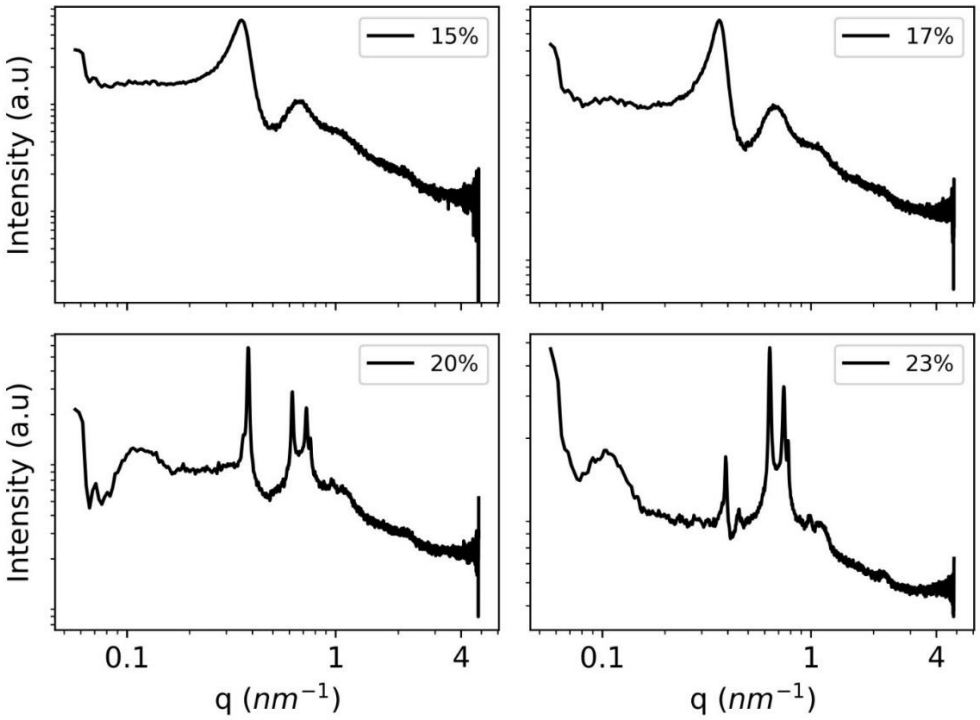


Figure 4.7. *SAXS data at 22 °C of the different concentrations of TFF-Chol:CPC DELOS-NV-loaded Plx407 hydrogels evaluated in the present study (15%, 17%, 20%, and 23% w/w Plx407). 15 and 17% w/w DELOS-NV-loaded Plx407 correspond to the liquid of the Plx407 micelles structure after gelation with short-range order, while 20 and 23% DELOS-NV-loaded w/w Plx407 showed crystallization with Bragg peaks.*

At 22 °C, the SAXS profiles for the TFF-Chol:CPC DELOS-NV-loaded Plx407 hydrogels with 15% and 17% w/w Plx407 correspond to a structurization of Plx407 micelles after gelation[45], exhibiting only a short range of order and a low solid-like behavior. In contrast, the TFF-Chol:CPC DELOS-NV-loaded hydrogels with higher concentrations of Plx407 (20% and 23% w/w), displayed a crystalline-like SAXS profile. This evolution in the state of the TFF-Chol:CPC DELOS-NV-loaded hydrogels observed by SAXS might be attributed to the dehydration of the Plx407 micelles at higher polymer concentrations, resulting in an entropic change of state into a partly ordered cubic liquid crystalline gel state[29].

The low degree of organization at 22 °C of the hydrogels with 15% and 17% w/w Plx407 suggest that these concentrations of Plx407 will present low viscosity and flow easily through a syringe at room temperature. In contraposition, the higher structurization observed in the hydrogels with 20% and 23% w/w Plx407 could indicate lower flowability of these hydrogels at injection conditions. Actually, the hydrogels obtained with the 23% w/w Plx407 gelled very quickly when removed from the fridge (**Figure 4.5**), thus hampering their injectability at RT. Due to this practical limitation, the 23% w/w Plx407 hydrogel was excluded from subsequent experiments. Further studies will focus on formulations containing 15%, 17%, and 20% w/w of Plx407.

4.3.4. Evaluation of the DELOS-NV integrity within the Poloxamer 407 hydrogels by cryogenic transmission electron microscopy

It is well known that the structure and stability of nanovesicles are notably affected by the dispersion medium[1,3]. Certain media, such as buffers with high salt content, can destabilize the nanovesicles, leading to the formation of aggregates and/or membrane breakage. To demonstrate the preservation of DELOS-NV structure when incorporated in hydrogels, Cryo-TEM images of the different TFF-Chol:CPC DELOS-NV-loaded Plx407 hydrogels were obtained as described in **Section 9.3.4**.

Dilutions 1:5 of the TFF-Chol:CPC DELOS-NV-loaded hydrogels (15%, 17% and 20% w/w Plx407) in water were prepared to adjust the viscosity for analysis. The concentration of Plx407 of the different TFF-Chol:CPC DELOS-NV-loaded hydrogels upon this dilution was in the range of 2.8 to 4.0 mM Plx407. At these low concentrations and room temperature, the hydrogels behave as liquids. It should be noted that the polymer may exist in its monomeric state at these concentrations, as its critical micellar concentration (CMC) is highly temperature-dependent, and is around 1.25 mM at 27 °C[48] and 2.8 μM at 37 °C[49]. Nonetheless, the goal is not to observe the hydrogel, but rather to assess the integrity of the nanovesicles after their exposure to high concentrations of Plx407 polymer.

Cryo-TEM images (**Figure 4.8**) showed well-formed spherical, unilamellar, and homogeneous nanovesicles in all the tested formulations. Worth noting: higher concentrations of Plx407 hydrogel resulted in the coating of some TFF-Chol:CPC DELOS-NV, probably due to partial adsorption of the polymer's hydrophobic chains into the nanovesicle membrane. This can be appreciated by an increase in the nanovesicle membrane's width in the Cryo-TEM images. In fact, Plx407 has been employed in the literature for surface engineering of nanoparticles in suspension[50], since its integration on nanovesicle surfaces can modify the biological fate of nanoparticles *in vivo* by reducing protein adsorption and increasing circulation time.

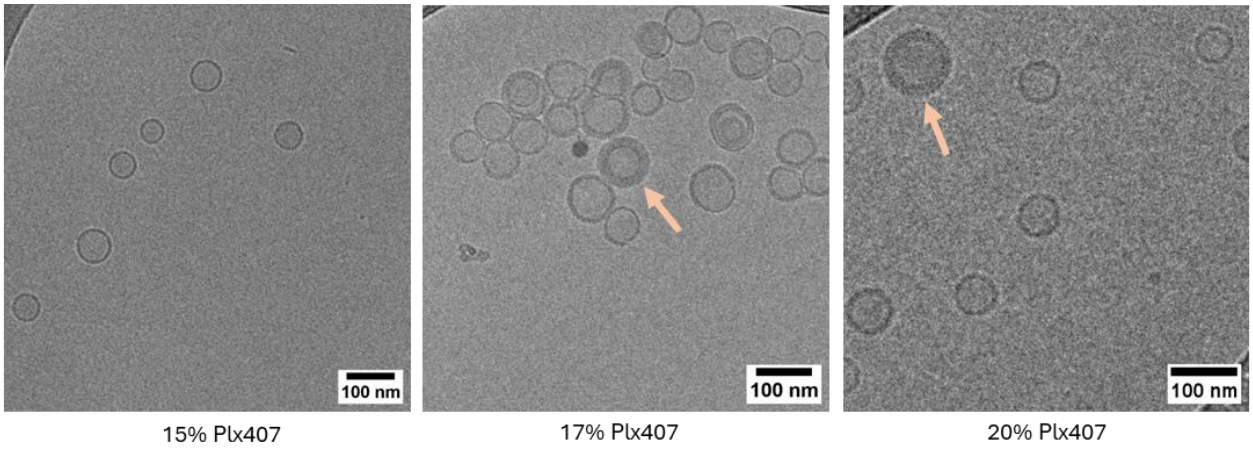


Figure 4.8. *Cryo-TEM images of the TFF-Chol:CPC-DELOS-NV embedded in Plx407 (from left to right: 15%, 17% and 20% w/w Plx407). The arrows highlight an increase in the membrane's width.*

4.3.5. *Evaluation of the DELOS-NV integrity within the Poloxamer 407 hydrogels by Förster resonance energy transfer analysis*

After having confirmed maintenance of the spherical and unilamellar structure of Chol:CPC DELOS-NV within the hydrogels by Cryo-TEM, a characterization of the bulk stability of the colloidal dispersion was conducted using FRET phenomenon (see **Section 9.3.9**). The FRET phenomenon occurs between a pair of light-sensitive molecules, where the emission spectrum of one molecule (the donor) overlaps with the excitation spectrum of the other (the acceptor). When these pairs of molecules are closer than 10 nm of each other, there is an energy transfer from the donor chromophore, initially in its electronically excited state, to the acceptor chromophore (**Figure 4.9A**). This technique is known as the spectroscopic ruler because the efficiency of the energy transfer is inversely proportional to the sixth power of the distance between the donor and acceptor[51]. For this reason, it can be employed as a research tool to determine nanovesicle stability and integrity (**Figure 4.9B**): If nanovesicles break down or dissociate, a decrease in FRET efficiency should be detected[3,52].

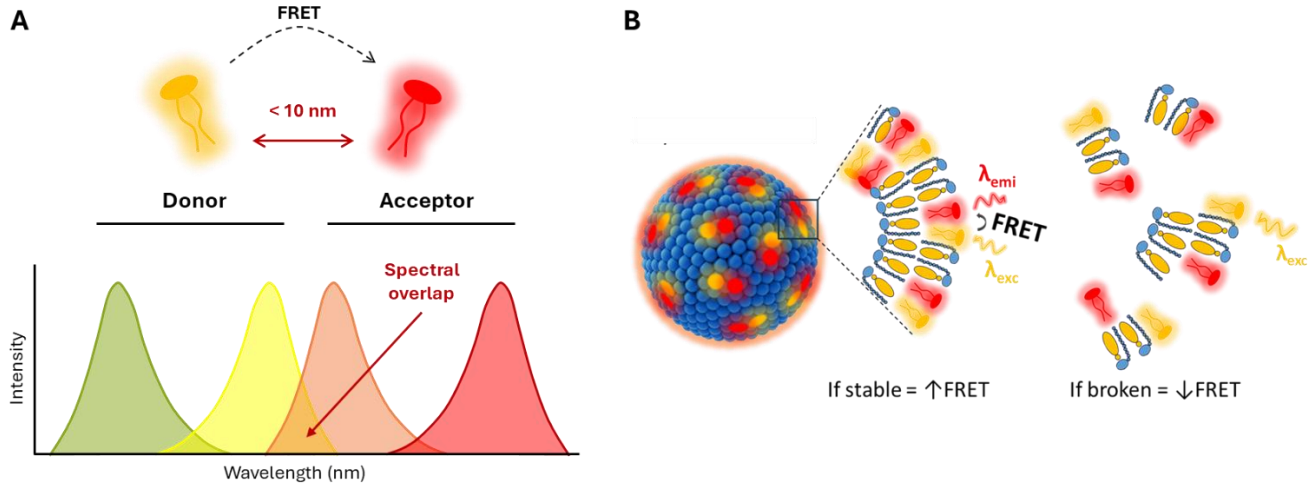


Figure 4.9. *A) Representation of the Förster resonance energy transfer phenomenon. The two requisites that must be complied with for FRET are written in bold red letters in the figure. B) Schematic representation of the employment of FRET phenomenon to study DELOS nanovesicles stability.*

An example of a well-known pair of FRET chromophores are 1,1'-dioctadecyl-3,3,3',3'-tetramethyl-indocarbocyanine perchlorate (DiI) and 1,1'-dioctadecyl-3,3,3',3'-tetramethyl-indodicarbocyanine perchlorate (DiD) (**Figure 4.10A**). They both have been successfully integrated in similar DELOS-NV in previous studies, and their FRET efficiency when embedded in the nanovesicles has been demonstrated[3,53,54]. Importantly, carbocyanine are amphiphilic molecules whose incorporation into the DELOS-NV membrane is driven by hydrophobic interactions and its leakage once entrapped at the membrane is negligible[54].

Based on this, the novel TFF-Chol:CPC DELOS-NV optimized for SC delivery were prepared by loading 45 µM DiI and 45 µM DiD. This new formulation was prepared by the DELOS method (see **Section 9.2.1**) and diafiltrated by TFF with a 100 kDa cut-off hollow fiber column to eliminate the EtOH (and any possible carbocyanine molecule that was not integrated in the nanovesicles and remained solubilized in the EtOH) (see **Section 9.2.2**). The formulation was named DiI/DiD-DELOS-NV and the detailed composition can be found in **Table 9.1.** As a control, a batch containing

exclusively DiD at the same concentration as it is present in DiI/DiD-DELOS-NV formulation (45 μM DiD) was also produced by DELOS and diafiltrated by TFF with the same hollow fiber (DiD-DELOS-NV), (see **Section 9.2.1**, **Section 9.2.2** and **Table 9.1**) (**Figure 4.10B**).

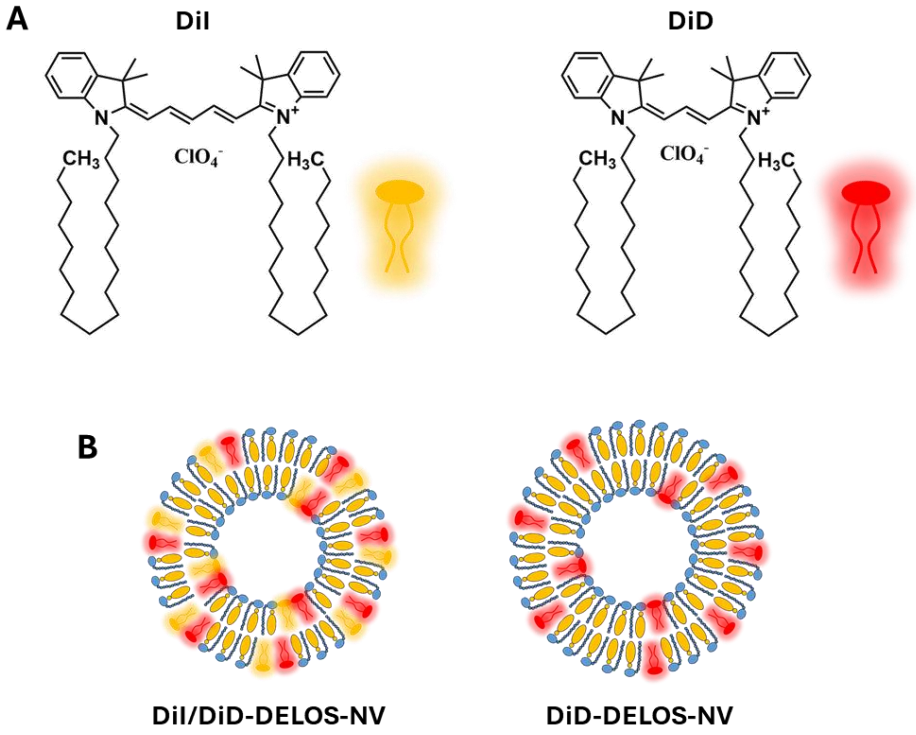


Figure 4.10. *A) Molecular structure of the DiI and DiD fluorophores. B) DELOS nanovesicle systems prepared for the stability evaluation of DELOS nanovesicles within hydrogels.*

Once produced and diafiltrated by TFF, the formulations were characterized prior to the FRET analysis.

Figure 4.11A shows the DLS and ELS results (see **Section 9.3.1** for DLS and ELS method details) after 14 days of maturation, which was the time defined in the previous **Chapter** for Chol:CPC-DELOS-NV. The DiI/DiD-DELOS-NV had a mean hydrodynamic diameter of 100.7 ± 0.6 nm, a size PdI of 0.349 ± 0.021 and an apparent Z-Potential of 76 ± 7 mV, and the DiD-DELOS-NV had a mean hydrodynamic diameter of 114.4 ± 2.8 nm, a size PdI of 0.432 ± 0.026 and an apparent Z-Potential of 52 ± 7 mV. The periodical analysis of these properties demonstrated the stability of the loaded nanovesicles for at least 2 months.

In addition, Cryo-TEM images were obtained (see method in **Section 9.3.4**). As shown in **Figure 4.11B,** both systems present spherical and unilamellar nanovesicles. In addition, their macroscopical appearance shows a homogeneous sample, which presents the typical color conferred by the dyes incorporated into the nanovesicles.

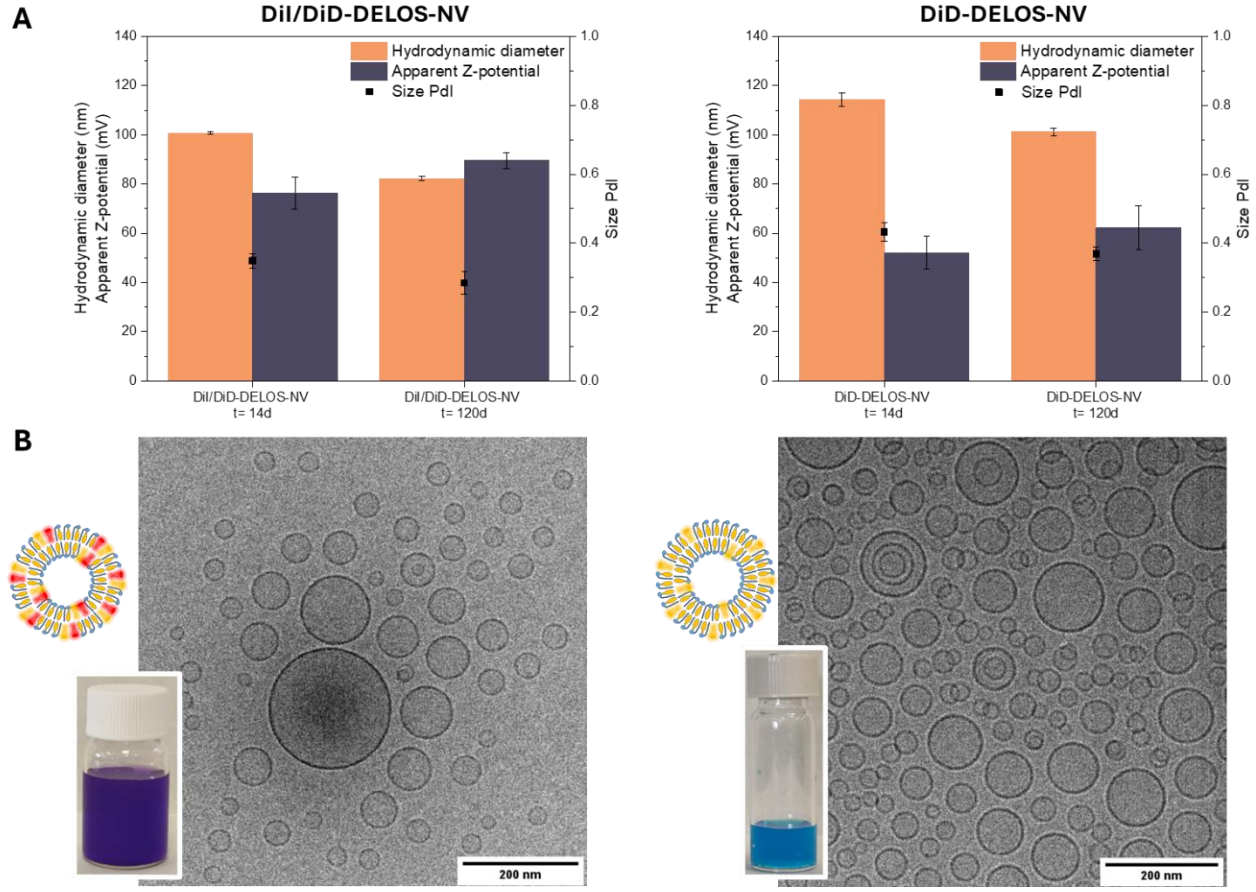


Figure 4.11. *Characterization of the DiI/DiD-DELOS-NV (left) and DiD-DELOS-NV (right). A) Average hydrodynamic diameter, apparent Z-potential, and average size PdI at t = 14 days and t = 120 days. B) Macroscopic images and Cryo-TEM images at t = 120 days.*

Once confirmed the appropriate physicochemical properties of the labelled-DELOS-NV (DiI/DiD-DELOS-NV and DiD-DELOS-NV), the DiI/DiD-DELOS-NV were gelled into 15%, 17%, and 20% w/w Plx407 (**Figure 4.12A**) to evaluate their stability and integrity through the fluorescence emission of the dye pair (see **Section 9.2.3** for the gelling method). The DiD-DELOS-NV were also gelled at 17% w/w Plx407 as a control (**Figure 4.12B**).

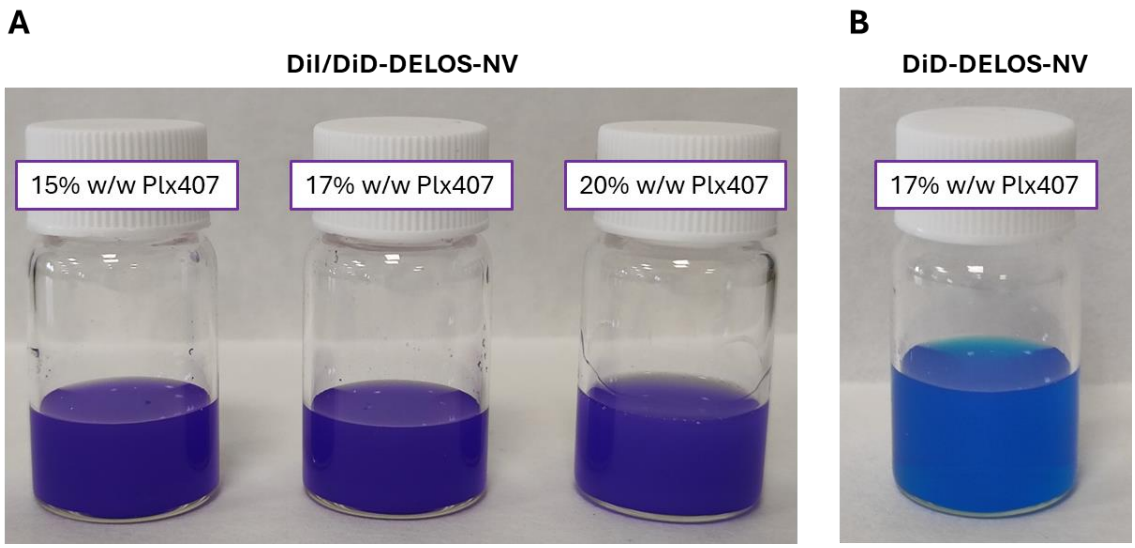


Figure 4.12. *Macroscopic images of the A) DiI/DiD-DELOS-NV gelled into 15%, 17% and 20% w/w Plx407 and B) DiD-DELOS-NV gelled into 17% w/w Plx407.*

Afterwards, the absorbance spectra of the pair of fluorophores incorporated into the DiI/DiD-DELOS-NV were recorded by ultraviolet-visible (UV-Vis) spectroscopy (see method in **Section 9.3.7**). The absorbance spectra of the pair of fluorophores incorporated into the DiI/DiD-DELOS-NV (**Figure 4.13A**) did not present significant variations from the liquid dispersion to the gelled state, indicating stability of the DiI/DiD-DELOS-NV and residence of the fluorophores in the membranes despite the formulation. The monomeric DiI and DiD fluorophores absorb at 551 nm and 650 nm, respectively; however, carbocyanines are prone to aggregate into H-aggregates and J-aggregates with differentiated absorption peaks[55,56]. The absorbance spectra of the DiI/DiD-DELOS-NV demonstrated the predominance of the non-aggregated carbocyanines, in both suspension and hydrogels. The absorbance spectra of the control with only DiD (**Figure 4.13B**) shows a peak at 650 nm as expected, and no peak at 551 nm. Predominance of monomers non-dependent on the formulation (suspension or gel) was also demonstrated with the DiD-DELOS-NV-loaded 17% w/w Plx407 hydrogel.

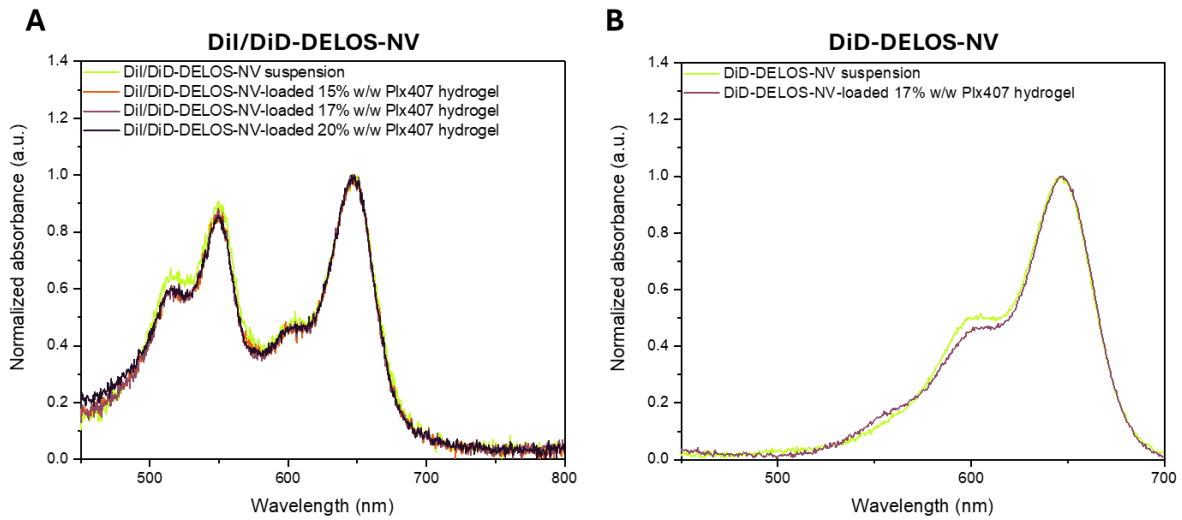


Figure 4.13. *UV-Vis absorbance spectra of the A) DiI/DiD-DELOS-NV and B) DiD-DELOS-NV, both in suspension and gelled with different concentrations of Plx407.*

Next, the FRET efficiency was investigated for the dispersion and the different concentrations of Plx407 hydrogels containing DiI/DiD-DELOS-NV or DiD-DELOS-NV. First, the excitation of the DiI at λ_{ex} = 490 nm resulted in two emission bands at ~569 nm and at ~673 nm, corresponding to the DiI and DiD emission, respectively, thus indicating the FRET phenomenon (**Figure 4.14**). As anticipated, excitation of the control DiD-DELOS-NV at λ_{ex} = 490 nm did not result in DiD emission due to the absence of FRET (**Figure 4.14**).

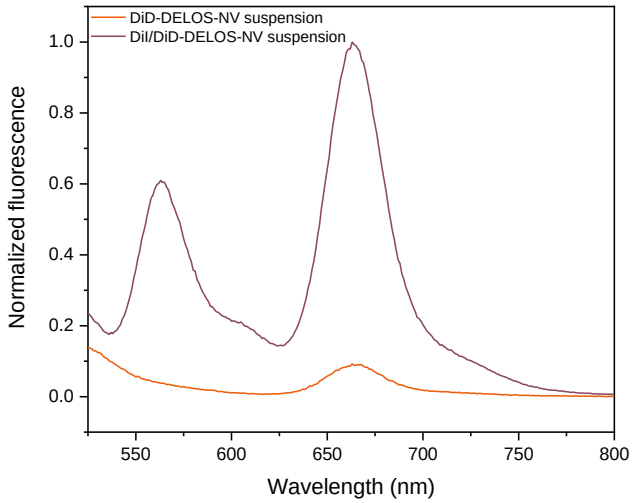


Figure 4.14. *Fluorescence spectra of the DiI/DiD-DELOS-NV and the DiD-DELOS-NV when exciting the DiI at λ_{ex} = 490 nm.*

Once confirmed that FRET was only observed on DELOS-NV containing DiI and DiD fluorophores, and not in the negative control DiD-DELOS-NV, the FRET efficiency of non-gelled and gelled DiI/DiD-DELOS-NV in Plx407 was measured 2 days and 30 days after gelation (**Figure 4.15A**). The FRET

efficiency was estimated through the ratiometric approach from emission spectra upon excitation at 490 nm using **Equation 9.4**[3] (see **Section 9.3.9**) (**Figure 4.15B**). As shown, the estimated FRET efficiencies were consistently around 70% for both states, aligning with previous findings on the stability of similar DELOS-NV formulations in both suspension and gelled with hydroxypropyl methylcellulose hydrogels[3]. In addition, stability tests over time showed no significant differences between the FRET efficiency measurements at time 2 days and time 30 days post-preparation, suggesting structural stability of the DiI/DiD-DELOS-NV within the Plx407 hydrogels for at least 30 days.

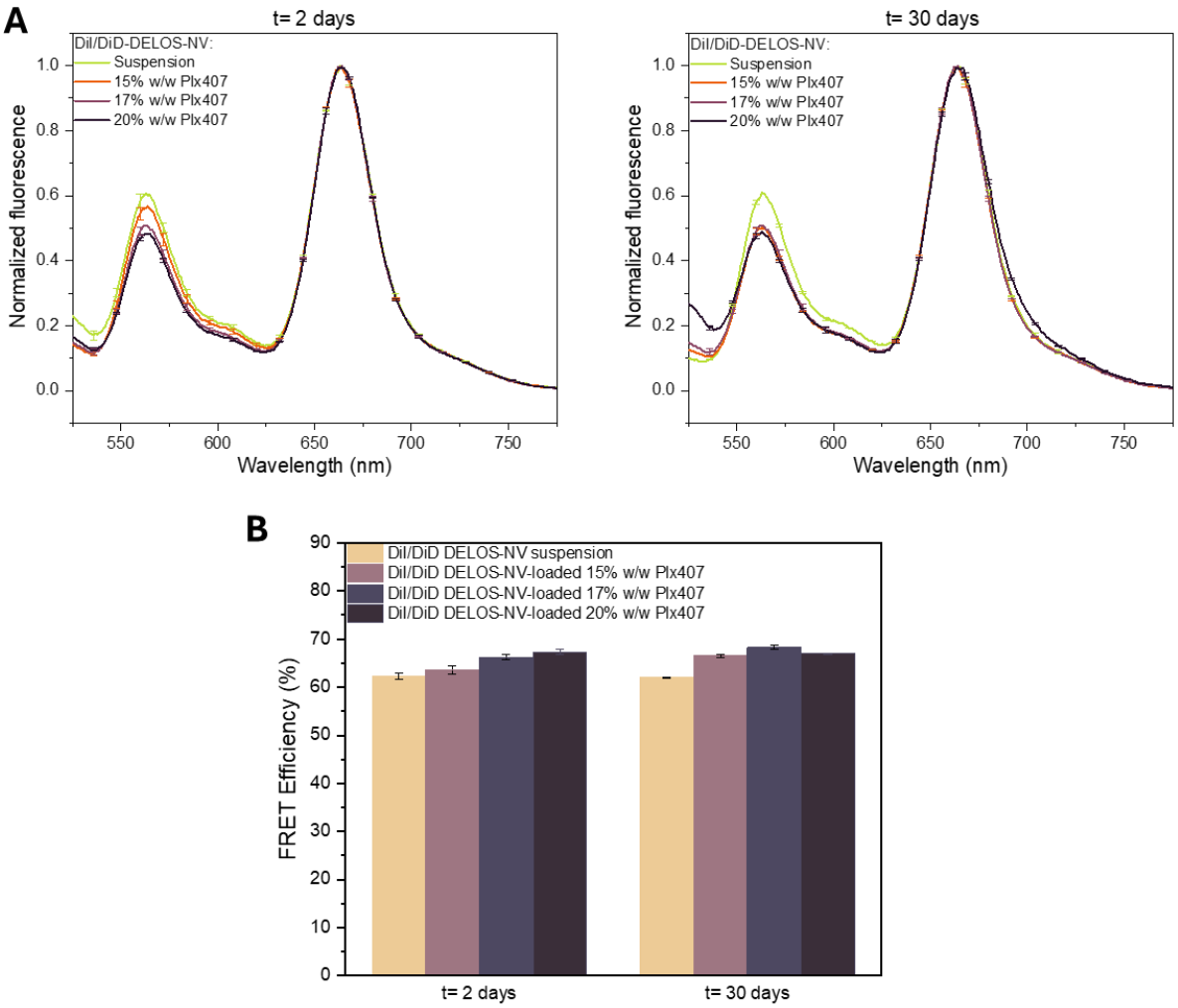


Figure 4.15. *Stability of labelled-DELOS-NV embedded in Plx407 hydrogels. A) FRET efficiency spectra (λ_{ex} = 490 nm) at 2 days after gelation (left) and 30 days after gelation (right) of the DiI/DiD-DELOS-NV (mean ± SD, n = 3; The SD is represented for only 20 randomized and representative data points for ease of interpretation). B) FRET efficiency percentages at 2 days and 30 days after gelation of the DiI/DiD-DELOS-NV (mean ± SD, n = 3).*

Overall, the experimental results confirmed the stability of the TFF-Chol:CPC DELOS-NV gelled with different concentrations of Plx407 polymer, which settles the basis for the development of a novel hybrid platform for SC delivery combining both systems: DELOS-NV and the thermoreversible Plx407 hydrogel.

4.3.6. Rheological behavior of TFF-Chol:CPC DELOS-NV-loaded Poloxamer 407 hydrogels

Once demonstrated stability of the DELOS-NV within the hydrogels, the next step was to assess the suitability of these hydrogels to be employed as *in situ* depots. In that sense, evaluating their flow properties is very important since it will determine the capacity of the hydrogels to flow during the injection and to form a cohesive depot once in the SC tissue.

The rheology is the science that studies the flow behavior of viscoelastic materials. According to rheology, most materials are not completely viscous or solids. They have a mix of both components. Materials with the highest viscous portion are called Viscous/Newtonian liquids, while materials with the highest elastic portion are called elastic/Hookean solids. An example of a very viscous material could be water and an example of a very elastic material could be steel.

Elasticity is the ability of a material to stretch in response to a force and to recover its original state when the force is removed. It is directly related to the resistance/stiffness of a material. If the material stiffness is higher than the force applied, the material will not deform. The elastic component of a material is defined by the following **Equation 4.2**:

$$\text{Young's Elastic modulus} = \frac{Stress}{Strain}$$

Equation 4.2. *Young's elastic modulus equation.*

It is depicted by this equation that the lower the deformation of a material in response to a force is, the greater its elasticity.

In purely elastic materials the energy applied for deformation is completely stored without any loss and employed to recover the original state.

In contraposition, viscosity measures the resistance to flow in response to a force, and it depends on the internal friction of the molecules of the material. The viscous component of a material is defined by the following **Equation 4.3**:

$$\text{Viscosity} = \frac{Shear\ stress}{Shear\ rate}$$

Equation 4.3. *Viscosity equation.*

Therefore, fluids with high viscosity will require higher energies to flow. Completely viscous materials lose all the energy applied to them, and that is why they are not able to return to their initial state after being deformed[57].

However, few materials are completely viscous or elastic, most of them present a mix of both components and are called viscoelastic materials.

Plx407 hydrogels are viscoelastic materials in which their viscous and elastic component is extremely influenced by the temperature. These materials behave mostly as liquids (predominance of the viscous component) at lower temperatures, while transform into mostly solids (predominance of the elastic component) at higher temperatures. The rheological characterization of these

hydrogels at different temperatures is very interesting to determine which concentration will be the most appropriate for the intended use.

The flow properties of the different concentrations of Plx407 hydrogel containing TFF-Chol:CPC DELOS-NV were assessed through a shear rate ramp in a rotational mode. The blank hydrogels (without DELOS-NV) were also characterized as controls (**Table 4.2**). These measurements were performed at storage temperature (4 °C), room temperature (22 °C), and body temperature (37 °C) according to the method described in **Section 9.3.12**. As shown in **Figure 4.16**, the rheological behavior of the evaluated hydrogels varies with temperature and Plx407 concentration. At 4 °C, all hydrogels exhibit a Newtonian fluid behavior, where the viscosity remains constant regardless of the applied shear force. In contrast, at 37 °C, all the hydrogels exhibit pseudo-plastic behavior with shear-thinning characteristics, showing yield stress, a minimum force required to start to flow, and decreasing viscosity with increasing shear rates. At 22 °C, the 20% w/w Plx407 hydrogel behaves as a pseudo-plastic fluid, while the other two lower concentrations (15% and 17% w/w Plx407) remain Newtonian fluids.

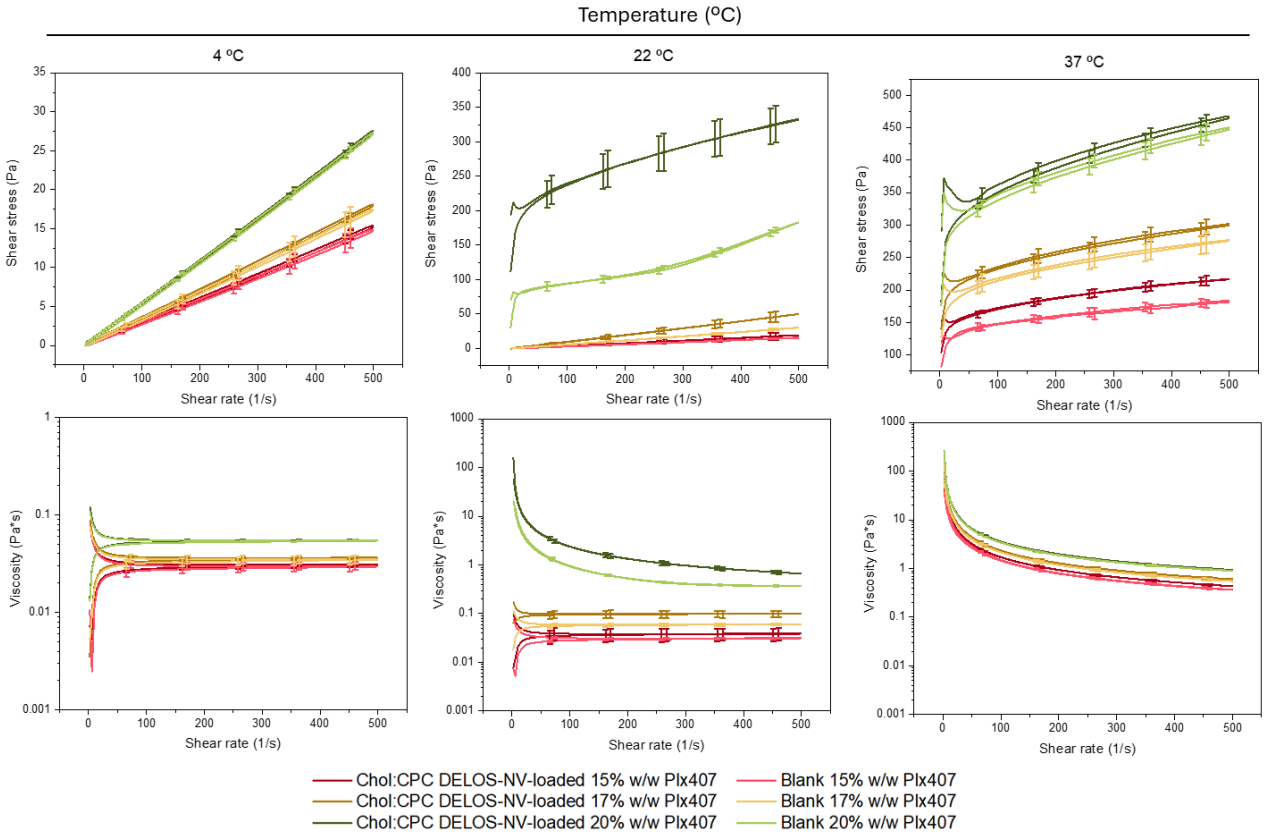


Figure 4.16. *Shear stress (above) and viscosity (below) as a function of shear rate, of the 15%, 17%, and 20% w/w Poloxamer 407 (Plx407) hydrogels with and without TFF-Chol:CPC-DELOS-NV analyzed at 4 °C, 22 °C and 37 °C, (mean ± SD, n = 3, the SD is represented only for 10 randomized and representative data points for ease of interpretation).*

The rotational analysis results suggest that the concentration of Plx407 employed in the formulation has a stronger impact on the hydrogels' flow behavior than the presence or absence of TFF-Chol:CPC DELOS-NV in the hydrogels. However, the inclusion of nanovesicles also impacts the hydrogels' flow

behavior. When behaving as Newtonian fluids, the flow curves of the hydrogels with and without DELOS-NV overlap, but when behaving as pseudo-plastic fluids, the inclusion of DELOS-NV into the Plx407 hydrogels has a small, yet consistent impact on the hydrogels' behavior since the shear stress *vs* shear rate curves of the TFF-Chol:CPC DELOS-NV-loaded hydrogels are always slightly above the curves of the blank hydrogels.

It is noteworthy that a notable difference in the flow curves of the 20% w/w Plx407 hydrogels with and without TFF-Chol:CPC DELOS-NV is observed at 22 °C. This is primarily due to the sharp change in viscosity of Plx407 hydrogels at their $T_{sol\text{-}gel}$ and the slight decrease in $T_{sol\text{-}gel}$ caused by DELOS-NV, as it will be observed with the following oscillatory tests (**Figure 4.17**). **Table 4.3** shows that the 20% w/w Plx407 hydrogels present a $T_{sol\text{-}gel}$ very close to 22 °C, and therefore, the presence of DELOS-NV can strongly impact the flow curve of this hydrogel at this temperature by decreasing the $T_{sol\text{-}gel}$.

All hydrogels exhibit low thixotropy at 37 °C (**Figure 4.16**). This is evidenced by their small or non-existent hysteresis loop area, indicating that their inner structure recovers quickly after shear-thinning. This property could facilitate prompt depot formation after injection, preventing spread.

Viscosity also plays a crucial role in preventing spread after SC injection. While low viscosities enable flow through SC syringes (injectability), higher viscosities can slow down water penetration during injection, reducing burst release and hydrogel dissolution rate in body fluids[58]. Viscosities were compared between samples at 22 °C and 500 s^{-1} (**Table 4.3**), the closest conditions to real injection scenarios. However, note that typical shear rates during injections are higher[59], leading to lower Plx407 hydrogel viscosities due to their shear-thinning behavior.

The viscosity results presented in **Table 4.3** confirm that hydrogels containing TFF-Chol:CPC DELOS-NV exhibit higher viscosities. As expected, the differences in viscosities between blank and TFF-Chol:CPC DELOS-NV-loaded Plx407 hydrogels are more pronounced for the 20% w/w Plx407 concentration. Further, lower polymer concentrations result in lower viscosities. The 15% w/w Plx407 hydrogels have viscosities below 0.05 Pa s, making them easily injectable through a 25 G syringe, which is the preferred option for SC administration[60]. The 17% w/w Plx407 viscosities are close to the injectability limit; nevertheless, the injectability test through a 25 G syringe demonstrated appropriate injectability despite their higher viscosity as will be explained in **Section 4.3.7** and **Figure 4.18**. Eventually, the 20% w/w Plx407 hydrogels present viscosity values above 0.1 Pa s, thus potentially requiring either the use of a larger gauge syringe or pre-treatment to reduce viscosity. This highlights the importance of tuning Plx407 concentration to achieve good injectability, ensuring effective delivery and patient comfort.

The $T_{sol\text{-}gel}$ was studied by determining the storage (*G'*) and loss (*G''*) modulus at different temperatures through an oscillatory test, as described in **Section 9.3.12**. The storage modulus relates to the material's ability to store energy elastically, and the loss modulus relates to the material's ability to dissipate energy through heat and describes the viscose part of the sample.

Plx407 hydrogels exhibit a unique behavior in which they perform as viscous fluids at lower temperatures and become solid-like at higher temperatures. This behavior is reflected by a predominance of *G''* over *G'* at lower temperatures, which is then inverted to *G' > G''* at higher temperatures. The temperature at which *G''* equals *G'* is called the transition temperature ($T_{sol\text{-}gel}$) or low critical solution temperature.

The ramp temperatures showed a gradual decrease of the $T_{sol\text{-}gel}$ in response to the Plx407 concentration increase (**Figure 4.17**). Blank hydrogels and TFF-Chol:CPC DELOS-NV-loaded hydrogels with 15% and 17% w/w Plx407 present $T_{sol\text{-}gel}$ values above 25 °C, thus being appropriate for their injection at 22 °C. Oppositely, the blank 20% w/w Plx407 hydrogel presents a $T_{sol\text{-}gel}$ around 22 °C, which is in concordance with the elevated viscosities determined previously at this temperature; therefore, it was decided to discard this concentration of Plx407 for further studies since its injectability would not be adequate (**Table 4.3**). For this reason, the $T_{sol\text{-}gel}$ of the TFF-Chol:CPC DELOS-NV-loaded 20% w/w Plx407 hydrogel was not evaluated.

Again, the impact of the TFF-Chol:CPC DELOS-NV in the 15% and 17% w/w Plx407 hydrogels $T_{sol\text{-}gel}$ was evaluated (**Table 4.3**). The incorporation of Chol:CPC DELOS-NV in the hydrogels causes a small decrease in the $T_{sol\text{-}gel}$.

The 'phase angle' (δ) is a relative measure of the viscous and elastic properties of a material. It can be obtained by taking the arctangent of the ratio of the loss modulus to the storage modulus. It illustrates the lag between the movement of the sample with the oscillatory movement of the cone. A purely elastic material will have a phase angle of 0, while a purely viscous material will have a phase angle of 90°. Therefore, viscoelastic materials have phase angle values between 0 and 90°. The greater the value of G' concerning G'', the lower the value of the phase angle. Taking it into account, the presence of Chol:CPC DELOS-NV in the Plx407 hydrogels results in a more solid-like behavior of the hydrogels by decreasing their phase angle at 37 °C (**Table 4.3**). This is a positive feature as more solid-like hydrogels result in lower dissolution rates in body fluids and longer-lasting SC depots.

Overall, the results show how the Chol:CPC DELOS-NV influence the behavior of the Plx407 hydrogels by increasing their solid behavior, reducing their phase angle, and slightly decreasing their $T_{sol\text{-}gel}$. This effect is believed to occur due to the entrapment of water molecules into the hydrophilic core of nanovesicles[27]. This results in the dehydration of the core of hydrogel micelles, which is the primary mechanism of gelation[27,29].

All these rheological characterizations presented thus far suggest that the most appropriate hydrogels for SC depot formation with TFF-Chol:CPC DELOS-NV are the 15% and 17% w/w Plx407 concentrations. Both hydrogels present an appropriate $T_{sol\text{-}gel}$ to be injected at room temperature and very low thixotropy to form a quick depot at 37 °C. As expected, the 17% w/w Plx407 presents higher viscosity and a lower phase angle than the 15% w/w at 37 °C (**Table 4.3**) and, therefore, it is considered the best option of these two.

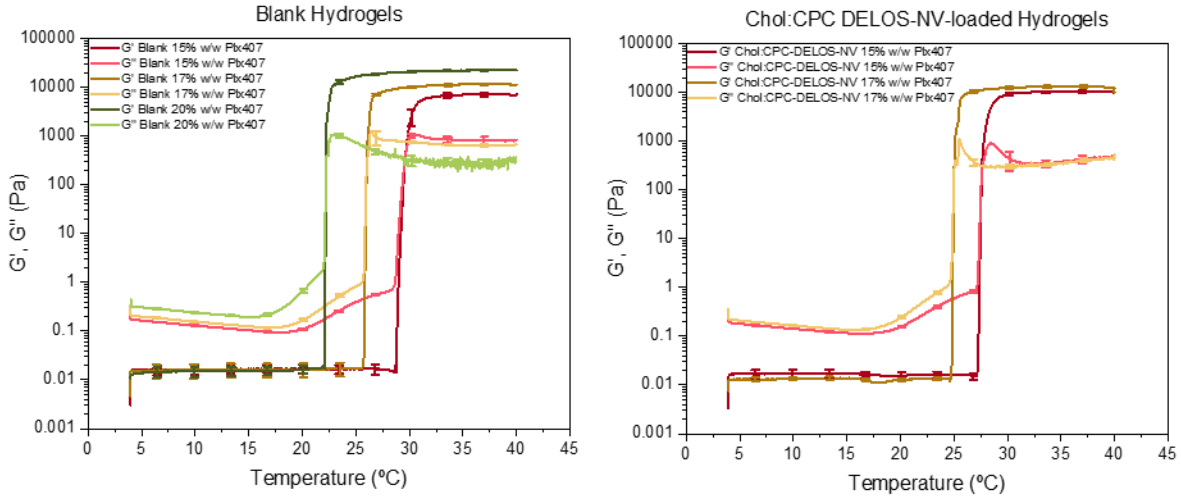


Figure 4.17. *Storage (G') and loss (G'') modulus as a function of temperature for blank hydrogels (left) and TFF-Chol:CPC DELOS-NV-loaded hydrogels (right) at different Plx407 concentrations (mean ± SD, n = 3; the SD is represented for only 10 randomized and representative data points for ease of interpretation).*

Table 4.3. *Rheological properties of the Plx407 blank hydrogels and TFF-Chol:CPC DELOS-NV-loaded hydrogels. Statistical analyses were done by T-test pairwise comparison. P < 0.05 are considered significant.*

Plx407 hydrogel formulation		*Rotational analysis*		*Oscillatory analysis*			
Concentration Plx407 (% w/w)	*Hydrogel Formulation*	*Viscosity (Pa s) (22 °C; 500 s^{-1})*	*P-Value*	*$T_{sol-gel}$ (°C)*	*P-Value*	*δ [a] (°) (37 °C)*	*P-Value*
15	Blank	0.0315 ± 0.0011	0.365	29.71 ± 0.14	0.001	6.5 ± 0.8	0.002
	TFF-Chol:CPC DELOS-NV	0.039 ± 0.011		27.9 ± 0.4		2.4 ± 0.7	
17	Blank	0.061 ± 0.003	0.053	26.17 ± 0.17	0.006	3.2 ± 0.3	0.004
	TFF-Chol:CPC DELOS-NV	0.100 ± 0.016		25.29 ± 0.23		1.78 ± 0.23	
20	Blank	0.366 ± 0.007	0.011	22.40 ± 0.19	NA	0.83 ± 0.12	NA
	TFF-Chol:CPC DELOS-NV	0.67 ± 0.05		NA		NA	

[a] *δ = phase angle at 37 °C*

4.3.7. In vitro injectability of the DiD-Chol:CPC DELOS-NV-loaded 17% w/w Poloxamer 407 hydrogel through a 25 G needle

In order to empirically corroborate the rheological properties determined by the rheological analysis, the 17% w/w Plx407 hydrogel loaded with DiD-DELOS-NV was manually injected at room temperature through a 25 G syringe into dPBS pH 7.4 at 37 °C (see method in **Section 9.4.1**). This hydrogel containing labelled-DELOS-NV was the same hydrogel employed as a control in FRET analysis (**Section 4.3.5**). The hydrogel was injected mimicking a SC injection. The flow through the syringe was effortless, and once the hydrogel encountered the 37 °C dPBS, an *in situ* depot was formed demonstrating its low thixotropy. In this way, the appropriate rheological properties of the DiD-DELOS-NV-loaded 17% w/w Plx407 hydrogel for SC administration were demonstrated. **Figure 4.18** comprises image captures extracted from a video documenting the injection of the studied hydrogel into dPBS. From these images can be appreciated the immediate conversion of the polymer solution into a solid-like depot when it meets the dPBS at 37 °C.

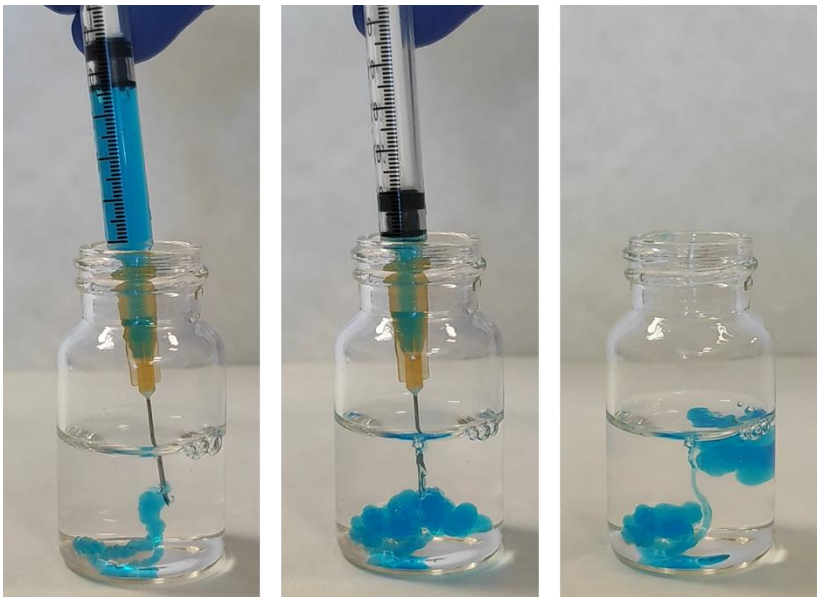


Figure 4.18. *Injection of the DiD-DELOS-NV-loaded 17% w/w Plx407 hydrogel into dPBS pH 7.4 pre-warmed at 37 °C.*

4.3.8. Gelation time of the TFF-Chol:CPC DELOS-NV-loaded Poloxamer 407 hydrogels

In addition to all the rheological characterizations, the gelation time of the different blank and TFF-Chol:CPC DELOS-NV-loaded hydrogels with 15% and 17% w/w Plx407 was also determined (see **Section 9.3.13**). The blank 15% w/w Plx407 hydrogel showed a gelation time of 46.3 ± 2.5 s, while the same concentration of Plx407 with TFF-Chol:CPC DELOS-NV only required 36.3 ± 2.1 s to become solid. Similarly, for the 17% w/w Plx407 hydrogels, the gelation time of the blank hydrogel was 35.7 ± 2.8 s, and for the hydrogel containing TFF-Chol:CPC DELOS-NV it was 14.0 ± 4.5 s (**Figure 4.19**). Those results are in line with the rheological observations shown in the previous section, and they

indicate that the presence of DELOS-NV in the hydrogels has a similar effect to increasing the Plx407 concentration, by reducing the time required to convert from liquid to gel.

It is important to emphasize that these results are intended solely for comparative analysis among different hydrogel formulations because the *in vitro/in vivo* correlation is low. In this test, the area of the hydrogel that allows for heat transfer is substantially smaller than the area involved in an actual injection. For this reason, the observed gelation times in this test appear significantly higher than the practically instantaneous gelation observed after injection of the DiD-DELOS-NV-loaded 17% w/w Plx407 hydrogel into dPBS at 37 °C showed in the previous section (**Section 4.3.7**).

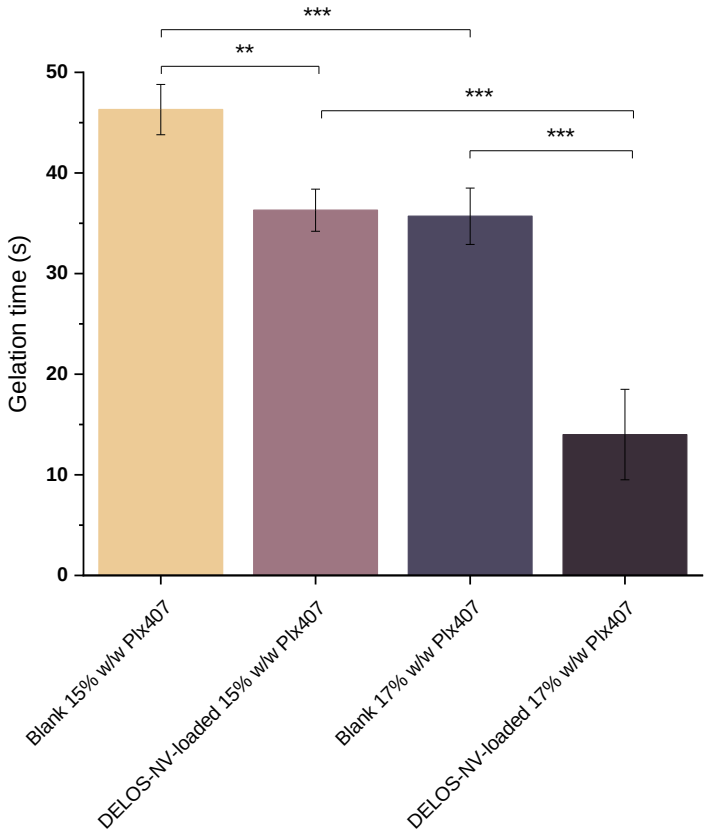


Figure 4.19. *The gelation time graphic bar of the blank- and TFF-Chol:CPC DELOS-NV-loaded 15% and 17% w/w Plx407 hydrogels (mean ± SD, n= 4). Statistical analyses were done by T-test pairwise comparison. ** p < 0.01, *** p < 0.001.*

4.3.9. In vitro DiD-Chol:CPC DELOS-NV release from Plx407 hydrogels

Following the extensive characterization of the hydrogels, a release test of the DiD-Chol:CPC DELOS-NV from the hydrogels was performed to assess the release kinetics of the system. The previous rheological characterization of the hydrogels demonstrated that the 15% and 17% w/w Plx407 hydrogels loaded with TFF-Chol:CPC DELOS-NV are appropriate for SC injection and depot

formation. In this case, the 17% w/w Plx407 was chosen for the *in vitro* release test since it was more solid-like, expecting it to provide longer-lasting depots.

The *in vitro* release of the DELOS-NV from the 17% w/w Plx407 hydrogel was followed by employing a labelled-DELOS-NV hydrogel, specifically the DiD-DELOS-NV hydrogel previously described (**Section 4.3.5**). As mentioned before, DiD is an amphiphilic carbocyanine that integrates hydrophobically within the DELOS-NV membranes, and due to its very low solubility in water, presents a negligible leakage. Thus, as it would occur with a hydrophobic drug, the integration of this molecule into nanovesicles is an effective strategy for stabilizing it in aqueous media. Further, this molecule was chosen for its easiness to be quantified by spectroscopic techniques.

With the DiD-DELOS-NV-loaded 17% w/w Plx407 hydrogel, a membrane-less[61] release and dissolution test was conducted (see method details in **Section 9.4.2** and **Section 9.4.3**). In this method, there is no physical barrier between the hydrogel and the release medium. Briefly, the DiD-DELOS-NV-loaded hydrogel was placed in a vial and incubated at 37 °C with orbital agitation. The release medium, consisting of dPBS at pH 7 and pre-warmed to 37 °C, was then added over the solid-like hydrogel. The release medium was replaced with fresh medium every hour, and both, the release of nanovesicles and the degree of hydrogel dissolution were quantified.

Following this methodology, an extended release of 8 hours was achieved (**Figure 4.20A**). The release of the DiD-DELOS-NV was quantified by UV-Vis taking the absorbance intensity at λ = 647 and converting it into concentration with a calibration curve (R^2 = 0.995). The release was steady and constant, without any initial burst release. Even if the graphical representation resembled a zero-order release, the results were fitted to a Korsmeyer-Peppas[62,63] model to mathematically determine the mechanism of release and the release kinetics of the system (see **Equation 4.4**). This equation describes drug release from polymeric systems and was used to distinguish the release mechanism. When n = 0.5 the system is classified as Fickian with a diffusion mechanism driving a first-order release, and when n = 1, the system is non-Fickian, and polymer chain relaxation (hydrogel dissolution/erosion) is the mechanism that leads the release, correlating with a zero-order drug delivery. Values of n in between 0.5 and 1 indicate a combination of diffusion and erosion release mechanisms[62,63].

$$\frac{Mi}{M\infty} = Kt^n$$

Equation 4.4. *Korsmeyer-Peppas model, where* $\boldsymbol{Mi}$ *refers to the amount of drug released over time,* $\boldsymbol{M\infty}$ *is the amount of drug in equilibrium,* $\boldsymbol{K}$ *is the release velocity constant and* n *the exponent of release.*

The model was fitted with a K value of 8.5 and n value of 1.0. The goodness of the model was assessed by the R^2, which was 0.9999. An n value of 1 indicates that the model is non-Fickian and correlates with zero-order kinetics, which is governed by the hydrogel dissolution rate[62,63]. This mathematical approach was conducted only with the first 60% of the release as later-stage release conditions do not meet the assumptions used to derive the equation. According to this first result, the zero-order mathematical model was next employed to fit the complete release curve (see **Equation 4.5**). The graphic with the fitting (R^2 = 0.9997) is represented in **Figure 4.20A**. At the end of the experiment, a cumulative release of > 70% was achieved.

$$\frac{Mi}{M\infty} = Kt$$

Equation 4.5. *Zero-order model, where* $\boldsymbol{Mi}$ *refers to the amount of drug released over time,* $\boldsymbol{M\infty}$ *is the amount of drug in equilibrium and* $\boldsymbol{K}$ *is the zero-order release kinetic constant.*

In parallel to the release test, a dissolution test of the same Plx407 hydrogel was also performed with the same methodology (see **Section 9.4.2**), by weighing the remaining hydrogel every hour. The dissolution test showed again a zero-order kinetics dissolution (**Figure 4.20B**). The weight loss of the hydrogel over time was constant and it aligns with the dissolution kinetics, providing evidence that the release kinetics mechanism of the DELOS-NV is led by the hydrogel dissolution and not by diffusion of the DiD-DELOS-NV through the hydrogel channels, a commonly observed release mechanism in hydrogels[32].

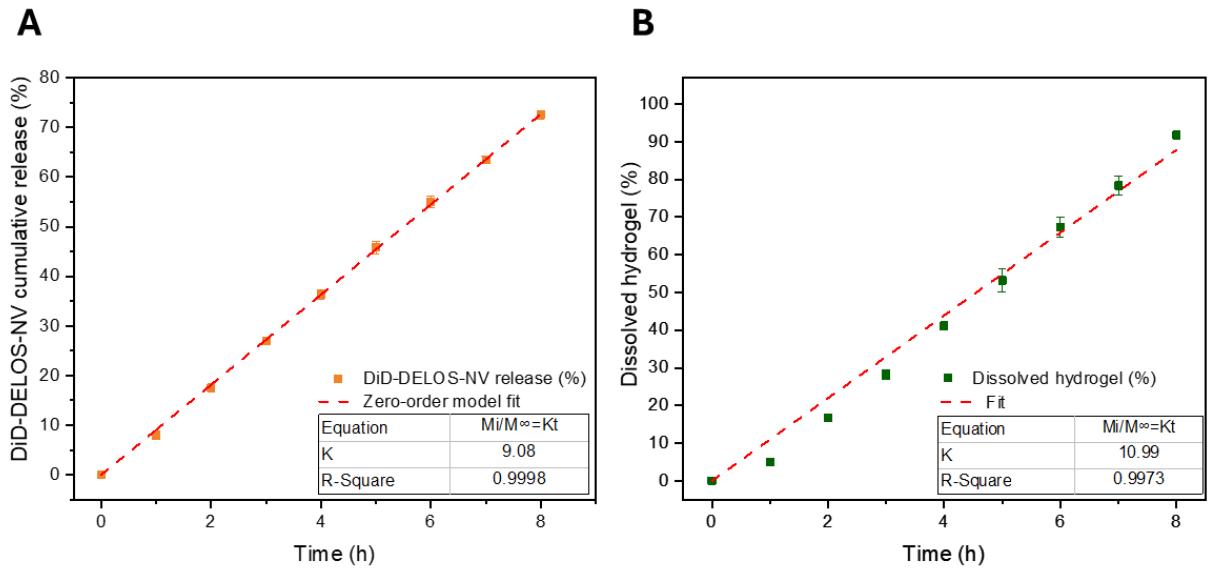


Figure 4.20. *A) In vitro DiD-DELOS-NV release (cumulative %) from 17% w/w Plx407 hydrogel, and B) in vitro hydrogel dissolution (dissolved hydrogel wt%) as a function of time (hours), using the membrane-less model at 37 °C. Data are expressed as mean ± SD (n = 3) and has been fitted into a zero-order mathematical model.*

As a control, to study the impact of the presence of nanovesicles in this hybrid system, a release test without DELOS-NV was carried out containing exclusively the free DiD solubilized in the formulation (1:2:97 EtOH:benzyl alcohol:water + 17% w/w Plx407). The free DiD-loaded 17% w/w Plx407 hydrogel presented a good macroscopical appearance; however, the absorbance intensity of the DiD in this formulation was significantly lower than the same concentration of DiD formulated into the DELOS-NV and 17% w/w Plx407 (**Figure 4.21A**).

The same membrane-less methodology with the same conditions mentioned above was employed to study the release of the free DiD (see details in **Section 9.4.3**). However, the free DiD release could not be quantified because sedimentation of the DiD in the dPBS occurred during the release test due to the very low solubility of this amphiphilic molecule in the aqueous release media despite the presence of the organic solvents employed for its formulation (**Figure 4.21B**). This result also

highlights the potential of the DELOS-NV as nanocarriers for stabilizing highly hydrophobic compounds in physiological media.

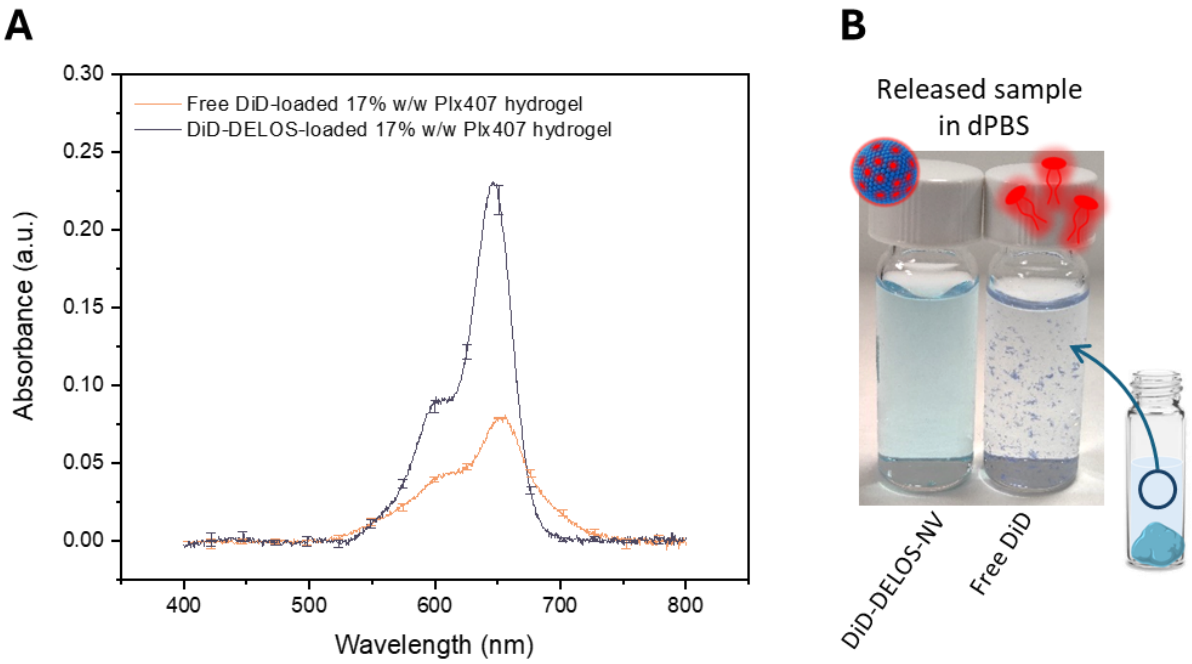


Figure 4.21. *A) Overlapped UV-Vis absorption spectra of 17% w/w Plx407 hydrogels containing 45 µM DiD freely dissolved in 1:2:97 EtOH:benzyl alcohol:water vs loaded into DELOS-NV. The DiD-DELOS-NV sample was diluted in water to achieve an absorbance reading of 0.1-0.3, and the same dilution factor was employed for the free DiD formulation to obtain a comparable spectrum. B) Macroscopical images of the released samples in dPBS pH 7.4. The images correspond to the in vitro release samplings obtained at t = 1 h. The released DiD-DELOS-NV stay stable in suspension in the dPBS while the free DiD precipitates.*

These *in vitro* release and dissolution tests demonstrate the immeasurable potential of formulating DELOS-NV into hydrogels to achieve extended release with zero-order kinetics. Zero-order kinetics is the desired release kinetics for drug delivery because it allows the maintenance of drug concentrations within the therapeutic window (controlled release) for an extended period, thus, reducing dosing frequency and adverse effects[63]. The dissolution test demonstrates that the DELOS-NV release is driven by hydrogel dissolution rather than diffusion of the DELOS-NV through the polymeric matrix. This lack of diffusion of the DELOS-NV, which is ideal for avoiding an initial burst release, is probably caused by the hydrophobic interaction of the amphiphilic DELOS-NV with the hydrophobic cores of the polymer micelles[32]. Another possible reason could be a reduction of the diffusion rate due to the entrapment of the DELOS-NV into the diffusion channels of the polymeric matrix caused by their bigger size in comparison to hydrophilic small molecules and/or actives.

In addition to exhibiting promising zero-order kinetics, the DELOS-NV have demonstrated the ability to stabilize a hydrophobic molecule in water media. Although the primary objective of the release test was to determine the release kinetics of the DELOS-NV from the Plx407 hydrogel, it also provided insights into the behavior that hydrophobic compounds could have in the presence of the TFF-Chol:CPC DELOS-NV. These DELOS-NV stabilized the hydrophobic DiD in aqueous media, thus

ensuring the formation of a homogeneous hydrogel. It also resulted in the vehiculation of the DiD once released from the depot into the dPBS, as shown in **Figure 4.21B**. Furthermore, aside from stabilizing compounds in physiological media, these DELOS-NV can confer protection to the payloads, prolong the plasmatic half-life, and favor a controlled release and site-specific targeting, as demonstrated in previous publications[1,4,64,65].

4.4. Alternative polymers for subcutaneous *in situ* depots

The promising results obtained with the Plx407 path the way for testing alternative stimulus-responsive hydrogels which can cover different medical needs. In that sense, in this section the aim is to test an alternative thermoreversible polymer which could provide with longer-lasting depots.

We decided to test the poly(lactide-co-glycolide) –block- poly (ethylene glycol)–block-poly (lactide-co-glycolide) (PLGA-PEG-PLGA). This triblock polymer is also thermoreversible, biocompatible and biodegradable[26,33]. It has been tested in clinical trials as an *in situ* hydrogel depot (ReGel™) for the delivery of the poorly soluble drug Paclitaxel (OncoGel™)[66]. The gelation mechanism of the PLGA-PEG-PLGA polymers resembles that of the Plx407, with the particularity that in this specific case, the hydrophobic molecules are the PLGA blocks flanking the PEG, and are the ones that form the core of the micelles, exposing the PEG to the media (**Figure 4.22**). It is well known that the gelation and degradation properties of this copolymer can be controlled by many internal factors such as MW of polymers, dl-lactide (LA)/glycolide (GA) block ratio and, of course, concentration[26,67,68]. In this first feasibility assay, PLGA-PEG-PLGA with MW 1700-1500-1700 and LA/GA ratio 95:5, was tested. Increasing the ratio LA/GA the hydrophobic interactions increase among the copolymer molecules resulting in more cohesive hydrogels with longer release rates of the incorporated payloads[67,69]. In addition, Dutta *et al.* selected among different PLGA-PEG-PLGA copolymers, one with a very similar composition in terms of size and LA/GA ratio due to its optimum stability, gelation properties, and desired release kinetics[26].

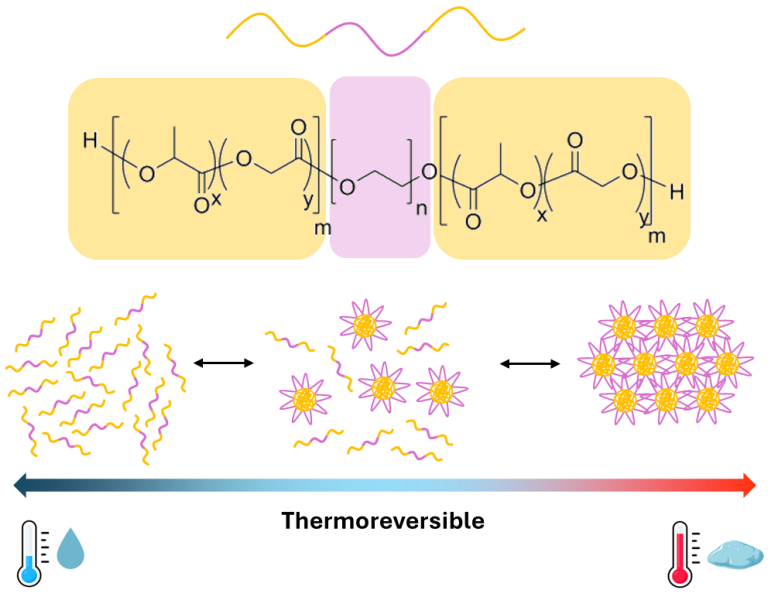


Figure 4.22. Schematic representation of the PLGA-PEG-PLGA behavior in response to temperature.

For the hydrogel preparation, the TFF-Chol:CPC DELOS-NV were employed (see formulation details in **Table 9.1**). The hydrogel was produced as described in **Section 9.2.3** by first weighting the polymer and after adding the volume of nanovesicles suspension over it to achieve a final concentration of 25% w/v PLGA-PEG-PLGA. The concentration of polymer was chosen based on the bibliography[26]. Afterward, the mixture was kept in the fridge for 3 days to promote dissolution of the polymer in the nanovesicles suspension. After this time, agitation at 4 °C was applied to ensure homogeneity.

The obtained hydrogel presented a homogeneous macroscopic appearance and a thermoreversible behavior (**Figure 4.23**): it became solid-like at 37 °C. The sol-gel transition changed the color of the hydrogel, from being more translucid in the sol state to becoming more whitish in the gel state. Importantly, the transition was reversible, and the hydrogel recovered its initial morphology when the temperature decreased.

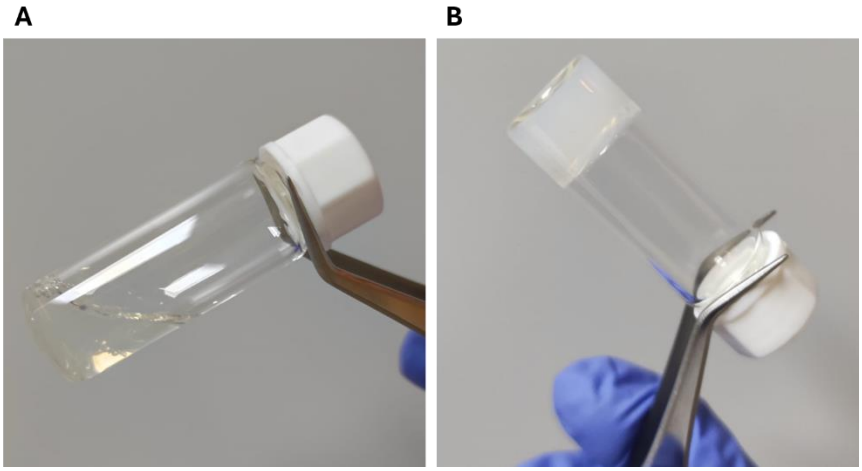


Figure 4.23. *Images of the 25% w/v PLGA-PEG-PLGA (MW: 1700-1500-1700; LA/GA ratio: 95:5) loaded with TFF-Chol:CPC DELOS-NV. A) Image obtained at 22 °C; B) Image obtained at 37 °C.*

The integrity of the DELOS-NV within the polymer matrix was assessed by Cryo-TEM (see **Figure 4.24**) following the procedure described in **Section 9.3.4.** To ensure a proper viscosity for the technique, the hydrogel was diluted 1:5. At this dilution it presented a water-like viscosity. The Cryo-TEM images show spherical and small nanovesicles, mostly unilamellar and homogenous. Thus, the results suggest stability of the nanovesicles within the PLGA-PEG-PLGA matrix. In addition, the images' background is covered of smaller electrodense and homogeneous dots. These small dots present the typical morphology of micelles[70,71] observed by Cryo-TEM and might correspond to the PLGA-PEG-PLGA micelles.

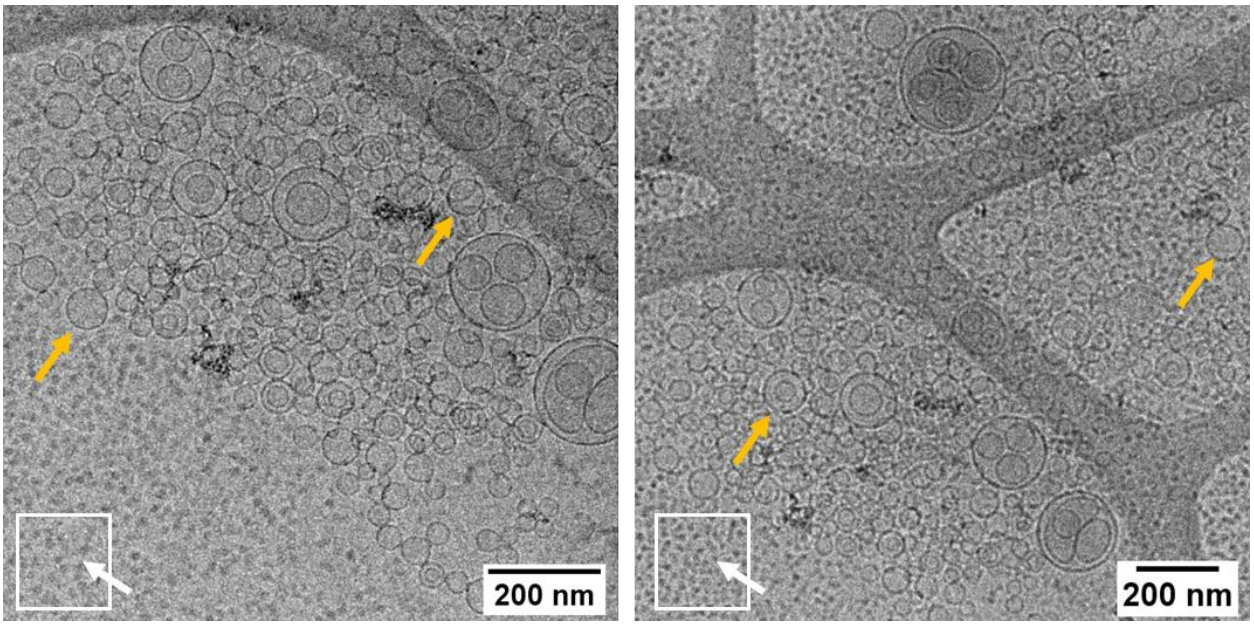


Figure 4.24. *Cryo-TEM images of the TFF-Chol:CPC DELOS-NV loaded into the 25% w/v PLGA-PEG-PLGA (MW: 1700-1500-1700; LA/GA ratio: 95:5) hydrogel. The sample was diluted 1:5 for the analysis. The yellow arrows point out some representative DELOS-NV. The dark circles within the white square might correspond to micelles of PLGA-PEG-PLGA.*

Afterward, the dissolution time of the hydrogel under *in vitro* conditions was tested following the same methodology employed with Plx407 hydrogels (see **Section 9.4.2**). However, PLGA-PEG-PLGA swells in the presence of the dPBS dissolution medium. This indicates that before fully dissolving in a physiological medium, it first absorbs water, increasing its size and weight, making weight loss measurements over time inaccurate. Nonetheless, the test determined that complete dissolution of the hydrogel takes more than 10 days.

This preliminary feasibility test with the PLGA-PEG-PLGA demonstrates the potential of employing this hydrogel as a subcutaneous depot for longer *in situ*-forming depots. Further investigations are required to develop the system, but the preliminary results are favorable. Moreover, the bases and methods to work with DELOS-NV-loaded hydrogels have been settled up with the Plx407 hydrogels and it is expected to leverage all this knowledge for a quicker development of novel systems based on DELOS-NV and hydrogels.

4.5. Summary of the chapter and perspectives

In the present **Chapter**, a novel hybrid platform based on the Plx407 thermoreversible hydrogel loaded with DELOS-NV has been implemented for obtaining a SC *in situ*-forming depot for prolonged delivery of the DELOS-NV, and therefore, of the potential active compounds loaded on them.

To develop this novel system, the Chol:CPC DELOS-NV optimized by a design of experiments (DoE) in **Chapter 3** have been employed. These nanovesicles, consisting of 5 mg/mL of cholesterol and CPC at an equimolar ratio, have been prepared by DELOS method and diafiltrated by TFF to eliminate the EtOH present in the formulation. The obtained formulation, called TFF-Chol:CPC DELOS-NV, demonstrated suitable critical quality attribute values and exhibited stability for a minimum of 12 months, thus demonstrating its potential as a drug delivery system.

Next, the TFF-Chol:CPC DELOS-NV were integrated into different concentrations of Plx407, and their integrity and stability within the polymer matrix was demonstrated by FRET efficiency evaluation and Cryo-TEM images. The best hydrogel for forming a SC *in situ* depot was the TFF-Chol:CPC DELOS-NV-loaded 17% w/w Plx407 hydrogel, which was selected based on its rheological properties at injection and subcutaneous temperatures (i.e., 22 °C and 37 °C, respectively). This hydrogel flows easily through a 25 G syringe at 22 °C but quickly forms an *in situ* depot at 37 °C. The *in vitro* release test revealed a consistent zero-order kinetics release of the TFF-Chol:CPC DELOS-NV over an 8-hour period, led by the hydrogel dissolution rate. This profile represents the preferred release kinetic for effective drug delivery and highlights the superior control and predictability of the developed system, suggesting a steady and extended therapeutic effect.

The results show that this hybrid drug delivery platform consisting of DELOS-NV loaded into a thermoreversible hydrogel can improve the kinetics release profile, as well as enhance the vehiculation and, therefore, the pharmacokinetics of new drug modalities challenging-to-formulate, such as hydrophobic molecules and biologics, among others. To further evaluate this promising approach, in **Chapter 5**, this hybrid platform will be assessed for formulating a highly hydrophobic compound of therapeutic interest in the frame of a collaborative project with the pharmaceutical company Boehringer Ingelheim.

In addition, the promising results from this initial proof of concept pave the way for testing and developing novel DELOS-NV-loaded hydrogels to create hybrid subcutaneous depots, which can be customized to meet various needs, such as extended-duration depots. As an initial feasibility test, the DELOS-NV have been also loaded into a PLGA-PEG-PLGA matrix, and their stability has been confirmed by Cryo-TEM. This polymer is also a thermoreversible polymer which can confer longer depots because it is less prone to be dissolved in physiological media. Beyond the scope of this thesis, the project will continue with the development of a portfolio of hydrogels offering different release profiles to address diverse therapeutic requirements.

- The results of this **Chapter** have led to a patent application: "L. Ferrer-Tasies, **C. Castellar-Álvarez**, E. González-Mira, N. Ventosa, L. Ballell-Hosa, A. Córdoba, S. Sala, and Y. Ronda-Lopez. DELOS nanovesicles embedded in thermoreversible hydrogels as *in situ*-forming subcutaneous depots."

As well as the submission of a scientific article: "**C. Castellar-Álvarez**, L. Ballell-Hosa, Y. Ronda-Lopez, A. Gimó-Santamaria, A. Güell-Bara, C. Huck-Iriart, J. Skov-Pedersen, A. Córdoba, S. Sala, N. Ventosa, E. González-Mira and L. Ferrer-Tasies. Extended release of DELOS nanovesicles from thermoreversible *in situ*-forming subcutaneous depots." -

4.6. References

1. G. Vargas-Nadal, M. Muñoz-Ubeda, P. Alamo, et al. MKC-Quatsomes: a stable nanovesicle platform for bio-imaging and drug-delivery applications. *Nanomedicine Nanotechnology, Biol. Med.* **2020**, 24, 102136.

2. I. Cabrera, E. Elizondo, O. Esteban, et al. Multifunctional nanovesicle-bioactive conjugates prepared by a one-step scalable method using CO2-expanded solvents. *Nanoletters* **2013**, 13, 3766–3774.

3. L. Ballell-Hosa, E. González-Mira, H. Santana, et al. DELOS nanovesicles-based hydrogels: An advanced formulation for topical use. *Pharmaceutics* **2022**, 14 (1), 1–20.

4. L. Ferrer-Tasies, H. Santana, I. Cabrera-Puig, et al. Recombinant human epidermal growth factor/Quatsome Nanoconjugates: A robust topical delivery system for complex wound healing. *Adv. Ther.* **2021**, 4 (6), 2000260.

5. A. Bauer, P. Berben, S.S. Chakravarthi, et al. Current state and opportunities with long-acting injectables: Industry perspectives from the innovation and quality consortium "long-acting injectables" working group. *Pharm. Res.* **2023**, 40 (7), 1601–1631.

6. Y. Shi, A. Lu, X. Wang, et al. A review of existing strategies for designing long-acting parenteral formulations: Focus on underlying mechanisms, and future perspectives. *Acta Pharm. Sin. B* **2021**, 11 (8), 2396–2415.

7. D. Sleep, J. Cameron, L.R. Evans. Albumin as a versatile platform for drug half-life extension. *Biochim. Biophys. Acta - Gen. Subj.* **2013**, 1830 (12), 5526–5534.

8. Y. Zhang, T. Sun, C. Jiang. Biomacromolecules as carriers in drug delivery and tissue engineering. *Acta Pharm. Sin. B* **2018**, 8 (1), 34–50.

9. Y. Gao, M. Joshi, Z. Zhao, S. Mitragotri. PEGylated therapeutics in the clinic. *Bioeng. Transl. Med.* **2024**, 9 (1), 1–28.

10. H. Wang, Y. Wang, C. Yuan, et al. Polyethylene glycol (PEG)-associated immune responses triggered by clinically relevant lipid nanoparticles in rats. *npj Vaccines* **2023**, 8 (1).

11. F. Zhang, M.R. Liu, H.T. Wan. Discussion about several potential drawbacks of PEGylated therapeutic proteins. *Biol. Pharm. Bull.* **2014**, 37 (3), 335–339.

12. P. Zhang, F. Sun, S. Liu, S. Jiang. Anti-PEG antibodies in the clinic: Current issues and beyond PEGylation. *J. Control. Release* **2016**, 244, 184–193.

13. S.B. van Witteloostuijn, S.L. Pedersen, K.J. Jensen. Half-life extension of biopharmaceuticals using chemical methods: Alternatives to PEGylation. *ChemMedChem* **2016**, 11 (22), 2474–2495.

14. E. Sanchez Armengol, A. Unterweger, F. Laffleur. PEGylated drug delivery systems in the pharmaceutical field: past, present and future perspective. *Drug Dev. Ind. Pharm.* **2022**, 48 (4), 129–139.

15. I. Ozer, A. Slezak, P. Sirohi, et al. An injectable PEG-like conjugate forms a subcutaneous depot and enables sustained delivery of a peptide drug. *Biomaterials* **2023**, 294, 121985.

16. W. Chen, G. Wang, B.C. Yung, et al. Long-acting release formulation of Exendin-4 based on biomimetic mineralization for type 2 diabetes therapy. *ACS Nano* **2017**, 11 (5), 5062–5069.

17. W. Chen, B.C. Yung, Z. Qian, X. Chen. Improving long-term subcutaneous drug delivery by regulating material-bioenvironment interaction. *Adv. Drug Deliv. Rev.* **2018**, 127, 20–34.

18. T. Thambi, Y. Li, D.S. Lee. Injectable hydrogels for sustained release of therapeutic agents. *J. Control. Release* **2017**, 267, 57–66.

19. S. Bashir, M. Hina, J. Iqbal, et al. Fundamental concepts of hydrogels: Synthesis, properties, and their applications. *Polymers (Basel).* **2020**, 12 (11), 1–60.

20. F. Andrade, M.M. Roca-Melendres, E.F. Durán-Lara, D. Rafael, S. Schwartz. Stimuli-responsive hydrogels for cancer treatment: The role of ph, light, ionic strength and magnetic field. *Cancers (Basel).* **2021**, 13 (5), 1–17.

21. C. Caddeo, M. Gabriele, X. Fernàndez-Busquets, et al. Antioxidant activity of quercetin in Eudragit-coated liposomes for intestinal delivery. *Int. J. Pharm.* **2019**, 565, 64–69.

22. M. Manconi, M.L. Manca, E. Escribano-Ferrer, et al. Nanoformulation of curcumin-loaded eudragit-nutriosomes to counteract malaria infection by a dual strategy: Improving antioxidant intestinal activity and systemic efficacy. *Int. J. Pharm.* **2019**, 556, 82–88.

23. T. Xiang, T. Lu, W.F. Zhao, C.S. Zhao. Ionic-strength responsive zwitterionic copolymer hydrogels with tunable swelling and adsorption behaviors. *Langmuir* **2019**, 35 (5), 1146–1155.

24. L. Li, J.M. Scheiger, P.A. Levkin. Design and Applications of Photoresponsive Hydrogels. *Adv. Mater.* **2019**, 31 (26), 1807333.

25. V.M. Shah, D.X. Nguyen, D.A. Rao, R.G. Alany, A.W.G. Alani. Thermogel polymers for injectable drug delivery systems: Chemistry, properties and applications. In *Temperature-Responsive Polymers: Chemistry, Properties, and Applications*; **2018**; pp 313–327.

26. K. Dutta, R. Das, J. Ling, et al. In Situ Forming Injectable Thermoresponsive hydrogels for controlled delivery of biomacromolecules. *ACS Omega* **2020**, 5 (28), 17531–17542.

27. S. Nie, W.W. Hsiao, W. Pan, Z. Yang. Thermoreversible pluronic® F127-based hydrogel containing liposomes for the controlled delivery of paclitaxel: In vitro drug release, cell cytotoxicity, and uptake studies. *Int. J. Nanomedicine* **2011**, 6 (1), 151–166.

28. E. Giuliano, D. Paolino, M. Fresta, D. Cosco. Drug-loaded biocompatible nanocarriers embedded in Poloxamer 407 hydrogels as therapeutic formulations. *Medicines* **2018**, 6 (1), 7.

29. P.K. Sharma, M.J. Reilly, D.N. Jones, P.M. Robinson, S.R. Bhatia. The effect of pharmaceuticals on the nanoscale structure of PEO-PPO-PEO micelles. *Colloids Surfaces B Biointerfaces* **2008**, 61 (1), 53–60.

30. FDA. FDA inactive ingredient database https://www.accessdata.fda.gov/scripts/cder/iig/index.cfm.

31. J.H. Jeon, Y.W. Seong, J.E. Han, et al. Randomized trial of Poloxamer 407-based Ropivacaine hydrogel after thoracoscopic pulmonary resection. *Ann. Thorac. Surg.* **2021**, 114 (4), 1189–1196.

32. H. Abdeltawab, D. Svirskis, M. Sharma. Formulation strategies to modulate drug release from poloxamer based in situ gelling systems. *Expert Opin. Drug Deliv.* **2020**, 17 (4), 495–509.

33. D. Cao, X. Zhang, Y. Luo, et al. Liposomal doxorubicin loaded PLGA-PEG-PLGA based thermogel for sustained local drug delivery for the treatment of breast cancer. *Nanomedicine, Biotechnol.* **2019**, 47 (1), 181–191.

34. P. Mura, N. Mennini, C. Nativi, B. Richichi. In situ mucoadhesive-thermosensitive liposomal gel as a novel vehicle for nasal extended delivery of opiorphin. *Eur. J. Pharm. Biopharm.* **2018**, 122, 54–61.

35. T. Kojarunchitt, S. Hook, S. Rizwan, T. Rades, S. Baldursdottir. Development and characterisation of modified poloxamer 407 thermoresponsive depot systems containing cubosomes. *Int. J. Pharm.* **2011**, 408 (1–2), 20–26.

36. L. Ferrer-Tasies, E. Moreno-Calvo, M. Cano-Sarabia, et al. Quatsomes: Vesicles formed by self-assembly of sterols and quaternary ammonium surfactants. *Langmuir* **2013**, 29 (22), 6519–6528.

37. M. Köber, S. Illa-Tuset, L. Ferrer-Tasies, et al. Stable nanovesicles formed by intrinsically planar bilayers. *J. Colloid Interface Sci.* **2023**, 631, 202–211.

38. J. Tomsen-Melero, J. Merlo-Mas, A. Carreño, et al. Liposomal formulations for treating lysosomal storage disorders. *Adv. Drug Deliv. Rev.* **2022**, 190, 114531.

39. A. Shah, S. Aftab, J. Nisar, M.N. Ashiq, F.J. Iftikhar. Nanocarriers for targeted drug delivery. *J. Drug Deliv. Sci. Technol.* **2021**, 62, 102426.

40. Z. Fatfat, M. Karam, B. Maatouk, D. Fahs, H. Gali-Muhtasib. Nanoliposomes as safe and efficient drug delivery nanovesicles. In *Advanced and modern approaches for drug delivery*; Kumar Nayak, A., Laha, B., Hasnain, M. S., Maiti, S., Eds.; Elsevier, **2023**; pp 159–197.

41. S.Z. Alshawwa, A.A. Kassem, R.M. Farid, S.K. Mostafa, G.S. Labib. Nanocarrier drug delivery systems: Characterization, limitations, future perspectives and implementation of artificial intelligence. *Pharmaceutics* **2022**, 14 (4), 1–26.

42. S. Mantripragada. A lipid based depot (DepoFoam® technology) for sustained release drug delivery. *Prog. Lipid Res.* **2002**, 41 (5), 392–406.

43. I. Usach, R. Martinez, T. Festini, J.E. Peris. Subcutaneous injection of drugs: Literature review of factors influencing pain sensation at the injection site. *Adv. Ther.* **2019**, 36 (11), 2986–2996.

44. P.J.S. C Rowe, and S.C. Owen. Handbook of pharmaceutical excipients; Libros digitales-Pharmaceutical press, **2009**.

45. A.C.S. Akkari, J.Z.B. Papini, G.K. Garcia, et al. Poloxamer 407/188 binary thermosensitive hydrogels as delivery systems for infiltrative local anesthesia: Physico-chemical characterization and pharmacological evaluation. *Mater. Sci. Eng. C* **2016**, 68, 299–307.

46. F.E. Antunes, L. Gentile, C. Oliviero Rossi, L. Tavano, G.A. Ranieri. Gels of Pluronic F127 and nonionic surfactants from rheological characterization to controlled drug permeation. *Colloids Surfaces B Biointerfaces* **2011**, 87 (1), 42–48.

47. A.M. Bodratti, P. Alexandridis. Formulation of poloxamers for drug delivery. *J. Funct. Biomater.*

2018, 9 (1).

48. H. He, C. Liu, J. Ming, et al. Accurate and sensitive probing of onset of micellization based on absolute aggregation-caused quenching effect. *Aggregate* **2022**, 3 (5), 1–13.

49. BASF. Kolliphor® P 407 Technical Information; **2020**.

50. S. Stolnik, B. Daudali, A. Arien, et al. The effect of surface coverage and conformation of poly(ethylene oxide) (PEO) chains of poloxamer 407 on the biological fate of model colloidal drug carriers. *Biochim. Biophys. Acta - Biomembr.* **2001**, 1514 (2), 261–279.

51. W.R. Algar, N. Hildebrandt, S.S. Vogel, I.L. Medintz. FRET as a biomolecular research tool — understanding its potential while avoiding pitfalls. *Nat. Methods* **2019**, 16 (9), 815–829.

52. X. Sun, G. Wang, H. Zhang, et al. The blood clearance kinetics and pathway of polymeric micelles in cancer drug delivery. *ACS Nano* **2018**, 12 (6), 6179–6192.

53. J. Morla-Folch, G. Vargas-Nadal, T. Zhao, et al. Dye-loaded Quatsomes exhibiting FRET as nanoprobes for bioimaging. *ACS Appl. Mater. Interfaces* **2020**, 12 (18), 20253–20262.

54. A. Ardizzone, S. Kurhuzenkau, S. Illa-Tuset, et al. Nanostructuring lipophilic dyes in water using stable vesicles, Quatsomes, as scaffolds and their use as probes for bioimaging. *Small* **2018**, 14 (16), 1–6.

55. F. Würthner, T.E. Kaiser, C.R. Saha-Möller. J-aggregates: From serendipitous discovery to supramolecular engineering of functional dye materials. *Angew. Chemie - Int. Ed.* **2011**, 50 (15), 3376–3410.

56. A. Eisfeld, J.S. Briggs. The J- and H-bands of organic dye aggregates. *Chem. Phys.* **2006**, 324 (2–3), 376–384.

57. P.A. Janmey, M. Schliwa. Rheology. *Curr. Biol.* **2008**, 18 (15), 1–13.

58. M. Parent, C. Nouvel, M. Koerber, et al. PLGA in situ implants formed by phase inversion: Critical physicochemical parameters to modulate drug release. *J. Control. Release* **2013**, 172 (1), 292–304.

59. A. Rył, P. Owczarz. Injectability of thermosensitive, low-concentrated chitosan colloids as flow phenomenon through the capillary under high shear rate conditions. *Polymers (Basel).* **2020**, 12 (10), 1–17.

60. M.A. Miller, J.D. Engstrom, B.S. Ludher, K.P. Johnston. Low viscosity highly concentrated injectable nonaqueous suspensions of lysozyme microparticles. *Langmuir* **2010**, 26 (2), 1067–1074.

61. S.Y. Lee, S.I. Jeon, S.B. Sim, Y. Byun, C.H. Ahn. A supramolecular host-guest interaction-mediated injectable hydrogel system with enhanced stability and sustained protein release. *Acta Biomater.* **2021**, 131, 286–301.

62. H. Karimi, S. Rabbani, D. Babadi, S. Dadashzadeh, A. Haeri. Piperine liposome-embedded in hyaluronan hydrogel as an effective platform for prevention of postoperative peritoneal adhesion. *J. Microencapsul.* **2023**, 40 (4), 279–301.

63. M.L. Laracuente, M.H. Yu, K.J. McHugh. Zero-order drug delivery: State of the art and future

prospects. *J. Control. Release* **2020**, 327, 834–856.

64. A. Boloix, N. Feiner-Gracia, M. Köber, et al. Engineering pH-sensitive stable nanovesicles for delivery of microRNA therapeutics. *Small* **2022**, 18 (3), 2101959.

65. J. Tomsen-Melero, S. Passemard, N. García-Aranda, et al. Impact of chemical composition on the nanostructure and biological activity of α-galactosidase-loaded nanovesicles for Fabry disease treatment. *ACS Appl. Mater. Interfaces* **2021**, 13 (7), 7825–7838.

66. N.L. Elstad, K.D. Fowers. OncoGel (ReGel/paclitaxel) - Clinical applications for a novel paclitaxel delivery system. *Adv. Drug Deliv. Rev.* **2009**, 61 (10), 785–794.

67. L. Yu, Z. Zhang, J. Ding. Influence of la and GA sequence in the PLGA block on the properties of thermogelling PLGA-PEG-PLGA block copolymers. *Biomacromolecules* **2011**, 12 (4), 1290–1297.

68. B. Jeong, Y.H. Bae, S.W. Kim. Thermoreversible gelation of PEG-PLGA-PEG triblock copolymer aqueous solutions. *Macromolecules* **1999**, 32 (21), 7064–7069.

69. M. Qiao, D. Chen, X. Ma, Y. Liu. Injectable biodegradable temperature-responsive PLGA-PEG-PLGA copolymers: Synthesis and effect of copolymer composition on the drug release from the copolymer-based hydrogels. *Int. J. Pharm.* **2005**, 294 (1–2), 103–112.

70. E.G. Kelley, R.P. Murphy, J.E. Seppala, et al. Size evolution of highly amphiphilic macromolecular solution assemblies via a distinct bimodal pathway. *Nat. Commun.* **2014**, 5, 3599.

71. Y.Y. Won, A.K. Brannan, H.T. Davis, F.S. Bates. Cryogenic transmission electron microscopy (cryo-TEM) of micelles and vesicles formed in water by poly(ethylene oxide)-based block copolymers. *J. Phys. Chem. B* **2002**, 106 (13), 3354–3364.

5

5 Formulation of *Beyond the rule of 5* molecules into DELOS-NV-loaded thermoreversible hydrogels as subcutaneous depot

5.1. Introduction

The present **Chapter** is a case study in which the hybrid platform composed of DELOS-NV and the thermoreversible Plx407 developed in **Chapter 4** is employed for the formulation of challenging-to-formulate molecules with therapeutic potential. Specifically, the molecules formulated in this **Chapter** are highly hydrophobic compounds that do not comply with Lipinski's Rule of Five statements.

5.1.1. Lipinski's rule of 5

In 1996 Lipinski et al.[1] conceived the Rule of Five (Ro5) to predict oral absorption of drugs, based on their physicochemical attributes. The favorable attributes to achieve systemic effect after oral administration were identified from the computational analysis of a library of approved or in clinical phase II drugs. They identified four parameters, and their cutoffs were all close to five or multiples of five. Because of this, they called it the "Rule of Five".

The parameters that favor systemic effect for orally administered molecules were:

- There are less than 5 H-bond donors (expressed as the sum of OHs and NHs).
- There are less than 10 H-bond acceptors (expressed as the sum of Os and Ns).
- The LogP is below 5.
- The MW is below 500 Da.

They found that less than 10% of the analyzed drugs that achieved systemic circulation through oral administration had two of these four parameters outside the limits specified. Importantly, they stated that drugs that are substrates of biological transporters are exceptions to this rule, and they found that there are five specific families within the exceptions: antibiotics, antifungals, vitamins and cardiac glycosides[1,2].

This mnemonic rule has been employed since then for the discovery of new drugs. However, two decades later, in 2017, the Ro5 was revised by comparing the physicochemical attributes of drugs

approved since then. It was observed a steady increase of the size and the LogP of the drugs approved on the last years. These results suggested that attributes to predict oral absorption do not exist, since repeating the experiment today would confer different rules to the ones stated in 1996[2].

Despite the controversy, this rule is still employed as a reference to identify molecules with expected high oral bioavailability.

5.1.2. Beyond the rule of 5 (bRo5) compounds

Over the past two decades, there has been a slow but steady transition from traditional orally bioavailable small molecules to novel drug modalities designed to modulate complex biological targets once considered "undruggable". Advances in molecular biology, coupled with the completion of the Human Genome Project in the early 2000s, resulted not only in a better understanding of critical disease-relevant targets but also in increasing interest in addressing these targets[3–5].

Large biomolecules, such as antibodies, growth factors and hormones (e. g. insulin) are well-known examples of alternatives to small molecules able to effectively target more complex therapeutic targets. In comparison to small molecules, they present higher specificity and lower side effects, however, they fall clearly outside the Ro5 frame and, as expected, present low oral bioavailability[5]. Large biomolecules have a long history of success -insulin was first introduced in 1922 for the treatment of diabetes[6]-, thus, they can be somehow considered as a classical alternative to small molecules.

Alternatives to these more classical approaches have been named "new drug modalities". This broadly employed expression is defined in a review[3] as rationale-designed drugs that aim to combine the specificity and potency of proteins with the higher permeability and stability of small molecules. In this group can be included next-generation peptides and peptidomimetics, designed to improve plasma stability and membrane permeability of peptides; nucleic acid-based therapeutics, such as the use of oligonucleotides, which will be explained in detail in **Chapter 7**; and also, mixed modalities based on the combinations of different drug molecules[3,5].

Within this new drug modalities can be also considered the "Beyond the Rule of Five" (bRo5) compounds[5]. bRo5 refers to a chemical space that does not have an agreed definition but has been described previously[7] as MW 700 to 3000 Da (the upper limit is to exclude large biologics such as proteins), LogP <0 or >7.5, hydrogen bond donors >5, and hydrogen bond acceptors >10. Note that there is a small difference between the upper limits in Ro5 and the lower limits in bRo5. The chemical space in between those limits was considered an "extended Ro5" by the authors[7]. More loosely, bRo5 compounds can be understood as those that are neither as simple as small molecules that comply with Ro5 rules nor as complex as large biologics. Initially, they were mostly compounds of a biological origin and semi-synthetic compounds, but later, especially since 2010, *the novo* synthesized bRo5 compounds become predominant[8]. Their higher complexity in comparison to small molecules makes them appropriate for complex targets.

Some bRo5 compounds present good oral bioavailability, thus in concordance with the increase in size and logP trends observed in approved oral drugs (e.g., paclitaxel, an anticancer drug; ivermectin, an antiparasitic)[2,8]. However, some other bRo5 compounds with high potency and selectivity, and

thus with strong therapeutic potential, might present low oral bioavailability and require alternative administration routes.

This is the case of the bRo5 compounds formulated in this **Chapter**. Boehringer Ingelheim, one of the world's largest pharmaceutical companies, through their OpnMe innovation platform (https://www.opnme.com/), called for proposals to formulate molecules with poor drug-like properties for subcutaneous application in preclinical studies. Nanomol Technologies S.L. proposed to formulate the bRo5 compounds within the thermoreversible subcutaneous depot developed in the previous **Chapter 4** (**Figure 5.1**). The optimized hybrid subcutaneous depot is based on Chol:CPC DELOS-NV loaded into the Plx407 thermoreversible polymer. This system is ideal for the subcutaneous delivery of highly hydrophobic bRo5 compounds since the polymer permits the obtainment of an *in situ*-forming subcutaneous depot while the Chol:CPC DELOS-NV can stabilize the hydrophobic compounds in aqueous media and increase their loading and homogeneity within the hydrogel, as well as modulate the release kinetics.

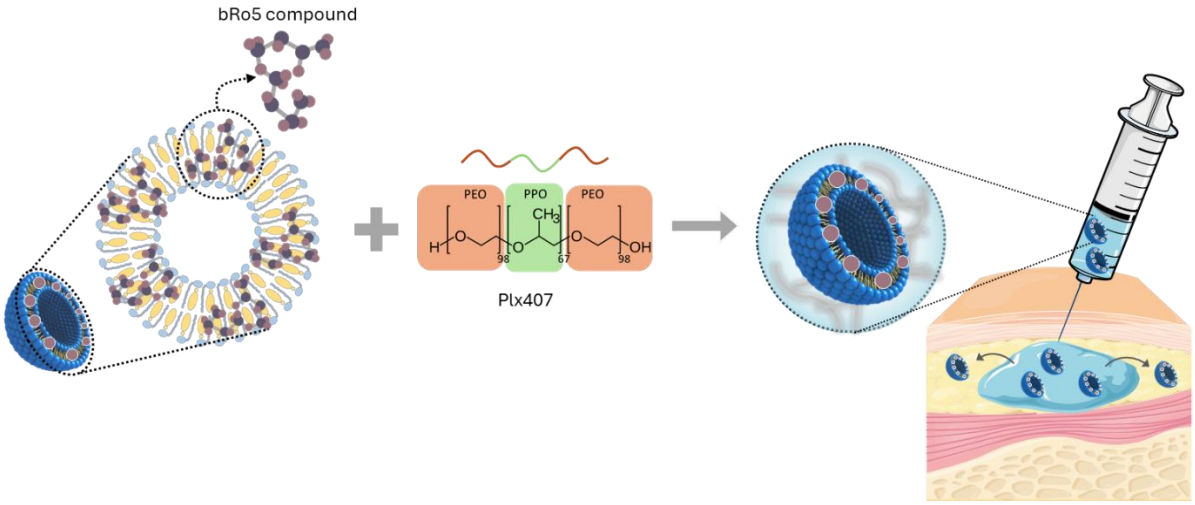


Figure 5.1. *Schematic representations of the bRo5 compounds integration into the hybrid DELOS-nanovesicles-loaded Plx407 hydrogel. First, the compound will be incorporated into the nanovesicles membranes driven by hydrophobics forces. After, the nanoconjugates will be gelled with Plx407 to obtain a thermoreversible hydrogel as a subcutaneous in situ depot.*

5.2. Selection of the Beyond rule of 5 compounds and production of the preliminary prototypes by DELOS method

Boehringer Ingelheim, in the frame of the OpnMe project, provided us with five different bRo5 compounds with therapeutic interest (**Table 5.1**). To select the most appropriate compounds for the development of the formulation, the EtOH solubility and the LogP values provided by Boehringer Ingelheim were examined. As explained in the **Introduction** of the present dissertation, the DELOS method employs an organic solvent to dissolve the membrane components and the hydrophobic substances. Although different organic solvents can be employed, typically EtOH is the solvent used, and for this reason, it was decided to run a screening only with those compounds with higher

solubility in EtOH (bRo5.1, bRo5.2, bRo5.3 and bRo5.4). The bRo5.5 compound was excluded from the initial screening due to its low solubility in EtOH (see **Table 5.1**).

The LogP is also a relevant characteristic since it can influence the EE% achieved in the DELOS-NV. The higher the LogP is, the more hydrophobic the compound is, and very high hydrophobic compounds are more prone to accumulate in lipidic bilayers such as DELOS-NV membranes.

Table 5.1. *Beyond the Rule of 5 (bRo5) compounds provided by Boehringer Ingelheim in the frame of the OpnMe project.*

Compound internal code	***Drug target defined by Boehringer Ingelheim***	***MW (Da)***	***EtOH solubility (mg/mL)***	***LogP/D$_{pH\ 7.4}$***
bRo5.1	*MDM2 compound*	*593.43*	*> 20*	*6.3*
bRo5.2	*HCV protease meglumine*	*1010.99*	*> 10*	*5.6*
bRo5.3	*ACB1 protac*	*936.12*	*> 10*	*6.4*
bRo5.4	*HCV protease base*	*819.98*	*9.8*	*3.7*
bRo5.5	*LFA1 antagonist*	*742.60*	*3.7*	*3.8*

Therefore, and considering the different points explained, an initial screening by DELOS was conducted with the bRo5.1, bRo5.2, bRo5.3 and bRo5.4 compounds. The screening consisted of producing 4 different DELOS formulations (see **Section 9.2.1** for DELOS method) with one of each bRo5 compound. In order to conserve the limited amount of compounds available, the initial screening was conducted using the small laboratory-scale reactor. This reactor produces a final colloidal formulation volume of 32 mL. The DELOS-NV composition employed in the screening was inspired on the one optimized in **Chapter 3**: Chol and CPC in a molar ratio 1:1, and a total concentration of membrane components of 6 mg/mL, in buffer histidine 5 mM pH 7. The concentration of membrane components was slightly more concentrated than it was in the one optimized in **Chapter 3** (6 mg/mL instead of 5 mg/mL) to force slightly the system to entrap the maximum hydrophobic bRo5 compounds on the DELOS-NV bilayers. In all the experiments, 1 mg/mL of bRo5 compounds were loaded per DELOS-NV formulation, by weighting and dissolving them in the ethanol organic phase. A control, consisting of Chol:CPC DELOS-NV with exactly the same composition of membrane components and buffer but without bRo5 compounds, was also produced. The formulations obtained were called by the bRo5 compound internal code followed by a hyphen and "DELOS-NV" (e.g., "bRo5.1-DELOS-NV"), and their compositions is summarized in **Table 9.2** in **Chapter 9**. The macroscopical appearance right after the DELOS production already showed significant differences between the obtained batches (**Figure 5.2**). The bRo5.1- and bRo5.2-DELOS-NV presented a translucid appearance similar to the control DELOS-NV. Oppositely, bRo5.3- and bRo5.4-DELOS-NV had an opaque appearance, indicating presence of larger-size DELOS-NV/structures.

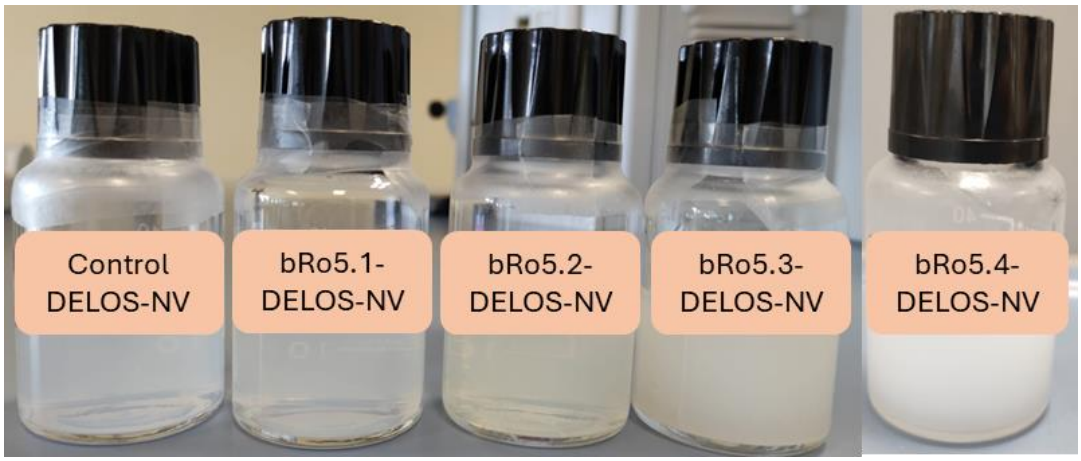


Figure 5.2. *Macroscopical images at t = 0 days after DELOS production of the different bRo5-loaded DELOS-NV formulations. The control DELOS-NV (without bRo5), and the bRo5.1- and bRo5.2-DELOS-NV present the typical translucid macroscopical appearance of colloidal dispersions of SUVs.*

Achieving nice colloidal suspensions with the bRo5.1 and bRo5.2 compounds in the initial screening, without needing to optimize the formulations, indicates a strong affinity of these compounds for the Chol:CPC DELOS-NV. From this initial screening, it was decided to discard the bRo5.3 and bRo5.4 compounds from future drug development and focus the efforts on developing the novel formulations with the bRo5.1 and bRo5.2 compounds. To further confirm the adequacy of these two formulations, they were physiochemically characterized by DLS and ELS (see method in **Section 9.3.1**) at time 0 (right after the DELOS method). **Figure 5.3** shows the characterization of the bRo5.1-, bRo5.2-DELOS-NV and control DELOS-NV for comparison purposes. It can be observed that the three formulations are very similar in terms of average hydrodynamic diameter and size PdI. The Z-potential is slightly higher for the control DELOS-NV, however, all the formulations present Z-potentials significantly above 30 mV, which favor their colloidal stability.

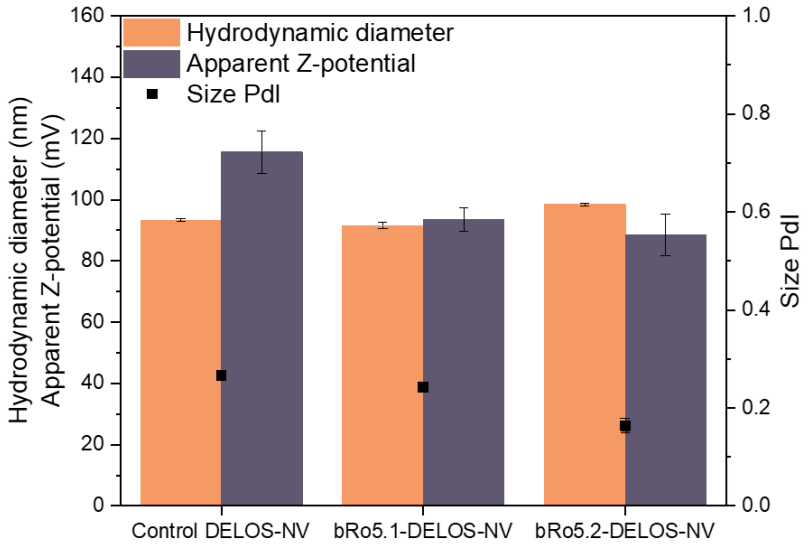


Figure 5.3. *Average hydrodynamic diameter, size PdI and apparent Z-potential measurements at t = 0 (right after DELOS method) of the Control DELOS-NV (without bRo5 compound), the bRo5.1-DELOS-NV and the bRo5.2-DELOS-NV.*

Overall, the results from **Section 5.2** show that the bRo5 compounds can be successfully entrapped in the Chol:CPC DELOS-NV developed in the present thesis, maintaining the good physicochemical properties of the colloidal suspensions. Hence, as a next step, the bRo5.1- and bRo5.2-DELOS-NV nanoconjugates will be further explored and developed as potential novel nanomedicines.

5.3. Advancement of the bRo5.1- and bRo5.2-DELOS-NV nanoconjugates and physicochemical characterization

5.3.1. Diafiltration and concentration of the bRo5.1- and bRo5.2-DELOS-NV nanoconjugates. Quantification of the entrapment efficiency and the final bRo5 concentration

To advance the pharmaceutical development and characterization of the selected prototypes, the bRo5.1- and bRo5.2-DELOS-NV were post-processed to eliminate the non-integrated bRo5 compounds and concentrate the bRo5 in the formulations.

As a target, Boehringer Ingelheim suggested that a concentration of 2-3 mg/mL bRo5 compounds in the formulations would be appropriate to carry out the preclinical studies. Therefore, to attain this concentration TFF post-process was applied to the samples with a 100 kDa hollow fiber column. As explained before in this thesis, TFF allows to exchange the media of colloidal samples, as well as eliminates the non-integrated molecules in solution (free molecules dissolved in the media), but it also can be used to concentrate samples (see configuration set up for each objective in **Section 9.2.2**).

Therefore, the bRo5.1- and bRo5.2-DELOS-NV produced with the DELOS process in the small laboratory-scale reactor were first diafiltrated by TFF to eliminate the remanent EtOH and the possible non-integrated bRo5 compounds that could still be dissolved in the EtOH, and afterward, concentrated by TFF 2.4 times to achieve the target concentration of bRo5 compounds. The control DELOS-NV were also diafiltrated and concentrated by TFF.

After conducting the TFF post-processing, the final bRo5 concentration in each formulation was quantified through UV-Vis spectrophotometer (see method in **Section 9.3.7**) by diluting the samples in 90% v/v EtOH to disrupt the DELOS-NV and dissolve all the components to avoid interferences. The concentration of bRo5 was quantified in the samples obtained right after DELOS, in the samples diafiltrated by TFF and in the samples concentrated by TFF (the final samples), to be able to calculate the EE% (**Equation 9.3** in **Section 9.3.6**). Calibration curves with known concentrations of bRo5.1 and bRo5.2 compounds were prepared in 90% v/v EtOH and 10% v/v histidine 5 mM pH 7. The calibration curves were fitted to a regression line and from the absorbance results of the samples and the regression line, the concentration of bRo5 compound in each sample was quantified (see results for bRo5.1-DELOS-NV in **Figure 5.4** and for bRo5.2-DELOS-NV in **Figure 5.5**).

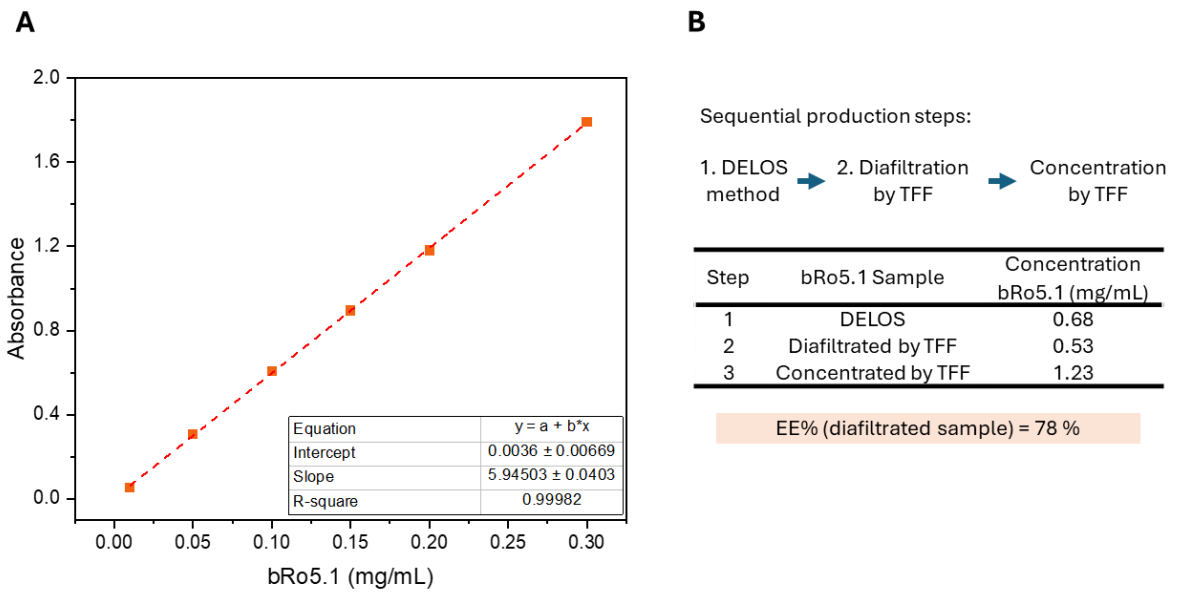


Figure 5.4. *A) Calibration curve of the bRo5.1 compound diluted in 90% EtOH and 10% histidine 5 mM pH 7. Absorbance intensity at λ = 342 nm. B) Concentration of bRo5.1 compound in mg/mL after each production step of the bRo5.1-DELOS-NV: 1st, DELOS method; 2nd, DELOS method and diafiltration by TFF; and 3rd, DELOS method, diafiltration by TFF and concentration by TFF. The EE% is calculated by dividing the bRo5.1 concentration in the diafiltrated sample by the concentration in the DELOS sample.*

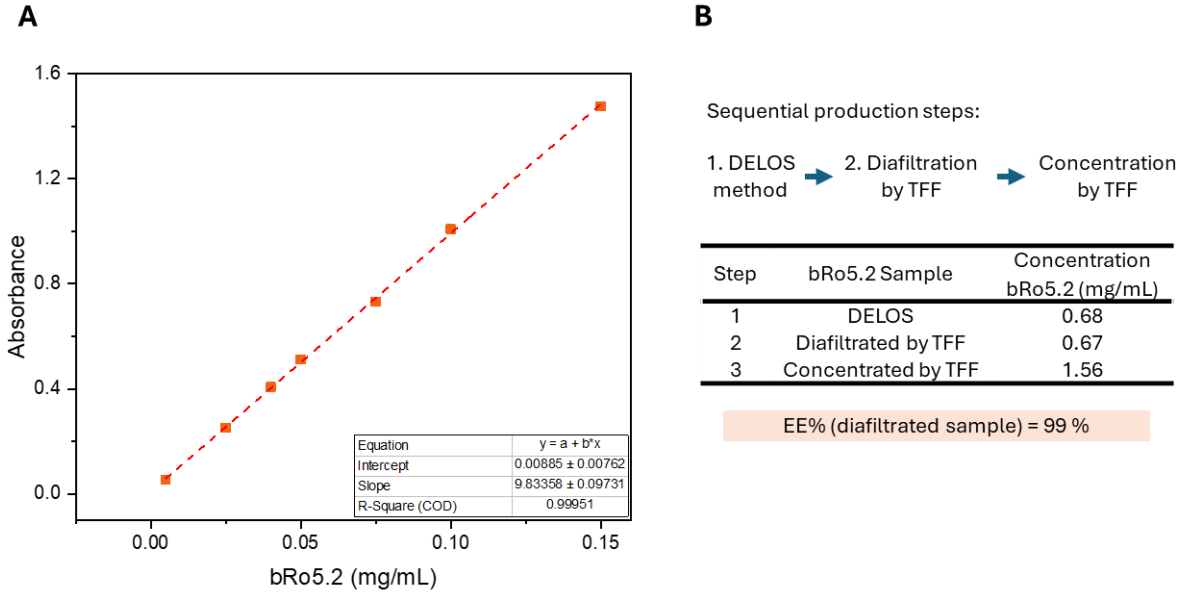


Figure 5.5. *A) Calibration curve of the bRo5.2 compound diluted in 90% EtOH and 10% histidine 5 mM pH 7. Absorbance intensity lectures made at λ = 349.5 nm. B) Concentration of bRo5.2 in mg/mL after each production step of the bRo5.2-DELOS-NV: 1st, DELOS method; 2nd, DELOS method and diafiltration by TFF; and 3rd, DELOS method, diafiltration by TFF and concentration by TFF. The EE% is calculated by dividing the bRo5.1 concentration in the diafiltrated sample by the concentration in the DELOS sample.*

To calculate the EE% of each bRo5 compound shown in **Figure 5.4** and **Figure 5.5**, the concentration of bRo5 compounds in the diafiltrated samples was divided by the concentration of bRo5 compounds in the samples right after DELOS (**Equation 9.3**), and the percentage of integrated bRo5 compounds in the bRo5-DELOS-NV calculated. The high EE% achieved with both formulations (78% for the bRo5.1-DELOS-NV and 99% for the bRo5.2-DELOS-NV) indicates that there is a strong affinity between the evaluated bRo5 compounds and the Chol:CPC DELOS-NV.

The concentration in the samples right after DELOS was 0.68 mg/mL in both formulations, indicating that some loss occurred during the DELOS method. Note that these small losses are frequent when working with the small laboratory-scale reactor and are reduced when working with bigger reactors that confer also higher reproducibility. After the diafiltration and concentration steps by TFF, the concentration of bRo5.1 was 1.23 mg/mL in the bRo5.1-DELOS-NV, and the concentration of bRo5.2 was 1.56 mg/mL in the bRo5.2-DELOS-NV. As expected, the concentration in the concentrated samples was 2.4 times the concentration in the diafiltrated sample, demonstrating that the concentration post-process works well for adjusting the bRo5 concentration in the samples. Therefore, despite working on the small laboratory-scale reactor, the concentration achieved in the concentrated formulations is close to the 2-3 mg/mL target in both formulations.

By purifying the formulations though TFF it has been possible to calculate the EE%, which is very high for both formulations, bRo5.1-DELOS-NV and bRo5.2-DELOS-NV. In addition, it has been demonstrated that the concentration step is adequate to increase the bRo5 in the samples. High bRo5 compound concentrations were achieved using the small laboratory-scale reactor. However, the Boehringer Ingelheim's target could not be reached due to insufficient sample volume, which limited the concentration through TFF. This limitation can be easily overcome by transitioning to a larger-scale reactor and working with greater sample volumes, as will be demonstrated in **Section 5.4**.

In the following **Section 5.3.2**, the physicochemical attributes of the concentrated samples were characterized to demonstrate their suitability as novel nanoconjugates for integration into Plx407 hydrogels.

5.3.2. Characterization of the average hydrodynamic diameter, size PdI and apparent Z-potential in the concentrated bRo5.1- and bRo5.2-DELOS-NV

As explained, the bRo5.1- and bRo5.2-DELOS-NV nanoconjugates were diafiltrated and concentrated by TFF successfully. The previous **Section** confirmed that these post-processes are appropriate to purify the sample and eliminate the non-integrated bRo5 compounds, and to modulate the final concentration of bRo5 in the formulations. These samples obtained after the concentration step were then characterized in detail by different techniques. The control DELOS-NV (same formulation as the bRo5-DELOS-NV but without bRo5 compound) diafiltrated and concentrated were also characterized for comparison purposes.

The average hydrodynamic diameter, size PdI and apparent Z-potential were assessed by DLS and ELS as explained in **Section 9.3.1**. These attributes were measured over a period of 360 days to

assess the stability of the formulations. The following **Figure 5.6** shows the results for the bRo5.1- and bRo5.2-DELOS-NV, and also for the control DELOS-NV.

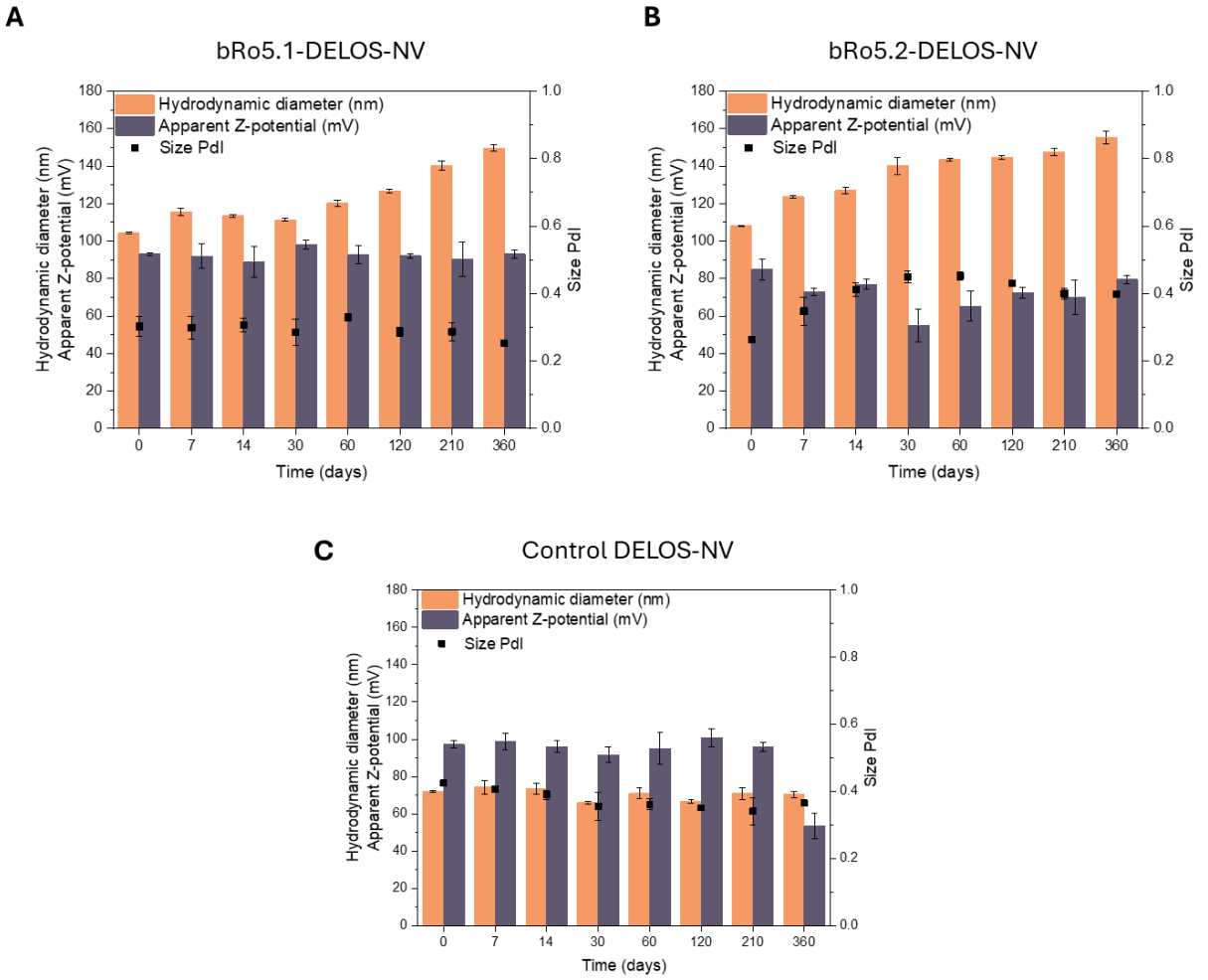


Figure 5.6. Average hydrodynamic diameter, size PdI and apparent Z-potential measurements over one year period for the A) bRo5.1-DELOS-NV concentrated 2.4 times, B) bRo5.2-DELOS-NV concentrated 2.4 times and C) Control DELOS-NV concentrated 2.4 times.

The results show that there are no major differences between the control DELOS-NV and the bRo5.1- and bRo5.2-DELOS-NV. The hydrodynamic diameter is slightly larger for the later ones, but the size PdI is still very low indicating high homogeneity. The consecutive measurements made over time show a slight trend of the bRo5.1- and bRo5.2-DELOS-NV to increase their hydrodynamic diameter. However, the hydrodynamic diameter increase is small considering the long period evaluated. In addition, the Z-potential is very stable over time and around 90 mV for the three formulations, despite the integration of the hydrophobic bRo5 compounds on the DELOS-NV bilayers. Therefore, it can be confirmed that these samples present appropriate physicochemical properties and are stable for at least 1 year stored at 5 ± 3 ºC.

5.3.3. Cryogenic transmission electron microscopy images of the concentrated bRo5.1- and bRo5.2-DELOS-NV

In addition to the DLS and ELS characterizations, images of the bRo5.1- and bRo5.2-DELOS-NV were obtained with the Cryo-TEM as explained in **Section 9.3.4**. The images were obtained one month after the production and post-processing by TFF of the samples. The images in **Figure 5.7** and **Figure 5.8** show different modifications in the nanovesicles membranes which are indicative of interaction between the bRo5 compounds and the DELOS-NV membranes.

The bRo5.1-DELOS-NV show in some DELOS-NV an increase in their membrane width which could be caused by the interaction between the nanovesicles and the bRo5.1 compound (**Figure 5.7)**. In addition, the images show a large presence of disk-like micelles, which are precursors of the nanovesicles, and will eventually convert into nanovesicles[9]. This indicates that this formulation requires longer maturation periods than 30 days. The longer maturation time required by the sample could explain the slight trend to increase size observed in **Section 5.3.2.**

The bRo5.2-DELOS-NV also differ from the classical DELOS-NV morphology due to the presence of some vesicles with planar phases in the bilayer that can be caused by the entrapment of the bRo5.2 (**Figure 5.8**). This sample also presents some structures with very low contrast that resemble nanoemulsions[10]. In addition, a significant number of DELOS-NV precursors (disk-like micelles) are also present.

Importantly, no precipitation was detected in any sample, suggesting that the bRo5 compounds are nanostructured in water through the DELOS process without the formation of precipitates/destabilization. Besides, it is important to highlight that the DELOS-NV detected in the Cryo-TEM images present some signs on their membranes that are indicative of interaction between the bRo5 compounds and the nanovesicles bilayers.

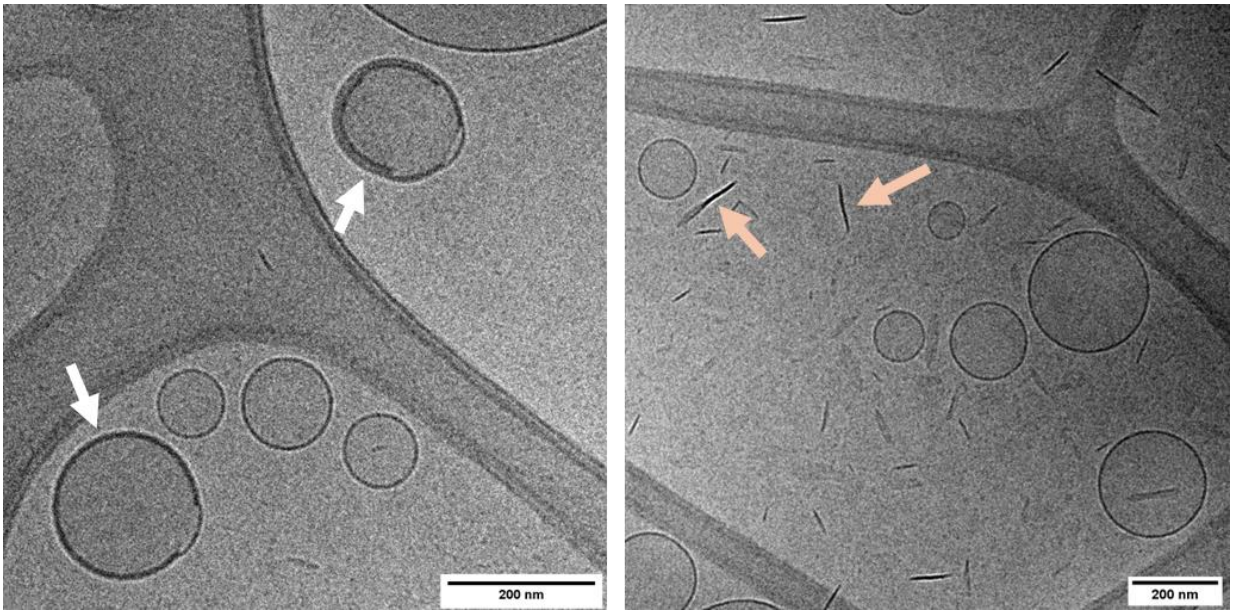


Figure 5.7. *Cryo-TEM images of the bRo5.1-DELOS-NV. The white arrows highlight an increase in the DELOS-NV membrane width. The orange arrows point out DELOS-NV precursors (disk-like micelles).*

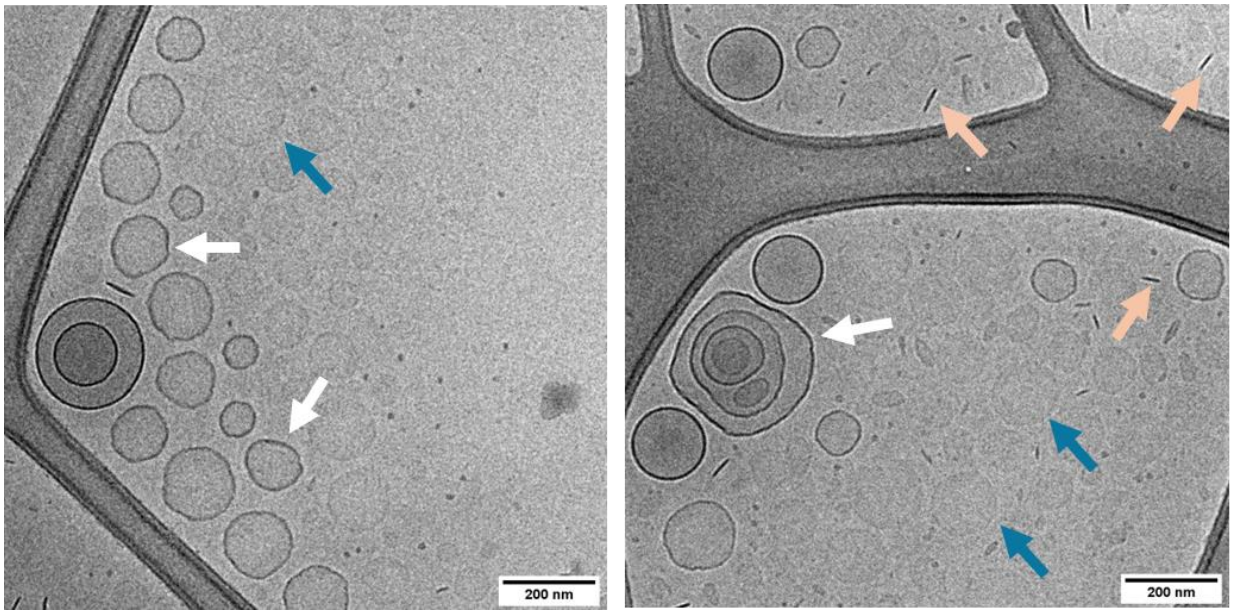


Figure 5.8. *Cryo-TEM images of the bRo5.2-DELOS-NV. The white arrows highlight DELOS-NV with planar phases in the bilayer. The orange arrows point out DELOS-NV precursors (disk-like micelles). The blue arrows point out low-contrast structures that resemble nanoemulsions.*

After confirming the stability of the samples at 5 ± 3 °C and observing the nanoscopic morphology of the bRo5-DELOS-NV formulations through Cryo-TEM, the next step consisted of evaluating the stability of the samples at 40 °C.

5.3.4. Stability at 40 °C of the concentrated bRo5.1- and bRo5.2-DELOS-NV

All the DELOS-NV produced in the framework of this thesis have been stored in the fridge at 5 ± 3 °C, and therefore, the stability results reported are for this specific storage condition. However, the formulations produced in the present **Chapter** are meant to be administered as subcutaneous *in situ* depots for their extended release. Therefore, they should be stable at body temperature too. For this reason, the stability of the concentrated bRo5.1- and bRo5.2-DELOS-NV at 40 ± 3 °C was assessed. With this intention, aliquots of both formulations were stored in the oven at 40 ± 3 °C for 30 days. After this period, these samples were characterized, and the results were compared with the same samples stored in the fridge (5 ± 3 °C). Next **Figure 5.9** shows the comparison between the bRo5.1- and bRo5.2-DELOS-NV stored at different temperatures. It can be observed that in terms of hydrodynamic diameter, size PdI and apparent Z-potential, the samples are very similar. Also, the UV-Vis spectra did not show a decrease in the absorbance or unexpected peaks that could indicate degradation of the bRo5 compounds.

Overall, the results presented suggest stability of the developed formulations stored at 40 ± 3 °C for 30 days, indicating that they could be administered subcutaneously without risk of degradation caused by the body temperature. Importantly, this test is just a preliminary study to observe tendencies. Repeating the test with more samples to have enough statistical power would allow running statistical analysis to confirm the results.

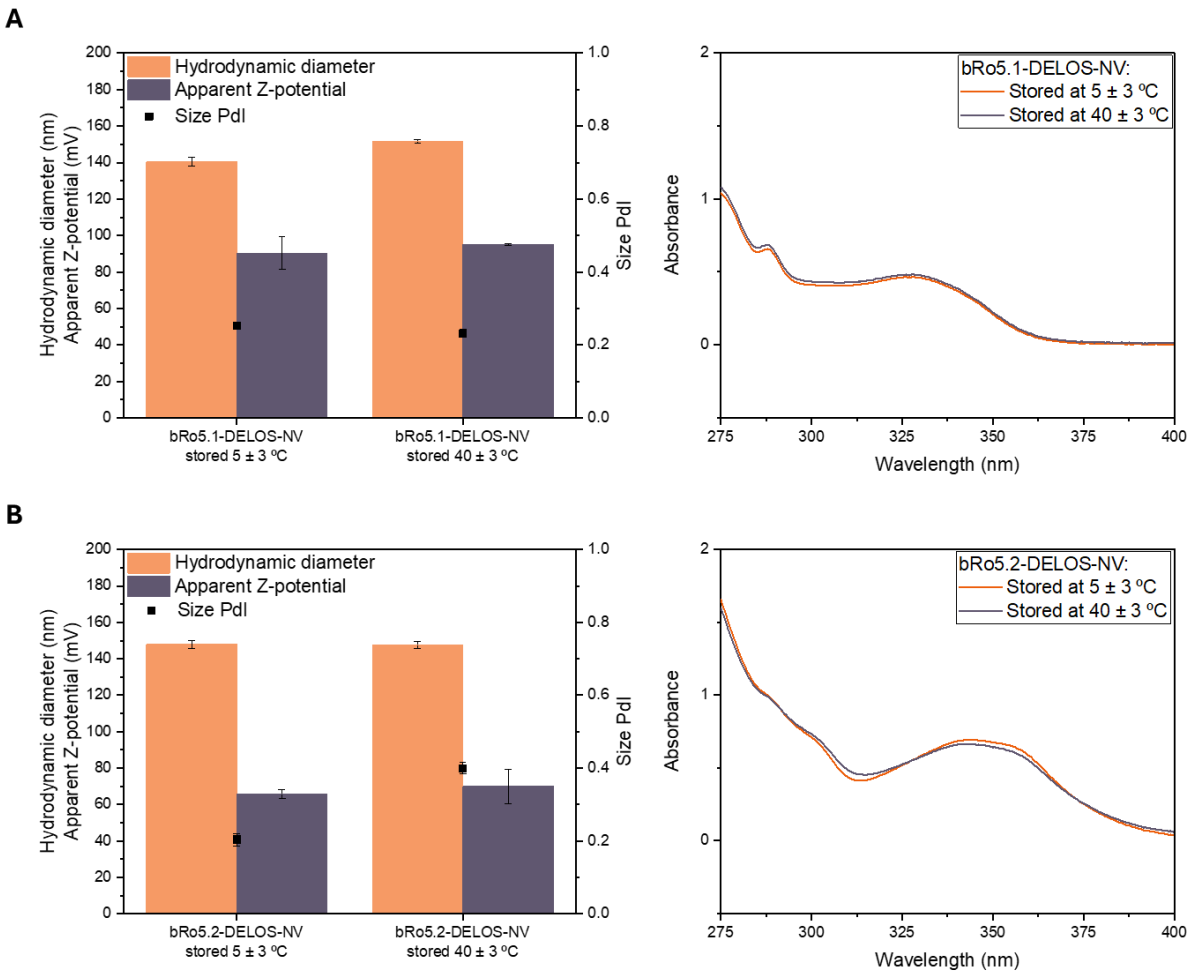


Figure 5.9. *Physicochemical comparison between bRo5.1- and bRo5.2-DELOS-NV stored at 5 ± 3 ºC and 40 ± 3 ºC for a 30-day period. A) bRo5.1-DELOS-NV. Left: Hydrodynamic diameter, size PdI and apparent Z-potential (Mean + SD; n= 3 consecutive measurements). Right: UV-Vis absorbance spectrum. B) bRo5.2-DELOS-NV. Left: Hydrodynamic diameter, size PdI and apparent Z-potential (Mean + SD; n= 3 consecutive measurements). Right: UV-Vis absorbance spectrum.*

Through various physicochemical characterizations and stability tests, the potential of the concentrated bRo5.1- and bRo5.2-DELOS-NV formulations as subcutaneous drug delivery systems has been highlighted. In the following section, the reproducibility of these promising formulations will be assessed, as it is a critical aspect of drug development.

5.3.5. Reproducibility of the concentrated bRo5.1- and bRo5.2-DELOS-NV formulations

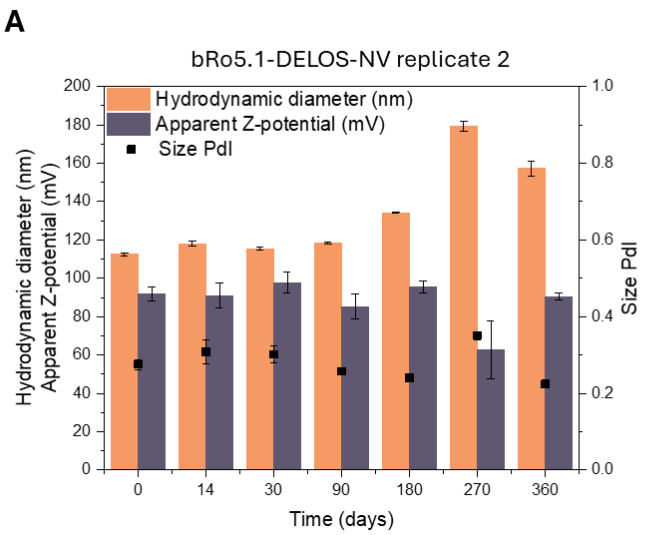
A crucial step in developing a drug formulation is ensuring its reproducibility. While the results obtained so far are promising, the formulations must be reproducible to qualify as potential drug candidates for the market. To confirm the reproducibility of the bRo5.1- and bRo5.2-DELOS-NV formulations, replicates were produced. The replicates were produced following exactly the same steps and with the same formulation recipe as in **Section 5.2** and **Section 5.3.1**. First, the DELOS

method was carried out in the small laboratory-scale reactor, to obtain the bRo5.1- and bRo5.2-DELOS-NV replicates. Afterward, through TFF, the formulations were diafiltrated and concentrated to eliminate the non-integrated bRo5 compounds and increase the final bRo5 concentration in the formulation replicates. They were called bRo5.1-DELOS-NV replicate 2 and bRo5.2-DELOS-NV replicate 2 (see details of the formulations in **Table 9.2**). Finally, the replicates were characterized by DLS, ELS (see method in **Section 9.3.1**) and UV-Vis spectroscopy (see method in **Section 9.3.7**) to determine the concentration of bRo5 in the formulations, as well as the EE%. The calibration curves shown in **Figure 5.4** and **Figure 5.5** were used to calculate the concentration of bRo5 compounds in the samples. The characterization of the bRo5.1-DELOS-NV replicate 2 is shown in **Figure 5.10** and the characterization of bRo5.2-DELOS-NV replicate 2 in **Figure 5.11**.

In **Figure 5.10A**, it can be observed that the average hydrodynamic diameter of the bRo5.1-DELOS-NV replicate 2 is around 120 nm at the beginning and slightly increases to 140-160 nm after 1 year. The PdI and the apparent Z-potential are stable over 1 year and are around 0.3 and 90 mV, respectively. These results are very similar to the results obtained with the bRo5.1-DELOS-NV replicate 1 shown in **Figure 5.6**. The final EE% achieved in the formulation (**Figure 5.10B**) is also very similar to the one obtained with the first replicate and shown in **Figure 5.4**.

In the case of bRo5.2-DELOS-NV replicate 2, the hydrodynamic diameter and its evolution over time (**Figure 5.11A**) are similar to those of bRo5.2-DELOS-NV replicate 1 shown in **Figure 5.6**. However, the hydrodynamic diameter increases slightly more over time in replicate 2 (from 100 to 180 nm) compared to replicate 1 (from 100 to 160 nm), although the difference is minimal considering the long period of time evaluated. Additionally, the PdI is slightly smaller in replicate 2 (around 0.2) compared to replicate 1 (around 0.4). The apparent Z-potential remains consistently around 90 mV throughout the year, closely matching the apparent Z-potential of replicate 1. On the other hand, the EE% of the bRo5.2 compound in replicate 2 is marginally lower than in replicate 1 (**Figure 5.5**), yet it remains high at 76%. Therefore, despite the small differences detected between the two replicates produced with the bRo5.2 compound at the small laboratory-scale reactor, the reproducibility of this formulation is also very high.

Based on the set of characterizations performed, it can be concluded that there is a high degree of reproducibility for the designed formulations, especially considering the use of a small laboratory-scale reactor for their production. It is well known that variability between batches is typically greater when using smaller reactors. Therefore, the strong reproducibility results achieved underscore the potential of the novel bRo5.1- and bRo5.2-DELOS-NV formulations as subcutaneous drug delivery systems.



B

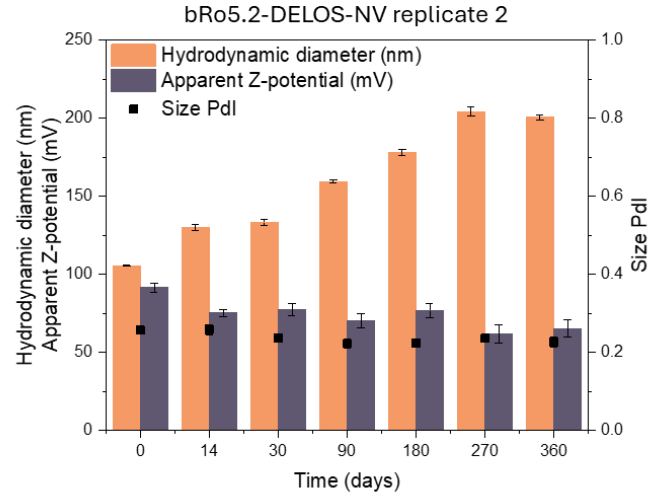
Sequential production steps:

1. DELOS method → 2. Diafiltration by TFF → Concentration by TFF

Step	bRo5.1 replicate 2	Concentration bRo5.1 (mg/mL)
1	DELOS	0.83
2	Diafiltrated by TFF	0.63
3	Concentrated by TFF	1.42

EE% (diafiltrated sample) = 76 %

Figure 5.10. Characterization of the bRo5.1-DELOS-NV replicate 2. A) 1 year stability of the hydrodynamic diameter (nm), size PdI and apparent Z-potential (mV). B) bRo5.1 concentration in mg/mL after each step of the bRo5.1-DELOS-NV replicate 2 production: DELOS method; DELOS method and diafiltration by TFF; and DELOS method, diafiltration by TFF and concentration by TFF. The EE% is calculated by dividing the bRo5.1 concentration in the diafiltrated sample by the concentration in the DELOS sample.



B

Sequential production steps:

1. DELOS method → 2. Diafiltration by TFF → Concentration by TFF

Step	bRo5.2 replicate 2	Concentration bRo5.2 (mg/mL)
1	DELOS	0.54
2	Diafiltrated by TFF	0.41
3	Concentrated by TFF	1.06

EE% (diafiltrated sample) = 76 %

Figure 5.11. Characterization of the bRo5.2-DELOS-NV replicate 2. A) 1 year stability of the hydrodynamic diameter (nm), size PdI and apparent Z-potential (mV). B) bRo5.1 concentration in mg/mL after each step of the bRo5.-DELOS-NV replicate 2 production: DELOS method; DELOS method and diafiltration by TFF; and DELOS method, diafiltration by TFF and concentration by TFF. The EE% is calculated by dividing the bRo5.1 concentration in the diafiltrated sample by the concentration in the DELOS sample.

Very promising results have been achieved in **Section 5.3**. The EE% in the bRo5.1- and bRo5.2-DELOS-NV was assessed, and very high values were achieved. Additionally, it was demonstrated that

the concentration of bRo5.1 and bRo5.2 in the formulations could be modulated through a TFF concentration step. The physicochemical characterization of the concentrated formulations revealed the presence of nanovesicles that were homogeneous in size, with a high apparent Z-potential, which favors colloidal stability. In fact, the stability of the formulations was demonstrated for at least one year under storage conditions (5 ± 3 °C). Their stability for 30 days at 40 ± 3 °C was also confirmed, indicating their potential for subcutaneous delivery without the risk of degradation due to body temperature. Although both bRo5.1-DELOS-NV and bRo5.2-DELOS-NV formulations demonstrated high reproducibility, the following sections will focus on bRo5.1-DELOS-NV, as it was even more reproducible than bRo5.2-DELOS-NV. In the next **Section**, the aim is to scale up the production of bRo5.1-DELOS-NV from a production volume of 30 mL to a volume of 250 mL.

5.4. Scaling up the production of bRo5.1-DELOS-NV and estimating the maximum achievable bRo5.1 concentration

In the present section, the aim is to demonstrate the scalability of the bRo5.1-DELOS-NV production, since the overspread of a nanomedicine to the market is strongly dependent on the capability of scaling its production. The scaling-up is a common challenge in nanovesicles formulations, given that, as explained in the **Introduction** of this thesis, conventional methods for nanovesicles production require several steps and are difficult to scale-up.

By scaling-up the DELOS production of the bRo5.1-DELOS-NV a larger volume of formulation will be obtained, which will permit to concentrate further the sample through TFF and increase the amount of bRo5.1 in the formulation. However, increasing the formulation volume requires a greater expenditure of production materials. This is not a concern for the Chol and CPC membrane components, as they are inexpensive and readily available. However, since bRo5.1 compound is a limited resource, its loading in the DELOS method was reduced from 1 mg/mL to 0.5 mg/mL during this preliminary phase to avoid unnecessary waste.

The new batch, composed of 6 mg/mL Chol and CPC at equimolar ratios and 0.5 mg/mL bRo5.1 was produced by DELOS in the intermediate laboratory-scale reactor (V_{final} = 250 mL) as described in **Section 9.2.1**. This batch, called from now on as scaled-bRo5.1-DELOS-NV (see details of the formulation **Table 9.2**) had a good macroscopical appearance (**Figure 5.12A**). In addition, the sample was characterized by DLS and ELS as described in **Section 9.3.1** (**Figure 5.12B**) at time 0 (right after DELOS method). By DLS was obtained an average hydrodynamic diameter of 78.0 ± 0.3 nm and a size PdI of 0.242 ± 0.009. The low size PdI value obtained indicates that the nanovesicles are very homogeneous in terms of size. Moreover, the apparent Z-potential was around 100 mV, contributing to the stability of the colloidal dispersion.

It can be noted that the scaled-bRo5.1-DELOS-NV produced in the intermediate laboratory-scale reactor are very similar to the bRo5.1-DELOS-NV produced in the small laboratory-scale reactor (**Figure 5.3**) in terms of hydrodynamic diameter, size PdI and apparent Z-potential. These results confirm that the production of DELOS-NV with bRo5.1 compounds can be scaled from V_{final} = 30 mL to V_{final} = 250 mL.

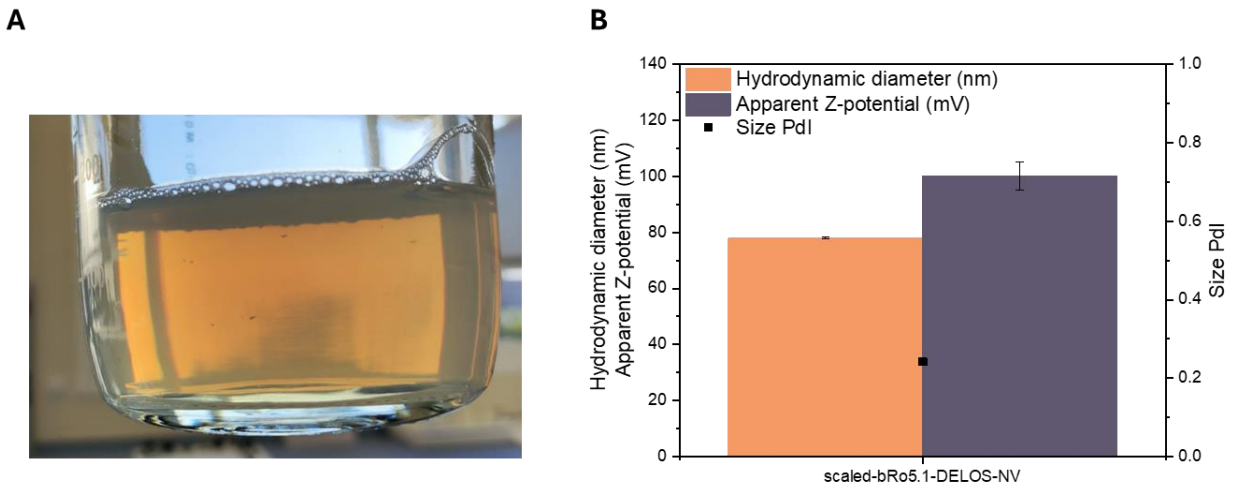


Figure 5.12. Characterization of the scaled-bRo5.1-DELOS-NV obtained in the intermediate laboratory-scale reactor at t = 0, (right after DELOS method, before the diafiltration and concentration steps). A) Macroscopical appearance. B) Hydrodynamic diameter (nm), size PdI and apparent Z- potential.

Afterward, the sample was diafiltrated and concentrated by TFF as described in **Section 9.2.2,** following the same procedure carried out with the bRo5.1-DELOS-NV. To assess the maximum concentration of the bRo5.1 compound achievable in the formulation at the current intermediate laboratory-scale production, the 250 mL formulation was concentrated to its maximum extent, 17 times. The obtained concentrated formulation was physiochemically characterized by DLS and ELS (**Figure 5.13A**) following the methodology described in **Section 9.3.1**, over a 1-year period. The results show a slight trend to increase the average hydrodynamic diameter over time as well as decrease the size PdI. Oppositely, the Z-potential remains consistent over time. Despite the small changes in size, the colloidal suspension obtained is stable, and no sedimentation appears even after 12 months.

In addition, the concentration of bRo5.1 in the sample after each production step was quantified by UV-Vis spectroscopy (**Figure 5.13B**) following the method described in **Section 9.3.7** and employing the calibration curve shown in **Figure 5.4.** It can be observed that the mass balance by the DELOS method is remarkably higher working in the intermediate laboratory-scale reactor, in comparison to the small laboratory-scale reactor. As expected, losses during the DELOS method are below 2% when working at this larger-scale reactor, which is a promising result. Note that in the small laboratory-scale reactor, there was a bRo5.1 loss of 32%. The EE%, calculated by dividing the concentration of bRo5.1 after the diafiltration process by the concentration of bRo5.1 after the DELOS method, was 83%. Hence, the EE% has been slightly improved by scaling the bRo5.1-DELOS-NV production (83% *vs* 75-80%). Furthermore, the final concentration of bRo5.1 in the scaled-bRo5.1-DELOS-NV, after the diafiltration and concentration step, was 4.52 mg/mL. It must be noted that in this specific case, the actual concentration of the bRo5.1 compound increased 13.3 times, rather than the theoretical 17 times. Despite this small difference, the results are still promising, as the use of the intermediate laboratory-scale reactor allowed for significantly greater concentration of the sample, exceeding the target proposed by Boehringer Ingelheim.

Therefore, the bRo5.1-DELOS-NV have been successfully scaled from the small laboratory-scale reactor to the intermediate laboratory-scale reactor, growing the obtained colloidal suspension from 30 mL to 250 mL. Having a larger volume of sample has permitted to concentrate the sample 13.3 times through TFF, exceeding the target concentration of bRo5.1 in the suspension. All these results have been achieved while maintaining the physicochemical properties and stability of the DELOS-NV obtained. These results are very positive not only because they demonstrate our ability to meet the Boehringer Ingelheim's bRo5.1 concentration specifications but also because they show that the formulation production is scalable. This is critical in drug development, as non-scalable formulations cannot be translated to the market.

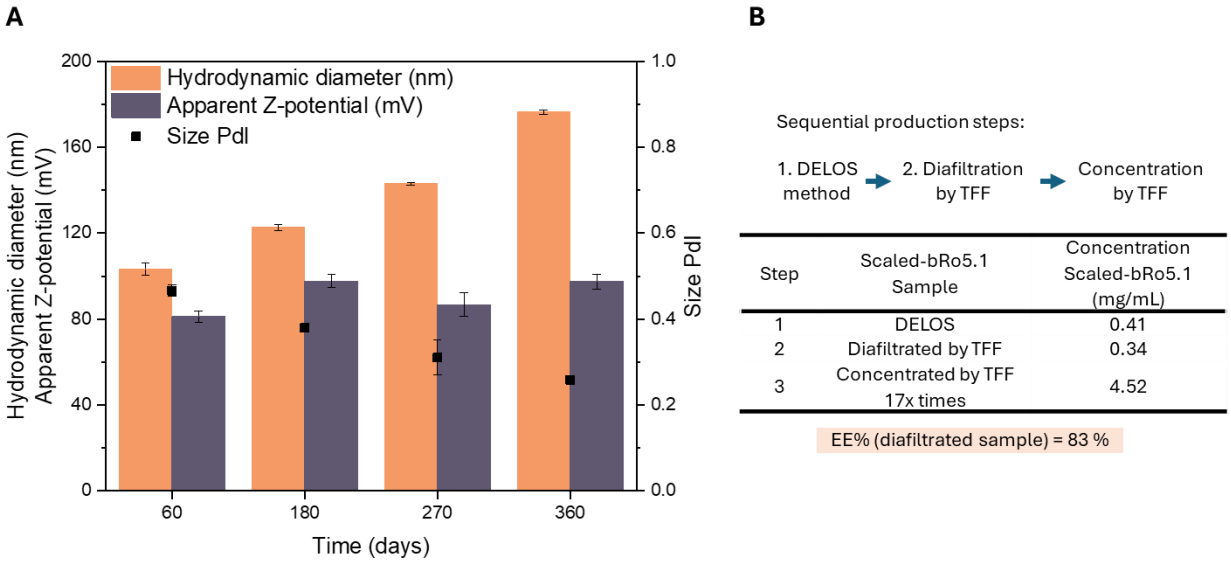


Figure 5.13. *Physicochemical characterization of the bRo5.1-DELOS-NV produced in the mid-scale reactor, after the diafiltration and concentration steps by TFF. A) Hydrodynamic diameter (nm), size PdI and apparent Z-potential (mV) evolution from 2 months to 1 year. B) Quantification of the bRo5.1 concentration after each production step and EE% calculated by dividing the bRo5.1 concentration after the diafiltration by TFF by the concentration after DELOS.*

To summarize, this **Section** describes the successful scale-up of the bRo5.1-DELOS-NV production from a small laboratory-scale reactor to an intermediate laboratory-scale reactor, increasing the DELOS volume from 30 mL to 250 mL. The scaled-bRo5.1-DELOS-NV formulation was then concentrated to a very high concentration of bRo5.1 (4.52 mg/mL). Additionally, the scaled formulation maintained good physicochemical properties and a high EE%. This demonstrates both, the scalability of the bRo5.1-DELOS-NV production and the ability to modulate the final concentration of bRo5.1 through TFF. In the following **Section**, the feasibility of integrating the bRo5.1-DELOS-NV into the thermoreversible Plx407 as a novel *in situ* subcutaneous depot will be assessed.

5.5. Formulation of bRo5.1-DELOS-NV into Poloxamer 407 hydrogels

In this final **Section** of the **Chapter**, the bRo5.1-DELOS-NV have been integrated into Plx407 to obtain a hybrid formulation for extended subcutaneous release, marking the culmination of the study.

Up to this point, it has been demonstrated the feasibility of entrapping the bRo5.1 compound in the optimized DELOS-NV with Chol and CPC. The bRo5.1-DELOS-NV have been deeply characterized. Their high reproducibility and stability over time have been demonstrated. In addition, bRo5.1-DELOS-NV maintain their integrity at 40 °C, hence being suitable for subcutaneous delivery. Moreover, their production can be scaled to obtain larger volumes of formulation.

These promising bRo5.1-DELOS-NV with outstanding characteristics to be employed as subcutaneous drug delivery systems, have been gelled with the Plx407 polymer to obtain a potential subcutaneous depot that permits their extended-release over time. The benefits of having a subcutaneous depot have been discussed in detail in the introduction of **Chapter 4**, as well as the advantages of employing DELOS-NV to transport and stabilize hydrophobic compounds and load them into the thermoreversible polymer.

Specifically, the bRo5.1-DELOS-NV replicate 2, produced in the small laboratory-scale reactor and concentrated 2.4 times (see its physicochemical characterization in **Figure 5.10**), has been gelled by adding Plx407 as described in **Section 9.2.3**. It was decided to work with the bRo5.1-DELOS-NV produced in the small laboratory-scale reactor, diafiltrated and concentrated, because the concentration of bRo5.1 in this formulation was closer to the target concentration compared to the concentration in the scaled-bRo5.1-DELOS-NV ($[bRo5.1]_{formulation}$ = 1.42 mg/mL; $[bRo5.1]_{target}$ = 2-3 mg/mL). Note that during the concentration process, the DELOS-NV membrane components also get concentrated. Hence, according to the 2.4 times concentration applied, the bRo5.1-DELOS-NV replicate 2 has the following theoretical composition: 14.4 mg/mL membrane components (Chol + CPC) at an equimolar ratio and 1.42 mg/mL bRo5.1 compound, as a colloidal formulation in histidine 5 mM buffer pH 7.

Specifically, the bRo5.1-DELOS-NV replicate 2 formulation was gelled with 17% w/w Plx407, which was the most appropriate concentration to obtain subcutaneous depots, as defined in **Chapter 4**. Afterward, the obtained bRo5.1-DELOS-NV-loaded 17% w/w Plx407 hydrogel was characterized. Images of the hydrogel at 22 °C and 37 °C were obtained after 30 minutes of stabilization at each temperature to demonstrate its thermoreversible behavior (**Figure 5.14A**). In addition, Cryo-TEM images of the bRo5.1-DELOS-NV in the hydrogel have been obtained by diluting the samples 1:5 in water to adjust their viscosity to the technique, as explained in **Section 9.3.4** (**Figure 5.14B**). The Cryo-TEM images show spherical, unilamellar nanovesicles demonstrating the stability of the bRo5.1-DELOS-NV gelled in 17% w/w Plx407. As discussed in **Chapter 4**, some of the DELOS-NV formulations exhibit an increase in membrane width, likely due to the adsorption of Plx407[11].

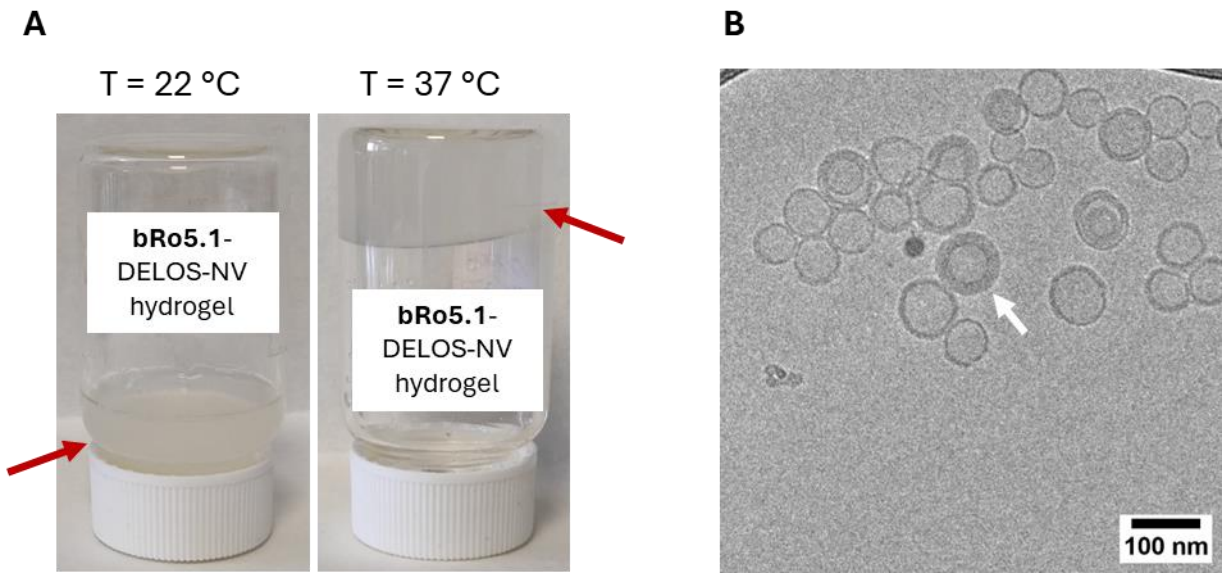


Figure 5.14. *Characterization of the bRo5.1-DELOS-NV-loaded 17% w/w Plx407 hydrogel. A) Macroscopical images at 22 °C and 37 °C showing the thermoreversible behavior of the hydrogel. The hydrogel does not flow to the cap of the vial at 37 °C because it is behaving as a solid-like material. The red arrows point out the position of the hydrogel. B) Cryo-TEM images of the bRo5.1-DELOS-NV gelled with 17% w/w Plx407. The white arrow highlights an increase in the bRo5.1-DELOS-NV membrane probably caused by the Plx407 adsorption.*

The obtained formulation with the bRo5.1-DELOS-NV and the Plx407 is macroscopically homogeneous and behaves as a thermoreversible hydrogel. It is liquid at room temperature (thus being easily injectable) and becomes solid at body temperature, forming a cohesive depot for the extended release of the nanovesicles. In addition, the stability of the nanovesicles in the hybrid formulation has been demonstrated through Cryo-TEM.

5.5.1. In vitro degradation and release test with the bRo5.1-DELOS-NV-loaded 17% w/w Plx407 hydrogel

After the satisfactory results achieved in the gelation of the bRo5.1-DELOS-NV, next step consisted in testing the *in vitro* degradation of the hydrogel and *in vitro* release of the bRo5.1-DELOS-NV replicate 2.

In **Chapter 4** great results were obtained with the DiD-Chol:CPC DELOS-NV-loaded 17% w/w Plx407 hydrogel. The *in vitro* release test demonstrated a zero-order release of the DELOS-NV labeled with DiD for an extended period of 8 hours. The degradation of the hydrogel was steady and constant, showing an optimal fit with the zero-order mathematical model (**Equation 4.5**). These results indicated that the release of the nanovesicles from the hydrogel was solely influenced by the hydrogel dissolution rate, and that no diffusion occurred. In addition, it was found that the DELOS-NV could stabilize the hydrophobic DiD dye in the release medium (dPBS pH 7.4) of the *in vitro* release test. Oppositely, the free-DiD formulated into the thermoreversible hydrogel precipitated in the aqueous release medium of the test, despite the solvents employed for its solubilization and formulation in the hydrogel.

In this section, the release of the bRo5.1-DELOS-NV gelled in 17% w/w Plx407 will be described. To assess the release, the same methodology employed in **Chapter 4** and described in **Section 9.4.3** was employed. Very briefly, 1.5 mL of the bRo5.1-DELOS-NV-loaded 17% w/w Plx407 hydrogel were placed in a vial and incubated at 37 °C until their conversion into solid-like hydrogels. Then, 4 mL of dPBS, also prewarmed at 37 °C, were layered over the solid-like hydrogel. The preparative was incubated at 37 °C with orbital agitation until the whole dissolution of the hydrogel. Every hour, the dPBS was completely replaced by fresh dPBS at 37 °C. The hydrogel degradation kinetics were determined by weighing the remaining hydrogel at each time point. Additionally, the release kinetics of bRo5.1-DELOS-NV were assessed by measuring the bRo5.1 concentration in each dPBS sample using UV-Vis spectrophotometry. The absorbance intensity at λ = 330 nm was converted to concentration using a calibration curve fitted to a regression line (R^2 = 0.9995). The percentage of dissolved hydrogel and the bRo5.1-DELOS-NV cumulative release are shown in **Figure 5.15**.

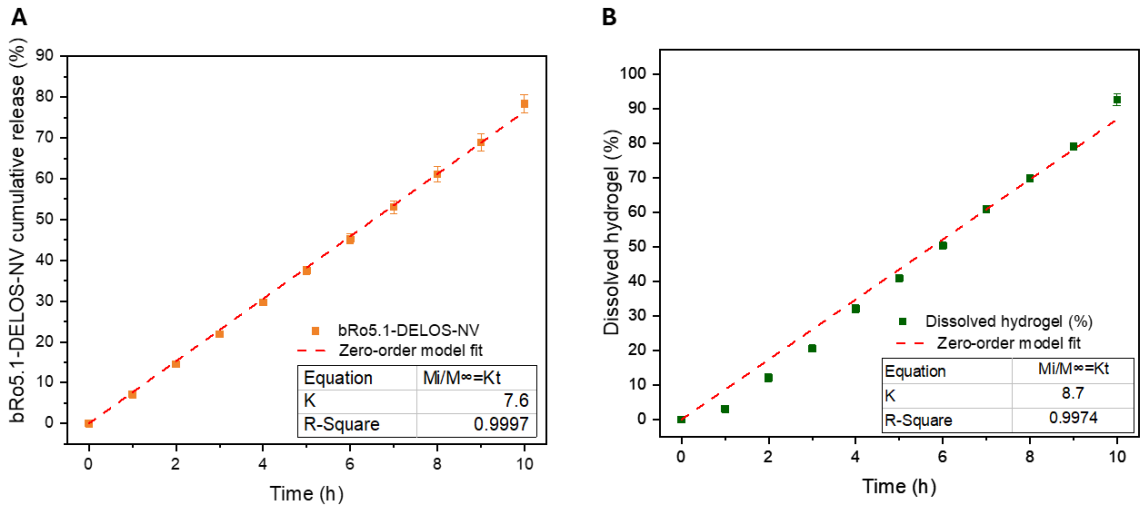


Figure 5.15. *A) In vitro bRo5.1-DELOS-NV replicate 2 release (cumulative %) from 17% w/w Plx407 hydrogel, and B) in vitro hydrogel dissolution (dissolved hydrogel wt%) as a function of time (hours), using the membrane-less model at 37 °C. dPBS pH 7.4 was employed as release media. Data are expressed as mean ± SD (n = 3) and has been fitted into a zero-order mathematical model (**Equation 4.5**).*

As it can be observed, the *in vitro* test results shown in **Figure 5.15** are very similar to those obtained in **Chapter 4** and were also fitted to the zero-order mathematical model (**Equation 4.5**). The results fit properly the zero-order model fit, with an R^2 above 0.997 for both, the bRo5.1-DELOS-NV release kinetics and the hydrogel dissolution kinetics. As explained in **Chapter 4**, this zero-order release kinetics of the bRo5.1-DELOS-NV is led by the hydrogel dissolution rate, which also follows zero-order kinetics. Zero-order kinetics are the preferred release kinetics in drug development because result in consistent drug levels in the blood, reducing the side effects associated with peak concentrations of the drug in the bloodstream.

Unexpectedly, the release of the novel bRo5.1-DELOS-NV took 10 hours, instead of 8 hours as it took with the DiD-DELOS-NV in **Chapter 4**. It was found in **Chapter 4** that the presence of nanovesicles affected the hydrogel behavior similarly as it would affect increasing the concentration of Plx407. Thus, the presence of DELOS-NV in the hydrogels reduced their $T_{sol\text{-}gel}$ and increased their cohesivity

at 37 ºC, probably resulting in longer-lasting depots compared to blank hydrogels (hydrogels without DELOS-NV). The rationale explanation for these results is the entrapment of water molecules into the nanovesicles core[12]. The nanovesicles employed in this **Chapter** are significantly more concentrated than the nanovesicles employed in **Chapter 4**. They were produced with 6 mg/mL membrane components, instead of 5 mg/mL, and were further concentrated 2.4 times through TFF, thus reaching a theoretical concentration of membrane components of ≈ 14 mg/mL. The higher concentration of DELOS-NV in the hydrogel could explain the longer release achieved. The proportion of Plx407 per water molecule is lower, hence the hydrogel is behaving as it was more concentrated, more cohesive and resistant to the dissolution.

In addition, it must be highlighted that during and after the *in vitro* degradation and release test, no precipitation was detected in the release media. The DELOS-NV can stabilize the highly hydrophobic bRo5.1 compound even after the release test. Importantly, the DELOS-NV act as a second release barrier which has not been assessed with the current release test. The bRo5.1-DELOS-NV, by extending the circulation time in the bloodstream, could contribute to extending the therapeutical effect of the administered compounds. In addition, the nanovesicles could protect the compounds, and the lipid bilayer that forms their membranes can be tailored to target specific organs, as it has been demonstrated before[13–16].

Hence, in present **Section 5.5**, it has been demonstrated the possibility to formulate the bRo5.1-DELOS-NV into a thermoreversible hydrogel for obtaining a potential subcutaneous depot. The stability of the nanovesicles within the hydrogel has been confirmed. And to conclude, the *in vitro* release test showed a zero-order kinetics release of the bRo5.1-DELOS-NV over a 10-hour period and demonstrated the feasibility of stabilizing the bRo5.1 compound in an aqueous release media by DELOS-NV composed of Chol and CPC.

5.6. Summary of the chapter and perspectives

In the present **Chapter** a case study has been shown in which a molecule with clinical interest has been formulated into the hybrid platform developed in **Chapter 4** based on Chol:CPC DELOS-NV and Plx407 hydrogel.

Fifth different challenging-to-formulate bRo5 compounds were proposed for the case study. All of them were highly hydrophobic compounds with poor drug-like properties. In a first preliminary test it was found that the bRo5.1 and bRo5.2 compounds could be successfully entrapped in the DELOS-NV with very high EE%. The formulations were diafiltrated and concentrated through TFF to eliminate the non-integrated bRo5 molecules and to increase the final concentration of bRo5 in the samples. Characterization of the formulations demonstrated the efficacy of the DELOS-NV in incorporating these payloads:

- The TFF technique permits to modulate the final concentration of bRo5 compounds in the formulations.
- The bRo5.1- and bRo5.2-DELOS-NV concentrated 2.4 times presented appropriate physicochemical attributes and were stable for at least 1 year stored in the fridge at 5 ± 3 ºC.

- Their observation by Cryo-TEM revealed morphological changes in the nanovesicles membranes. These changes might be caused by the interaction of the bRo5 compounds with the DELOS-NV. Moreover, no precipitates were detected in the images indicating nanostructuration of bRo5.1 compounds in water medium.
- Integrity of the formulations stored at 40 ± 3 °C for 30 days was demonstrated. Thus, the formulation can be administered subcutaneously without risk of degradation caused by the body temperature.
- The bRo5.1- and bRo5.2-DELOS-NV are highly reproducible by DELOS method and TFF.

Motivated by the promising initial results, in a second step, it was demonstrated the technical feasibility of scaling up the bRo5.1-DELOS-NV production from the small laboratory-scale reactor (V_{final} = 30 mL) to the intermediate laboratory-scale reactor (V_{final} = 250 mL). Demonstrating formulation scalability is crucial in drug development, as it is essential for a successful market transition. In addition, scaling up the production increased the volume of formulation obtained. The larger volume could then be further concentrated, allowing the target concentration of bRo5.1 in the formulation to be exceeded.

Finally, the bRo5.1-DELOS-NV were gelled with 17% w/w Plx407. The liquid formulation was converted into a thermoreversible hydrogel that behaved as a liquid at room temperature, being easily injectable, and became solid-like at 37 °C, forming a cohesive depot. The *in vitro* release test of the bRo5.1-DELOS-NV demonstrated an extended release for 10 h. The zero-order mathematical model fitted properly the release results as well as the hydrogel dissolution results. These results confirm the findings in **Chapter 4**: The DELOS-NV release is led by the hydrogel dissolution, and not by diffusion through the hydrogel pores, thus avoiding burst release that could be associated to side effects. In addition, the bRo5.1 compound did not precipitate in the release medium during and after the test. It has been demonstrated again that the DELOS-NV can stabilize highly hydrophobic compounds in aqueous environments.

The set of results highlights the potential of the hybrid system composed of DELOS-NV and a thermoreversible hydrogel for the subcutaneous extended administration of the highly hydrophobic bRo5.1 compound. The DELOS-NV can stabilize and increase the loading of the bRo5.1 compound in the thermoreversible Plx407. The Plx407 thermoreversible behavior permits the obtainment of a subcutaneous *in situ*-forming depot for extended release of the bRo5.1-DELOS-NV.

Hence, the formulation of the bRo5.1 compound within the thermoreversible subcutaneous depot developed in the previous **Chapter 4** has been a success. As a next step, outside the scope of this thesis, a release test using dialysis bags will be conducted to differentiate the bRo5.1 released as a free compound from the bRo5.1-DELOS-NV, since it was not evaluated with the membrane-less method employed. In addition, the *in vivo* release will be assessed with the contribution of Boehringer Ingelheim to further evaluate the potential of the system as a novel drug candidate. Furthermore, as mentioned in **Chapter 4**, different polymers that can modulate the release duration and kinetics will be studied beyond this thesis. Thus, the gelation of bRo5.1-DELOS-NV in these novel hydrogels and the *in vitro* release will also be investigated, especially with the objective of achieving longer-lasting depots.

5.7. References

1. C.A. Lipinski, F. Lombardo, B.W. Dominy, P.J. Feeney. Experimental and computational approaches to estimate solubility and permeability in drug discovery and development settings. *Adv. Drug Deliv. Rev.* **2001**, 46, 3–26.

2. M.D. Shultz. Two decades under the influence of the rule of five and the changing properties of approved oral drugs. *J. Med. Chem.* **2019**, 62, 1701–1714.

3. E. Valeur, S.M. Guéret, H. Adihou, et al. New modalities for challenging targets in drug discovery. *Angew. Chemie - Int. Ed.* **2017**, 56 (35), 10294–10323.

4. M.J. Blanco, K.M. Gardinier, M.N. Namchuk. Advancing new chemical modalities into clinical studies. *ACS Med. Chem. Lett.* **2022**, 13 (11), 1691–1698.

5. M.J. Blanco, K.M. Gardinier. New chemical modalities and strategic thinking in early drug discovery. *ACS Med. Chem. Lett.* **2020**, 11 (3), 228–231.

6. Leader B, Baca Q J, Golan D E. Protein therapeutics: a summary and pharmacological classification. *Nat. Rev. Drug Discov.* **2008**, 7 (1), 21–39.

7. B.C. Doak, B. Over, F. Giordanetto, J. Kihlberg. Oral druggable space beyond the rule of 5: Insights from drugs and clinical candidates. *Chem. Biol.* **2014**, 21 (9), 1115–1142.

8. M. Tyagi, F. Begnini, V. Poongavanam, B.C. Doak, J. Kihlberg. Drug syntheses beyond the rule of 5. *Chem. - A Eur. J.* **2020**, 26 (1), 49–88.

9. L. Ferrer-Tasies, E. Moreno-Calvo, M. Cano-Sarabia, et al. Quatsomes: Vesicles formed by self-assembly of sterols and quaternary ammonium surfactants. *Langmuir* **2013**, 29 (22), 6519–6528.

10. K.K. Short, S.K. Lathrop, C.J. Davison, et al. Using dual toll-like receptor agonism to drive Th1-biased response in a Squalene- and α-Tocopherol-containing emulsion for a more effective SARS-CoV-2 vaccine. *Pharmaceutics* **2022**, 14 (7), 1455.

11. S. Stolnik, B. Daudali, A. Arien, et al. The effect of surface coverage and conformation of poly(ethylene oxide) (PEO) chains of poloxamer 407 on the biological fate of model colloidal drug carriers. *Biochim. Biophys. Acta - Biomembr.* **2001**, 1514 (2), 261–279.

12. S. Nie, W.W. Hsiao, W. Pan, Z. Yang. Thermoreversible pluronic® F127-based hydrogel containing liposomes for the controlled delivery of paclitaxel: In vitro drug release, cell cytotoxicity, and uptake studies. *Int. J. Nanomedicine* **2011**, 6 (1), 151–166.

13. G. Vargas-Nadal, M. Muñoz-Ubeda, P. Alamo, et al. MKC-Quatsomes: a stable nanovesicle platform for bio-imaging and drug-delivery applications. *Nanomedicine Nanotechnology, Biol. Med.* **2020**, 24, 102136.

14. L. Ferrer-Tasies, H. Santana, I. Cabrera-Puig, et al. Recombinant human epidermal growth factor/quatsome nanoconjugates: a robust topical delivery system for complex wound healing. *Adv. Ther.* **2021**, 4 (6), 2000260.

15. A. Boloix, N. Feiner-Gracia, M. Köber, et al. Engineering pH-sensitive stable nanovesicles for delivery of microrna therapeutics. *Small* **2022**, 18 (3), 2101959.

16. J. Tomsen-Melero, S. Passemard, N. García-Aranda, et al. Impact of chemical composition on the nanostructure and biological activity of α-galactosidase-loaded nanovesicles for Fabry disease treatment. *ACS Appl. Mater. Interfaces* **2021**, 13 (7), 7825–7838.

6

6 DELOS-NV as theragnostic carriers for the oral administration route

6.1. Introduction

In previous **Chapters** of this thesis, the focus was set on formulating and evaluating the feasibility of DELOS-NV for subcutaneous administration. As mentioned in the **Introduction**, it is the preferred option between the parenteral administration routes, and therefore, a convenient approximation for drugs with low oral bioavailability.

However, the oral administration route is still the most attractive for patients, mainly because it is the simplest and most familiar.

The oral route can be employed for systemic treatments, however, the bioavailability of orally administered hydrophobic molecules and biologics is a major drawback of this route. Typically, less than 10 percent of an orally administered biological compound is systemically available[1].

In addition, the oral route is especially favorable when the therapeutic target is in the gastrointestinal tract[2]. As mentioned in the **Introduction**, the prevalence of gastrointestinal diseases and cancers is increasing in Europe[3] and the US[4], highlighting a growing medical need for effective local treatments in the gastrointestinal tract. Unfortunately, the harsh conditions within the gastrointestinal tract can degrade labile molecules, reducing the efficacy of administered drugs.

Given these challenges, exploring the potential of DELOS-NV for oral administration is a highly compelling area of research.

6.1.1. The physiological barriers of the gastrointestinal tract

The gastrointestinal tract is specifically designed to break down large molecules into small molecules that are easily absorbable[5]. This plays a major role in humans' nutrition, but also in humans' immune protection, thus making it difficult for pathogens to enter through the mouth.

Biologics are large molecules that depend on their structure to engage with pharmaceutical targets. Thus, it is expected that their bioavailability is low after oral administration.

Several biological barriers must be overcome to reach the intestinal epithelium. These barriers play their role in different environments of the gastrointestinal tract (**Figure 6.1**)[6].

The lumen is the internal cavity of the gastrointestinal tract. In the lumen, we find a pH gradient, with the hardest conditions in the stomach (pH 1.5-2.2). This low pH can denaturalize the biologics, lowering their bioavailability. In addition, in the lumen, there are gastric enzymes such as peptidases and pancreatic enzymes such as trypsin. These enzymes can also decompose the biologics. DELOS-NV can protect the entrapped molecules from enzymes, as it has been demonstrated previously with nucleases[7,8], however, the strong acidic pH in the stomach could affect their integrity. A way to protect them from the acidic pH is to further integrate the nanovesicles in a pH-responsible hydrogel that can be swallowed at neutral pH but precipitates at the low pH found in the stomach, protecting the nanovesicles[9–12]. Arnau Güell, researcher at Nanomol Technologies S.L., demonstrated *in vitro* the possibility of using the pH-responsible Eudragit to protect the nanovesicles from very acidic pH and the promising results obtained were published in his master's thesis "DELOS nanovesicles as novel pharmaceutical candidates for oral delivery" in 2021.

Apart from the barriers in the lumen, there is the mucus barrier, located in the interface between the lumen and the gastrointestinal epithelium. The mucus is mostly composed of water and mucin protein molecules coated with proteoglycans, giving the mucus a negative charge. It is formed by an outer layer loosely adherent that promotes clearance of the molecules that get captured, and an inner layer, in contact with the epithelium, that contributes to the absorption/uptake of molecules[13]. Therefore, it has a dual behavior in drug absorption. Drug delivery systems can be modulated to enhance their mucopenetrating and mucoadhesive properties[14–16].

When these barriers are overcome, the drugs can finally get in contact with the gastrointestinal epithelium. This tissue acts as a mechanical barrier against the entrance of pathogens into the organism. Systemic drugs must surpass this barrier to reach the blood vessels and/or lymph vessels to exert their systemic function. Oppositely, locally acting gastrointestinal drugs should present very low permeation rates through the gastrointestinal tract to enhance their local effect and avoid systemic side effects. Examples of local drugs are mesalamine and its prodrugs, employed for the treatment of inflammatory bowel disease (IBD)[17], some locally-acting steroids (e.g., budenosine), also employed for IBD treatment[18]; locally-acting antibiotics (e.g., vancomycin) and agents that modify gastrointestinal motility (e.g., loperamide)[19].

Regarding systemic drugs, there are two different pathways to cross the epithelium and reach the systemic circulation: The transcellular pathway, which involves entering the cells, and the paracellular pathway, which involves crossing in between cells (**Figure 6.1**). Typically, only small hydrophilic drugs can cross in between cells due to the presence of tight junctions. Therefore, large biomolecules, hydrophobic molecules, and nanovesicles are more prone to cross through transcellular routes. However, in the case of nanovesicles, the high polar density of hydrophilic head groups on their surface could make it difficult to pass through the cell's bilayer[5,6].

Due to the lack of information on the permeability of DELOS-NV through the intestinal epithelium, this **Chapter** focuses on characterizing this phenomenon. Understanding the behavior of DELOS-NV in contact with the gastrointestinal epithelium will help identify the most suitable diseases to target.

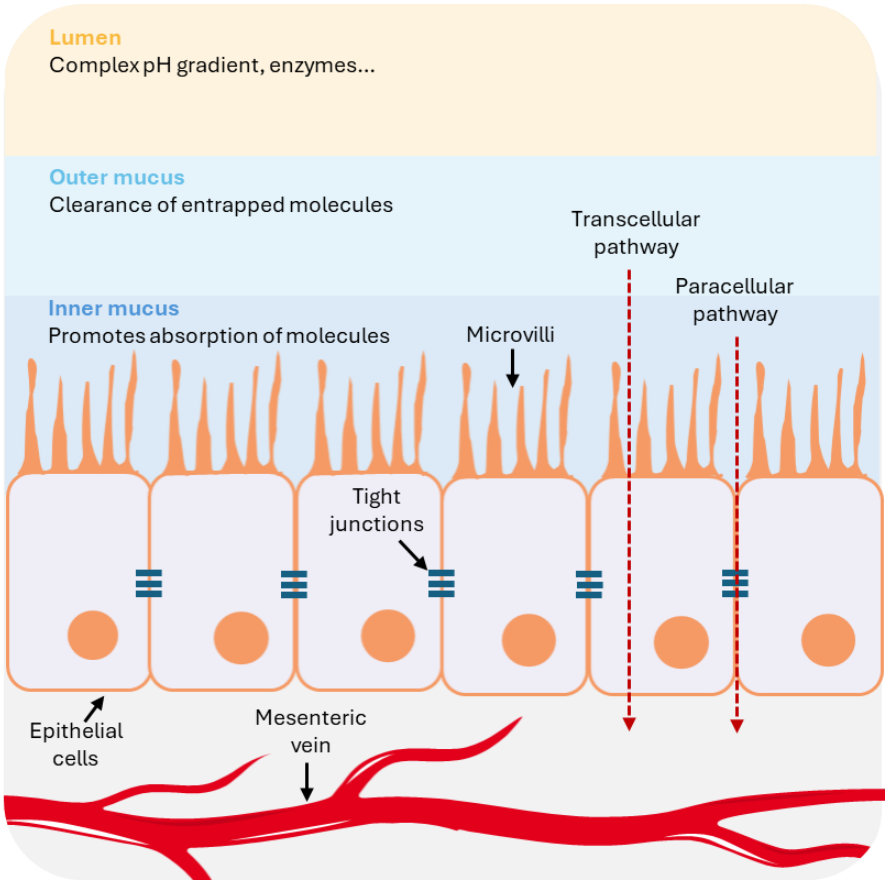


Figure 6.1. *Schematic representation of the gastrointestinal barriers, and the permeation pathways of systemic drugs.*

6.1.2. Gastrointestinal models for drug permeation evaluation

Many gastrointestinal models can be employed to investigate the intestinal permeability, the transport mechanisms and even the plasma pharmacokinetic profile throughout the drug discovery/development process.

Those preclinical models can be classified into different groups and are often applied in the following order: *in silico*, *in vitro*, *in situ* and, most importantly, *in vivo*[20].

In silico models are those conducted by means of computer modeling or simulation. They can confer prediction of gastrointestinal absorption. However, they require experimental *in vitro* and *in vivo* data to increase their accuracy[21].

In vitro, in situ and *in vivo* models are experimental models. *In vivo* models are performed on live organisms and are the most clinically relevant. These models take into account physiological factors

such as gastric emptying time, luminal water content, drug degradation, and post-absorption first-pass metabolism, which can all affect the predicted outcome. However, *in vivo* models do not always indicate how each physiological factor affects the final bioavailability of the drug[20].

In situ models, in contrast, are appropriate to unravel the mechanisms underlying intestinal drug absorption. *In situ* perfusion models in rodents consists of cannulating an anesthetized animal and perfusing a segment of its intestine with a solution containing a defined concentration of drug. In the simplest setup, comparing the concentration of the donor solution and the solution that exits from the isolated segment allows the calculation of the drug that has permeated the intestine. However, the calculated concentration of the drug does not necessarily give a reliable prediction of the amount of drug that reaches the systemic circulation. To solve this limitation, more complex setups include mesenteric blood samplings or even mesenteric veins cannulation[22]. Although these models are particularly informative, their setup is complex and time-consuming. Moreover, they still require the usage of animals, which can present ethical concerns. For these reasons, these models are typically utilized after *in vitro* experiments[20,22].

In vitro models are the simplest of the experimental models and are the most employed in the drug discovery phase. Most *in vitro* models are cell-based. However, there are also synthetic models such as the Parallel Artificial Membrane Permeability Assay (PAMPA) and the Phospholipid Vesicle-based Permeation Assay (PVPA). These synthetic permeation systems reproduce *in vitro* the phospholipid composition of the desired human biological barrier. Despite their potency and elevated biomimetism acquired over the years, they still do not express significant morphological and physiological features of epithelial cells, such as active transport proteins[23]. In that sense, *ex-vivo* models of an intestinal tissue sample mounted in a diffusion chamber, and even cell-based models, can reproduce better *in vivo* conditions.

Regarding *in vitro* models, cell-based models are the most widely employed models. There are several cell lines and growing supports that can be employed for the obtainment of 2D and even 3D models of the gastrointestinal epithelium[23]. The most common models include monolayers of cells grown on permeable filter supports[20].

There are endless possibilities of gastrointestinal models, however, there is a clear gold-standard in the field accepted by the regulatory agencies[24,25]. This is the Caco-2 cells monolayer model.

6.1.3. In vitro Caco-2 cell model

Caco-2 cells used in this model come from a human colon adenocarcinoma[23,26]. When they are grown in permeable supports (called transwells) and reach confluence, they differentiate spontaneously into a mature epithelium. The differentiation process takes around 3 weeks, and the cells have a useful window to carry on the permeation assays of 3 to 5 days[26,27]. These cells were first established in the late 1980s, and they are very well characterized, which improves their usefulness[26,28]. They present numerous advantages over other systems. The apical and basal sides of the epithelium are exposed allowing the study of excretion or efflux of drugs. In addition, they require low volumes of sample, thus being a cost-effective approach in screening stages. However, it must be noted that they also present some limitations. For compounds that permeate cells

passively, the permeability results correlate with the absorption *in vivo*. However, for compounds transported through a carrier-mediated mechanism, the obtained permeability is typically lower than it would be. This could be caused by the different profile of transporter proteins present in Caco-2 cells in comparison to the human gastrointestinal cells. In addition, these cells do not present mucus, which as mentioned in the previous section, is an important component of the gastrointestinal tract that can greatly influence the absorption of drugs[23,26].

It is important to note that Caco-2 cell model is the intestinal permeation model most used by pharmaceutical industries and academic laboratories[23,26], and one of the few models recognized by the FDA and the European Medicines Agency (EMA)[24,25]. For these reasons, this cell monolayer model was used to assess the permeability of a prototype molecule loaded into DELOS-NV. In this way, it will be possible to determine whether the Chol:CPC DELOS-NV are better suited for the delivery of local or systemic drugs.

To test the permeation through the intestinal epithelium, a novel nanoconjugate based on DELOS-NV loading the Fluorescein Isothiocyanate – Bovine Serum Albumin (FITC-BSA) protein was prepared by a DoE. This protein has been employed previously in the literature as a model molecule for permeation assays in Caco-2 models[29–31]. Afterward, the thermodynamics of the binding between the protein and the DELOS-NV were assessed. This permitted us to deeply characterize the system and to better understand the possible interactions in the integration of the protein in the nanovesicles. Finally, intestinal permeation was evaluated employing the well-designed and characterized nanoconjugate and the Caco-2 intestinal model (**Figure 6.2**).

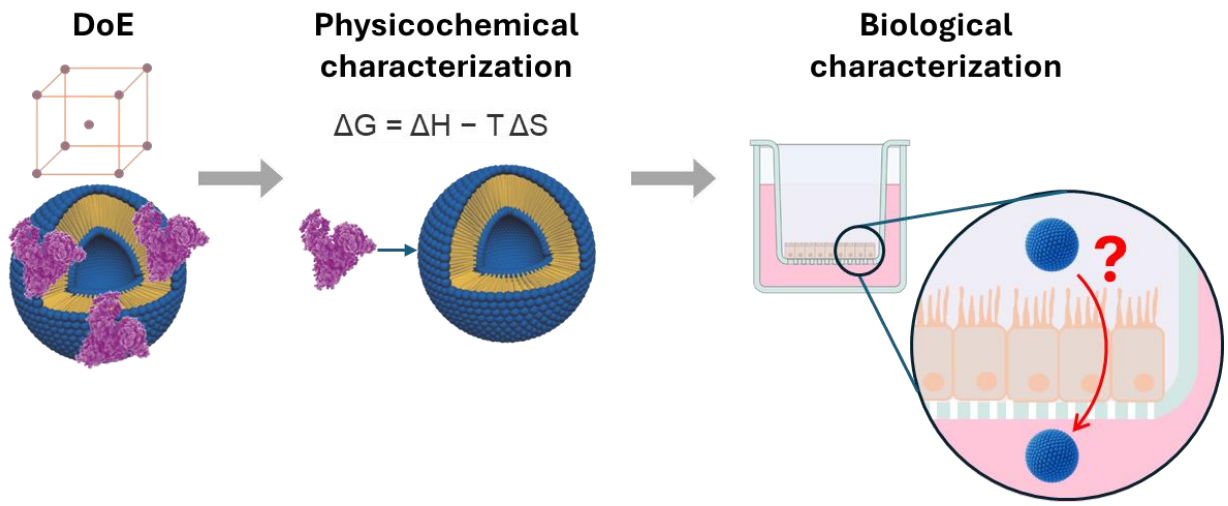


Figure 6.2. *Steps followed for the final characterization of the permeability of DELOS-NV nanoconjugates through the Caco-2 cell intestinal epithelium model.*

6.2. Obtainment of the optimum nanoconjugate prototype of DELOS-NV loaded with FITC-BSA using DoE

Chol:CPC DELOS-NV in histidine 5 mM pH 7 buffer have demonstrated potential as a regulatory-oriented drug delivery system for the subcutaneous administration route (see **Chapter 3**). In the present section, it was decided to continue using the FDA-recognized CPC and Chol excipients for the oral administration route, with the objective of developing a drug delivery system composed exclusively of excipients listed in the FDA IID[32].

As previously mentioned, the objective of this **Chapter** is to determine whether DELOS-NV increase permeation through the intestinal epithelium. This will help define whether they are more appropriate for local or systemic theragnostic applications. Therefore, experiments in Caco-2 cells were conducted. Permeation experiments in Caco-2 cells are typically carried out in Hank's balanced salt solution (HBSS) buffer at pH 7.4[27]. For this reason, in this work, the nanovesicles were produced in the same buffer to avoid changes in the medium that could affect the physicochemical properties of the samples.

In addition, a model biomolecule was entrapped in the DELOS-NV, to follow its permeation through the Caco-2 cells. The Fluorescein Isothiocyanate – Bovine Serum Albumin (FITC-BSA) was selected as a model biomolecule. BSA is a 66 kDa protein present in large quantities in serum, which in this specific case is labeled with the FITC fluorophore through covalent bonds with the isothiocyanate reactive groups (**Figure 6.3**). The labeling will facilitate the easy detection of the model molecule in the permeation assays in Caco-2 cells. According to the manufacturer, there are 7 to 12 moles of FITC per mole of BSA. The BSA protein has an isoelectric point (pI) of 4.7, meaning that in HBSS pH 7.4 it will be charged negatively[33]. Since DELOS-NV have a positive net charge due to the presence of a quaternary ammonium surfactant, it is expected that at pH 7.4 the FITC-BSA binds the nanovesicles' surface through electrostatic interaction. In addition, FITC is also negatively charged at pH 7.4[34] contributing to the electrostatic binding with the nanovesicles.

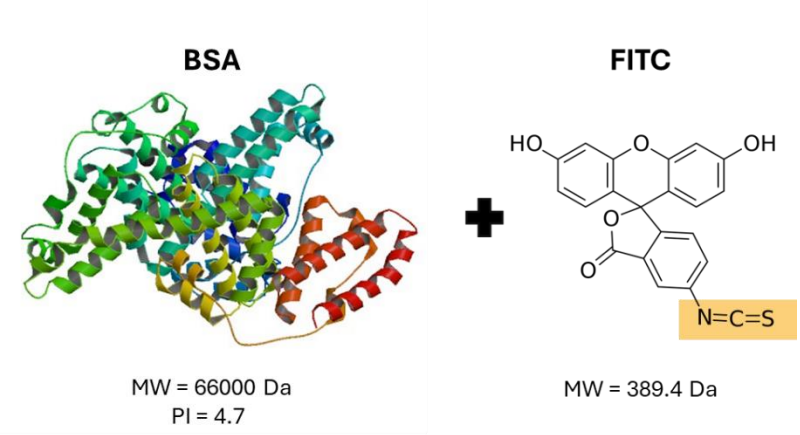


Figure 6.3. *Bovine serum albumin (BSA) and Fluorescein Isothiocyanate (FITC). The isothiocyanate group (highlighted in yellow) covalently binds the BSA lysins. (PI = Isoelectric point; MW = Molecular weight)*

First of all, a new DoE was carried out to test how different formulation factors affect the physicochemical attributes of nanoconjugates based on Chol:CPC DELOS-NV and the biomolecule

FITC-BSA in HBSS buffer. With this intention, a full-factorial two-level model was conducted (**Figure 6.4**). The independent variables considered in the DoE were the molar ratio between membrane components, the concentration of membrane components and the concentration of FITC-BSA (**Table 6.1**). The dependent variables, or responses evaluated in the DoE, were the selected CQA of the nanovesicles which were already defined in **Section 3.2** from **Chapter 3**, and were the hydrodynamic diameter, the size PdI and the apparent Z-potential (**Table 6.2**). It must be noted that for this specific case, the size PdI maximum limit considered was 0.5. As mentioned in **Chapter 3**, this limit is common in lipidic colloidal formulations. With blank DELOS-NV (DELOS-NV without cargoes), this limit could be reduced to 0.4, however, when integrating proteins, it is common to have larger PdI values. This might be caused by the interaction of the protein with the nanovesicles surface, which causes certain variability reducing the homogeneity in terms of size.

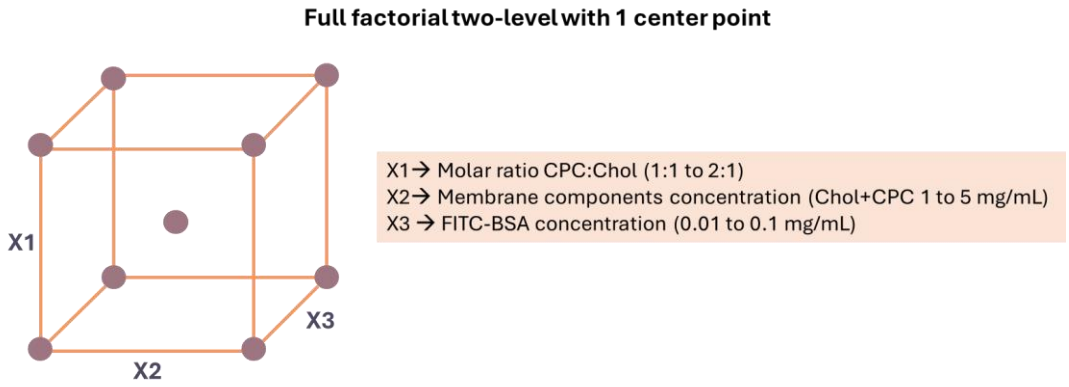


Figure 6.4. *Schematic representation of the full factorial two-level model with one center point employed in the DoE.*

Table 6.1. *Full factorial two-level model employed in the DoE, providing the lower (-1) and upper (+1) level values for each factor (independent variables).*

Factors (Independent variables)	*Type*	*Levels*	
		Lower level (-1)	*Higher level (+1)*
FITC-BSA	*Numeric*	*0.01*	*0.1*
Concentration of membrane components (Chol + CPC) (mg/mL)	*Numeric*	*1*	*5*
CPC:Chol molar ratio	*Numeric*	*1:1*	*2:1*

Table 6.2. *The CQA of DELOS-NV introduced in the DoE as response variables, and the established specifications.*

Critical quality attributes (CQA)	*Criterium*	*Lower limit*	*Higher limit*
Mean hydrodynamic diameter	*Minimize*	*20 nm*	*220 nm*
Size polydispersity Index (PdI)	*Minimize*	*0.01*	*0.5*
Apparent zeta potential (Z-potential)	*Maximize*	*±30 mV*	*±150 mV*

As it can be observed in the schematic representation of the model in **Figure 6.4**, there are several combinations of factors that must be evaluated in the full factorial two-level with one center point model. A frequently utilized approach to streamline the number of runs needed in a DoE, while still maintaining significant reproducibility, involves conducting replicates solely at the center point. Hence, this approach was employed due to the large number of factor combinations possible. Considering the different combinations of factors and the replicates at the center point, 10 experimental runs were required.

On the other hand, when working with proteins some considerations must be taken into account. Proteins are typically labile, thus meaning that the environment can affect their structure. The BSA folding is affected by the pH[33], therefore, controlling the pH of the media can confer more robust results. In addition, FITC bleaches quickly at a pH below 7. Therefore, working in HBSS at pH 7.4 can avoid bleaching. Regarding the pH, it must be noted that, during the DELOS method, the CO_2 works as a co-solvent in the reactor. In the final step of the DELOS process, the CO_2 is evaporated by pressure changes. However, part of it can be mixed with the aqueous media and converted into carbonic acid, lowering the pH of the colloidal suspension which is typically around 6 right after DELOS despite working in buffers at pH 7-8. DELOS-NV formulations recover their initial pH with time, when all the CO_2 evaporates. However, it takes a few days. For this reason, it was decided to exchange the media of the colloidal suspensions right after the DELOS method by TFF. In that way the recovery of the pH was much quicklier contributing to preserving the fluorescence of the FITC. In addition, the TFF serves to eliminate the non-integrated FITC-BSA, allowing for the calculation of the EE%.

Hence, the samples employed for the DoE analysis were produced by the DELOS method in HBSS buffer (see **Section 9.2.1** for details) and diafiltrated by TFF with a 300 kDa MW cut-off hollow fiber column (see **Section 9.2.2**). The HBSS buffer employed in the DELOS and the TFF was prepared as described in **Section 9.1**. Controls of the pH were done as described in **Section 9.3.2**. The pH right after DELOS was around 6 in all samples, while the pH after the TFF was restored to ≈ 7.4.

In addition, the non-integrated FITC-BSA was removed through the TFF process. The EE% was calculated from a reference sample by measuring the UV-Vis spectra before and after the TFF process, yielding an approximate value of 100%, as shown in **Figure 6.5A**. Furthermore, since FITC-

BSA gives the medium an orange color, and no orange color was observed in the permeate, it can be inferred that no protein was lost during the TFF.

As a control, a free 0.1 mg/mL FITC-BSA solution (without DELOS-NV), solubilized in the same medium as the Chol:CPC DELOS-NV containing FITC-BSA (HBSS with 10% ethanol), was diafiltrated using the same hollow fiber column. In this control, all the protein was eliminated through the TFF column into the permeate, turning the permeate orange while the initial 0.1 mg/mL FITC-BSA solution became transparent (**Figure 6.5B**). This result demonstrates that the EE% of FITC-BSA in the Chol:CPC DELOS-NV was reliable, as the FITC-BSA was retained in the sample during TFF due to its interaction with the Chol:CPC DELOS-NV. Otherwise, it would have been removed, as occurred with the free FITC-BSA.

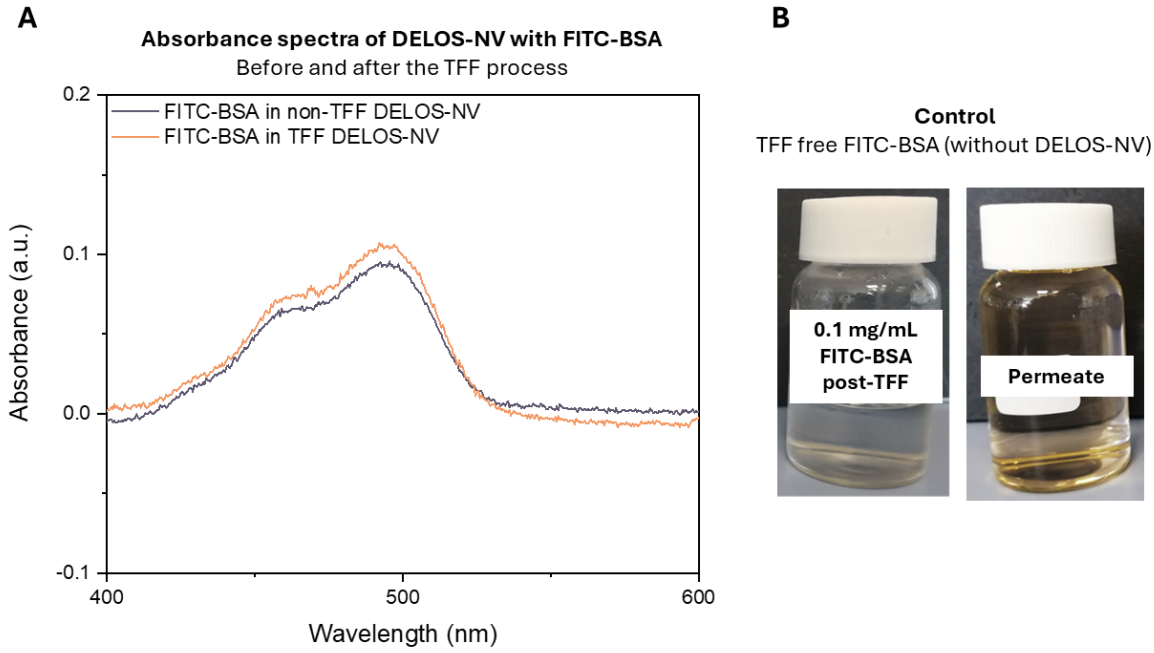


Figure 6.5. A) Ultraviolet-visible (UV-Vis) absorbance spectrum of a reference sample of DELOS-NV entrapping 0.1 mg/mL FITC-BSA, before and after the TFF process. B) Macroscopical images of a control solution of free 0.1 mg/mL FITC-BSA in HBSS + 10% ethanol diafiltrated by TFF. It can be observed that the initial 0.1 mg/mL FITC-BSA solution became transparent after the TFF, while the permeate became orange.

The samples were named as BSA-Chol:CPC DELOS-NV, followed by a sequential number corresponding to the production run order. **Figure 6.6** shows the 10 samples prepared and diafiltrated by TFF for the DoE, with their identifying production run order number, and showing the combinations of factors evaluated in each sample. All the prepared samples were protected with foil and stored in the fridge at 5 ± 3 °C.

Figure 6.6 also shows macroscopical images at time 0. As shown, in all cases homogeneous samples with an orange tonality are obtained. As expected, samples with higher concentrations of FITC-BSA are more colored. It is important to note that the macroscopical images were not considered as a response in the DoE due to their qualitative nature.

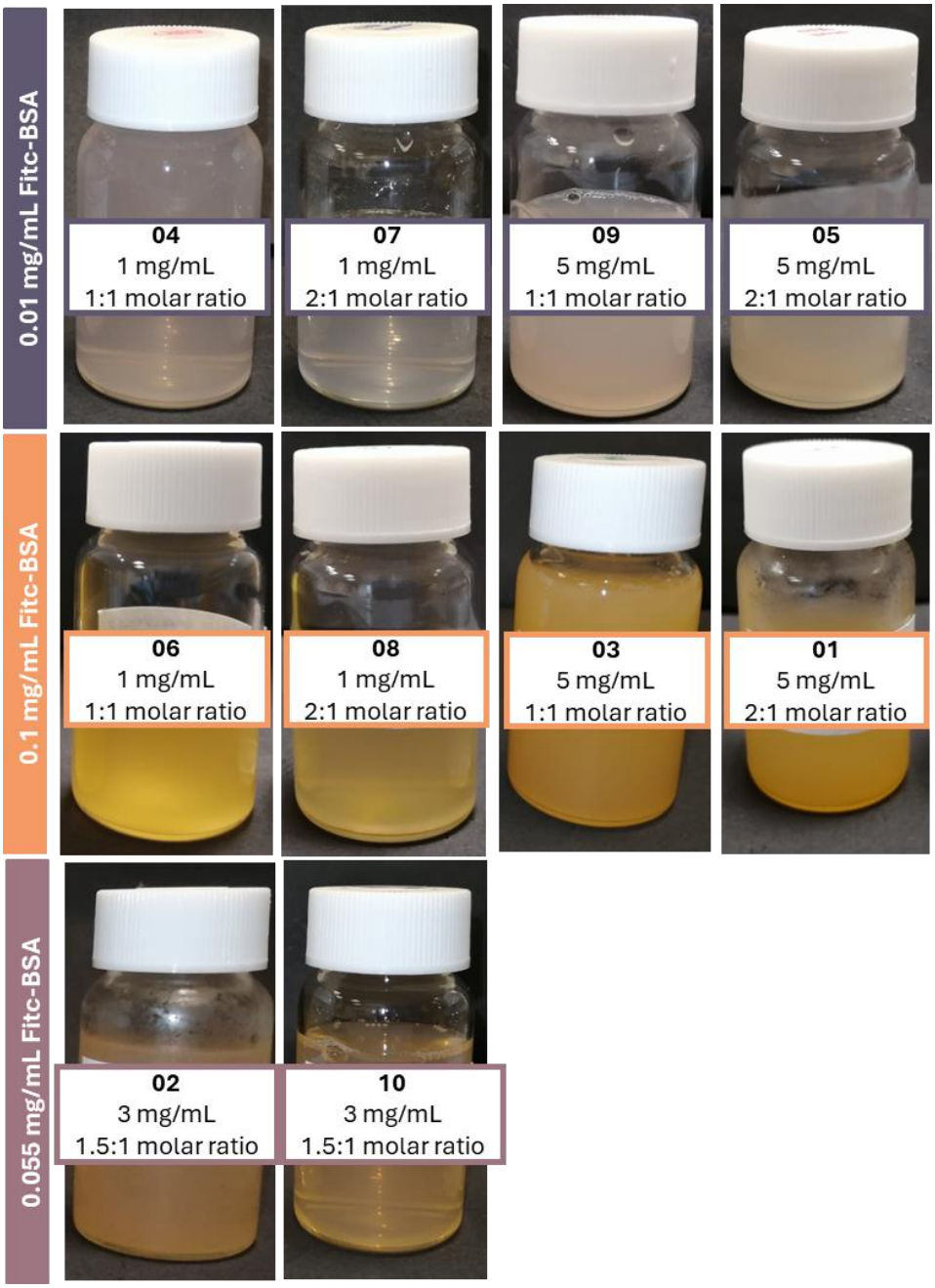


Figure 6.6. *Macroscopical images at time 0 of the different BSA-Chol:CPC DELOS nanovesicles (DELOS-NV) produced for the design of experiments (DoE) in HBSS pH 7.4. The mg/mL refers to the total membrane components concentration and the molar ratio between membrane components is expressed as CPC:Chol. The run number considers the order of performance of the experiments.*

The formulations' CQA (**Table 6.2**) were measured periodically to evaluate their stability. The results of these periodical measurements over two months are shown in **Figure 6.7**.

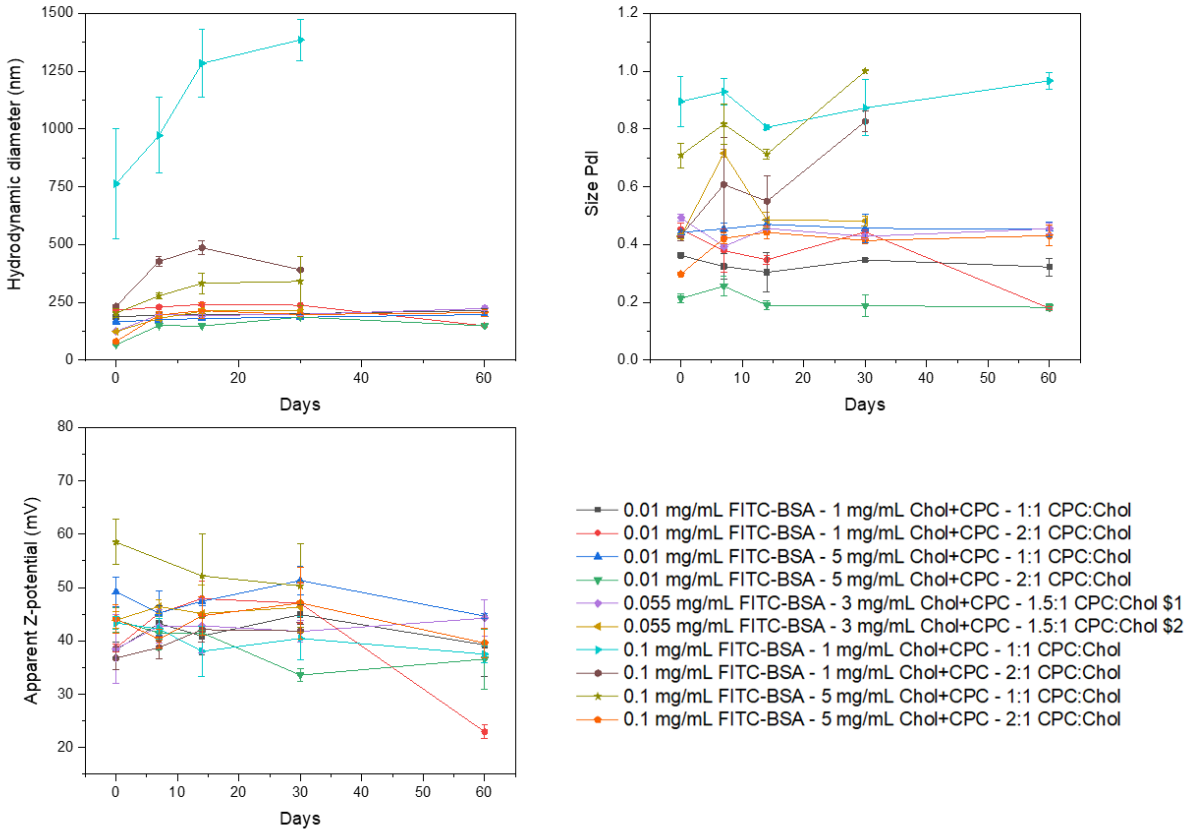


Figure 6.7. Two-month evolution of the selected CQA (mean hydrodynamic diameter, size PdI, and apparent Z-potential) of the investigated formulations of BSA-Chol:CPC DELOS-NV in HBSS pH 7.4, produced in the DoE. The results correspond to the average and SD of three consecutive measurements of one experimental run.

Figure 6.7 illustrates that most formulations achieve stability within 14 days following production and diafiltration via TFF. Moreover, it reveals that those formulations that attain stability after this two-week period are consistently stable for at least 2 months. However, certain combinations of factors containing 0.1 mg/mL of FITC-BSA led to formulations that significantly exceeded the specifications for the CQA (**Table 6.2**) and did not reach stabilization at 14 days. Due to this fact, the stability of these formulations was followed for only 30 days.

Based on the presented results, having confirmed that 14 days are enough to let the stable formulations maturate, the CQA at this time point were employed for the DoE analysis. The results of the CQA at 14 days are shown in **Table 6.3**. This table shows notably high hydrodynamic diameter and size PdI values for the samples with 0.1 mg/mL FITC-BSA. Coupled with the instabilities observed in **Figure 6.7** for these same samples, it can be concluded that samples with 0.1 mg/mL FITC-BSA tend to aggregate and precipitate.

Table 6.3. *Matrix of the two-level full factorial design for the BSA-Chol:CPC DELOS-NV (independent variables: FITC-BSA concentration, CPC:Chol molar ratio and nanovesicles membrane components concentration (Chol+CPC, mg/mL); dependent variables at t = 14 days: hydrodynamic diameter, size PdI and apparent Z-potential (mean ± SD of 3 consecutive measurements of one experimental run). The run number considers the randomized order of performance of the experiments.*

Random. Run	FITC-BSA concentration (mg/mL)	Membrane components concentration (mg/mL)	CPC: Chol Molar ratio	Hydrodynamic diameter (nm)	Size PdI	Apparent Z-potential (mV)
4	0.01	1	1:1	196 ± 4	0.30 ± 0.07	41 ± 4
7	0.01	1	2:1	241 ± 6	0.348 ± 0.016	48 ± 3
9	0.01	5	1:1	180.4 ± 1.2	0.470 ± 0.016	47.4 ± 0.9
5	0.01	5	2:1	147.6 ± 0.9	0.190 ± 0.016	41.5 ± 0.5
2	0.055	3	1.5:1	194 ± 4	0.456 ± 0.007	43 ± 5
10	0.055	3	1.5:1	210 ± 10	0.49 ± 0.03	45 ± 5
6	0.1	1	1:1	1300 ± 100	0.806 ± 0.009	38 ± 5
8	0.1	1	2:1	490 ± 30	0.55 ± 0.09	42 ± 2.3
3	0.1	5	1:1	330 ± 40	0.713 ± 0.017	52 ± 8
1	0.1	5	2:1	210 ± 30	0.443 ± 0.021	45 ± 4

To statistically analyze the data presented in **Table 6.3**, it was adjusted to an MLR model with the Modde software as described in **Section 9.5.** The goodness of the fitting was assessed with the R2 and Q2 values, which for the hydrodynamic diameter were 0.69 and 0.31, for the size PdI 0.84 and 0.63 and for the apparent Z-potential 0.23 and -0.2, respectively. As mentioned in **Chapter 3**, R2 shows the model fit, and it should be above 0.5 to have enough significance, and Q2 estimates the future predictions' precision. Q2 should be above 0.1 for a significant model, and ideally, above 0.5 for a good model predictability. In this specific case, the Z-potential presented very low R2 and Q2 values, thus indicating that the model fit and predictive capacity for this response are low. **Table 6.3** shows that all the Z-potential values are very similar between samples (all are around 40 mV) making it difficult to fit the model. Since the Z-potential fitting was not reliable, this response was excluded from the statistical analysis. The other two responses were included in the analysis. The size PdI presents high R2 and Q2 values demonstrating the appropriate adjustment of the model. The hydrodynamic diameter R2 value is above 0.5, however, the Q2 value is below 0.5. Having a Q2 value between 0.1 and 0.5 indicates that the software has identified some significative trends, however, it is not able to predict with confidence the results of novel batches based on these results. This is probably because the fitting is extremely influenced by the hydrodynamic diameter results obtained for runs 6 and 8, which were identified as out of tendency by the Modde software according to

Turkey's test. These results considered out of tendency were not eliminated from the fitting because they are very informative since they indicate that the nanovesicles are larger in hydrodynamic diameter when working with higher concentrations of FITC-BSA. However, the hydrodynamic diameter obtained for these runs is not reliable and probably is influenced by the presence of aggregates/precipitation.

Below, **Figure 6.8** shows the coefficients of the regression equation plot (represented as green columns). A positive coefficient indicates that as the value of the factor (independent variable) increases, the mean of the dependent response also increases. A negative coefficient suggests the opposite behavior. The statistical significance of each coefficient is indicated by the black interval. If the interval falls within the columns, the coefficient is considered statistically significant; otherwise, it is not. In this specific case, it can be observed that all factors were statistically significant.

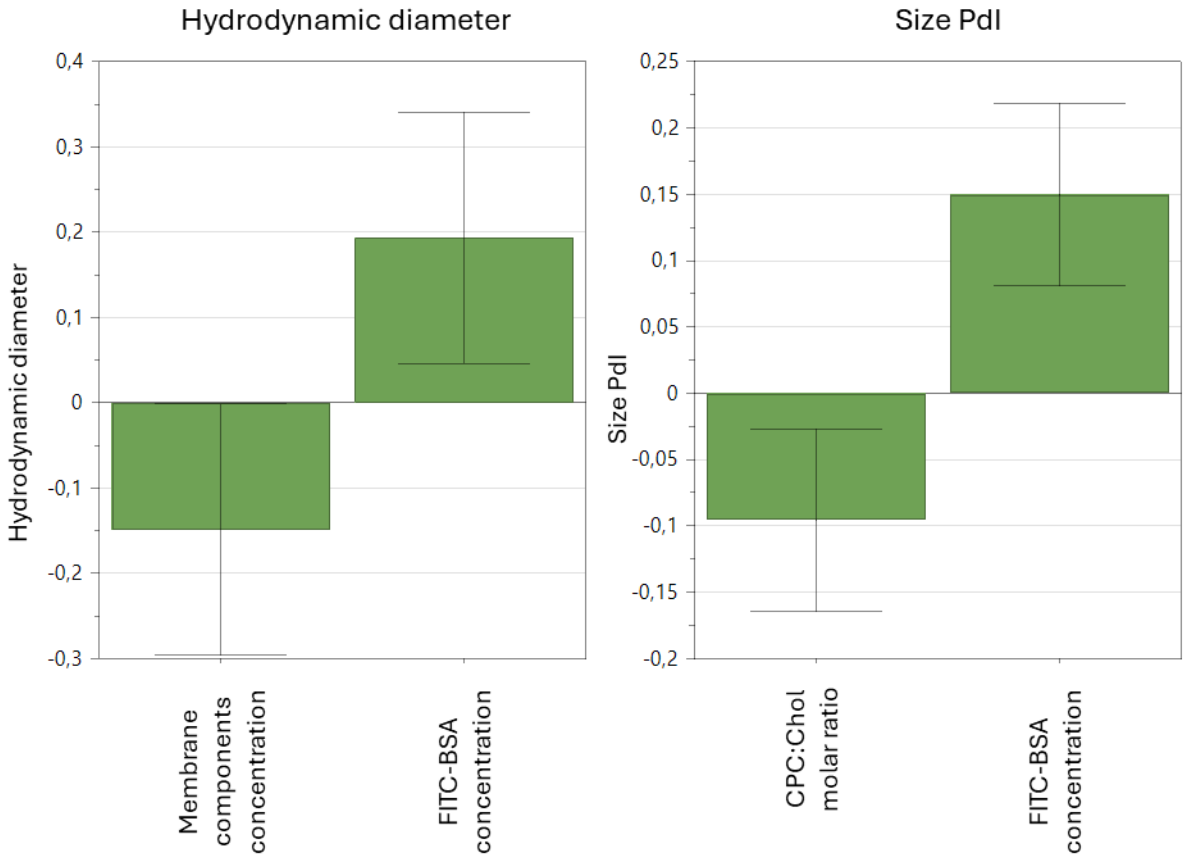


Figure 6.8. *Scaled and centered coefficients of the regression equations describing the influence of formulation parameters (molar ratio CPC:Chol and FITC-BSA concentration), on the nanoconjugates mean hydrodynamic diameter and size PdI.*

From **Figure 6.8**, it can be concluded that the factor with the strongest effect in the hydrodynamic diameter and the size PdI is the concentration of FITC-BSA. At higher concentrations of protein, the hydrodynamic diameter and size PdI increase. The membrane components concentration has a significative and opposite impact on the hydrodynamic diameter. When the concentration of membrane components increases, the hydrodynamic diameter decreases. However, it does not

affect significantly the size PdI, and for this reason, it is not represented in the PdI coefficient plot. In contrast, the CPC:Chol molar ratio has a significant impact on the size PdI but not on the hydrodynamic diameter. When the ratio increases, the size PdI decreases. Factors and their interactions not shown in the coefficient plot did not present a significative effect on the responses and were excluded from the model.

Figure 6.9 shows each predicted response for the CQA as a function of the combination of the different factors studied. The black dotted line indicates the established limit for each CQA as specified in **Table 6.2**.

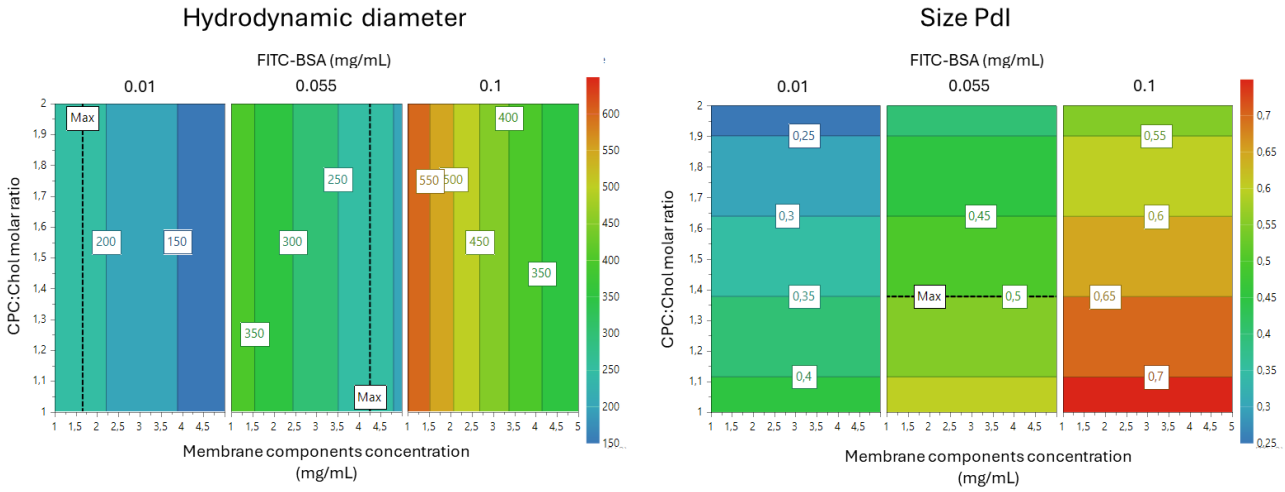


Figure 6.9. Contour plots for the hydrodynamic diameter (left) and size PdI (right) of the different BSA-Chol:CPC DELOS nanovesicles (DELOS-NV) produced for the design of experiments (DoE) in HBSS pH 7.4.

The design space of the BSA-Chol:CPC DELOS-NV formulations in HBSS was also determined, considering only those responses that ensured enough predictive capacity. The limits defined for the hydrodynamic diameter and size PdI were shown in **Table 6.2**. Considering those limits, the design space shown in **Figure 6.10** was obtained. The color scale in this design space was adjusted from those used in **Chapter 3** to avoid the entire space appearing red, which would have obscured the trends. However, the information provided remains unchanged; it still reflects the probability of obtaining nanoconjugates within the defined CQA limits based on the different factors studied. As mentioned, it is evident that the protein concentration significantly impacts the responses. Increasing the concentration of FITC-BSA reduces the probability of obtaining nanoconjugates with the CQA defined in **Table 6.2**. Also, the design space suggests that working at higher concentrations of nanovesicle membrane components increases the probability of obtaining nanoconjugates with the CQA desired. It can be observed that a certain degree of risk must be assumed in all cases if when producing BSA-Chol:CPC DELOS-NV within the ranges evaluated in the present study. The risk is lower if working at a concentration of FITC-BSA of 0.01 mg/ml.

It is important to remark that this design space should be considered as a reference because it is significantly influenced by the high hydrodynamic diameter values obtained in runs 6 and 8 (**Table 6.3**). If these two results had been excluded from the fitting due to being outliers, the predicted design space would likely have been different, showing increased probabilities of obtaining BSA-Chol:CPC DELOS-NV within the defined CQA limits.

Considering all the results shown so far, BSA-Chol:CPC DELOS-NV in HBSS with 0.01 mg/mL FITC-BSA will be produced for the permeation assays. Working at this low protein concentration increases the likelihood of meeting the CQA specifications. The production of the batches and the permeation assays will be explained in more detail in **Section 6.4**. Before conducting the permeation assays, a thermodynamic characterization of the interaction between FITC-BSA and the nanovesicles will be performed. This study is crucial for gaining deeper insights into the physicochemical properties of this prototype.

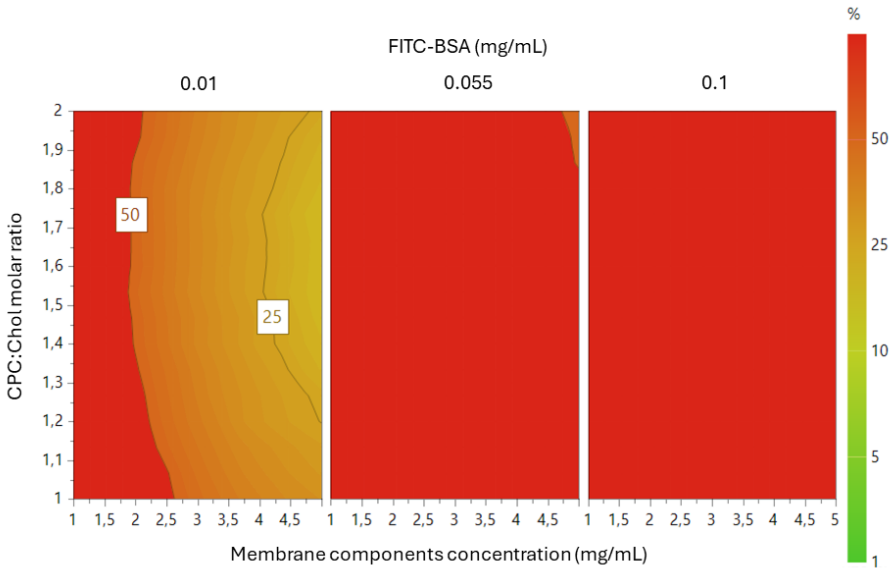


Figure 6.10. *Design space for the BSA-Chol:CPC DELOS nanovesicles in HBSS according to the CPC:Chol molar ratio, the membrane components concentration (mg/mL), and the FITC-BSA concentration (mg/mL), expressed as the probability of failure (%). CQA limits defined: hydrodynamic diameter 20 to 220 nm and size PdI 0.01 to 0.5. This design space must be considered as a reference because it is significantly influenced by outliers.*

6.3. Physicochemical characterization of nanoconjugates based on FITC-BSA integrated in DELOS-NV. Binding thermodynamics by isothermal titration microcalorimetry (ITC)

Understanding the thermodynamics underlying the binding interaction between a drug and its nanocarrier yields invaluable insights crucial for drug development. It enables the determination of binding mechanisms (e.g., electrostatic, hydrophobic), thereby facilitating predictions of binding stability across various media. Moreover, it provides the ability to anticipate drug efficacy by comparing the affinity of the drug and the nanocarrier with that of the drug and its pharmacological receptor -if the affinity is higher for the receptor, the protein can release the nanocarrier to bind its receptor-. It also aids in establishing the maximum loading capacity of the nanocarrier, thereby enhancing drug entrapment efficiency, and creating a more potent delivery system.

The isothermal titration microcalorimetry (ITC) technique is the only one that directly measures the enthalpy change undergone in any process such as a binding interaction. This technique is a label-free technique that only uses heat as a signal[35] (see **Section 9.3.11** for a detailed explanation of the ITC equipment). Characterizing the binding interaction between the DELOS-NV and the FITC-BSA can contribute to understanding better the nanoconjugate model developed in **Section 6.2**. Moreover, and in a more general sense, the present section will establish a methodology to determine the binding thermodynamics between DELOS-NV and therapeutic proteins for future drug developments.

Before starting with the thermodynamic analysis, it is important to remark that a reaction -such as the protein binding to the DELOS-NV membranes- to occur spontaneously requires a negative free energy of Gibbs change (ΔG), which depends on the temperature (T), the enthalpy change of the reaction (ΔH) and the entropy change of the reaction (ΔS), according to the thermodynamic **Equation 6.1**:

$$\Delta G = \Delta H - T * \Delta S$$

Equation 6.1. *Thermodynamic equation of the free energy of Gibbs, where ΔG is the change in Gibbs energy, ΔH is the enthalpy change; T is the temperature and ΔS is the entropy change.*

Therefore, if a reaction has a positive enthalpy change (+ΔH), means that the reaction is necessarily entropy-driven (+ΔS). Oppositely, if the reaction has a negative enthalpy change (-ΔH), the ΔS can be negative, as long as the absolute value of T*ΔS (see that are preceded by a minus in the thermodynamic equation) is smaller than the absolute value of the enthalpy change.

These considerations are relevant to elucidate the interactions driving the binding and adsorption of proteins onto the DELOS-NV membranes, which are typically hydrophobicity, electrostatics, and hydrogen bonding. According to the literature, protein adsorption in a lipidic membrane is driven by electrostatic or hydrophobic forces that are commonly accompanied by conformational transitions facilitated, in part, by hydrogen bonding mechanisms[36].

All these thermodynamic parameters can be obtained with an ITC assay, as well as the binding ratio between the ligand (e.g. FITC-BSA) and the receptor (e.g. DELOS-NV). Therefore, this technique is a very strong technique to characterize the binding thermodynamics of a system.

6.3.1. Setting up the procedure to determine binding thermodynamics between proteins and DELOS-NV by isothermal titration microcalorimetry

A typical ITC experiment consists of titrating one reagent over another, or vice versa (see **Section 9.3.11** for a schematic representation of the ITC equipment and an example of a single-reaction thermogram). Although the experimental design is apparently simple, several critical factors must be considered: the injection protocol (e.g., volume, number of injections, concentration of reagents), the kinetics of the interaction and the noise caused by unrelated signals[37]. Because of this, it was decided to set up the methodology with a very well-known nanoconjugate at Nanomol-Bio group and Nanomol Technologies S.L. It was decided to establish the protocol by characterizing first the binding

interaction between DELOS-NV and the recombinant human epidermal growth factor (rhEGF), a protein that promotes wound healing through keratinocyte division and epidermal regeneration[38].

In 2010, the Nanomol-Bio group and the Center of Genetic Engineer and Biotechnology (CIGB) in Cuba began a collaboration to prepare a novel nanoconjugate based on the rhEGF -produced by CIGB- and the DELOS-NV for the treatment of complex wounds. The promising results obtained under the framework of the Ph.D. thesis of Dr. Ingrid Cabrera of the Nanomol-Bio group, led to a technological development platform protected under the patent "Vesicles comprising epidermal growth factor and composition - wo2014 / 019555" in 2014[39]. The obtainment of the patent evolved in 2016 into a new project between Nanomol Technologies S.L. and Heber Biotec, the commercializing company of CIGB, for the pharmaceutical development and clinical testing of DELOS-NV conjugated to rhEGF for the treatment of chronic wounds, such as diabetic foot ulcers.

Therefore, more than 14 years of investigation of the rhEGF-DELOS-NV nanoconjugate have resulted in a very well-understood technological platform. However, the thermodynamics of the binding interaction had never been studied before. For this reason, the binding interaction of the system was characterized in this thesis, thus contributing to the advancement of this technological platform, and also, helping to establish the methodology for characterizing binding thermodynamics through ITC studies.

The DELOS-NV employed for the rhEGF delivery are composed of cholesterol and CTAB (cetyltrimethylammonium bromide, see chemical structure in **Figure 1.4** in the **Introduction**) at an equimolar ratio. The concentration of membrane components in the formulation is 5.5 mg/mL, and the dispersion medium is histidine 5 mM pH 7[40]. The concentration of rhEGF optimized for the rhEGF-DELOS-NV nanoconjugates is 100 µg/mL rhEGF, however, for the ITC analysis the nanovesicles were produced without rhEGF, since the experiment would consist of titrating the protein over the blank DELOS-NV.

These DELOS-NV were produced by DELOS method as explained in **Section 9.2.1**. Next, the nanovesicles were diafiltrated by TFF to eliminate the remanent EtOH, since this solvent has high calorimetric power, and a small mismatch in the EtOH concentration between the nanovesicles suspension and the rhEGF titrated could generate noise in the ITC analysis (see **Section 9.2.2** for TFF methodology). The sample was named ITC-Chol:CTAB DELOS-NV (see **Table 9.3** for details on sample composition). This sample was further filtrated with a 0.22 µm pore polyethersulfone (PES) filter to avoid heat noise during the experiments caused by contaminants or impurities. Different dilutions of the sample in histidine 5 mM buffer were prepared for the ITC analysis. The rhEGF, which is provided by CIGB lyophilized, was also resuspended in the same histidine 5 mM buffer pH 7 at different concentrations for the different ITC analyses and filtered with a 0.22 µm pore PES filter.

Before starting the titration experiments, the ITC-Chol:CTAB DELOS-NV were characterized by DLS and ELS (see **Section 9.3.1**) and by Cryo-TEM (see **Section 9.3.4**). The following **Figure 6.11A** shows the DLS and ELS results 30 days after production and permits confirmation that the obtained nanovesicles present an appropriate hydrodynamic diameter of around 60 nm, a low size PdI and a high apparent Z-potential of 104 mV that promotes stability of the colloidal suspension. **Figure 6.11B** shows a Cryo-TEM image consisting of spherical, unilamellar nanovesicles, very homogeneous in size and morphology. The results suggest that the samples produced are appropriate for the ITC assays.

In addition, the membrane components concentration in the ITC-Chol:CTAB DELOS-NV after all the production steps (DELOS method, diafiltration and the filtration steps) was measured by HPLC using an Evaporative Light Scattering Detector (ELSD) (see method in **Section 9.3.3**). Knowing the exact concentration of membrane components (Chol + CTAB) is very important in ITC assays since it will strongly influence the thermodynamic results. It was found that the concentration was 3.14 mg/mL of membrane components in the ITC-Chol:CTAB DELOS-NV. Hence, the concentration was lower than the theoretical one (5.5 mg/mL), meaning that some membrane components were lost during the different production and process steps.

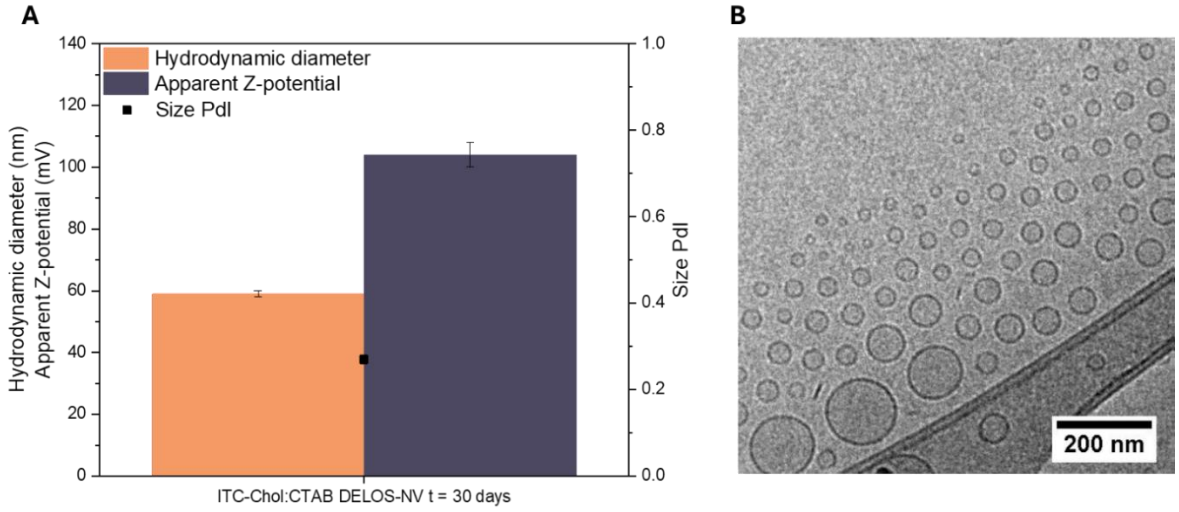


Figure 6.11. *Physicochemical characterization of the ITC-Chol:CTAB DELOS-NV employed for the ITC studies. A) Hydrodynamic diameter, size PdI and apparent Z- potential. B) Representative Cryo-TEM image at t = 30 days.*

Once it is confirmed that ITC-Chol:CTAB DELOS-NV exhibit favorable physicochemical properties, the experiments titrating rhEGF over these nanovesicles were conducted. The ITC experimental procedure is described in more detail in **Section 9.3.11**.

In order to facilitate the ITC calculations, an estimated molecular weight of the ITC-Chol:CTAB DELOS-NV was used to calculate the concentration of nanovesicles in the sample. The MW of Chol:CTAB DELOS-NV is around 1.44 x 10^7 g/mol as estimated by Multiangle light scattering (MALS) in previous studies performed in the Nanomol-Bio group[41]. MALS is a technique that allows studying the absolute molar mass of a sample by detecting how it scatters the light of an incident laser. From the exact amount of Chol and CTAB in the ITC-Chol:CTAB DELOS-NV measured by HPLC (3.14 mg/mL) and the MW of the Chol:CTAB DELOS-NV, the molar concentration of the sample was calculated. The ITC-Chol:CTAB DELOS-NV produced for the ITC studies had a concentration of 2.18 x 10^{-7} M nanovesicles.

Specifically, the titration experiments consisted of titrating the rhEGF in histidine 5 mM pH 7 (placed on the syringe) over the ITC-Chol:CTAB DELOS-NV in histidine 5 mM pH 7 (placed on the sample cell). Blank experiments titrating the rhEGF over buffer histidine 5 mM pH 7 (without DELOS-NV) were also performed to determine the heat associated to the rhEGF dilution. The isotherms of the blank experiments are shown in **Figure 6.12**.

Figure 6.12A shows a slope-like distribution of the peaks that indicates that the rhEGF is forming dimers in the syringe at the concentration tested (0.4 mM). The endothermic (positive) peaks recorded correspond to the de-dimerization of the protein at the lower concentrations of rhEGF encountered in the sample cell. Following the increase in protein concentration in the sample cell, the de-dimerization balance slows down and the heat of de-dimerization loses strength, resulting in the slope-like distribution of the peaks. In contrast, when titrating 0.05 mM rhEGF (**Figure 6.12B**), the intensity of the peaks is constant over time. At this lower concentration of rhEGF, the protein is not forming dimers in the syringe and the heat recorded corresponds to the dilution heat of monomeric rhEGF proteins.

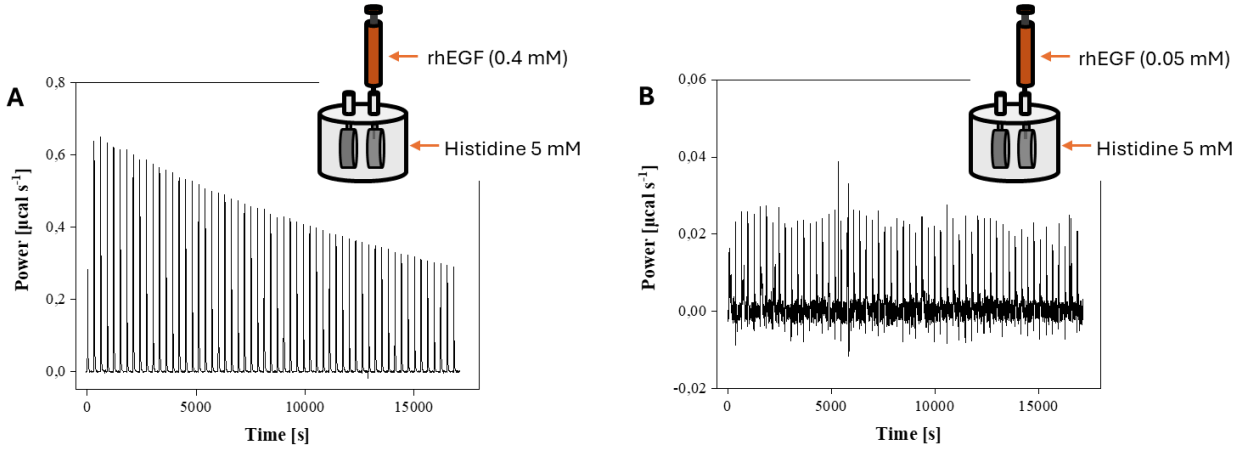


Figure 6.12. Thermogram of blank experiments of rhEGF titrated into histidine 5 mM pH 7. A) 0.4 mM rhEGF titrated into histidine 5 mM buffer. B) 0.05 mM rhEGF titrated into histidine 5 mM buffer.

Figure 6.13 shows the isotherms obtained from titrating different concentrations of rhEGF over different concentrations of ITC-Chol:CTAB DELOS-NV. These isotherms show the sum of exothermic (negative) and endothermic (positive) peaks. The endothermic peaks correspond to the de-dimerization and dilution heat of the rhEGF (see **Figure 6.12**), while the exothermic peaks correspond to the rhEGF binding to the ITC-Chol:CTAB DELOS-NV. Depending on the ratios tested, the negative peaks are more evident (**Figure 6.13A** and **Figure 6.13B**), or can be deduced by the mountain-like shape of the isotherm (**Figure 6.13C**). In **Figure 6.13C**, at the beginning of the titration a sum of endothermic and exothermic energies is observed, which results in smaller endothermic peak. When the biding sites of the rhEGF and the ITC-Chol:CTAB DELOS-NV are saturated, only the endothermic energy (corresponding to the rhEGF de-dimerization) is recorded, resulting in higher intensities of the endothermic peaks. Afterward, the intensity of the endothermic peaks starts to decrease, caused by a slowing down of the de-dimerization balance due to the higher concentration of free proteins in the sample cell.

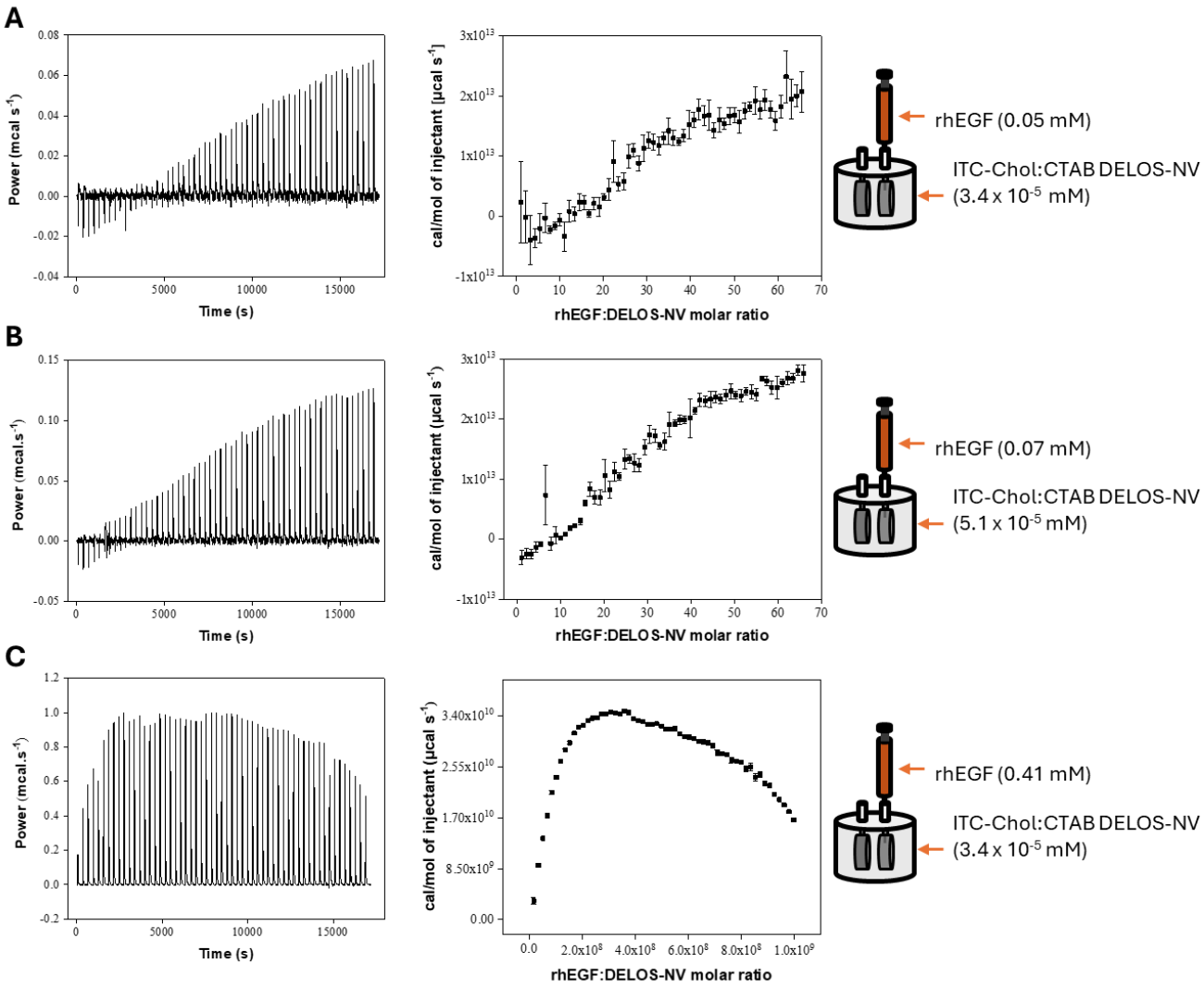


Figure 6.13. *ITC assays of rhEGF titrated over ITC-Chol:CTAB DELOS-NV in histidine 5 mM pH 7. Thermogram (left side) and binding isotherm (right side). (A) 3.4 x 10^{-5}mM of ITC-Chol:CTAB DELOS-NV titrated with 0.05 mM rhEGF. (B) 5.1 x 10^{-5} mM of ITC-Chol:CTAB DELOS-NV titrated with 0.07 mM rhEGF. (C) 3.4 x 10^{-5} mM of ITC-Chol:CTAB DELOS-NV titrated with 0.41 mM rhEGF.*

The blank isotherm corresponding to the rhEGF (0.41 mM) titrated over histidine 5 mM cannot be subtracted from the corresponding titration experiments (**Figure 6.13C**) to account for the heat of dilution, because the de-dimerization heat in each injection might change when nanovesicles are present in the experiment. Oppositely, the blank obtained with the rhEGF (0.05 mM) titrated over histidine 5 mM did not show de-dimerization (**Figure 6.12B**), meaning that at low concentrations, the protein is not dimerized. Therefore, this blank could be subtracted from the experiments conducted with 0.05 mM rhEGF (**Figure 6.13A**).

The thermograms shown in **Figure 6.12** and **Figure 6.13** were fitted using the software AFFINImeter (https://www.affinimeter.com/site/) to obtain the binding thermodynamic parameters. Typically, using this software, when the stoichiometry of a system is not well-known, the independent sites approach is employed for the fitting of the thermograms. This fitting does not use schemes based on

equilibria between stoichiometric species. Instead, it assumes a receptor with a certain number of binding sites (the DELOS-NV) where the ligand binds. However, it has certain limitations; it does not allow to include the heat associated with the rhEGF de-dimerization in the analysis. For this reason, a stoichiometric approach was employed to create an original stoichiometric binding model in which the de-dimerization of the protein could be included (**Figure 6.14**). The designed model comprised two different equilibriums, one corresponding to the rhEGF de-dimerization and one corresponding to the rhEGF binding to the ITC-Chol:CTAB DELOS-NV.

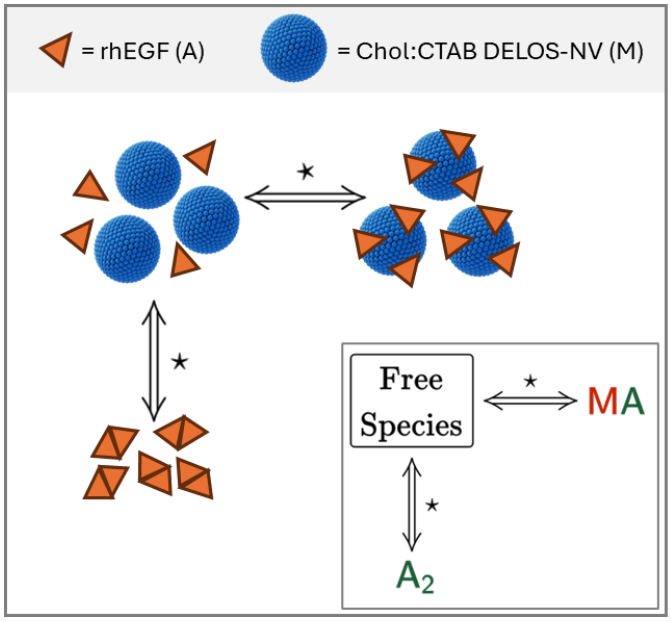


Figure 6.14. Graphical representation of the stoichiometric binding model employed in AFFINImeter global fitting of the isotherms (in the inset is represented with AFFINImeter nomenclature). M refers to the ITC-Chol:CTAB DELOS-NV and A refers to the rhEGF. MA is the interaction between the protein and the DELOS-NV and A2 the dimerized rhEGF.

The model described was applied for a global fitting where all the 5 isotherms shown in **Figure 6.12** and **Figure 6.13** were simultaneously fitted and from which thermodynamic parameters were calculated (**Table 6.4**). Those isotherms in which no de-dimerization (**Figure 6.13A**) or in which no interaction rhEGF-ITC-Chol:CTAB DELOS-NV (**Figure 6.12**) was occurring were fitted only to one (the required) equilibrium. The affinity constant and the enthalpy change of each equilibrium were assumed to be equal between experiments and were linked and fitted together. Global fitting is particularly useful for the analysis of this kind of complex interactions that involve the presence of more than one equilibrium and in which isotherms share some fitting parameters.

Table 6.4. *Thermodynamic parameters -Enthalpy change (ΔH), Free energy of Gibb's change (ΔG) and the product of temperature and entropy change (–TΔS)-, binding ratio and binding affinity constant (K_a) for the binding reaction between rhEGF and ITC-Chol:CTAB DELOS-NV (Free Species → MA) and for the dimerization of the rhEGF (Free Species → A2) fitted with the AFFINImeter software. Results are shown as mean ± SD; global analysis of 5 experiments.*

Binding equilibrium	Binding ratio	K_a (M^{-1})	ΔH (cal mol^{-1})	-TΔS (cal mol^{-1})	ΔG (cal mol^{-1})
Free Species → MA	70 ± 20	(5.00 ± 0.05) x 10^5	(-6.69 ± 0.05) x 10^4	(5.91 ± 0.05) x 10^4	(-7.758 ± 0.006) x 10^3
Free Species → A_2	1	(1.11 ± 0.01) x 10^3	(-4.48 ± 0.05) x 10^5	(4.44 ± 0.05) x 10^5	(-4.140 ± 0.005) x 10^3

By this global fitting obtained with AFFINImeter software, the number of rhEGF proteins binding per ITC-Chol:CTAB DELOS-NV surface was found to be 70±20 at the tested conditions. As shown in **Table 6.4**, the rhEGF interaction with the ITC-Chol:CTAB DELOS-NV is an exothermic reaction (negative ΔH). It was expected to be an electrostatic interaction since at pH 7 the rhEGF (isoelectric point of 4.6) is negatively charged, and the ITC-Chol:CTAB DELOS-NV are positively charged, and for charged proteins, electrostatic attraction is predominant, as described in the literature[36]. However, electrostatic bindings are characterized by small ΔH values; a typical example is the binding of heparan sulfate to charged vesicles with ΔH = –2 x 10^3 cal mol^{-1} [36]. In the studied system, the ΔH of this first equilibrium was higher, ΔH = (–6.69 ± 0.05) x 10^4 cal mol^{-1}, indicating that another kind of binding was acting together with the electrostatic binding. This extra energy registered could correspond to hydrogen bonding between the head of the CTAB molecules and the rhEGF protein[42] or a reorganization of the rhEGF structure upon contact with the ITC-Chol:CTAB DELOS-NV.

Circular dichroism (CD) studies were performed by CIGB collaborators, comparing the far-UV CD spectrum of Chol:CTAB DELOS-NV incorporating the rhEGF with the CD spectrum resulting from the sum of the individual spectra of the free rhEGF and the Chol:CTAB DELOS-NV without rhEGF[43]. The results showed the loss of a positive band at 230 nm in the Chol:CTAB DELOS-NV incorporating the rhEGF. This band is likely associated with the aromatic amino acids (Trp and Tyr) and, possibly, the disulfide bonds of rhEGF. Therefore, its loss is probably indicating some changes on this groups when the protein binds the nanovesicles, then, extra energy could also come from π-cation and π-stacking interactions of aromatic amino acids (Trp and Tyr) in rhEGF with CTAB and cholesterol, respectively.

Considering all the experiments performed, it seems that the rhEGF gets in contact with the ITC-Chol:CTAB DELOS-NV attracted by the electrostatic forces and binds to them with electrostatic bindings. Also, hydrogen bonding or protein reorganization occurs at this stage, releasing energy. Importantly, the results show that the interaction has a binding affinity constant K_a equal to (5.00 ± 0.05) x 10^5 M^{-1} (**Table 6.4**), therefore a dissociation constant K_d (= K_a^{-1}) of 2 x 10^{-6} M. The dissociation constant of the rhEGF and the EGF receptor is well described in the literature and is close to 1 x 10^{-9} M[44]. This indicates that the rhEGF has a stronger affinity for its receptor than for the Chol:CTAB DELOS-NV, which makes the DELOS-NV appropriate delivery systems, desirable for the

transportation of the protein since the interaction between the rhEGF and the DELOS-NV do not compromise thermodynamically the interaction of the protein with its receptor.

The fitting of the results also permitted the characterization of the binding thermodynamics of the protein dimerization (**Table 6.4**). Note that the enthalpy reported is negative because corresponds to the dimerization of the protein (the peaks recorded in the titration assays were endothermic -positive enthalpy- because corresponded to the opposite process of de-dimerization).

This study provided a better understanding of the interaction between a model protein, the rhEGF, and the DELOS-NV, and also to gain experience with the ITC technique and the software AFFINImeter for data analysis. This initial study serves as a first proof of concept, and in the next section the interaction between DELOS-NV and FITC-BSA will be expanded upon.

- The results of this **Section 6.3.1** have been published as a scientific paper in: "L. Ferrer-Tasies, H. Santana, I. Cabrera-Puig, E. González-Mira, L. Ballell-Hosa, **C. Castellar-Álvarez**, A. Córdoba, J. Merlo-Mas, H. Gerónimo, G. Chinea, V. Falcón, E. Moreno-Calvo, J. Skov-Pedersen, J. Romero, C. Navarro-Requena, C. Valdés, M. Limonta, J. Berlanga, S. Sala, E. Martínez, J. Veciana and N. Ventosa. Recombinant human epidermal growth factor/quatsome nanoconjugates: a robust topical delivery system for complex wound healing. *Adv. Ther.* 2021, 4 (6), 2000260"-

6.3.2. Determining the FITC-BSA and Chol:CPC DELOS-NV binding thermodynamics by isothermal titration microcalorimetry

The same procedure as the one explained for the characterization of the binding thermodynamics between the rhEGF and the Chol:CTAB DELOS-NV was conducted, adapting the concentrations in the syringe and the sample cell to the current samples.

Chol:CPC DELOS-NV were produced as described in **Section 9.2.1**. They consisted of 3 mg/mL of membrane components (Chol+CPC) at an equimolar ratio in HBSS pH 7.4 buffer (see **Section 9.1** for details on buffer composition). Next, they were diafiltrated by TFF (see **Section 9.2.2**) and filtrated with a 0.22 µm pore PES filter, to eliminate the remanent EtOH of DELOS process and any impurity which could result in noise in the analysis. The sample was named ITC-Chol:CPC DELOS-NV and details on its composition can be found in **Table 9.3**. Afterwards, appropriate dilutions in the same media were prepared for the ITC analysis.

The FITC-BSA, which is purchased as a solid powder, was dissolved in the same HBSS pH 7.4 buffer, and filtrated with a 0.22 µm pore PES filter to eliminate any possible aggregate or impurity. Afterward, dilutions of the protein to the working concentrations were prepared in the same media.

As quality controls, the hydrodynamic diameter, size PdI and apparent Z-potential of the obtained ITC-Chol:CPC DELOS nanovesicles were measured 14 days and 30 days after production (**Figure 6.15A**) as explained in **Section 9.3.1**. Cryo-TEM images (see **Figure 6.15B**) were also obtained with the method described in **Section 9.3.4** at 30 days.

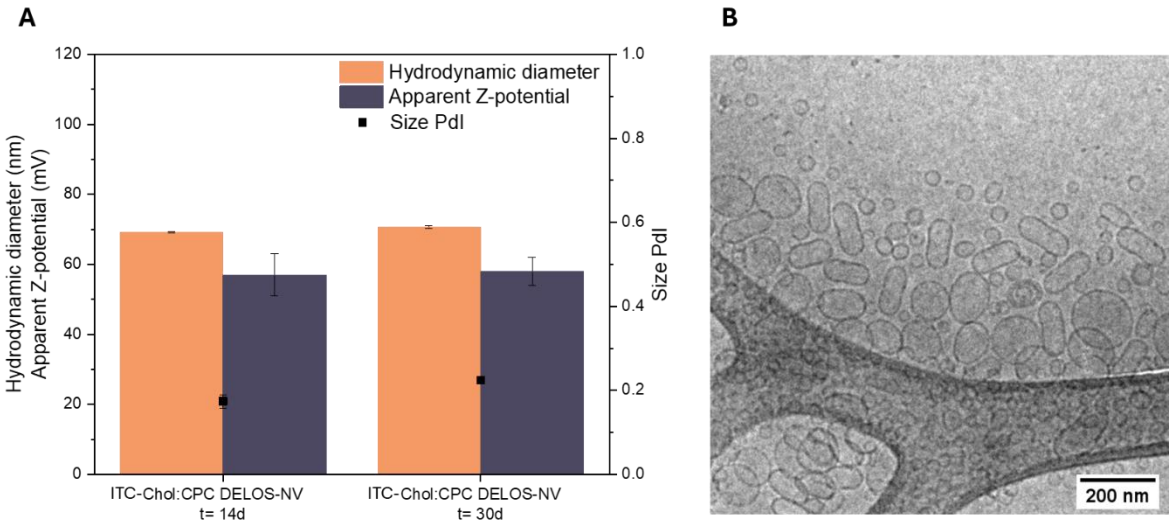


Figure 6.15. Physicochemical characterization of the ITC-Chol:CPC DELOS-NV employed for the ITC studies. A) Hydrodynamic diameter, size PdI and apparent Z-potential. B) Representative Cryo-TEM image at t = 30 days.

Figure 6.15A shows that the ITC-Chol:CPC DELOS-NV present a similar hydrodynamic diameter to that of ITC-Chol:CTAB DELOS-NV (**Figure 6.11A**). In addition, they have a low size PdI indicating high homogeneity in terms of size, and an appropriate apparent Z-potential above 30 mV. The Cryo-TEM image (**Figure 6.15B**) shows a mix of spherical and elongated nanovesicles. This elongated structure might be caused by the high concentration of salts present in the HBSS buffer. This phenomenon has been observed previously when working in media with high concentrations of salts[45].

It is important to note that for this study, an approximation has been made regarding the MW of nanovesicles. In this case, as ITC-Chol:CTAB and ITC-Chol:CPC DELOS-NV present similar hydrodynamic diameter (**Figure 6.11** and **Figure 6.15**), and CPC and CTAB surfactants have also similar MW (340 g/mol and 364 g/mol, respectively, according to PubChem - https://pubchem.ncbi.nlm.nih.gov/-), it has been assumed for ITC-Chol:CPC DELOS-NV the same MW of ITC-Chol:CTAB DELOS-NV (1.44×10^7 g/mol).

The concentration of membrane components in ITC-Chol:CPC DELOS-NV was quantified by HPLC with a PDA 2998 detector (see **Section 9.3.3**). The final concentration of total membrane components after the production by DELOS, the diafiltration and the filtration steps was 2.58 mg/mL. Therefore, since the theoretical concentration was 3 mg/mL, only a small amount of membrane components was lost during the different production and process steps. Considering the membrane components concentration in the sample and the MW of the nanovesicles (1.44×10^7 g/mol), the final concentration of nanovesicles in the ITC-Chol:CPC DELOS-NV was 1.79×10^{-7} M.

Once the ITC-Chol:CPC DELOS-NV sample was well characterized, the ITC experiments were carried out. The experiments were performed by titrating the FITC-BSA in HBSS pH 7.4, placed on the syringe, into the ITC-Chol:CPC DELOS-NV in HBSS pH 7.4, placed in the sample cell. Different concentrations were tested to evaluate different ratios FITC-BSA to DELOS-NV. **Figure 6.16** shows

the isotherms of the titration experiments over ITC-Chol:CPC DELOS-NV for the different concentrations evaluated.

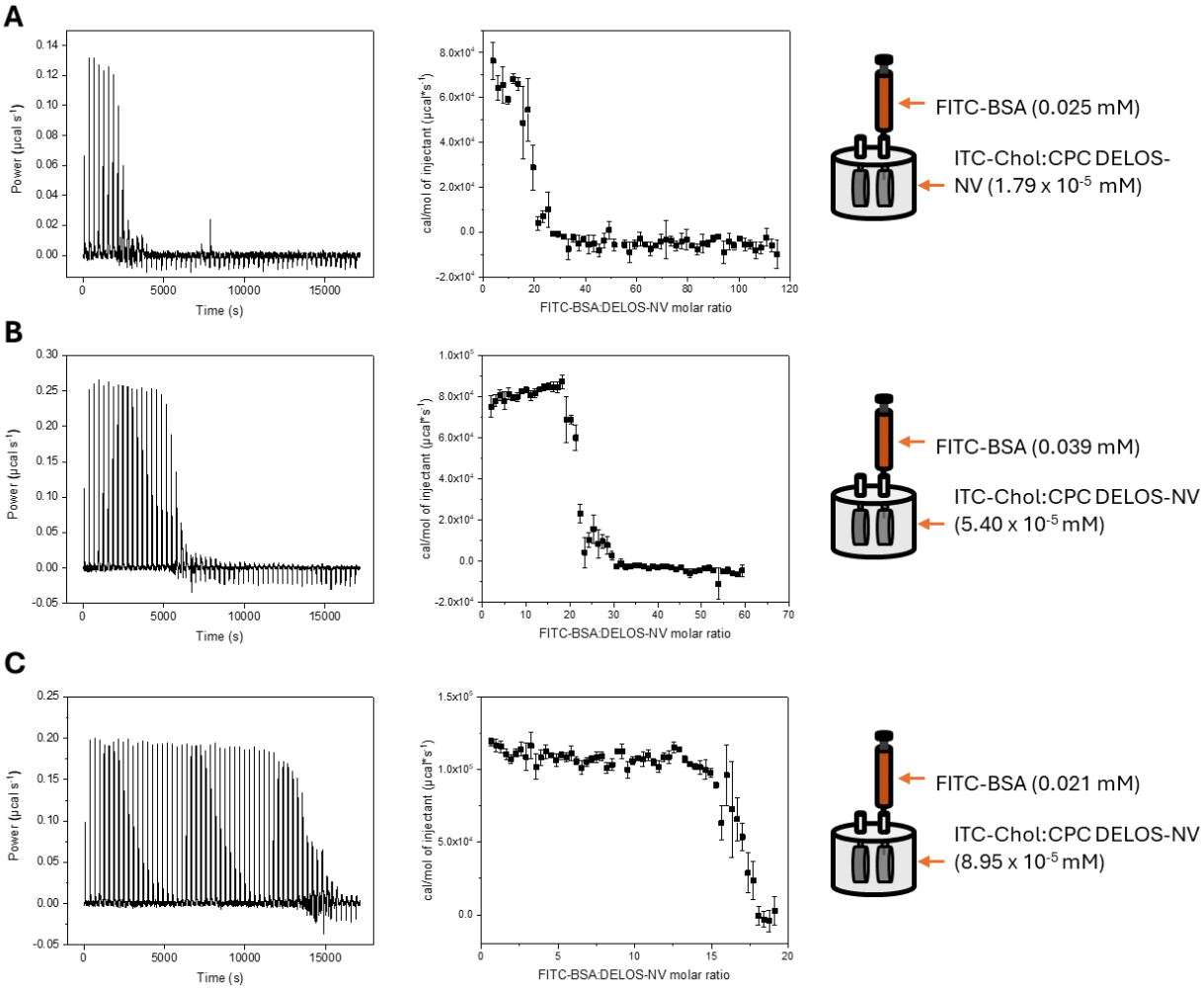


Figure 6.16. *ITC interaction of FITC-BSA with ITC-Chol:CPC DELOS-NV in HBSS pH 7.4. Thermogram (left side) and binding isotherm (right side). (A) 1.79 x 10^{-5}mM of ITC-Chol:CPC DELOS-NV titrated with 0.025 mM FITC-BSA. (B) 5.4 x 10^{-5} mM of ITC-Chol:CPC DELOS-NV titrated with 0.039 mM FITC-BSA. (C) 8.95 x 10^{-5} mM of ITC-Chol:CPC DELOS-NV titrated with 0.021 mM FITC-BSA.*

Two main differences can be detected in **Figure 6.16** isotherms with respect to the isotherms shown in **Figure 6.13** in the previous **Section 6.3.1**. The current isotherms show a unique interaction, which is represented by a sigmoidal distribution of the peaks. Therefore, oppositely to the results obtained with the rhEGF, the FITC-BSA is not forming dimers in the syringe at any of the concentrations tested. The interaction recorded between the FITC-BSA and the ITC-Chol:CPC DELOS-NV is endothermic (positive peaks), oppositely to the interaction between the rhEGF and the ITC-Chol:CTAB DELOS-NV. As shown in **Figure 6.16,** several ratios between the FITC-BSA and the nanovesicles were tested and the results were consistent. Therefore, these experiments indicate that at the conditions tested an endothermic interaction is predominantly occurring. Endothermic interactions indicate that the driving force is a large entropy gain, which is typically related to hydrophobic forces[36,46]. This result

aligns well with the literature; Yocouchi et al., observed that a negatively charged BSA in PBS buffer at pH 7.4 interacted with negatively charged liposomes[47]. This interaction became even stronger as the proportion of negative components in the liposome membrane increased, despite the potential for electrostatic repulsion. Therefore, their results also suggest that the adsorption of the BSA in the nanovesicles membrane might be predominantly led by hydrophobic forces.

The result does not mean that no electrostatic interaction is occurring in the experiment, however, electrostatic bindings are characterized by small and negative ΔH values in the order of 10^3 cal mol^{-1}, as mentioned in previous **Section 6.3.1**, and this exothermic energy might be overshadowed by the hydrophobic large and positive ΔH.

The fitting of the results was done again with the AFFINImeter software. For this analysis, a global fitting could be employed, because no energy corresponding to a de-dimerization process had to be considered. As mentioned previously, this approach is the most appropriate when the stoichiometry of the reaction is not well-known.

The three isotherms were fitted together in a global fitting, assuming the affinity constant and the enthalpy change of the binding equilibrium to be equal in all the experiments. Accurate fittings were obtained, and the results are shown in **Table 6.5**.

As shown, saturation of the binding sites is reached at a ratio of 19.74 moles of FITC-BSA per moles of ITC-Chol:CPC DELOS-NV. The affinity constant Ka of the interaction is very high, indicating that the protein quickly binds the nanovesicles. This high affinity is probably influenced by the electrostatic attractive forces that contribute to bringing closer the protein and the nanovesicles. The enthalpy is positive, meaning that the interaction is endothermic. Despite requiring energy to occur, the binding reaction has a positive entropy change that favors the spontaneity of the reaction. For all these reasons, Gibb's energy change is negative meaning that the reaction is spontaneously driven at the assay conditions. As mentioned before, an entropy-driven interaction is typically caused by hydrophobic forces, which is in line with the findings in the bibliography[47].

Table 6.5. *Thermodynamic parameters -Enthalpy change (ΔH), Free energy of Gibb's change (ΔG) and the product of temperature and entropy change (–TΔS)-, binding ratio and binding affinity constant (K_a) for the binding reaction between FITC-BSA and ITC-Chol:CPC DELOS-NV fitted with the AFFINImeter software. Results are shown as mean ± SD; global analysis of 3 experiments.*

Binding ratio	K_a (M^{-1})	ΔH (cal mol^{-1})	-TΔS (cal mol^{-1})	ΔG (cal mol^{-1})
19.74 ± ~0*	3.64×10^8 ± ~0*	1.00×10^5 ± ~0*	1.12×10^5 ± ~0*	-1.16×10^4 ± ~0*

** The error is considered negligible because it is more than 10 orders of magnitude lower than the result.*

The knowledge gained from these ITC studies is very valuable, as it provided a better understanding of the binding of different proteins to DELOS-NV and facilitated the learning of ITC study design and result adjustment using the AFFINImeter software. As mentioned previously, characterizing the binding thermodynamics between DELOS-NV and the loaded drugs is crucial in drug development. This information allows for the prediction of system stability and drug release in different media. Additionally, it helps characterize the maximum loading capacity of DELOS-NV, facilitating the optimization of the potential nanoformulation. Furthermore, understanding these thermodynamics

enables the prediction of the efficacy of the entrapped drug by comparing its affinity for DELOS-NV versus its target receptor.

In addition, the high enthalpy obtained for the binding between FITC-BSA and DELOS-NV indicates a very strong interaction. This underscores FITC-BSA as an excellent model molecule for Chol:CPC DELOS-NV, as it will not be easily released from the nanoconjugates. Consequently, it is expected that the high EE% achieved remains constant over storage time and during permeation assays. Therefore, the permeation assays were carried out with the well-characterized nanoconjugates based on FITC-BSA and Chol:CPC DELOS-NV, and are described in the following **Section**.

6.4. Biological characterization of nanoconjugates based on FITC-BSA integrated in DELOS-NV. Permeation assays in a Caco-2 intestinal model.

Once the nanoconjugates based on FITC-BSA integrated into DELOS-NV were deeply characterized, the intestinal permeation was evaluated in Caco-2 models. The introduction of the present **Chapter** highlighted the significance of the oral administration route for both systemic and local treatments in gastrointestinal diseases. Intestinal permeation assays with DELOS-NV have never been conducted before and gaining insight into the behavior of the DELOS-NV in the intestinal epithelium is crucial. This understanding will provide valuable knowledge, enabling the identification of the most attractive diseases for targeting with the DELOS-NV formulations.

As aforementioned, the Caco-2 intestinal model is the most widely used model to test permeation of drugs through the intestine in pre-clinical studies, and one of the few models recognized by the FDA and the EMA. Therefore, as outlined in the introduction, this model was chosen to evaluate the effect of DELOS-NV on the permeation of FITC-BSA.

6.4.1. Permeation assays in Caco-2 cells grown in transwells

6.4.1.1. Production and characterization of the formulations for the *in vitro* permeation studies

For the *in vitro* studies, 4 formulations were produced based on the design space shown in **Figure 6.10**. All the nanoconjugates produced contained 0.01 mg/mL of FITC-BSA, since it was observed that higher concentrations of protein resulted in lower probabilities of getting nanoconjugates with the CQA desired. For the permeation assays, different combinations of ratios and membrane components concentration were tested, to see if those factors affected the permeation assays. With this intention, the DELOS-NV were produced again with 1 to 5 mg/mL of membrane components and 1:1 to 2:1 molar ratio of CPC:Chol. The formulations were produced by the DELOS method (see **Section 9.2.1**) and diafiltrated by TFF (see **Section 9.2.2**). The formulations produced for the permeation assays were named Abs1-DELOS-NV, Abs2-DELOS-NV, Abs3-DELOS-NV, and Abs4-DELOS-NV. Their composition is listed in **Table 9.4**, and **Figure 6.17** shows the macroscopical images of the formulations prepared right after the diafiltration by TFF.

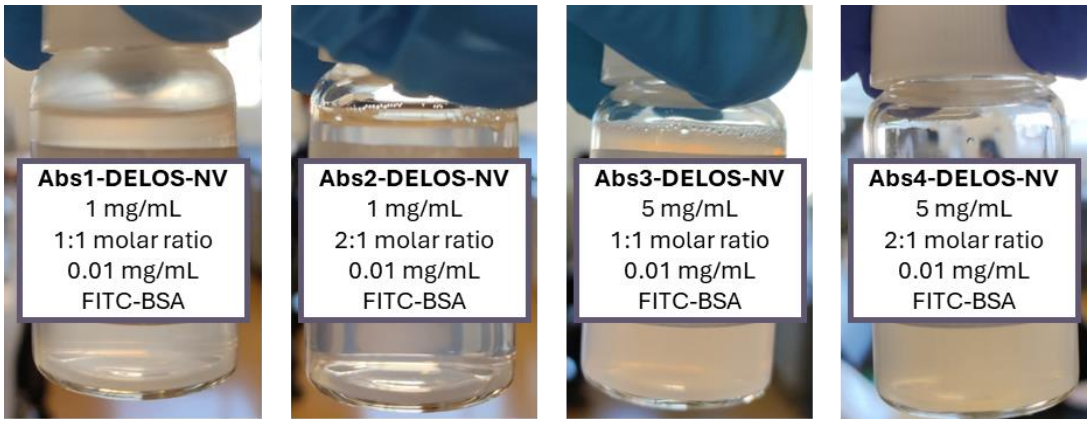


Figure 6.17. *Macroscopical images at time 0 of the Abs1-; Abs2-; Abs3- and Abs4-DELOS-NV produced in HBSS pH 7.4 for the permeation assays in Caco-2 cells. The mg/mL refers to the total membrane components concentration and the molar ratio between membrane components is expressed as CPC:Chol. All of them contain 0.01 mg/mL FITC-BSA.*

The formulations obtained were characterized by DLS and ELS (see **Section 9.3.1**) over three months to account for their stability (**Figure 6.18**). The stability results show that the samples are stable over time. As stated before, there is only a small increase in the hydrodynamic diameter from 0 days to 14 days caused by the maturation time required by this kind of samples. **Figure 6.19** shows the CQA measured at 14 days for easier comparison between samples. From this graphic can be appreciated that all the samples present similar hydrodynamic diameter and apparent Z-potential. The samples Abs2 and Abs4, which correspond to the two samples with ratio Chol:CPC 1:2, present lower size PdI than the other two samples. Most important, all the samples present CQA within the limits established in **Section 6.2**, that were a size PdI between 0.01 and 0.5 and a hydrodynamic diameter between 20 and 220 nm. Since their diameter is lower than 220 nm, these samples can be sterile filtered previous to the permeation assays with 0.22 µm PES filters. In addition, all the samples present apparent Z-potential values above 30 mV meaning that the nanovesicles present enough repulsive forces between them to be stabilized in the colloidal dispersion.

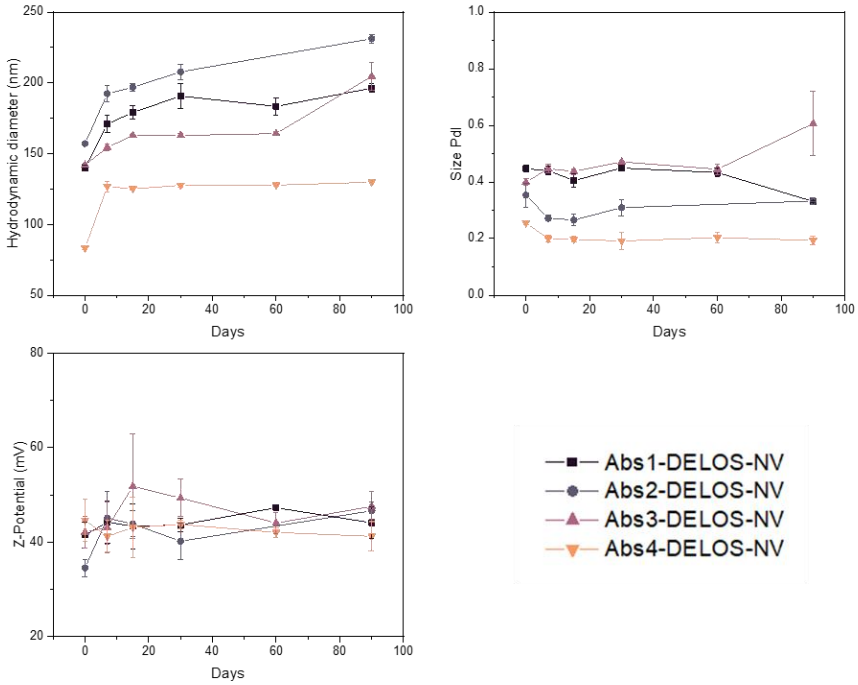


Figure 6.18. *3 months evolution of the CQA (mean hydrodynamic diameter, size PdI and apparent Z- potential) of the nanoconjugates Abs1-, Abs2-, Abs3- and Abs4-DELOS-NV produced for the permeation assays in Caco-2 cells. The results correspond to the average and SD of three consecutive measurements of one experimental run.*

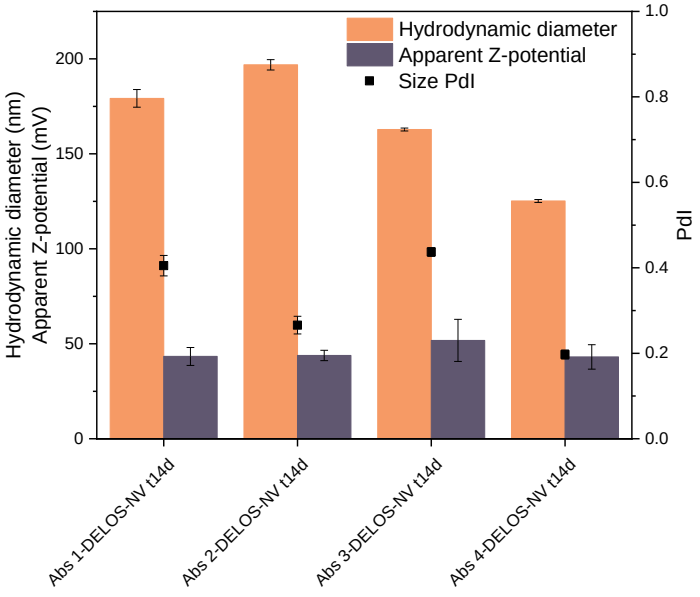


Figure 6.19. *Hydrodynamic diameter, size PdI and apparent Z-potential of the nanoconjugates Abs1-, Abs2-, Abs3- and Abs4-DELOS-NV produced for the permeation assays in Caco-2 cells, at time 14 days after production and diafiltration by TFF. The results correspond to the average and SD of three consecutive measurements of one experimental run.*

Cryo-TEM images were also obtained (see method in **Section 9.3.4**) to assess the morphology of the nanoconjugates (**Figure 6.20**). The Cryo-TEM images showed a "glue effect" due to the presence of FITC-BSA in the samples. Probably, the protein interacts with different nanovesicles at the same time, causing a certain degree of agglomeration. The force that the protein exerts on the DELOS-NV membrane causes a slight deformation in some nanovesicles, however, the majority of nanovesicles present spherical morphology without the presence of multilamellar nanovesicles. As it has been observed in the previous **Section**, with the ITC assays, the interaction of the FITC-BSA is hydrophobic and very strong, hence, it makes sense that the protein can interact with more than one DELOS-NV at a time, and also it can affect the nanovesicles membranes.

These 4 formulations of nanoconjugates, based on FITC-BSA integrated in DELOS-NV, using different combinations of ratios and membrane components concentration, were stable over time and presented an appropriate morphology, therefore, they have been employed for the *in vitro* permeation assays.

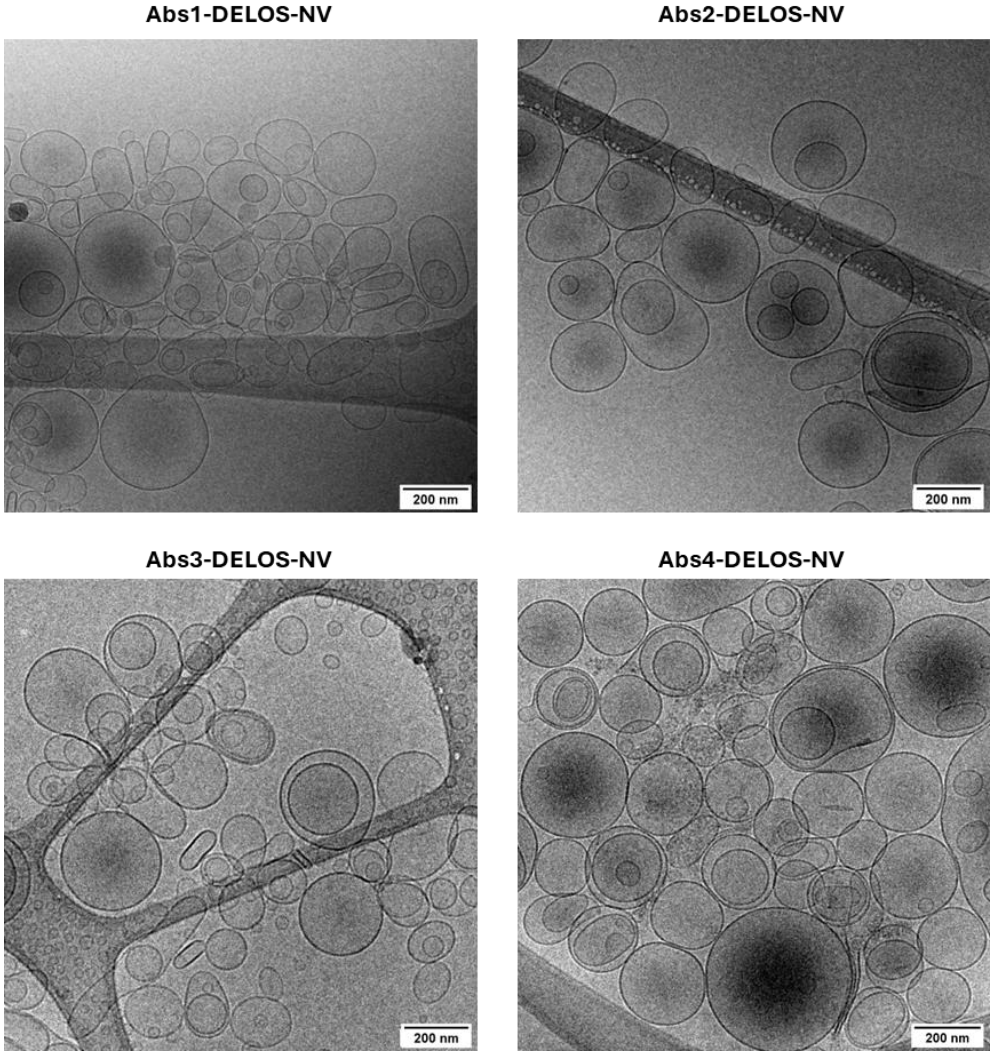


Figure 6.20. *Representative Cryo-TEM images of the nanoconjugates Abs1-, Abs2-, Abs3- and Abs4-DELOS-NV produced for the in vitro permeation studies.*

6.4.1.2. Viability assays in Caco-2 cells with the 4 prepared nanoconjugates based on FITC-BSA integrated in DELOS-NV

The permeation assays were conducted at the Cell Culture, Antibody Production and Cytometry Service of the UAB. This service can be used as a self-service by authorized personnel after completing the required training, or the assays can be subcontracted and performed by the service technicians. In this specific case, I received training in cell culture assays from Francisco Cortés, the technical coordinator at the service, and subsequently performed the experiments in self-service mode.

To perform the permeation assays in Caco-2 cells, first, it is required to test the viability of the cells when in contact with the nanoconjugates. With this objective, different concentrations of nanoconjugates were tested in Caco-2 cells grown in 96-well plates for 9 days (see method in **Section 9.4.4**).

The viability assays were conducted with the four formulations produced and characterized in **Section 6.4.1.1** (Abs1-, Abs2-, Abs3- and Abs4-DELOS-NV). The four formulations were diluted in HBSS pH 7.4 to assess the Caco-2 viability in the presence of different concentrations of nanoconjugates (DELOS-NV membrane components assessed: 1, 0.5, 0.1, 0.01, 0.001 and 0.0001 mg/mL). The final specifications of all dilutions tested are outlined in **Table 6.6**. Further, it is noteworthy that the different samples specified in this table were filtered right before the cytotoxicity assays with a 0.22 µm sterile PES filter to avoid contamination that could bias the viability results in cells. Following this, the different samples and dilutions were added to the Caco-2 cells, which were then incubated for 4 hours at 37 ºC and 5% CO_2 to assess their viability. 6 replicates (corresponding to 6 independent wells of a 96-well plate) were performed per each sample and dilution.

Table 6.6. *Original samples and dilutions tested in the viability assay in Caco-2 cells.*

Original sample	Ratio Chol:CPC	Dilution tested	Membrane components concentration (mg/mL) after dilution	FITC-BSA concentration (mg/mL) after dilution
Abs1-DELOS-NV	1:1	NA	1	0.01
Abs1-DELOS-NV	1:1	1:2	0.5	0.005
Abs1-DELOS-NV	1:1	1:10	0.1	0.001
Abs1-DELOS-NV	1:1	1:100	0.01	0.0001
Abs1-DELOS-NV	1:1	1:1000	0.001	0.00001
Abs1-DELOS-NV	1:1	1:10000	0.0001	0.000001
Abs2-DELOS-NV	1:2	NA	1	0.01
Abs2-DELOS-NV	1:2	1:2	0.5	0.005
Abs2-DELOS-NV	1:2	1:10	0.1	0.001
Abs2-DELOS-NV	1:2	1:100	0.01	0.0001
Abs2-DELOS-NV	1:2	1:1000	0.001	0.00001
Abs2-DELOS-NV	1:2	1:10000	0.0001	0.000001
Abs3-DELOS-NV	1:1	1:5	1	0.002
Abs3-DELOS-NV	1:1	1:10	0.5	0.001
Abs3-DELOS-NV	1:1	1:50	0.1	0.0002
Abs3-DELOS-NV	1:1	1:500	0.01	0.00002
Abs3-DELOS-NV	1:1	1:5000	0.001	0.000002
Abs3-DELOS-NV	1:1	1:50000	0.0001	0.0000002
Abs4-DELOS-NV	1:2	1:5	1	0.002
Abs4-DELOS-NV	1:2	1:10	0.5	0.001
Abs4-DELOS-NV	1:2	1:50	0.1	0.0002
Abs4-DELOS-NV	1:2	1:500	0.01	0.00002
Abs4-DELOS-NV	1:2	1:5000	0.001	0.000002
Abs4-DELOS-NV	1:2	1:50000	0.0001	0.0000002

In this initial viability test, due to the lack of prior knowledge regarding viability assays in Caco-2 cells with the nanoconjugates based in Chol:CPC DELOS-NV, a broad range of concentrations of all the formulations were tested. According to **Table 6.6**, those samples that had an initial concentration of membrane components of 5 mg/mL (Abs 3- and Abs4-DELOS-NV) were more diluted than those with an initial concentration of membrane components of 1 mg/mL (Abs1- and Abs2-DELOS-NV) to account for the same concentration of membrane components in the assay. Therefore, their final concentration of FITC-BSA was also lower.

The viability of the cells after being incubated for 4 hours with the different formulations presented in **Table 6.6** was assessed with the MTS tetrazolium salt (see method in **Section 9.4.4**). This chemical compound is reduced by living cells into colored formazan. Therefore, the more viable the cells are, the more color they produce, resulting in a higher absorbance intensity when read with a UV-Vis spectrophotometer.

Next, the absorbance in each well at 490 nm was measured with a plate spectrophotometer. To determine the optimal time for measuring the reduced MTS in the viability assays, the absorbance of the plate was monitored at various intervals (**Figure 6.21**). Consistent viability results were observed between 30 minutes and 3.5 hours, suggesting no saturation of the absorbance within this timeframe.

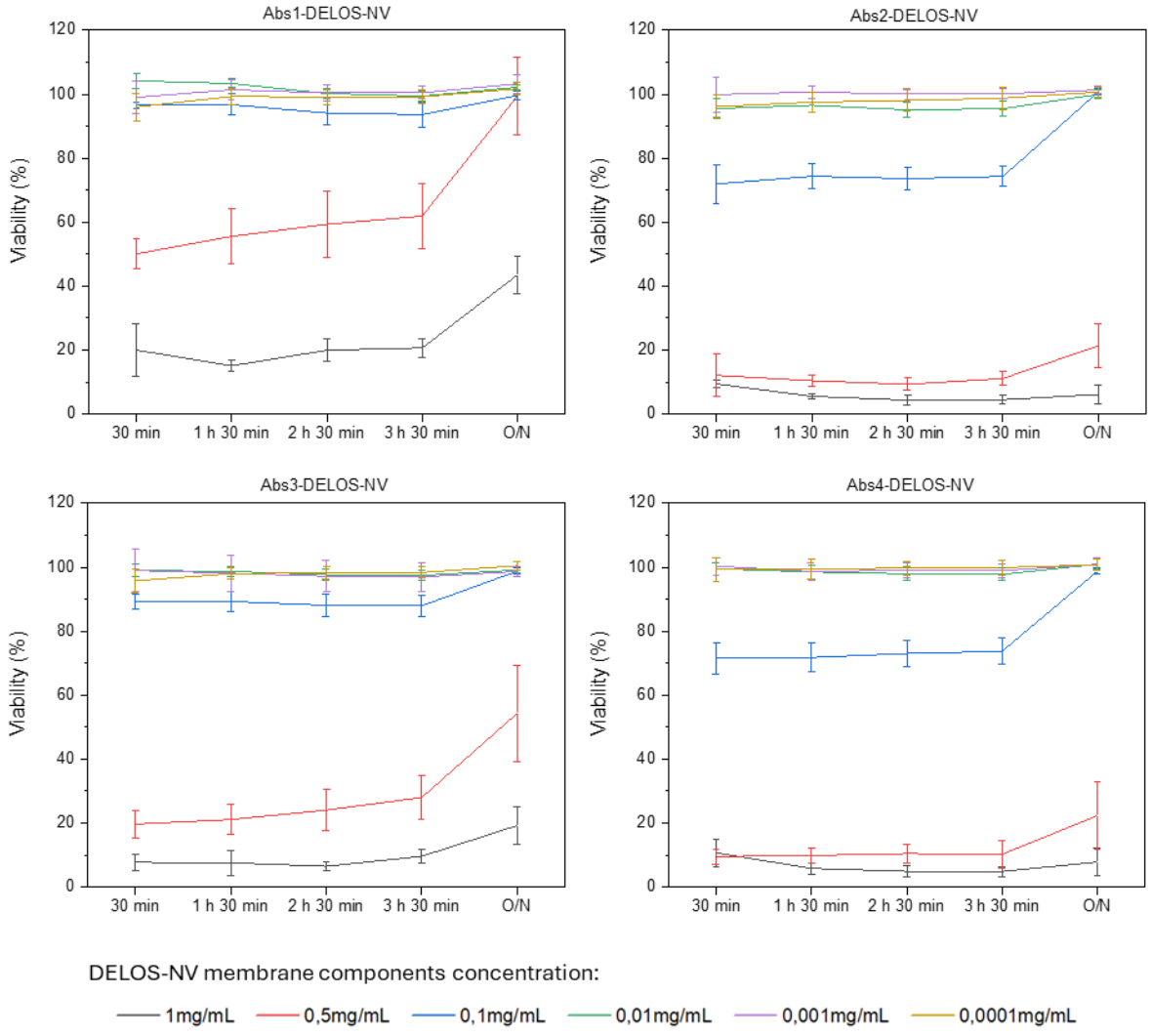


Figure 6.21. *Monitoring of the Caco-2 cells viability results calculated from the colorimetric assay at different timepoints (from 30 minutes to overnight). The data corresponds to the average and SD of one viability assay with 6 wells per formulation.*

Since the absorbance remained constant from 30 minutes to 3.5 hours, the percentage of viability between samples could be compared using the readings taken at 2.5 hours.

Once defined the appropriate measurement time, the viability results were carried out again, in a different day, to assess reproducibility. Since in the first viability assay the cells presented 100% viability with all concentrations of membrane components below or equal to 0.01 mg/mL, lower concentrations than 0.01 mg/mL were not tested in the following experiment. **Figure 6.22** shows the

viability of the different concentrations of each formulation tested. This figure corresponds to the average of the readings at 2.5 hours from the first viability assay (shown in **Figure 6.21**) and the new viability assay performed on a different day. Therefore, the results are the average of 12 replicates, with 6 replicates performed on each independent day.

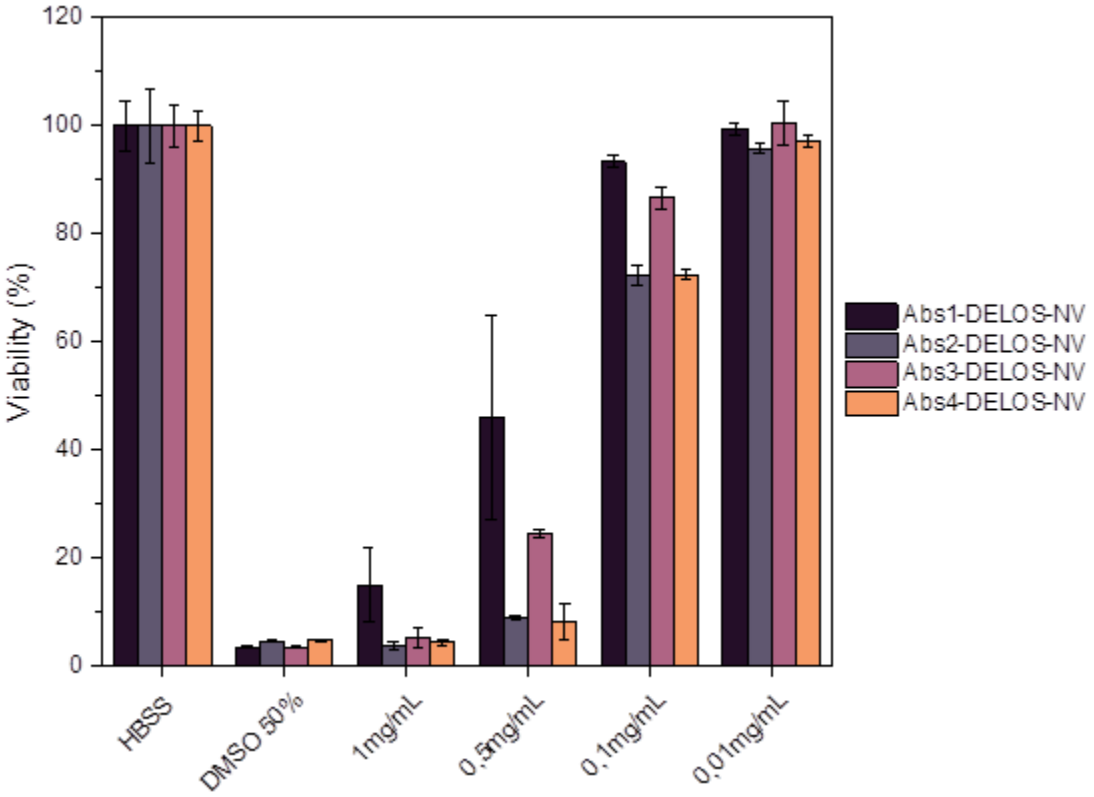


Figure 6.22. *Percentage of viability of the Caco-2 cells when exposed to different concentrations of Abs1-, Abs2-, Abs3- and Abs4-DELOS-NV membrane components for 4 hours. The HBSS group is the negative control and is considered the 100% viability sample, and the Dimethyl sulfoxide (DMSO) 50% group is the positive control. The data corresponds to the average and SD of 12 replicates, performed on two different days.*

Figure 6.22 shows that the factor with a higher impact on the toxicity is the concentration of the sample, understood as the concentration of nanovesicles' membrane components. The lower the concentration, the higher the viability of the cells. The concentration of FITC-BSA in the formulation does not seem to have a significant impact since Abs2- and Abs3-DELOS-NV give almost the same viability results despite Abs2- has a significantly higher amount of protein in the different dilutions tested (see **Table 6.6**). The same occurs with Abs1- and Abs3- formulations at the lower concentrations tested (0.1 mg/mL and 0.01 mg/mL). At the higher concentrations tested (1 mg/mL and 0.5 mg/mL) the Abs1- apparently results in higher viability percentages, however, these results also present larger error bars and therefore are less reliable. A consistent trend observed across all tested concentrations is that samples with a 2:1 CPC:Chol molar ratio (specifically Abs2- and Abs4-) exhibit lower cell viability in Caco-2 cells compared to those with a 1:1 CPC:Chol molar ratio. This suggests that the 2:1 CPC:Chol molar ratio formulations are slightly more toxic to Caco-2 cells.

After reviewing the viability results, it was determined that conducting the permeation assays at a concentration of membrane components of 0.1 mg/mL would be optimal. This concentration was

chosen as it represents the highest feasible concentration while ensuring the majority of cells remain viable, with over 70% viability observed in all cases. Therefore, the four samples (Abs1-, Abs2-, Abs3-, and Abs4-DELOS-NV) were diluted to a concentration of 0.1 mg/mL of membrane components, and permeation assays were conducted with these dilutions as detailed in **Section 6.4.1.4**. Prior to performing the permeation assays, the Caco-2 monolayer was cultured and differentiated.

6.4.1.3. Caco-2 cells differentiation and quality checks to perform permeation assays

Caco-2 cells are grown in permeable supports that allow their 3D differentiation into polarized monolayers that mimic the intestinal epithelium (**Figure 6.23**). This human colon carcinoma cell line, when mature, presents a differentiated phenotype with many functions of the small intestinal villus epithelium.

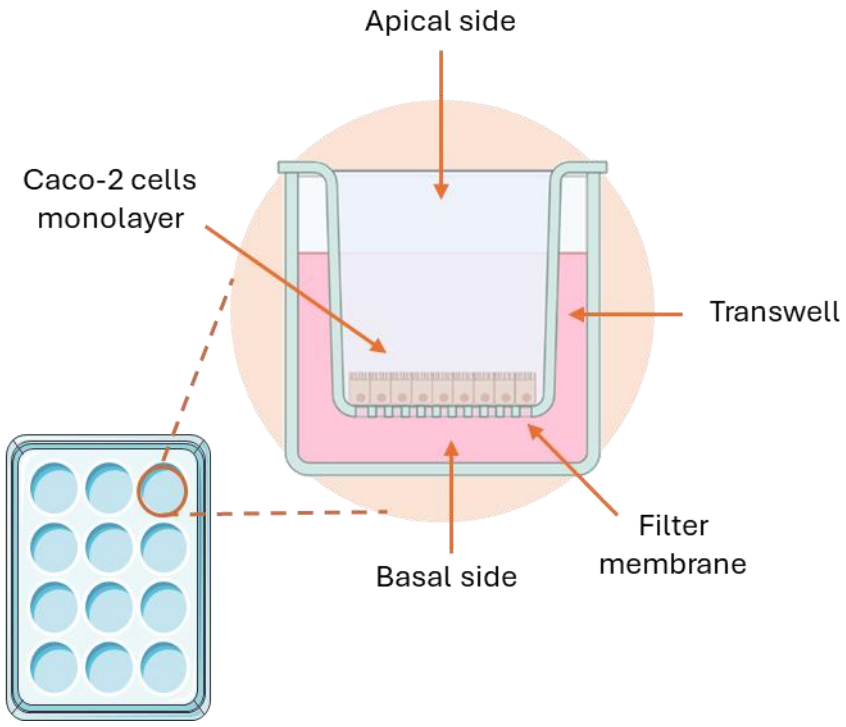


Figure 6.23. *Diagram of a Caco-2 monolayer grown on a permeable filter support.*

The differentiation process is long, it takes around three weeks. A lengthy differentiation process increases the risk of cell contamination or incorrect manipulation, potentially affecting the cells' morphology and functionality. Since the validity of the permeation results depends on the morphology and functionalities of the monolayer obtained, it is recommended to carry on quality tests to assess the proper differentiation of the cells. These tests are always important, but they are especially crucial when setting up the differentiation protocol in a new laboratory, as in this case.

Therefore, cells were grown and subsequently the quality tests were performed, as explained in **Section 9.4.5.1** and **Section 9.4.5.2**.

- Evaluation of cell morphology. The morphology of the cells is preferably evaluated by confocal microscopy[27]. This qualitative control involves visually inspecting the cells to confirm the presence of a monolayer. It is crucial to ensure that multiple layers of cells have not formed, as this would create an abnormal intestinal epithelium unsuitable for permeation assays. This can be done by staining the nucleus with Hoechst (see method in **Section 9.4.5.4**) and corroborating that all the nuclei appear in the same Z height. **Figure 6.24A** shows that all the nuclei appear in the same Z height, while no nuclei were observed in different heights, indicating that the Caco-2 cells are grown in a monolayer.

- Evaluation of the transepithelial electrical resistance (TEER). The TEER can be easily measured in the laboratory (see method in **Section 9.4.5.2**) and also confers relevant information regarding the monolayer integrity. However, the TEER values depend on several factors, such as the Caco-2 clone used, the number of days after seeding, the passage number, and the culture conditions. These conditions are not consistent between different laboratories and therefore, TEER values can be used exclusively for comparison purposes within the same laboratory. TEER is especially interesting to identify outliers in individual monolayers that can indicate some problem with the cell's differentiation. An example of TEER values obtained in the differentiated plates is shown in **Figure 6.24B**. There, it can be observed that all TEER values are very close to or above 1000 Ω cm^2. Cell monolayers with TEER values significantly lower than 1000 Ω cm^2 would have been excluded from the permeation assays.

- Permeation of a hydrophilic paracellular marker. Finally, the most relevant test in this kind of assay is to perform a permeation experiment with a hydrophilic paracellular marker. This type of test is quantitative. Several markers can be employed. In this specific case, the hydrophilic lucifer yellow fluorescent dye was selected (**Figure 6.24C**), since it is widely employed with this finality[27,48-51] following the method explained in **Section 9.4.5.2**. Using a calibration curve fitted to a regression line (R^2 = 0.9998), the fluorescence of lucifer yellow was converted to concentration. Afterward, the percentage was calculated by considering 100% permeability as the equilibrium concentration that would be achieved in the absence of a barrier (see **Equation 9.5** in **Section 9.4.5.6**). **Figure 6.24C** shows that for the control, without monolayer, the permeability is almost 100% while for the Caco-2 monolayer it is significantly lower (17%), indicating an appropriate differentiation of the monolayer.

Therefore, considering all the quality test presented in **Figure 6.24** it can be confirmed that the differentiation protocol was correctly established, assuring that permeation assays can proceed confidently on the Caco-2 monolayers. These are promising results, especially given the lack of prior experience with this cell line in Nanomol-Bio and Nanomol Technologies S.L. Establishing the protocol to properly differentiate the Caco-2 cells grown on permeable supports into intestinal epithelia will allow us to advance more confidently in optimizing DELOS-NV for the oral administration route.

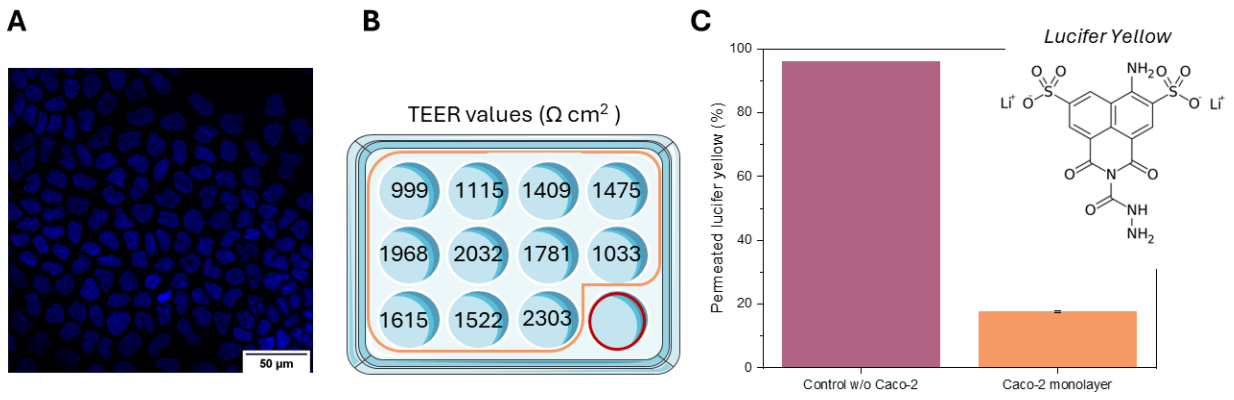


Figure 6.24. *Quality checks of the Caco-2 monolayer integrity. A) Confocal images of the nucleus stained with Hoechst (λ_{ex} = 405 nm, λ_{em} = 408 - 500 nm). No cells were detected at different Z heights. B) TEER values. The well marked with a red circle corresponds to the control without Caco-2 cells. The other 11 wells contain a Caco-2 monolayer. C) 1-hour long lucifer yellow permeation assay. Comparison between transwells without Caco-2 cells and transwells with Caco-2 cells monolayers. The lucifer yellow molecular structure is represented in the graphic.*

6.4.1.4. Caco-2 permeation assays and quantification of the permeability

After confirming the proper differentiation of the Caco-2 monolayer on the transwells, the permeation assays were conducted with the samples described and characterized in **Section 6.4.1.1**. The formulations were applied to the apical side of the Caco-2 monolayers. Following a four-hour incubation, the amount of formulation that permeated to the basal side was quantified using UV-Vis spectroscopy. In future studies, permeation kinetics could be assessed by sampling at various time points during incubation.

For the assays, HBSS buffer pH 7.4 was prepared as explained in **Section 9.1** and samples were diluted in this buffer to 0.1 mg/mL of membrane components, as determined from prior viability assays (see **Section 6.4.1.2**). With this finality, samples Abs1- and Abs2-DELOS-NV were diluted 1:10 and samples Abs3- and Abs4-DELOS-NV were diluted 1:50 (**Table 6.6**). The samples were then filtered through a 0.22 µm sterile PES syringe filter to avoid contamination.

The filtered samples were added to the apical side of the Caco-2 monolayers, and the permeation assays proceeded as detailed in **Section 9.4.5.3**. Controls with FITC-BSA alone were also included to compare permeability with and without DELOS-NV. Samples were collected from both the basal and apical sides at time 0 (immediately after sample addition) and after the four-hour incubation. These were stored in sterile Eppendorf tubes at 5 ± 3 °C until analysis.

At the experiment's conclusion, FITC-BSA in the permeation samples was quantified using a spectrofluorometer to calculate the permeated fraction, and stained Caco-2 cells were observed via confocal microscopy to detect FITC-BSA retention within the cells.

More in detail, right after the permeation assays, FITC-BSA quantification was conducted in the spectrofluorometer of the Luminescence and Biomolecule Spectroscopy Laboratory service from the UAB as self-service.

Quantification was performed directly on the samples without any pretreatment or dilution (see **Section 9.4.5.5**). The fluorescence of FITC-BSA was measured on the apical side of the Caco-2 monolayers at time 0 and 4 hours, as well as on the basal side of the Caco-2 monolayers at 4 hours. The same results were observed for all four samples tested in the permeation assays (Abs1-, Abs2-, Abs3-, and Abs4-DELOS-NV), as well as for the controls with free FITC-BSA. **Figure 6.25A** presents the results for Abs1-DELOS-NV as a representative example. Although the objective was to quantify the FITC-BSA that had permeated the cells, the fluorescence on the apical side after 4 hours was unexpectedly higher than at time 0. This increase in fluorescence on the apical side may be attributed to quenching of the FITC molecules.

Fluorescence quenching is known as any process that causes a reduction in the fluorescence of any given substance. Specifically, concentration quenching occurs when an increase in the concentration of a fluorophore results in a decrease in its fluorescence. As commented before, the commercial FITC-BSA has several FITC molecules attached per protein. It has been demonstrated in the literature that this multiple-FITC-labeled BSA results in a high-concentration quenching phenomena[52] that can be explained by several reasons. When the FITC molecules are too close they can associate and form non-fluorescent dimers. In addition, FRET phenomena can occur between fluorescent molecules and non-fluorescent dimers resulting even in a lower fluorescence emission. This transfer of energy is likely to happen because fluorescein presents a small difference between its maximum absorption and emission wavelength, thus fulfilling a requisite for FRET phenomena[52,53].

During the permeation assay, many factors may be at play when the nanoconjugates meet the cells, such as fusion or breakage of their membranes, resulting in conformational changes of the BSA that can subsequently result in different fluorescence of the multiple-FITC-labelled protein (**Figure 6.25B**). A good approximation to avoid changes in the fluorescence, would consist of dissolving the samples in 90% EtOH to ensure complete dissolution of the nanovesicles membranes as well as denaturalization of the protein. In that way, if the structuration of the protein is controlled in all samples, the fluorescence results could be compared. However, this approach could not be employed in this specific assay because, when diluting the samples, the FITC-BSA fluorescence signal was below the limit of detection.

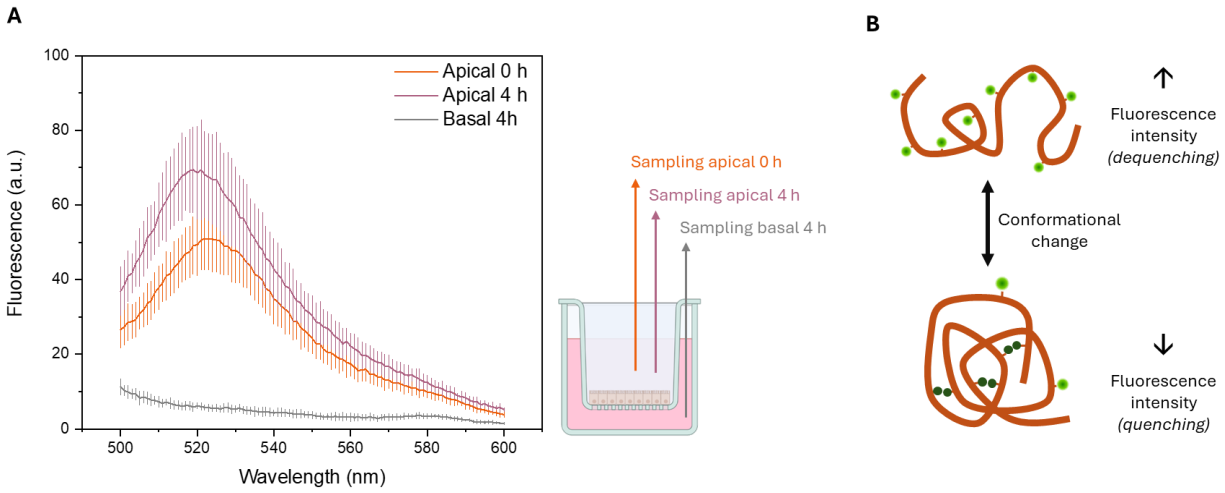


Figure 6.25. *A) Fluorescence quantification (λ_{ex} = 485 nm) of the different samplings (apical time 0, apical time 4 hours and basal time 4 hours) obtained from the permeation assay with Abs1-DELOS-NV. The results correspond to the average and SD of 4 permeation assays conducted in parallel in 4 independent Caco-2 monolayers. B) Scheme of fluorescence quenching/dequenching following protein conformation changes. The red line represents the protein folding and the green dots a labeling fluorophore (e.g. FITC). When two or more fluorophores are too close, concentration quenching can occur.*

Although the initial permeation assays did not yield conclusive results due to the difficult quantification of the FITC-BSA caused by the unexpected concentration quenching, the absence of fluorescence detected in the basal sample after 4 hours of incubation suggests a lack of FITC-BSA permeation with the tested samples.

As mentioned before, the Caco-2 cells were also observed in the confocal microscopy (see the staining and confocal imaging methods in **Section 9.4.5.4**) to search for differences in the internalized FITC-BSA between monolayers treated with the DELOS-NV and FITC-BSA nanoconjugates and treated with the controls with free FITC-BSA (without DELOS-NV). Note that confocal microscopy does not measure the permeated protein (the proportion of protein that would hypothetically reach the systemic circulation), but only the protein that gets internalized inside the Caco-2 cells.

To do so, right after the permeation assays, the filters containing the Caco-2 monolayer were cut and separated from the plastic structure of the transwell. Next, the nuclei of the cells were stained with Hoechst, and the membranes with Cell mask. The stained monolayers were further fixed with paraformaldehyde (PFA) 4% for 10 minutes and stored in HBSS buffer pH 7.4 until their analysis. The day after, images were acquired with the confocal microscope[c] (**Figure 6.26**). The images show that the Caco-2 control monolayers (Caco-2 monolayers not exposed to free FITC-BSA or DELOS-NV containing FITC-BSA) present auto-fluorescence (fluorescence intrinsic to the cell components) at the same wavelength filter (λ_{ex} = 488 nm) used to observe FITC. Therefore, the confocal images were not reliable for detecting internalization differences between the monolayers exposed to DELOS-NV and those not exposed.

[c] *The images were obtained in the Microscopy and X-ray Diffraction Service from the UAB by Dr. Meritxell Vendrell, Higher Research Support Technique from the service.*

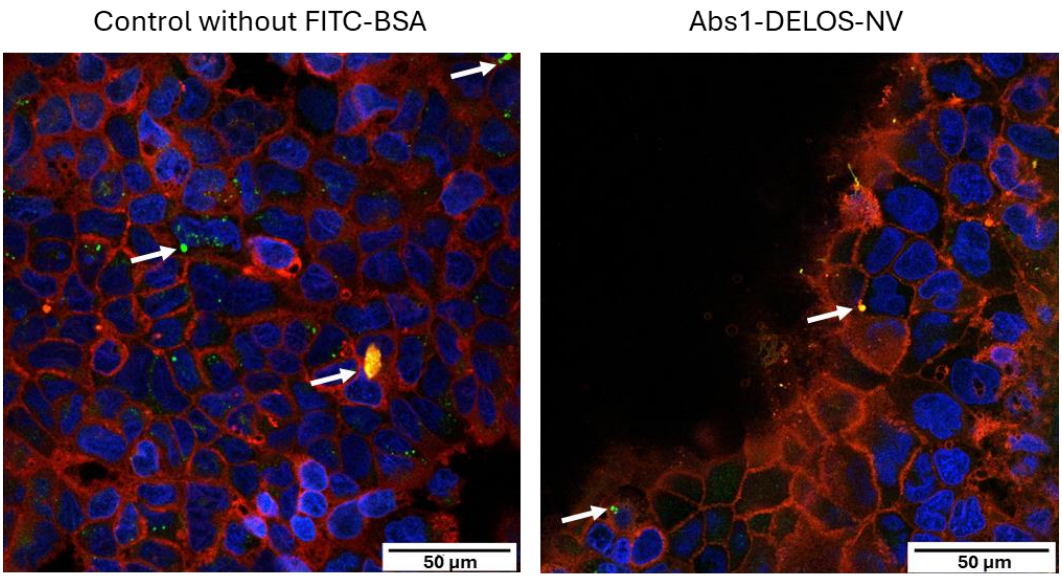


Figure 6.26. *Confocal images of the Caco-2 cells. Nuclei are shown in blue (Hoechst; λ_{ex} = 405 nm), membranes are shown in red (Cell mask; λ_{ex} = 639 nm) and FITC-BSA is in the green channel (λ_{ex} = 488 nm). Right) Caco-2 monolayers exposed to Abs1-nanoconjugates (DELOS-NV + FITC-BSA). Left) Control Caco-2 monolayers not exposed to FITC-BSA. The white arrows highlight the presence of fluorescence in the green channel. It can be observed fluorescence in the control despite the absence of FITC-BSA, indicating that this fluorescence might be intrinsic to the cells.*

As shown, confocal results were inconclusive as fluorescence at λ_{ex} = 488 nm was also detected in cells without FITC-BSA. In addition, spectrofluorometer results suggested that FITC-BSA loaded into the DELOS-NV does not permeate the Caco-2 cells. However, these results were unreliable due to quenching of the FITC-BSA, indicating that FITC-BSA may not be suitable for permeation assays. Moreover, since BSA is present in the media used for Caco-2 differentiation, quantification methods that directly measure BSA, such as an Enzyme-Linked ImmunoSorbent Assay (ELISA), could not be relied upon. Therefore, only the fluorescence of the FITC labeling molecule, which has quenching problems, could be tracked.

Although conclusive results were not obtained, the work developed in this **Section** is significant as it established a robust methodology for differentiating Caco-2 cells into a mature intestinal epithelium, assessing their quality, and conducting permeation assays. This foundation will enable future permeation assays with different nanoconjugates. Consequently, in the following section, the permeation assays were repeated using two newly introduced molecules. These assays were conducted using CacoReady models to expedite the process and obtain results more efficiently.

6.4.2. Permeation assays in CacoReady models

As stated before, the differentiation process of the Caco-2 cells into intestinal monolayers requires a significant investment of time, due to the length of the differentiation process and the set of tests required to assure the quality of the epithelium differentiation. There are alternatives that permit working with this well-known system recognized by the FDA and the EMA but saving time in the

process. Some laboratories have shortened the differentiation process with good results[54], however the phenotype of the cells is not exactly the same. There are also companies that differentiate the cells and provide the cells differentiated, so the experiments can be carried out right after the reception of the plates. This is the case of the Readycell S.L. company (https://readycell.com/). This company sells CacoReady cells, which are Caco-2 cells differentiated over permeable supports with the traditional and well-characterized protocol of 3 weeks. They have patented a medium that permits shipping the differentiated cells preventing their death or alteration.

In this thesis, to explore different alternatives, new permeation experiments were conducted using the CacoReady models acquired from Readycell S.L.

In addition, due to the unreliability of the permeation results obtained with FITC-BSA, the assays were repeated with two new molecules: insulin peptide and lucifer yellow fluorescent dye. The permeation of these molecules, both free in the media and incorporated into DELOS-NV, was compared.

6.4.2.1. Production and physicochemical characterization of nanoconjugates based on insulin integrated in DELOS-NV

Insulin peptide was chosen as a new model biomolecule for permeation assays for several reasons. Its EE% in DELOS-NV is anticipated to be high due to its small size (6 kDa) and its isoelectric point of 5.3. At pH 7.4 in HBSS, insulin is expected to carry a negative charge. This is comparable to rhEGF in terms of size and charge at pH >7. Consequently, electrostatic interactions between insulin and the positively charged polar heads of the nanovesicles are anticipated, as similar interactions were observed for rhEGF binding to Chol:CTAB DELOS-NV in ITC assays in **Section 6.3.1**. In addition, insulin peptide is convenient for permeation assays because it is not present in the medium employed for the Caco-2 differentiation in CacoReady models and it is not secreted by the Caco-2 cells. Therefore, it should be possible to quantify the insulin permeated through an ELISA test without risk of interference with endogenous insulin. This is something that was not possible with the BSA, since it is present in the media employed for the cell's differentiation. Finally, the oral administration of this therapeutical protein is still a challenge to be addressed for the pharmaceutical industry. Research and clinical trials are underway to develop oral forms of insulin[55,56], however, to the best of our knowledge, there are no approved oral insulin pills on the market yet. In addition, some laboratories have tested permeation of the insulin through Caco-2 cells employing liposomes as drug delivery systems[57,58], suggesting that insulin can be a good model molecule for the permeation assays.

For all these reasons, the intestinal permeation of the insulin entrapped in the DELOS-NV was assessed. To do so, nanoconjugates based on DELOS-NV with 1 mg/mL of membrane components and a molar ratio 1:1 CPC:Chol were produced in HBSS buffer pH 7.4 including the insulin at a final concentration of 0.1 mg/mL in the batch. Since the permeation assays explained before were conducted at 0.1 mg/mL membrane components (see **Section 6.4.1.2**), the novel nanoconjugates were produced with a low concentration of membrane components, specifically 1 mg/mL, to minimize the dilution required in the subsequent permeation assays. The nanoconjugates integrating insulin were produced as described in **Section 9.2.1**. Next, they were further diafiltrated by TFF following the procedure described in **Section 9.2.2** and named Ins-DELOS-NV. By this step, the

remanent EtOH and the non-integrated insulin in the DELOS-NV were eliminated (see **Table 9.3** for details on their composition).

The EE% of the insulin in the nanovesicles was calculated as explained in **Section 9.3.6**. The intrinsic tyrosine fluorescence (λ_{ex} = 276 nm and λ_{em} = 305 nm) was used to measure the amount of insulin in the nanoconjugates before and after the diafiltration process. Since the fluorescence peak of the insulin overlapped with the scattering of the nanovesicles, the nanovesicles were dissolved in EtOH 90% (v/v). However, this ethanol also caused the denaturalization of the protein. Right after making the dilutions in EtOH very variable results were obtained between replicates caused by the different exposure of the tyrosines in function of the protein conformation. I. Bekard et. Al.[59] demonstrated that the tyrosine fluorescence upon insulin denaturalization reaches stabilization after 12 h. Inspired by this paper, the dilutions were left overnight for their stabilization, obtaining in that way consistent measurements the day after. Following this methodology an EE% of 89% was determined (**Figure 6.27A)**.

The Ins-DELOS-NV were physiochemically characterized by DLS and ELS (see **Section 9.3.1** and **Figure 6.27B**) to determine their stability over time. The measurements demonstrate that the nanoconjugates are stable for at least two months. At time 14 days, they presented a hydrodynamic diameter of 188.8 ± 2.0 nm, a size PdI of 0.356 ± 0.017 and an apparent Z-potential of 47 ± 7 mV. In addition, Cryo-TEM images (see **Section 9.3.4** and **Figure 6.27C**) were obtained. The images show spherical and unilamellar nanovesicles in most cases. There is a certain degree of interaction between nanoconjugates probably caused by the binding of the insulin with different nanovesicles at the same time, which resembles the results obtained with the FITC-BSA (**Figure 6.20**). Moreover, some nanoconjugates present a wider membrane (marked with yellow arrows), recognized by being more electrodense in the Cryo-TEM images. This could be caused by an extensive coating of their membranes with the insulin peptide. Overall, the results suggest that the insulin peptide is integrated in the DELOS-NV successfully resulting in a stable nanoconjugate system with a high EE% and appropriate physicochemical properties. These results are promising, not only because this nanoconjugate will be used for the permeation assays in Caco-2 cells, but also because these results highlight the potential of employing DELOS-NV for the delivery of this very challenging-to-formulate molecule employed in diabetes treatment.

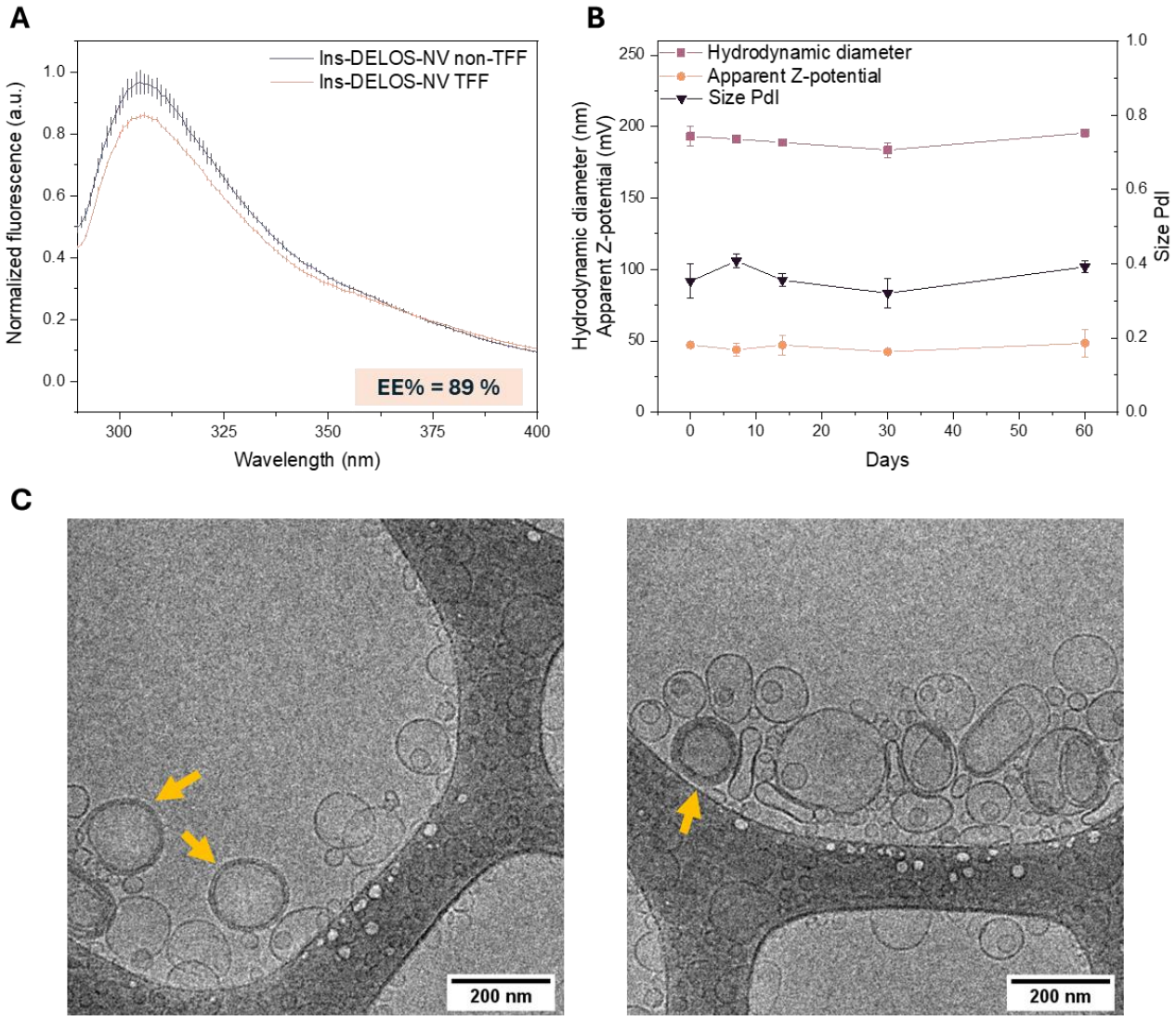


Figure 6.27. *Characterizations of the Ins-DELOS-NV. A) Insulin fluorescence in the Ins-DELOS-NV before and after the diafiltration by TFF (λ_{ex} = 276 nm). The spectra correspond to the average and SD of 4 dilutions of each sample in 90% EtOH (v/v). The EE% was calculated from the intensity at λ_{em} = 305 nm and is shown in the inset. B) Hydrodynamic diameter, apparent Z-potential and size PdI of the Ins-DELOS-NV (diafiltrated by TFF) over a period of 60 days. The results correspond to the averages and SD of 3 consecutive measurements. C) Representative Cryo-TEM images of the Ins-DELOS-NV (diafiltrated by TFF). The arrows highlight an increase in the membrane's width probably caused by the integration of insulin.*

6.4.2.2. Production and physicochemical characterization of nanoconjugates based on lucifer yellow integrated in DELOS-NV

In addition to the insulin peptide, a small molecule was selected to test its permeation through Caco-2 cells. As explained before, lucifer yellow is a hydrophilic paracellular marker employed for testing the integrity of the Caco-2 monolayer. This molecule has very low permeability in Caco-2 monolayers (**Figure 6.24C**). In addition, it is fluorescent and easy to quantify. For this reason, it was decided to

attempt to integrate this molecule in the Chol:CPC DELOS-NV, since an increase in its permeation would clearly indicate an enhancement of permeability facilitated by the DELOS-NV.

Lucifer yellow has two negatively charged sulfonate groups at pH 7.4 (see molecular structure in **Figure 6.24C**). Therefore, it is expected that lucifer yellow binds the positively charged DELOS-NV mainly through electrostatic interaction.

In a first attempt, nanoconjugates with lucifer yellow in HBSS pH 7.4 were produced, with a concentration of membrane components of 1 mg/mL and ratio CPC:Chol 1:1, as it was done with the Ins-DELOS-NV. However, the nanovesicles were not formed at these conditions and an aqueous suspension full of micro- and macroscopic precipitate was acquired (suspension discarded, results not shown).

Next, nanovesicles containing lucifer yellow were produced in a 5 mM histidine buffer at pH 7 to minimize salt concentration and improve the likelihood of obtaining intact nanovesicles. The concentration of membrane components was increased to 5 mg/mL to ensure sufficient entrapment of lucifer yellow and achieve stable formulations. The nanoconjugates were prepared using the DELOS method (see **Section 9.2.1**) with a CPC:Chol ratio of 1:1, and lucifer yellow was dissolved in the aqueous phase of the DELOS formulation to reach a final concentration of 0.4 mg/mL. This resulted in a dispersion of nanoconjugates with a good colloidal appearance—homogeneous and translucent. However, some microscopic orange particles, likely containing lucifer yellow, remained in suspension. These particles were removed by filtering the sample through a 0.45 µm PES syringe filter. Subsequently, the sample was diafiltrated by TFF (see **Section 9.2.2**) to remove residual ethanol and any unentrapped lucifer yellow. The final product, named LY-DELOS-NV, was used for the permeation assay. Details on the sample composition are provided in **Table 9.3**.

In this specific case, the EE% could not be calculated as a percentage of absorbance intensity with respect the theoretical concentration added during the DELOS method, since the sample obtained right after DELOS had precipitated particles. To solve this, a calibration curve was performed, with different concentrations of lucifer yellow dissolved in the same media as the LY-DELOS-NV as explained in **Section 9.3.6**. The calibration curve was measured in the UV-Vis spectrophotometer (lectures made at λ = 428 nm) and then fitted to a regression line with an R^2 of 0.9996 (**Figure 6.28A**). Then, the sample after DELOS filtrated with PES 0.45 µm, and the same DELOS sample filtrated and diafiltrated (LY-DELOS-NV) were measured by UV-Vis spectrophotometer and their concentration was calculated using the obtained regression line (**Figure 6.28B;C**). After the subsequent production steps, a final concentration of 0.2 mg/mL was achieved in the final LY-DELOS-NV sample. To calculate the EE%, the final concentration after TFF (0.2 mg/mL) was divided by the concentration obtained after the precipitate was removed using a 0.45 µm filter (0.24 mg/mL). This resulted in a high EE% of 83%.

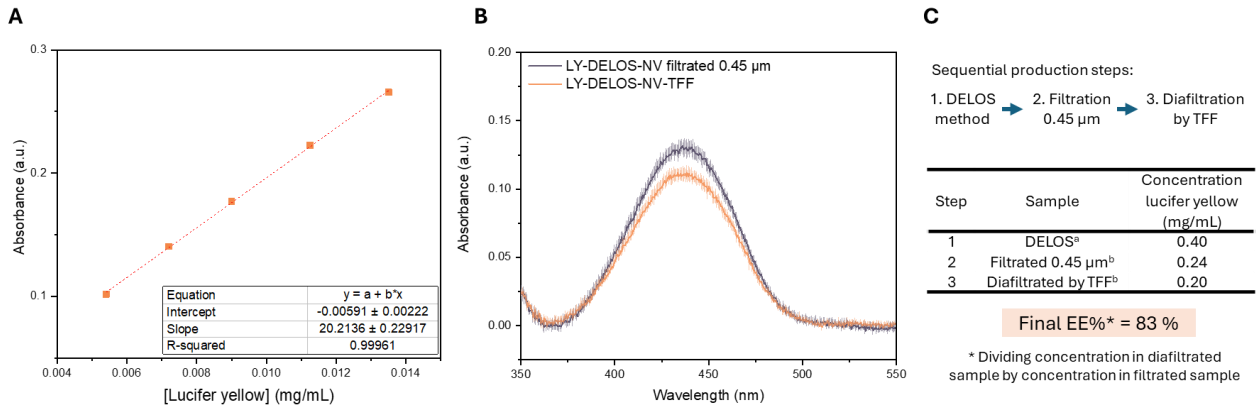


Figure 6.28. *A) UV-Vis calibration curve of the lucifer yellow dissolved in histidine 5 mM pH 7 + 10% EtOH. Lectures made at λ = 428 nm. The regression fit is in the inset. B) UV-Vis spectra of the DELOS-NV containing lucifer yellow after their filtration with PES 0.45 µm filter, and after the filtration and diafiltration by TFF. C) Concentration of lucifer yellow in the DELOS-NV loaded with lucifer yellow after the different production steps and EE%. [a]The concentration of the sample obtained right after DELOS corresponds to the lucifer yellow weighted and added to the reactor. [b]The concentrations of the samples after the 0.45 µm filtration step and after TFF were calculated based on UV-Vis measurements at λ = 428 nm and the corresponding regression fit.*

The LY-DELOS-NV was also characterized by DLS, ELS (see **Section 9.3.1** and **Figure 6.29A**) and Cryo-TEM (see **Section 9.3.4** and **Figure 6.29B**). The DLS and ELS results demonstrate that the obtained sample is composed of small vesicles, with an average hydrodynamic diameter of 142.9 ± 0.8 nm, a size PdI of 0.276 ± 0.007 and a Z-potential of 68.7 ± 1.7 mV. The Cryo-TEM images showed a predominance of SUVs. There were clusters of nanovesicles probably caused by the interaction of the lucifer yellow with different nanovesicles at the same time. In addition, some non-common infinite symbol-like structures, which resembled nanovesicles fusing or dividing, were observed in the sample. This could be caused by a restructuring of the nanovesicles due to the binding of lucifer yellow. In addition, the bilayer of these uncommon structures is very wide, which also suggests the binding of the lucifer yellow. These structures tended to "boil" when exposed to the electron beam of the microscope, as can be observed by the white spots inside the very electrodense membrane. This effect is called "bubbling" and is mainly caused by the radiolysis of water molecules, which results in free radical formation and pockets of hydrogen gas forming within the specimen[60]. All these physicochemical characterizations, which demonstrate the presence of DELOS-NV and lucifer yellow nanoconjugates, suggest that the sample is appropriate for the permeation assays in CacoReady models.

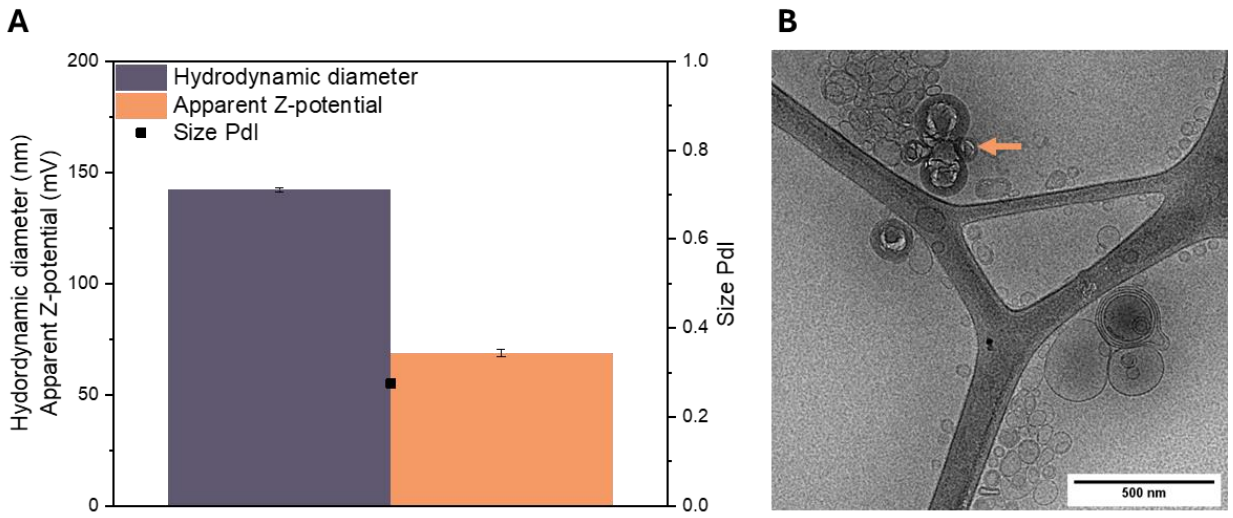


Figure 6.29. *A) Hydrodynamic diameter, apparent Z- and size PdI of the LY-DELOS-NV. The results correspond to the averages and SD of three consecutive measurements. B) Representative Cryo-TEM image of the LY-DELOS-NV. The orange arrow shows a structure with an infinite-like form that was found repeatedly in the sample.*

6.4.2.3. Viability assays in Caco-2 cells with the Ins-DELOS-NV and the LY-DELOS-NV

Before the experiments in the CacoReady models, viability assays were performed with these novel formulations just to confirm that the formulations were non-toxic at the concentration selected from the previous viability experiments **(Section 6.4.1.2)**. Similar results to those obtained in **Section 6.4.1.2** were anticipated, as previous experiments indicated that the concentration of membrane components (Chol + CPC) had the strongest effect on cell viability. Viability in Caco-2 cells was performed following the same procedure as for the previous experiments[d] (see **Section 9.4.4**). In this viability assay only two concentrations (0.5 mg/mL and 0.1 mg/mL of DELOS-NV membrane components) were tested per sample using as a reference the results from the previous assay. **Figure 6.30** shows the viability results. From this graphic, it can be concluded that the samples are non-toxic at the same concentration selected in the previous study with DELOS-NV and FITC-BSA nanoconjugates.

[d]*This second round of viability assays were contracted to the Cell Culture, Antibody Production and Cytometry Service from the UAB.*

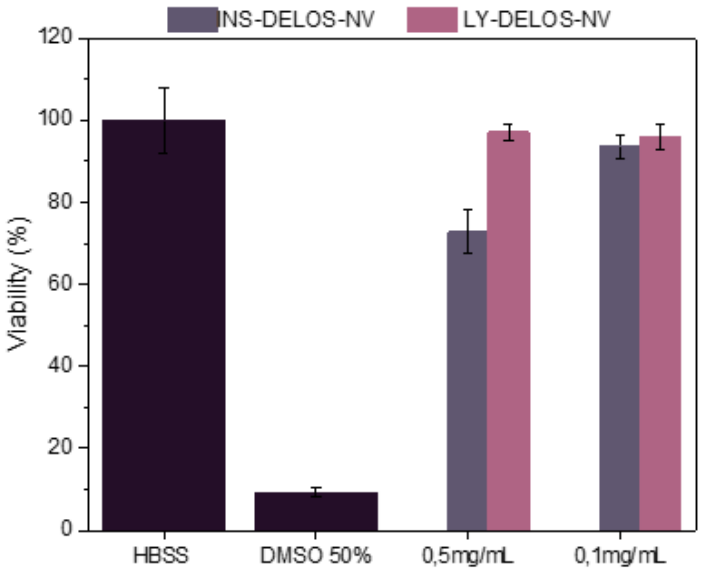


Figure 6.30. *Percentage of viability of the Caco-2 cells when exposed to different concentrations of Ins-DELOS-NV and LY-DELOS-NV membrane components for 4 hours. The HBSS is the negative control and is considered the 100% viability sample, and the DMSO 50% is the positive control. The data corresponds to the average and SD of 6-wells from one viability assay.*

Based on these results was concluded that the permeation assays using CacoReady models with the novel formulations prepared could be conducted at 0.1 mg/mL of membrane components concentration with a very low risk of cell damage.

6.4.2.4. CacoReady permeation assays and quantification of the permeability

The CacoReady cells are shipped in a solidified medium, which is liquified at 37 °C. Upon their receipt, they are left to stabilize at room temperature overnight and the day after they are liquified by incubating them for 4 hours at 37 °C. Next, the liquified medium is exchanged by the Caco-2 cells culture medium.

Prior to the permeation assays, the quality of the received cells was assessed by performing TEER measurements[e] (see **Section 9.4.5.2**). TEER values of all Caco-2 monolayers were in the range 1328.25 Ω cm^2 to 3017.19 Ω cm^2, hence, significantly above the acceptance criterion defined by Readycell for their CacoReady system, which is 1000 Ω cm^2. After having assessed the quality of the monolayers, and having confirmed that all TEER values were above 1000 Ω cm^2, the permeation assays were conducted.

The permeation assays were performed as described in **Section 9.4.5.3**. The cells were incubated with the samples, which were first diluted to a concentration of 0.1 mg/mL of membrane components in HBSS pH 7.4 buffer and then filtered using a 0.22 µm sterile PES syringe filter.

[e] *This second round of TEER measurements and permeation assays in CacoReady models were contracted to the Cell Culture, Antibody Production and Cytometry Service from the UAB.*

Controls with the free molecules (insulin or lucifer yellow) but without DELOS-NV were also considered in the permeation assay in order to detect differences with respect to the same amount of molecules integrated in the DELOS-NV. For each condition tested (free insulin, Ins-DELOS-NV, free lucifer yellow and LY-DELOS-NV), 4 replicates were performed. The Caco-2 cells were incubated in the presence of the samples for 4 hours at 37 ºC and 5% CO_2. Next, samplings were performed from the apical side immediately at time 0 (right after the addition of the sample) and at the end of the 4-hour incubation period. Samplings from the basolateral sides were also conducted at the end of the assay.

Quantification of the samples was performed as described in **Section 9.4.5.6** (lucifer yellow) and **Section 9.4.5.7** (insulin).

For the lucifer yellow, a calibration curve with different concentrations of free lucifer yellow dissolved in HBSS buffer pH 7.4 was performed and measured in a plate spectrofluorometer (λ_{ex} = 485 nm and λ_{em} = 535 nm). The calibration curve was fitted to a regression equation with an R^2 of 0.9998 (**Figure 6.31A**). The control samples with free lucifer yellow (without DELOS-NV), were measured directly in a plate spectrofluorometer. The fluorescence intensity values were converted to concentration using the calibration curve (**Figure 6.31A**), and the concentration balance was calculated using **Equation 6.2**, resulting in a balance of 78%. For the quantification of LY-DELOS-NV permeation samples, it was first confirmed that the small amount of DELOS-NV used in the permeation assays did not affect the fluorescence measurements, as it is known that the microenvironment of a molecule can influence its fluorescence[61]. Once confirmed, the LY-DELOS-NV samples were also measured directly, without dilution. The intensity values were converted to concentration, and a concentration balance of 87% was achieved.

Note that not achieving a 100% concentration balance might be due to some retention of the free LY and LY-DELOS-NV within the cells or on the cells surface.

$$\boldsymbol{Concentration\ balance\ =\ \frac{(Concentration\ apical\ t4h + Concentration\ basal\ t4h)}{Concentration\ apical\ t0h} x100}$$

Equation 6.2. *Concentration balance in the permeation assays.*

Next, the percentage of permeated lucifer yellow was calculated with **Equation 9.5** shown in **Section 9.4.5.6**. As shown in **Figure 6.31B**, the permeation of lucifer yellow to the basal side after 4 hours of assay is double the concentration observed in the absence of DELOS-NV, with a significant difference (p-value = 0.0013). This promising result suggests that DELOS-NV enhance the permeation of lucifer yellow through the intestinal epithelium. However, after 4 hours, only half of the lucifer yellow that could have potentially permeated actually reached the basal side, indicating room for further improvement. Optimizing DELOS-NV membranes, such as incorporating biotin receptors prevalent throughout the intestinal epithelium[62,63], could enhance permeability.

The apparent permeability coefficient (P_{app}), a relevant parameter in Caco-2 assays, was also calculated. P_{app} is the velocity at which a molecule crosses a membrane (it has units of distance over time, i.e., cm/s) and indicates how easy it is for a specific molecule to move across the Caco-2 monolayer. Using **Equation 6.3**, the P_{app} for the free lucifer yellow was (2.3 ± 0.1) x 10^{-5} cm/s, while for

the LY-DELOS-NV it was (4.4 ± 0.3) x 10^{-5} cm/s. This result further supports the enhancement of lucifer yellow permeation across Caco-2 monolayers by DELOS-NV.

$$P_{app} = \frac{dQ}{dT} x \frac{1}{AxC_0}$$

Equation 6.3. *Apparent permeability coefficient (P_{app}). dQ/dT is the amount of substance that crosses the monolayer at each time point (in seconds). A is the area of the filter (0.33 cm^2 for 24-wells CacoReady) and C_0 the concentration added to the apical side at time 0.*

It is important to note that the P_{app} values were calculated at a single time point (4 hours). Since the lucifer yellow permeability kinetics are unknown, these P_{app} values should be considered as references. Their accuracy needs confirmation by ensuring that the permeation remains linear at the 4-hour mark. Future experiments, beyond the scope of this thesis, will study the permeation kinetics of lucifer yellow through sampling at different time points. Nonetheless, these preliminary results suggest that DELOS-NV may be suitable for the systemic administration of certain molecules by facilitating their passage through the intestinal epithelium.

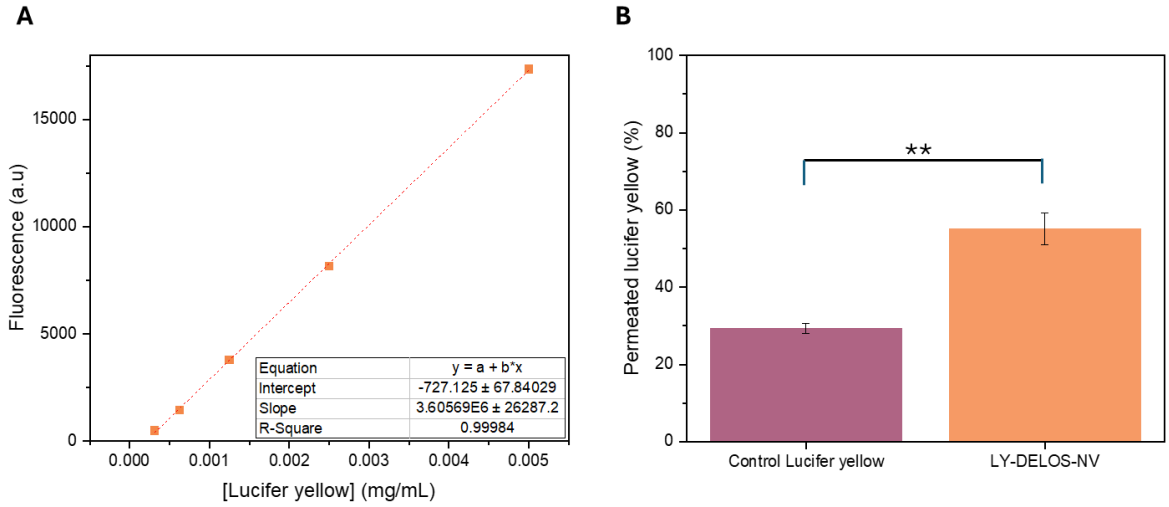


Figure 6.31. *A) Fluorescence calibration curve of the lucifer yellow in HBSS buffer pH 7.4 (λ_{ex} = 485; λ_{em} = 535). Results correspond to the average and SD of two replicates per concentration. The SD is very small for the graphic scale, and therefore it is not possible to observe it. B) Percentage of permeated lucifer yellow in the CacoReady permeation assays for the control with free lucifer yellow and for the samples containing LY-DELOS-NV. ** P-value < 0.01.*

As a second step, the samples obtained from the permeation assays with the Ins-DELOS-NV were also quantified to see what would occur with the permeation of a biomolecule. The Ins-DELOS-NV permeation was assessed by an ELISA test (see **Section 9.4.5.7**)[f]. A calibration curve with known concentrations of insulin standard was produced and fitted into a logistic equation (see **Figure 6.32A**). From the linear range of this calibration curve could be determined the LoD using the **Equation 9.6** shown in **Section 9.4.5.7 (Figure 6.32B)**. The LoD was found to be 7.6 pmol/L. Appropriate dilutions of the samples were made, and the ELISA test was performed. The results

[f] *The ELISA test was contracted to the Cell Culture, Antibody Production and Cytometry Service from the UAB.*

demonstrated that the insulin does not permeate the Caco-2 monolayer, either when free in solution (control) or when integrated into the DELOS-NV (Ins-DELOS-NV). The concentration in the basal compartment after 4 hours of assay was indetectable, thus meaning that it was below the LoD of 7.6 pmol/L (**Figure 6.32C)**. Therefore, in this specific case, it was concluded that with the current composition of DELOS-NV (Chol and CPC at an equimolar ratio), insulin does not permeate the Caco-2 monolayer. This result is consistent with initial experiments using FITC-BSA, which showed no fluorescence on the basal side after a 4-hour assay, suggesting that the protein did not permeate de Caco-2 monolayers.

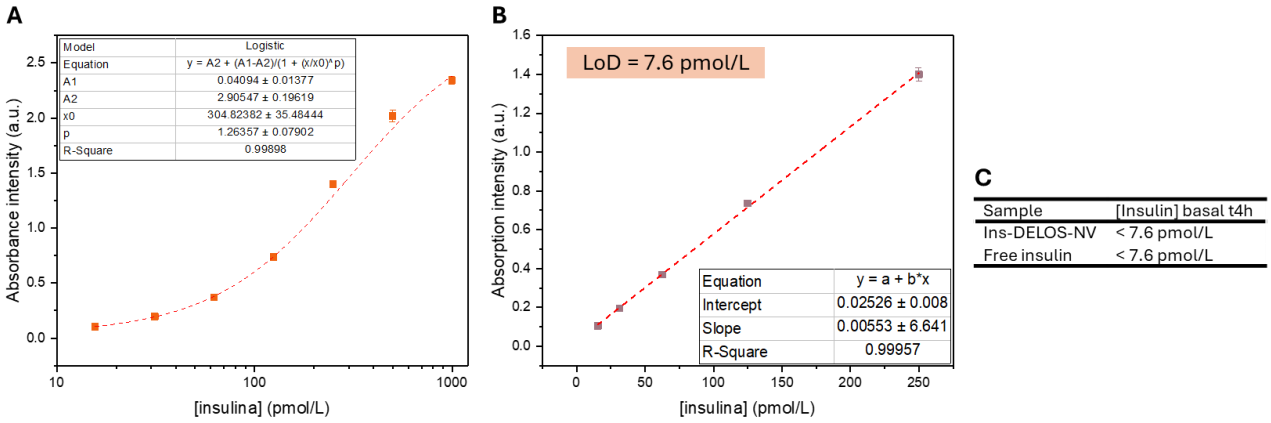


Figure 6.32. *A) Calibration curve and B) Linear range of the calibration curve with the LoD of the insulin with the ELISA assay. C) The permeated insulin in a 4-hour assay is indetectable for the two samples tested, free insulin and Ins-DELOS-NV, indicating that there is no significant permeation of insulin.*

In the present section different results have been obtained for the assays conducted with the lucifer yellow and with the insulin. The DELOS-NV showed potential for enhancing permeation of the lucifer yellow through the intestinal epithelium, since the permeability of the lucifer yellow with DELOS-NV was double the permeability of the free lucifer yellow. In contrast, the permeability of the insulin was below 7.6 pmol/L for both the control and the Ins-DELOS-NV indicating that no permeation of insulin occurred in either case. Note that preliminary results with the FITC-BSA and DELOS-NV nanoconjugates also suggested lack of permeability of the FITC-BSA, supporting the results achieved with the insulin. Hence, oral administration of DELOS-NV with Chol:CPC at an equimolar ratio might be appropriate for both, systemic and local delivery to the gastrointestinal tract, depending on the entrapped molecule.

The next steps, beyond the scope of this thesis, would involve repeating the assays with different small molecules and biomolecules to better characterized the capabilities of the DELOS-NV. In addition, for those molecules in which enhancement of the permeability is demonstrated, permeability kinetics should be studied (i.e., lucifer yellow permeability kinetics). Additionally, for molecules with low permeability across the monolayers, it would be valuable to investigate the ability of DELOS-NV to enter cells and exert their function within the lumen of gastrointestinal cells. This could potentially broaden their application to a wider range of gastrointestinal diseases, extending beyond just targeting surface receptors.

Finally, it must be noted that the Chol:CPC DELOS-NV developed in this thesis were not specifically designed to enhance intestinal permeation. Future work, which lies outside the scope of this thesis, will focus on incorporating specific molecules into the nanovesicle membranes to improve cell penetration by interacting with receptors, such as biotin (vitamin B7) receptors, which are prevalent throughout the intestinal tract[62,63]. This work will be carried forward by Marta Vieira, a Ph.D. student at the Nanomol-Bio group and Nanomol Technologies S.L., who will build on the foundations established in this thesis and contribute to further exploring the promising results achieved.

6.5. Summary of the chapter and perspectives

The objective of this chapter was to test the effect of Chol:CPC DELOS-NV on the permeability of the intestinal epithelium. This could shed light on the capabilities of the Chol:CPC DELOS-NV and help determine which diseases can be addressed with them.

The experimental results presented in this **Chapter** are divided into three major sections. One corresponds to the development of a novel nanoformulation with the Chol:CPC DELOS-NV and FITC-BSA as a model biomolecule (**Section 6.2**), a second one focuses on determining the binding thermodynamics between the FITC-BSA and the DELOS-NV using ITC (**Section 6.3**), and the last section focuses on testing the permeability of different model molecules through the Caco-2 cells intestinal epithelium model (**Section 6.4**).

- In the first experimental **Section 6.2**, a DoE was performed and permitted to identify the optimal combinations of factors to have higher probabilities of obtaining DELOS-NV loaded with FITC-BSA and meeting the desired CQA specifications. It was determined that working with lower concentrations of protein (0.01 mg/mL) increased the probabilities of obtaining DELOS-NV with the desired CQA specifications.

- Next, in **Section 6.3** the thermodynamics of the FITC-BSA binding to the Chol:CPC DELOS-NV were assessed. To set up the methodology for this study, first, the binding thermodynamics of a very well-known formulation were studied. The familiar system employed for the methodology setup was based on rhEGF attached to Chol:CTAB DELOS-NV in histidine 5 mM buffer at pH 7. This system has been studied for more than 10 years in Nanomol Technologies S.L. and Nanomol-Bio group, and is very well characterized; however, binding thermodynamics had not been studied before. By studying the thermodynamics of this system, experience with the ITC equipment and the AFFINImeter software for the data fitting was acquired. It was found that the rhEGF binding to DELOS-NV is exothermic with a high enthalpy gain. The obtained values suggest that the binding is led by electrostatic attraction together with restructuration of the protein in the DELOS-NV membrane such as π-cation and π-stacking interactions of aromatic amino acids (Trp and Tyr) with CTAB and cholesterol.

  Following the characterization of the rhEGF binding to the Chol:CTAB DELOS-NV, the characterization of the binding thermodynamics between the FITC-BSA and the Chol:CPC DELOS-NV in HBSS buffer at pH 7.4 was conducted. The results showed that the interaction

was mostly endothermic, indicating that an entropy increase was the leading cause of the binding. Thanks to these results, it could be determined that the FITC-BSA mostly binds the nanovesicles by hydrophobic forces in contrast with the rhEGF. Therefore, the **Section 6.3** helped to better understand the interaction of two different proteins with the DELOS-NV and allowed gaining experience with the ITC technique, paving the way for the characterization of other proteins. In addition, the high enthalpy characterizing the interaction between FITC-BSA and DELOS-NV indicates a strong binding, suggesting that the protein will not prematurely release the nanovesicles before the permeation assay in Caco-2 cells.

- In the last **Section 6.4** the permeability of nanoconjugates in the Caco-2 intestinal model was assessed. First, the procedure to differentiate the Caco-2 cells was established for the first time in Nanomol-Bio and Nanomol Technologies S.L. All the conducted quality tests demonstrated an appropriate differentiation of the cells into a mature epithelium.

  The permeability of the FITC-BSA DELOS-NV nanoconjugate through the Caco-2 monolayer was tested. The results obtained with this model molecule suggested that the nanoconjugate does not permeate the monolayer, as almost no fluorescence was detected in the basal side after a 4-hour incubation period. However, these results were not very reliable, as the FITC experienced concentration quenching, biasing the results. To confirm these findings, two different molecules were also loaded into the Chol:CPC DELOS-NV: the insulin peptide as a model protein and the lucifer yellow fluorescent dye as a model small molecule. The loading of both molecules was successful, achieving very high EE% in both cases (83% for the lucifer yellow and 89% for the insulin).

  Permeation assays were carried out with these two novel nanoconjugates in CacoReady models. CacoReady models were purchased from ReadyCell S.L. and correspond to Caco-2 cell monolayers differentiated and shipped in a special medium to protect them during transport. Permeation assays with the insulin showed no permeation of the protein in a 4-hour assay, confirming the preliminary results achieved with the FITC-BSA, and indicating that DELOS-NV might be more appropriate for local administration of certain proteins and molecules of high molecular weight in the gastrointestinal tract.

  On the other hand, DELOS-NV significantly increased the permeability of lucifer yellow, resulting in twice the concentration permeating the monolayer compared to the free form of the dye. The P_{app} also suggested an increase of the permeability mediated by the DELOS-NV. Therefore, these promising results suggest that DELOS-NV can also be employed for systemic delivery of certain molecules.

These results suggest that DELOS-NV have potential for either systemic or local delivery in the gastrointestinal tract, depending on the integrated molecule.

The next **Chapter 7** will explore the potential of DELOS-NV for the local diagnosis of colorectal cancers. The Chol:CPC DELOS-NV will be redesigned to incorporate a sensing biomolecule, transforming them into novel biosensors with potential applications in cancer diagnosis within the gastrointestinal tract, as a first proof of concept of a possible local application for DELOS-NV.

6.6. References

1. S. Davis. Alternative routes of administration – a focus on oral biologics. *Eur. Pharm. Rev.* **2020**, No. 5, 1–8.
2. M. Naeem, U.A. Awan, F. Subhan, et al. Advances in colon-targeted nano-drug delivery systems: challenges and solutions. *Arch. Pharm. Res.* **2020**, 43 (1), 153–169.
3. United european gastroenterology. Burden, economic impact and research gaps: Key findings from the Pan-European study on digestive diseases and cancers; **2023**.
4. R.L. Siegel, N.S. Wagle, A. Cercek, R.A. Smith, A. Jemal. Colorectal cancer statistics, 2023. *CA. Cancer J. Clin.* **2023**, 73 (3), 233–254.
5. P. Lundquist, P. Artursson. Oral absorption of peptides and nanoparticles across the human intestine: Opportunities, limitations and studies in human tissues. *Adv. Drug Deliv. Rev.* **2016**, 106, 256–276.
6. B. Homayun, X. Lin, H.J. Choi. Challenges and recent progress in oral drug delivery systems for biopharmaceuticals. *Pharmaceutics* **2019**, 11 (129), 1–29.
7. M. Rossetti, L. Stella, J. Morlà-Folch, et al. Engineering DNA-grafted quatsomes as stable nucleic acid-responsive fluorescent nanovesicles. *Adv. Funct. Mater.* **2021**, 31 (46), 1–9.
8. A. Boloix, N. Feiner-Gracia, M. Köber, et al. Engineering pH-sensitive stable nanovesicles for delivery of microRNA therapeutics. *Small* **2022**, 18 (3), 2101959.
9. V. De Leo, F. Milano, E. Mancini, et al. Encapsulation of curcumin-loaded liposomes for colonic drug delivery in a pH-responsive polymer cluster using a pH-driven and organic solvent-free process. *Molecules* **2018**, 23 (4), 1–15.
10. E.M. Coma-Cros, A. Biosca, E. Lantero, et al. Antimalarial activity of orally administered curcumin incorporated in Eudragit®-containing liposomes. *Int. J. Mol. Sci.* **2018**, 19 (5), 1361.
11. M.A. Amer, E.A. Essa, A.A. Donia, G.M. El Maghraby. Development and evaluation of liquid oral controlled release systems for Losartan potassium. *J. Appl. Pharm. Sci.* **2019**, 9 (8), 86–93.
12. V. Nikam. Eudragit a versatile polymer : A review. *Pharmacol. online* **2011**, 1, 152–164.
13. R. Bansil, B.S. Turner. The biology of mucus: Composition, synthesis and organization. *Adv. Drug Deliv. Rev.* **2018**, 124, 3–15.
14. X. Li, D. Chen, C. Le, et al. Novel mucus-penetrating liposomes as a potential oral drug delivery system: preparation, in vitro characterization, and enhanced cellular uptake. *Int. J. Nanomedicine* **2011**, 6, 3151.
15. P.R. Karn, Z. Vanić, I. Pepić, N. Škalko-Basnet. Mucoadhesive liposomal delivery systems: The choice of coating material. *Drug Dev. Ind. Pharm.* **2011**, 37 (4), 482–488.
16. Y.-Y. Wang, S.K. Lai, J.S. Suk, et al. Addressing the PEG mucoadhesivity paradox to engineer nanoparticles that “slip” through the human mucus barrier. *Angew Chem Int Ed Engl* **2008**, 47 (50), 9726–9729.

17. Y. Santos, A.P. Jaramillo. Effectiveness of mesalamine in patients with ulcerative colitis: A systematic review. *Cureus* **2023**, 15 (8).

18. T. Nunes, M. Barreiro-de Acosta, I. Marin-Jiménez, P. Nos, M. Sans. Oral locally active steroids in inflammatory bowel disease. *J. Crohn's Colitis* **2013**, 7 (3), 183–191.

19. FDA. FY2015 Regulatory science research report: Locally-acting gastrointestinal drugs https://www.fda.gov/industry/generic-drug-user-fee-amendments/fy2015-regulatory-science-research-report-locally-acting-gastrointestinal-drugs.

20. D. Dahlgren, H. Lennernäs. Intestinal permeability and drug absorption: predictive experimental, computational and in vivo approaches. *Pharmaceutics* **2019**, 11 (8).

21. K. Sugano. Introduction to computational oral absorption simulation. *Expert Opin. Drug Metab. Toxicol.* **2009**, 5 (3), 259–293.

22. J. Stappaerts, J. Brouwers, P. Annaert, P. Augustijns. In situ perfusion in rodents to explore intestinal drug absorption: Challenges and opportunities. *Int. J. Pharm.* **2015**, 478 (2), 665–681.

23. A. Fedi, C. Vitale, G. Ponschin, et al. In vitro models replicating the human intestinal epithelium for absorption and metabolism studies: A systematic review. *J. Control. Release* **2021**, 335, 247–268.

24. FDA. Biopharmaceutics classification system-based biowaivers: Guidance for industry; **2021**.

25. EMA. Guideline on biopharmaceutics classification system-based biowaivers; **2023**.

26. M. Hu, J. Ling, H. Lin, J. Chen. Use of Caco-2 cell monolayers to study drug absorption and metabolism. In *Optimazation of Drug Discovery: In Vitro Methods*; **2004**; pp 19–35.

27. I. Hubatsch, E.G.E. Ragnarsson, P. Artursson. Determination of drug permeability and prediction of drug absorption in Caco-2 monolayers. *Nat. Protoc.* **2007**, 2 (9), 2111–2119.

28. Y. Sambuy, I. De Angelis, G. Ranaldi, et al. The Caco-2 cell line as a model of the intestinal barrier: Influence of cell and culture-related factors on Caco-2 cell functional characteristics. *Cell Biol. Toxicol.* **2005**, 21 (1), 1–26.

29. C.S. Hu, C.H. Chiang, P. Da Hong, M.K. Yeh. Influence of charge on FITC-BSA-loaded chondroitin sulfate-chitosan nanoparticles upon cell uptake in human Caco-2 cell monolayers. *Int. J. Nanomedicine* **2012**, 7, 4861–4872.

30. F. Chen, Z.-R. Zhang, X. Qin, M. Wang, Y. Huang. In vitro and in vivo study of N-trimethyl chitosan nanoparticles for oral protein delivery. *Int. J. Pharm.* **2008**, 349, 226–233.

31. F. Lagarce, E. Roger. Nanocarrier absorption studies with Caco-2 cells. In *Caco-2 cells and their uses*; Nova Science Publishers, Inc, **2011**; pp 1–17.

32. FDA. FDA inactive ingredient database https://www.accessdata.fda.gov/scripts/cder/iig/index.cfm.

33. K. Baler, O.A. Martin, M.A. Carignano, et al. Electrostatic unfolding and interactions of albumin driven by pH changes: A molecular dynamics study. *J. Phys. Chem. B* **2014**, 118 (4),

921–930.

34. D.A. Ucko. pH indicators. In *Molecular probes™ handbook: A guide to fluorescent probes and labeling technologies*; **2010**; pp 883–902.

35. L. Damian. Isothermal titration calorimetry for studying protein-ligand interactions. *Methods Mol. Biol.* **2013**, 1008, 103–118.

36. J. Seelig. Thermodynamics of lipid-peptide interactions. *Biochim. Biophys. Acta - Biomembr.* **2004**, 1666, 40–50.

37. S.C. Tso, T.A. Jowitt, C.A. Brautigam. The feasibility of determining kinetic constants from isothermal titration calorimetry data. *Biophys. J.* **2022**, 121 (12), 2474–2484.

38. C. Alemdaroğlu, Z. Degim, N. Celebi, et al. Investigation of epidermal growth factor containing liposome formulation effects on burn wound healing. *J. Biomed. Mater. Res. Part A* **2008**, 85 (1), 271–283.

39. H. Santana, L. Ventosa, E. Martínez, et al. Vesiculas que comprenden factor de crecimiento epidermico y composiciones que las contienen. WO2014/019555, 2014.

40. L. Ballell-Hosa. Translation of DELOS nanovesicle formulations into new pharmaceutical candidates. *Doctoral Dissertation, Universitat Autonoma de Barcelona,* **2022**.

41. M. Köber, S. Illa-Tuset, L. Ferrer-Tasies, et al. Stable nanovesicles formed by intrinsically planar bilayers. *J. Colloid Interface Sci.* **2023**, 631, 202–211.

42. S.R. Feroz, S.N.A. Malek, S. Tayyab. Characteristics and thermodynamics of the interaction of 6-shogaol with human serum albumin as studied by isothermal titration calorimetry. *Brazilian J. Pharm. Sci.* **2016**, 52 (3), 443–446.

43. L. Ferrer-Tasies, H. Santana, I. Cabrera-Puig, et al. Recombinant human epidermal growth factor/Quatsome nanoconjugates: A robust topical delivery system for complex wound healing. *Adv. Ther.* **2021**, 4 (6), 2000260.

44. J.M. Sanders, M.E. Wampole, M.L. Thakur, E. Wickstrom. Molecular determinants of epidermal growth factor binding: a molecular dynamics study. *PLoS One* **2013**, 8 (1), e54136.

45. G. Vargas Nadal. Novel Quatsome nanovesicles, prepared using CO2, for the development of advanced nanomedicines. *Doctoral Dissertation, Universitat de Barcelona,* **2020**.

46. L. Salade, N. Wauthoz, M. Deleu, et al. Development of coated liposomes loaded with ghrelin for nose-to-brain delivery for the treatment of cachexia. *Int. J. Nanomedicine* **2017**, 12, 8531–8543.

47. Y. Yokouchi, T. Tsunoda, T. Imura, et al. Effect of adsorption of bovine serum albumin on liposomal membrane characteristics. *Colloids Surfaces B Biointerfaces* **2001**, 20 (2), 95–103.

48. C.L. Pires, C. Praça, P.A.T. Martins, et al. Re-use of Caco-2 monolayers in permeability assays—Validation regarding cell monolayer integrity. *Pharmaceutics* **2021**, 13 (10), 1563.

49. I.J. Hidalgo, T.J. Raub, R.T. Borchardt. Characterization of the human colon carcinoma cell line (Caco-2) as a model system for intestinal epithelial permeability. *Gastroenterology* **1989**, 96 (2), 736–749.

50. S. Aldrich. Barrier formation and permeability assays using Millicell® hanging cell culture inserts https://www.sigmaaldrich.com/ES/es/technical-documents/technical-article/cell-culture-and-cell-culture-analysis/cell-based-assays/barrier-formation-permeability-assays.

51. M.J.C. Santbergen, M. van der Zande, A. Gerssen, H. Bouwmeester, M.W.F. Nielen. Dynamic in vitro intestinal barrier model coupled to chip-based liquid chromatography mass spectrometry for oral bioavailability studies. *Anal. Bioanal. Chem.* **2020**, 412 (5), 1111–1122.

52. C. Wischke, H.H. Borchert. Fluorescein isothiocyanate labelled bovine serum albumin (FITC-BSA) as a model protein drug: Opportunities and drawbacks. *Pharmazie* **2006**, 61 (9), 770–774.

53. R.F. Chen, J.R. Knutson. Mechanism of fluorescence concentration quenching of carboxyfluorescein in liposomes: Energy transfer to nonfluorescent dimers. *Anal. Biochem.* **1988**, 172 (1), 61–77.

54. S. Yamashita, K. Konishi, Y. Yamazaki, et al. New and better protocols for a short-term Caco-2 cell culture system. *J. Pharm. Sci.* **2002**, 91 (3), 669–679.

55. R. Eldor, B.H. Francis, A. Fleming, et al. Oral insulin (ORMD-0801) in type 2 diabetes mellitus: A dose-finding 12-week randomized placebo-controlled study. *Diabetes, Obes. Metab.* **2023**, 25 (4), 943–952.

56. I.B. Halberg, K. Lyby, K. Wassermann, et al. Efficacy and safety of oral basal insulin versus subcutaneous insulin glargine in type 2 diabetes: a randomised, double-blind, phase 2 trial. *Lancet Diabetes Endocrinol.* **2019**, 7 (3), 179–188.

57. M. Niu, Y. Tan, P. Guan, et al. Enhanced oral absorption of insulin-loaded liposomes containing bile salts: A mechanistic study. *Int. J. Pharm.* **2014**, 460 (1–2), 119–130.

58. M. Cui, W. Wu, L. Hovgaard, et al. Liposomes containing cholesterol analogues of botanical origin as drug delivery systems to enhance the oral absorption of insulin. *Int. J. Pharm.* **2015**, 489, 277–284.

59. I.B. Bekard, D.E. Dunstan. Tyrosine autofluorescence as a measure of bovine insulin fibrillation. *Biophys. J.* **2009**, 97 (9), 2521–2531.

60. K. Daffner, E. Hanssen, I. Norton, et al. Imaging of dairy emulsions: Via a novel approach of transmission electron cryogenic microscopy using beam exposure. *Soft Matter* **2020**, 16 (34), 7888–7892.

61. A.K. Gaigalas, L. Li, O. Henderson, et al. The development of fluorescence intensity standards. *J. Res. Natl. Inst. Stand. Technol.* **2001**, 106 (2), 381–389.

62. Y. Han, Z. Gao, L. Chen, et al. Multifunctional oral delivery systems for enhanced bioavailability of therapeutic peptides/proteins. *Acta Pharm. Sin. B* **2019**, 9 (5), 902–922.

63. X. Zhang, J. Qi, Y. Lu, et al. Biotinylated liposomes as potential carriers for the oral delivery of insulin. *Nanomedicine Nanotechnology, Biol. Med.* **2014**, 10 (1), 167–176.



7 DNA-grafted DELOS-NV as a potential biosensor

7.1. Introduction

In the previous **Chapters**, the DELOS-NV have been optimized for their use as theragnostic nanocarriers in humans by using excipients of the FDA IID. The optimized nanovesicles have been specially formulated and evaluated for two different administration routes. Specifically, **Chapter 6** demonstrated *in vitro* that DELOS-NV has the potential to act both systemically and locally in the gastrointestinal tract when administered orally. Their local action is possible because certain integrated molecules have very low permeability across the intestinal epithelium, which may help reduce systemic side effects.

In this **Chapter**, the aim is to leverage this potential by exploring the feasibility of using the Chol:CPC DELOS-NV as a future theragnostic candidate for gastrointestinal diseases. While the primary emphasis has been on DELOS-NV as drug delivery systems, their characteristics also suggest promise as biosensors for diagnostic applications. With this goal in mind, efforts were made to design and develop DNA-grafted DELOS-NV capable of recognizing DNA sequences that are overexpressed in gastrointestinal cancers.

In pursuit of this objective, Nanomol Technologies participated in the Nano-Oligomed project, funded by the European Union's Horizon 2020 research and innovation program under Marie Skłodowska-Curie grant agreement number 778133. This project facilitates staff exchanges among participating organizations to foster collaborative research and development of advanced nanomaterials for the transportation of oligonucleotides in biomedical applications. The program brings together four European and three international groups of experts in the field of nanomaterials and/or oligonucleotides with the aim of developing hybrid systems based on oligonucleotides with different therapeutical functions.

As part of this thesis, this Nano-Oligomed project financed a two-month internship at the laboratory of Prof. Alessandro Porchetta at the University of Tor Vergata in Rome, Italy. The internship aimed to mix the capabilities and extensive knowledge generated by Prof. Alessandro Porchetta's group in the

field of oligonucleotides with the DELOS-NV optimized in the framework of this thesis for the obtainment of a novel biosensor for the diagnosis of gastrointestinal cancers.

7.1.1. Oligonucleotides in biomedicine

The increased knowledge of DNA expression mechanisms has raised interest in employing oligonucleotides for various purposes, from "primers" in polymerase nuclease reactions, to "probes" in microarrays[1], and even building blocks in DNA nanotechnology for the synthesis of nanoscale objects[2]. In biomedicine, oligonucleotides serve two main functions: as therapeutic agents and as biosensing materials.

The term "oligo" comes from Greek and means "few." Therefore, oligonucleotides are short sequences of nucleotides, typically less than 20 bases in length, and can be either single- or double-stranded. Nucleotides are the basic building blocks of DNA and RNA. They are composed of a nitrogenous base, a pentose sugar (deoxyribose for DNA and ribose for RNA), and a phosphate group attached to the 5' carbon of the sugar. The nitrogenous bases in DNA are adenine, cytosine, guanine, and thymine, while in RNA, uracil replaces thymine (**Figure 7.1**).

In vivo, oligonucleotides mostly exist as non-coding RNAs[1]. Non-coding RNAs (such as miRNAs) do not translate into proteins and play a role in gene expression control.

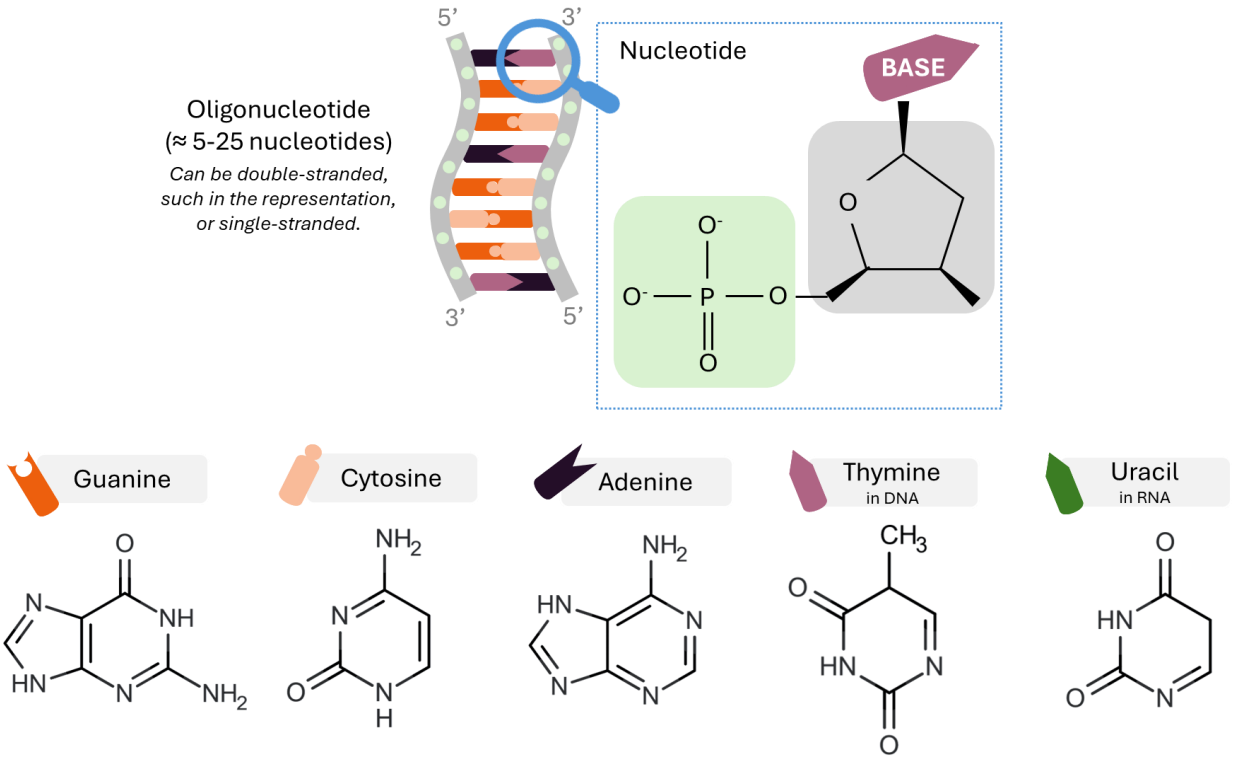


Figure 7.1. *Schematic representation of an oligonucleotide. The oligonucleotides are composed by short sequences of nucleotides, that are the building blocks of DNA and RNA. Each nucleotide has a pentose sugar bound with a phosphate group attached to the 5' carbon and a nitrogenous base in the 1' carbon. The nitrogenous bases are guanine, cytosine, adenine, thymine (only in DNA) and uracil (only in RNA).*

Several reasons highlight oligonucleotides as potential therapeutic and diagnostic tools:

- Most of the oligonucleotides interact with their target through Watson–Crick base pairing, thus making them relatively easily synthesized for both diagnosis and therapeutic finalities. Conventional small molecules require much larger screening and optimization efforts[3].
- Not all proteins are easily addressable through conventional small molecules. Some classes of proteins such as membrane receptors, enzymes, and ion channels respond well to small molecules, however, there are other proteins such as scaffold proteins, challenging to target through conventional drugs, that might respond better to oligonucleotide-based therapies[4].
- In principle, oligonucleotides are more specific than small molecules, since they require high complementarity with the target sequence to be functional, and therefore might present fewer side effects[4].
- Oligonucleotides are very versatile since they can be designed to either upregulate or downregulate gene expression, thus opening frontiers for the treatment of a wide range of diseases[3].
- In addition, they can be designed to target patient-specific sequences for the treatment and/or diagnosis of rare diseases[5], and to identify specific isoforms of key biomarkers, thus allowing the classification of patients within a disease to tailor their treatment[1].

However, despite all these benefits, achieving effective delivery or transportation of oligonucleotides *in vivo* is a major challenge. The difficulties align with typical challenges when working with biomolecules. Oligonucleotides are fragile and must resist degradation by extracellular nucleases[6]. Once in the target organ, they need to penetrate inside the cell, or even the nucleus, to exert their function, which is challenging due to their larger size (~4 to 14 kDa)[3] compared to small molecules.

In that sense, DELOS-NV can be an excellent strategy to improve oligonucleotides function in biological media, as DELOS-NV have shown promising results in delivering nucleotides. DELOS-NV can protect the DNA from nucleases and enhance cellular penetration[7,8], two advantages that are equally interesting for the use of oligonucleotides in therapeutic and/or diagnostic applications.

7.1.2. The intricacies of gene expression

The surge in interest in oligonucleotides was propelled by advancements in understanding gene expression regulation. In the early days, it was thought that gene expression was regulated solely through the transcription mechanism schematized in **Figure 7.2A**. Now, it is widely recognized that several mechanisms play equally important roles in gene expression regulation, thus opening the doors to novel therapeutic targets for protein regulation. The various mechanisms governing gene expression regulation can be classified based on their specific points of action within the biological pathway.

Prior to the transcription of DNA into RNA (**Figure 7.2A**), epigenetics play an important role in gene expression. Epigenetics refers to those modifications that occur in both chromatin and directly on the DNA sequence, which control DNA transcription into RNA. Chromatin is the packed structure formed by DNA and histone proteins. To facilitate the transcription of DNA, these proteins need to unpack their tight structure for the polymerase to be able to reach the gene and initiate the

transcription. This is why modifications to chromatin can result in a major or minor expression of certain genes. The same occurs with the DNA, which can be directly methylated at certain cytosines thus resulting in less transcriptionally active genes. Epigenetic modifications are reversible[9].

After the transcription of DNA into RNA, there are still several mechanisms that can regulate gene expression. Once the transcription is complete, the obtained RNA, which is called pre-messenger RNA (pre-mRNA), is modified by several post-processes to become a protein-coding messenger RNA (mRNA). These post-processes are highly regulated and typically occur in parallel with the transcription mechanism. Afterward, the mature mRNA needs to reach the cytoplasm for its translation into a protein (**Figure 7.2A**). The mRNA which is not properly formed remains in the nucleus. The well-formed mRNA is exported from the nucleus and transported to the ribosomes, where it is translated into a protein in three sequential steps which are also highly regulated: initiation, elongation, and termination[1,10].

However, not all RNAs are meant to be transcribed into proteins (**Figure 7.2B**). There are also non-coding RNAs that play a significant role in regulating gene expression. Some of them participate in the post-processing and translation of the RNA, such as the small nuclear RNA. There are also the long non-coding RNAs (>200 nucleotides in length) which primarily affect epigenetics and the short non-coding RNAs that mostly regulate gene expression after the transcription of DNA into RNA. These short non-coding RNAs are oligonucleotides of biological origin[1].

Among those short non-coding RNAs, miRNAs are particularly notable. miRNAs are very well-known RNAs that act by binding mRNA sequences thus reducing their translation into proteins or even targeting them for degradation. Therefore, they downregulate the expression of certain genes at the translational level. There are several diseases where the expression of certain miRNAs is aberrant, such as neurodegenerative diseases[11], cardiovascular diseases[12] and many cancers, including colorectal cancer[13–15]. The dysregulation of miRNA in these diseases provides the framework for the development of new therapies or diagnosis systems. The most straightforward approach to target these miRNAs for their detection (as disease markers) and/or modulation (as disease therapy) is through the use of oligonucleotides complementary to the specific miRNA[1,16].

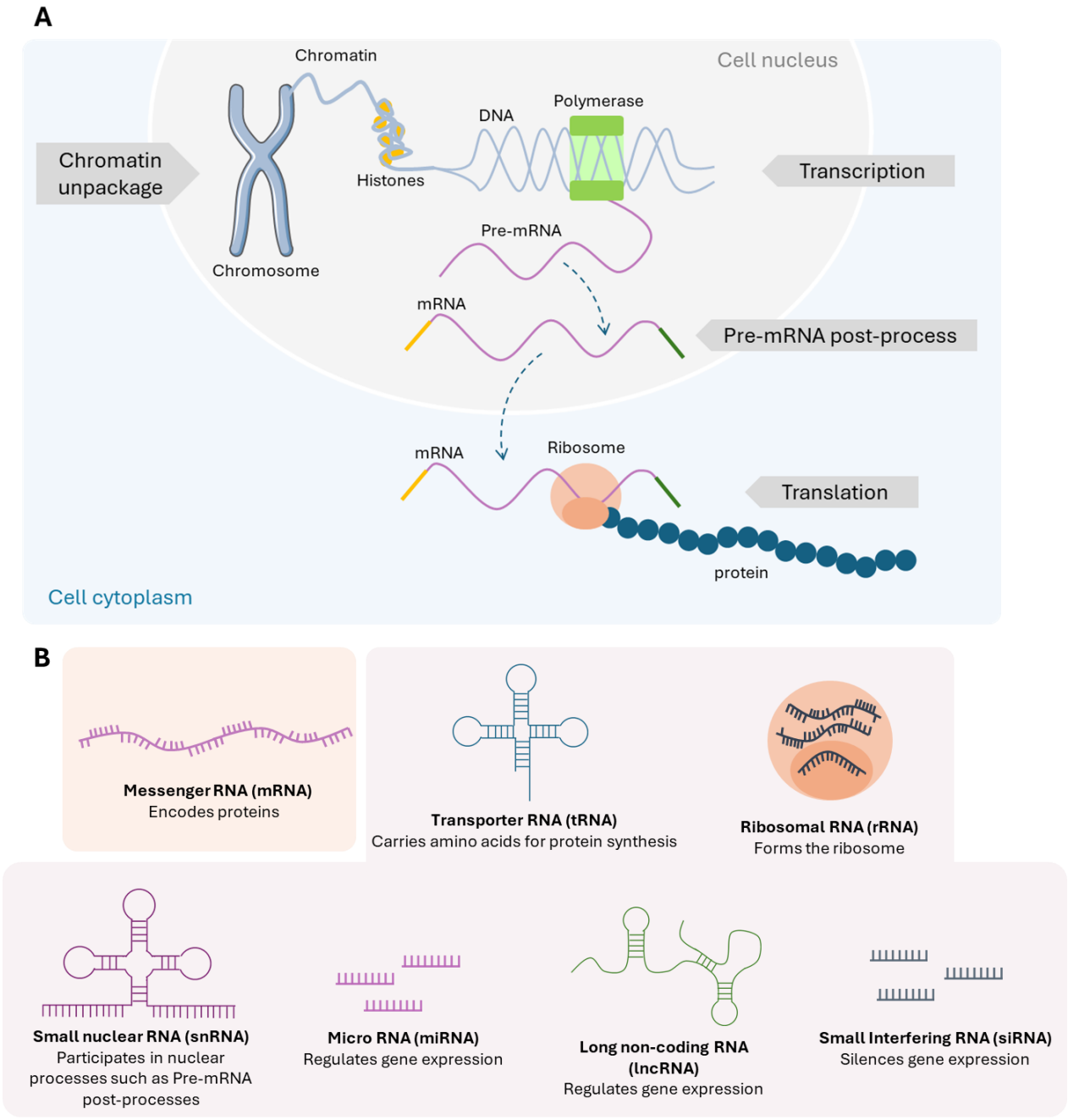


Figure 7.2. *A) Schematic representation of the gene expression in cells. B) Different RNA present in cells. In the orange box: Coding mRNA which encodes proteins. In the purple box: Non-coding RNAs.*

7.1.3. Overexpression of miR21 in gastrointestinal cancers

As commented before, the expression of miRNAs is altered in several diseases, such as gastrointestinal cancers. Of the ~1900 miRNA-encoding genes present in the human genome, ~250 miRNAs are reported to have altered functions in colorectal cancer[14].

Colorectal cancer is the second most common cause of death in the United States. In addition, the trends indicate that its burden is shifting to younger individuals[17]. In Europe colorectal cancer is responsible for the largest proportion of deaths due to digestive cancers, and its burden is also shifting to young adults (25 – 39 years)[18]. Consequently, there has been extensive research into the aberrant expression of miRNAs in this cancer type. Understanding these molecular signatures holds promise for improving diagnosis, prognosis, and treatment outcomes.

It is known that miR21 is one of the miRNAs overexpressed in colorectal cancers[15,19]. Several studies demonstrate that this miRNA plays a crucial role in cancer progression by promoting cell growth and invasion[15,20]. In these types of cancers, the expression of miR21 is significantly higher in cancer tissues than in adjacent tissues. In addition, its expression is positively correlated with the degree of malignancy and negatively correlated with the survival of patients[19]. Therefore, it is a reliable indicator for colorectal cancer diagnoses, and several studies have testified the diagnostic value of circulating miR21 in various human cancers as well as in colorectal cancer. However, most of these studies focus on the *ex vivo* detection of the miR21[21,22].

Considering all the points mentioned thus far, the *in vivo* detection of miR21 has an untapped potential in leading endoscopies and colorectal surgeries in colorectal cancers. Endoscopies are the most effective approach for early colorectal cancer detection[23], and nowadays treatment of colorectal cancer usually entails surgical removal[14]. However, detection of cancer in its early stages is not easy with conventional white light endoscopy. There is strong clinical interest in developing new endoscopy screening methods that facilitate the early diagnosis of cancerous malignancies at their initial stage. This would simplify the obtainment of biopsies and would allow a better definition of tissue limits in surgical procedures[24]. Taking this fact into consideration, in this **Chapter** the proposal is to combine the DELOS-NV with a well-designed oligonucleotide for the miR21 detection as a potential biosensor for fluorescent endoscopies. In addition, as discussed in **Chapter 6**, the Chol:CPC DELOS-NV developed in this dissertation demonstrated low permeation of two model proteins (FITC-BSA and insulin) through the intestinal epithelium. This characteristic makes them suitable for local delivery of specific molecules within the gastrointestinal tract with low risk of systemic side effects.

7.1.4. Design of a novel DNA-grafted DELOS-NV biosensor for miR21 detection

In a previous collaboration between the Nanomol-Bio group, Nanomol Technologies S.L. and Prof. Alessandro Porchetta's group, a nanoconjugate based on DELOS-NV and an oligonucleotide for the *in vitro* detection of miR21 was developed with promising results[8]. They developed programmable FRET[g]-active nanovesicles that translated miR21 recognition into a reduction of the FRET efficiency (**Figure 7.3**). The system used DELOS-NV labeled with a donor dye and functionalized with a miRNA probe containing an acceptor dye. Detection relied on FRET efficiency changes induced by the binding of the target miRNA on the DNA probe. In the absence of the miRNA, the probe folded, increasing FRET efficiency by bringing the dyes closer. In the presence of the miRNA, the probe hybridized with the target, reducing FRET efficiency by separating the dyes. Detection involved

[g] *The FRET phenomenon is explained in detail in* ***Chapter 4, Section 4.3.5****.*

measuring the emission peaks of the donor and acceptor dyes, with their ratio indicating the presence or absence of the target miRNA.

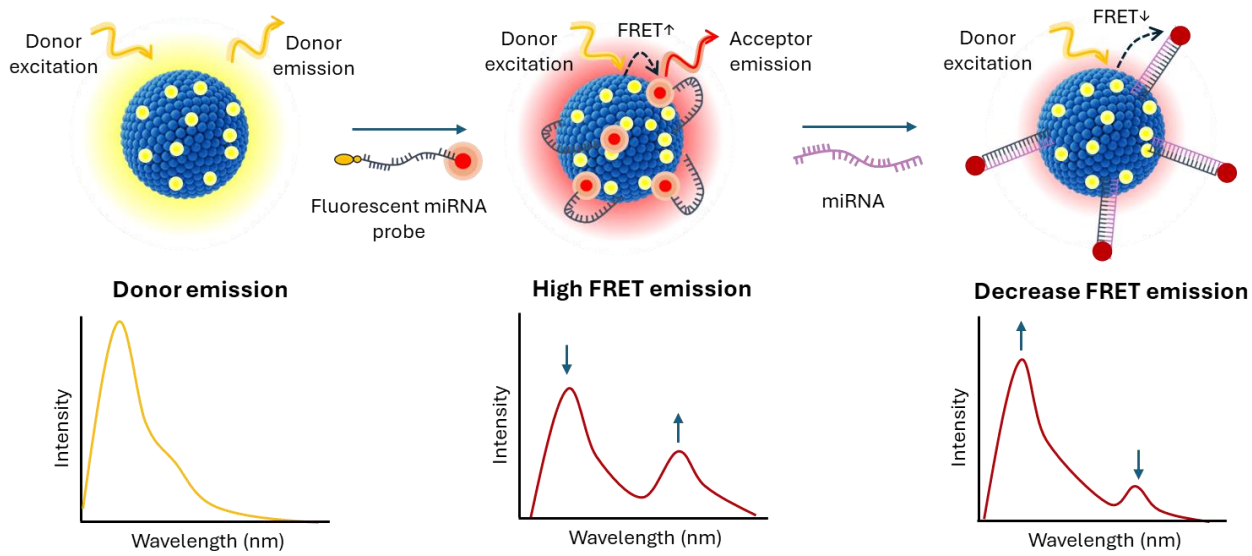


Figure 7.3. *Schematic representation of the nanoconjugate based on DELOS-NV and an oligonucleotide for the in vivo detection of miRNA developed in the collaboration between the Nanomol-Bio group, Nanomol Technologies S.L. and Prof. Alessandro Porchetta's group. The* ***Figure*** *has been adapted from M. Rosetti, et al.*[8]

In this **Chapter**, the goal is to redefine the approach for miR21 detection, aiming to create a more intuitive platform for endoscopic clinical diagnosis. To achieve this, direct quantification of miR21, rather than ratiometric analysis, may be more straightforward for professionals unfamiliar with FRET. The objective is to have a system that does not emit fluorescence in the absence of miR21 and emits fluorescence positively correlated with the detection of miR21. To be at least as good as the FRET-active nanovesicles (**Figure 7.3**), the system should have its limit of detection in the low nanomolar range and should be very specific to the miR21 sequence.

With this finality, a fluorophore and a quencher molecule will be employed, leveraging the strand-displacement reaction to detect the miR21 (**Figure 7.4**). More in detail, an oligonucleotide sequence complementary to the miR21 with a cholesteryl molecule and a fluorophore (Cholesteryl-ATTO488-anti-miR21; named Anti-miR21) will be attached to the Chol:CPC DELOS-NV membranes optimized in the framework of this thesis. The cholesteryl molecule will be incorporated into the vesicle's membrane through hydrophobic interactions. This sequence will also be hybridized with a short-oligonucleotide partially complementary containing the black hole quencher 1 (BHQ-short oligonucleotide; named OligoQ). In the absence of the miR21, the quencher will suppress the ATTO488 fluorescence. However, in the presence of miR21, miR21 will bind its complementary sequence displacing the OligoQ containing the quencher via a toehold-mediated strand-displacement reaction, thereby permitting the measurement of ATTO488 emission upon its excitation.

Toehold-mediated strand-displacement reactions were first introduced by Yurke *et al.* in the early 21st century[25,26]. In these reactions, the pre-hybridized sequences have a short non-complementary end sequence of DNA/RNA, which facilitates the binding of the single-strand sequence, triggering

the strand displacement reaction (the exchange of the pre-hybridized sequence by another one with a higher number of complementary bases) (**Figure 7.4**).

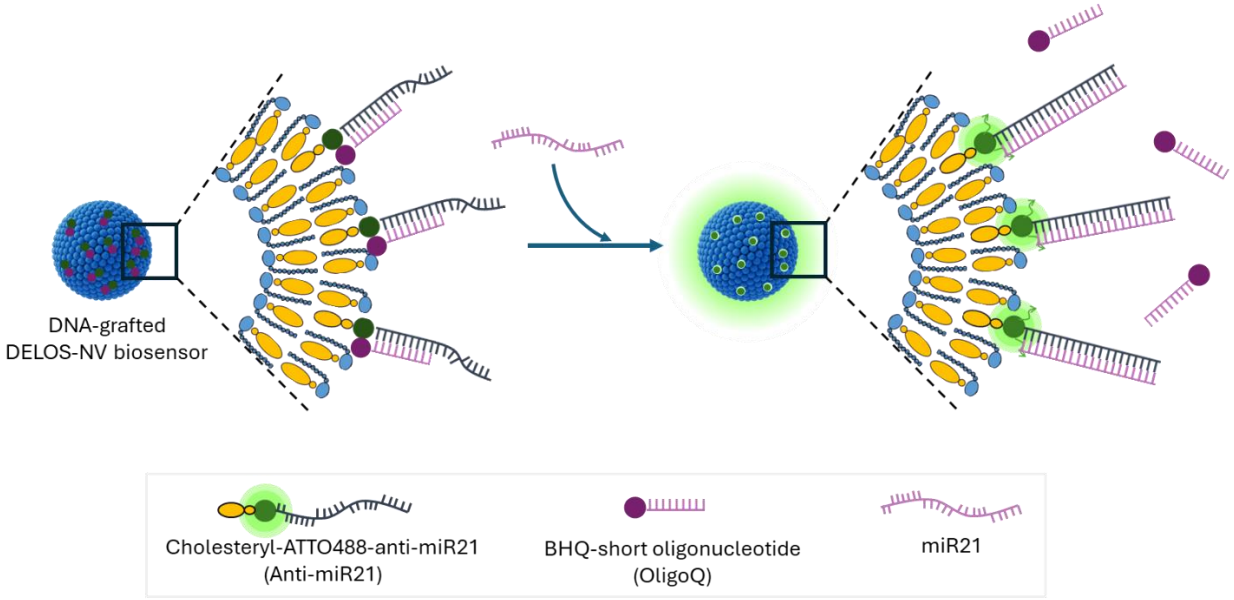


Figure 7.4. *Construction and operation of the DNA-grafted DELOS-NV miR21 biosensor. The Anti-miR21 labelled with an ATTO488 fluorophore is attached to the DELOS-NV membrane through a cholesteryl molecule and pre-hybridized with a partially complementary short-oligonucleotide with a black hole quencher (BHQ) (named OligoQ). When no miR21 is in contact with the system, the ATTO488 fluorescence is quenched by the BHQ. Upon incorporation of the miR21, it interacts primarily with the toehold of the Anti-miR21, to end up completely hybridizing the Anti-miR21, causing the displacement of the OligoQ with the BHQ. In that situation, the emission of the ATTO488 is not quenched anymore and can be quantified.*

7.2. Production and characterization of the DELOS-NV for the development of the DNA-grafted DELOS-NV biosensor

The nanovesicles for the present study were produced and physiochemically characterized at Nanomol Technologies installations before the secondment. DELOS-NV with Chol and CPC at an equimolar ratio and a final concentration of membrane components of 1 mg/mL were produced in dPBS (0.14 M NaCl, 0.0027 M KCl, 0.0081 M Na_2HPO_4 and 0.0015 M $NaH_2PO_4{\cdot}2H_2O$, pH 7.4). It was decided to employ dPBS because it is the same buffer used in the previous collaboration between Nanomol group, Nanomol Technologies and Prof. Alessandro Porchetta's group[8].

The nanovesicles were produced by the DELOS method (see **Section 9.2.1**) and diafiltrated by TFF to eliminate the EtOH (see **Section 9.2.2**). Specifically, they were called DNA-DELOS-NV (see **Table 9.4** for details on composition) and were employed for the experiments with DNA during the secondment at the University of Tor Vergata. Note that the DNA was not loaded in the DELOS-NV during the DELOS method. DNA was incorporated after production, by incubation, at Prof. Alessandro Porchetta's laboratory. The DNA-DELOS-NV (before the DNA incubation, therefore without DNA) were characterized at t = 14 days by DLS and ELS (see **Section 9.3.1**) to ensure their quality (see **Figure 7.5**).

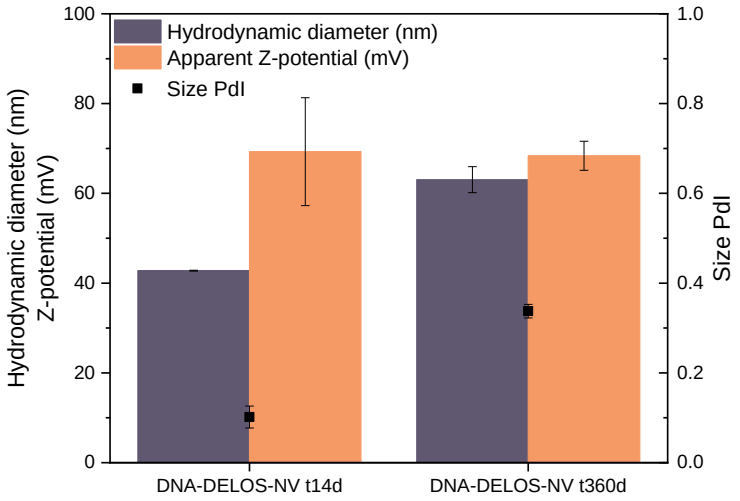


Figure 7.5. Hydrodynamic diameter, size PdI and apparent Z-potential of the DNA-DELOS-NV (before the DNA incubation, therefore without DNA) 14 days and 360 days after their production by DELOS method and diafiltration by TFF, stored at 5 ± 3 °C.

Figure 7.5 shows that DNA-DELOS-NV, obtained with Chol and CPC in dPBS, present appropriate physicochemical characteristics to be employed as biosensors. They present a small hydrodynamic diameter, low size PdI, and a high apparent Z-potential. In addition, as shown in **Figure 7.5**, these nanovesicles are stable at least for one year. Their hydrodynamic diameter and size PdI increase a little over time, however, the changes are small considering the long period evaluated. Therefore, these DNA-DELOS-NV were shipped to the University of Tor Vergata and were employed in the following experiments to obtain a novel biosensor platform for the detection of miR21 in colorectal cancers.

7.3. Design of the oligonucleotide sequences for the development of the DNA-grafted DELOS-NV biosensor

For the design of the biosensor nanoconjugate, the DNA sequences listed in **Table 7.1** were employed. Note that the sequences correspond to DNA instead of RNA because DNA is much more stable and easier to work in the laboratory. Thus, it is common to convert RNA sequences into complementary DNA sequences at the initial stages of an investigation to facilitate the technical work. The miR21 sequence in **Table 7.1** is the target sequence to be recognized with the developed biosensor. The Anti-miR21 sequence is a complementary sequence to the miR21 sequence. Note that the hybridization between two complementary single-stranded DNA sequences is antiparallel. Therefore, one nucleotide strand lies in the 5' to 3' direction, and the other strand lies in the 3' to 5' direction. The Anti-miR21 sequence also contains a cholesteryl molecule that enables the binding to the DELOS-NV membrane and an ATTO488 fluorophore responsible for the signal after miR21 recognition (**Figure 7.4**). The cholesteryl molecule is bonded through a TEG sequence which acts as

a spacer. The OligoQ sequence is partially complementary to the Anti-miR21, and in the absence of the miR21, it hybridizes the Anti-miR21 sequence. However, it is displaced by a strand-displacement reaction in the presence of miR21 because miR21 has a higher affinity (higher number of complementary bases). This OligoQ contains a quencher molecule responsible for suppressing the ATTO488 fluorescence when there is no miR21.

The **Table 7.1** shows the internal code that will be employed in this **Chapter** to refer to the sequences and the DNA sequences in the 5'-3' direction. It also shows the MW, the optical density at 260 nm (OD_{260}) and the quantity of oligonucleotide provided by the seller. OD_{260} is the amount of light at 260 nm absorbed by an oligo resuspended in 1 mL water and read in a 1 cm quartz cuvette. This information is relevant to calculate the molar concentration of DNA in the solutions prepared as described in **Section 9.4.6.1**.

Table 7.1. *Oligonucleotides employed for the development of the DNA-grafted DELOS-NV biosensor. The table shows the sequences and modifications, the molecular weight (MW), the optical density (OD_{260}) of the provided amount of oligonucleotides at λ= 260 nm, and the amount of oligonucleotides received from the provider in nmol.*

Internal code	*DNA sequence 5' – 3'*	*MW (Da)*	*OD_{260}*	*nmol*
miR21	*TAG CTT ATC AGA CTG ATG TTG A*	*6,764*	*9.0*	*41.1*
Anti-miR21	*Cholesteryl TEG-TT(ATTO 488-dT) CAA CAT CAGTCTGAT AAG CTA*	*8,719*	*2.4*	*9.4*
OligoQ	*CAG ACT GAT GTT GA-BHQ-1*	*4,857*	*5.9*	*39.7*

7.4. Development and optimization of the DNA-grafted DELOS-NV biosensor for miR21 detection

In the present section, the different steps to develop the novel DNA-grafted DELOS-NV biosensor will be disclosed. First, the functionality of the designed oligonucleotide sequences shown in **Table 7.1** has been assessed. Next, the most relevant conditions to produce the biosensor have been identified through preliminary tests. After determining the requirements for designing a well-constructed DNA-grafted biosensor, it has been developed, and its ability to recognize miR21 assessed.

7.4.1. Preliminary test to establish the most relevant conditions to develop the DNA-grafted DELOS-NV biosensor

7.4.1.1. Evaluation of the designed DNA sequences and selection of the optimal ratio for the pre-hybridized sequences

Before incorporating the DELOS-NV into the system, the behavior of the designed DNA sequences in the absence of DELOS-NV was evaluated (**Figure 7.4**). To do so, different titration experiments of the DNA sequences in solution were performed as described in **Section 9.4.6.2**. The experiments were carried out in dPBS buffer at pH 7.4. The titration injections were performed every 5 minutes to allow

enough time for the reactions to occur. In the first experiment, the OligoQ was titrated over a solution with 20 nM Anti-miR21 and the quenching of the ATTO488 fluorophore was followed (see **Figure 7.6A**). In this experiment the maximum quenching of the ATTO488 was achieved with 20-30 nM concentration of OligoQ, therefore, concluding that the molar ratios 1:1 to 1:1.5 Anti-miR21:OligoQ are the most appropriate to have the ATTO488 fluorescence suppressed (**Figure 7.6B**). Higher concentrations of OligoQ did not further decrease the fluorescence because all the Anti-miR21 sequences were already hybridized.

This result is relevant for the future development of the DNA-grafted DELOS-NV biosensor since the aim is to have the maximum quenching of the fluorescence in absence of the miR21 to have a bigger signal gain in response to the miR21 recognition.

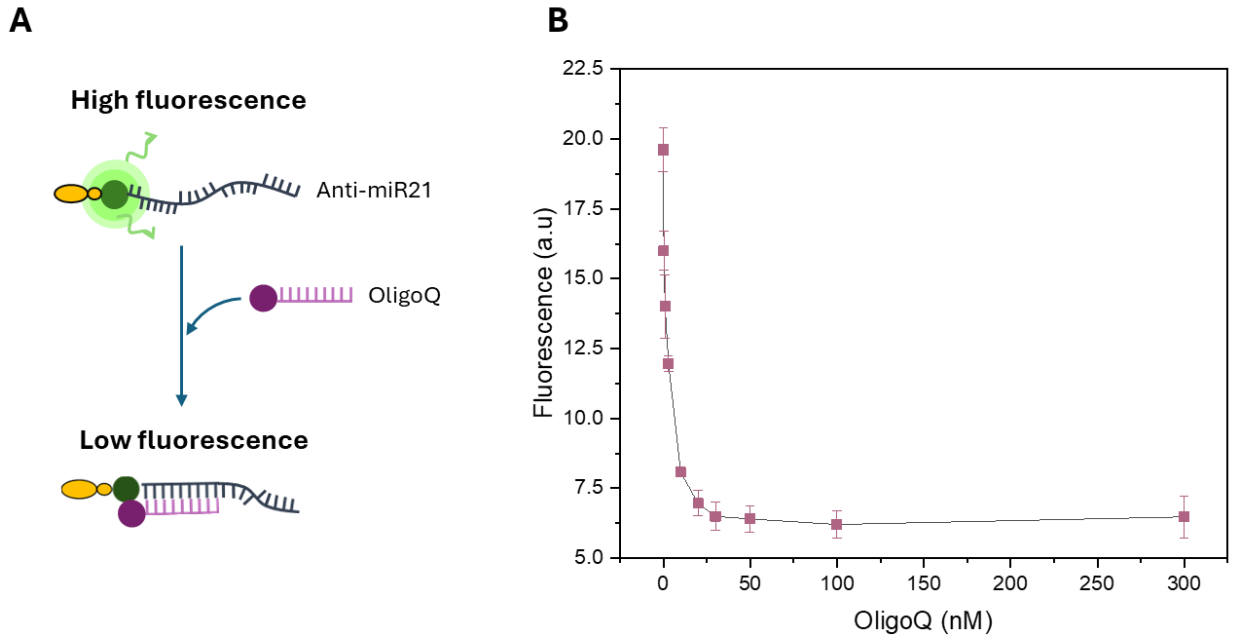


Figure 7.6. *Titration experiments with free DNA (without DELOS-NV) to confirm the functionality of the designed DNA oligonucleotides. The OligoQ sequence is titrated into the Anti-miR21 sequence. A) Schematic representation of the hybridization reaction and expected fluorescence change in response to the OligoQ titration into Anti-miR21. B) Experimental results showing the fluorescence change (λ_{ex} = 475 nm and λ_{em} = 526 nm) in response to the OligoQ titration into a solution of the Anti-miR1 sequence (20 nM).* The results correspond to the average and SD of two replicates.

In the next experiment, and following the previous results, the miR21 was titrated over 20 nM Anti-miR21 pre-hybridized with 30 nM OligoQ (**Figure 7.7A**), maintaining a molar ratio of 1:1.5 Anti-miR21:OligoQ. This experiment aimed to show the recovery of the fluorescence through the miR21 strand-displacement reaction of the OligoQ sequence. As expected, the complete recovery of the fluorescence was achieved with 20-30 nM of miR21 confirming the occurrence of the strand-displacement reaction (**Figure 7.7B**). Higher concentrations of miR21 did not further increase the fluorescence because all the Anti-miR21 was already hybridized.

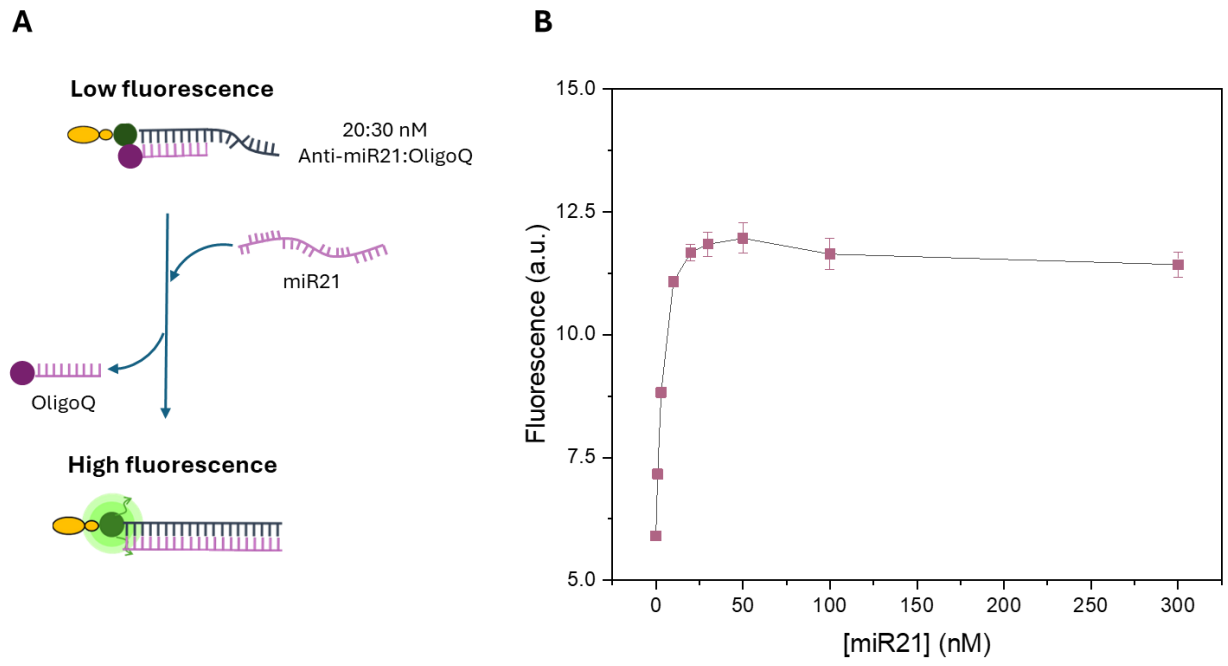


Figure 7.7. *Titration experiments with free DNA (without DELOS-NV) to confirm the functionality of the designed DNA oligonucleotides. The miR21 sequence is titrated into the Anti-miR21:OligoQ 20:30 nM pre-hybridized sequences. A) Schematic representation of the hybridization reaction and expected fluorescence change in response to the miR21 titration into Anti-miR21:OligoQ 20:30 nM. B) Experimental results showing the fluorescence change (λ_{ex} = 475 nm and λ_{em} = 526 nm) in response to the miR21 titration into Anti-miR21:OligoQ 20:30 nM*. The results correspond to the average and SD of two replicates.

Therefore, the results obtained with the free sequences show a predictable outcome and confirm that the sequences shown in **Table 7.1** were well designed, and the strand-displacement reaction occurs efficiently in the presence of miR21. These favorable results allowed continuing with the development of the DNA-grafted DELOS-NV biosensor.

7.4.1.2. Evaluation of the Anti-miR21 fluorescence in different scenarios as controls

To understand the behavior of the ATTO488 fluorophore of the Anti-miR21 sequence in different situations, and better characterize the system, some controls were performed prior to the development of the DNA-grafted DELOS-NV biosensor.

The titrations were performed as described in **Section 9.4.6.3**, in dPBS buffer and waiting 5 minutes between injections. In this test the fluorescence of the ATTO488 in different scenarios was compared (**Figure 7.8A**). Therefore, in all the scenarios evaluated the concentration of Anti-miR21 containing the ATTO488 fluorophore was maintained constant. First, it can be observed that the ATTO488 fluorophore in the Anti-miR21 sequence emits significantly lower fluorescence in the single-stranded Anti-miR21 compared to the hybridized Anti-miR21 with miR21 (**Figure 7.8B**, scenarios 2 *vs* 1), likely due to the conformational changes in the DNA. Single-strand sequences are more flexible than double-strand sequences and can fold over themselves hiding the ATTO488 and reducing its

fluorescence. As discussed previously in this dissertation, the microenvironment of a molecule directly affects its fluorescence[27].

In addition, the experiment showed that the fluorescence of the ATTO488 in the single-stranded Anti-miR21 is not affected by the inclusion of DELOS-NV (**Figure 7.8B**, scenarios 3 *vs* 1). However, what is most interesting is that adding miR21 over the DELOS-NV previously functionalized with the Anti-miR21 does not increase the fluorescence (**Figure 7.8B**, scenarios 4 *vs* 3), contrary to **Figure 7.8B,** scenarios 2 *vs* 1. This is likely because the positive charges of the nanovesicles polar heads entrap in their surface the negatively charged Anti-miR21 preventing its binding to the miR21. Oppositely, when the miR21 and the Anti-miR21 are first hybridized and next incorporated into the DELOS-NV (**Figure 7.8B**, scenario 5), the fluorescence of the ATTO488 increases, in concordance with **Figure 7.8B,** scenarios 2 *vs* 1. In this last scenario 5, the hybridization of both sequences before inclusion of the DELOS-NV avoids entrapment of the DNA in the surface of the nanovesicles. **Figure 7.8C** shows the possible explanation for scenarios 4 and 5. The pre-hybridized double-stranded DNA sequences have a more rigid structure, allowing exposure of the fluorophore even in the presence of the DELOS-NV.

Therefore, these results are very interesting because they indicate that for developing the DNA-grafted DELOS-NV biosensor it will be necessary to pre-hybridize the Anti-miR21 with the OligoQ, before incorporating the nanovesicles. Otherwise, the Anti-miR21 would get entrapped in the surface of the nanovesicles membrane and hybridization with OligoQ would not occur. Following the appropriate order (pre-hybridization Anti-miR21 with OligoQ and subsequent addition of the DELOS-NV), it is expected the Anti-miR21 to be more exposed for its hybridization with the target miR21 sequence.

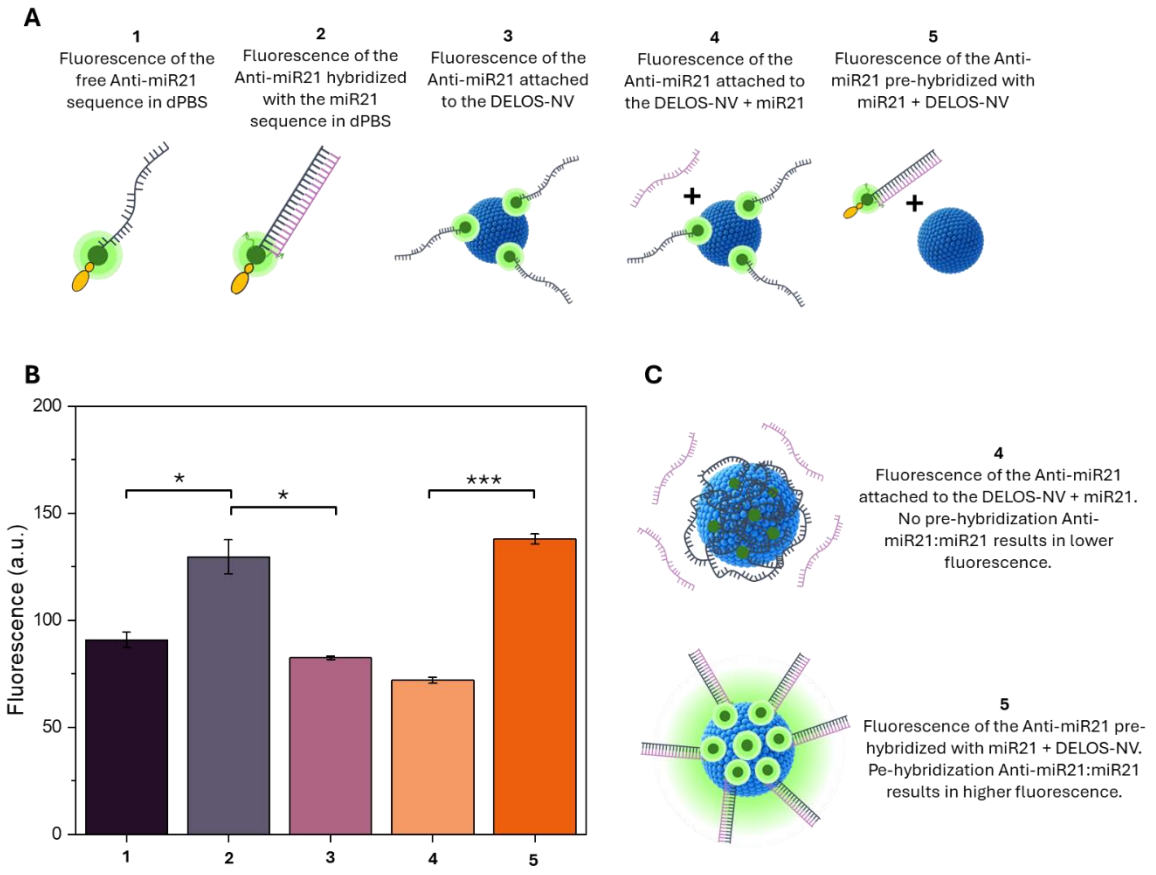


Figure 7.8. *A) Different scenarios evaluated to understand the fluorescence of the ATTO488 fluorophore in the Anti-miR21 sequence. Note that scenarios 4 and 5 have the same concentration of each molecule (Anti-miR21, miR21 and DELOS-NV) and the only difference between them is the order in which the molecules encounter each other. B) Bar graph showing the fluorescence emitted by the ATTO488 fluorophore attached to the Anti-miR21 in the different scenarios (λ_{ex} = 475 nm and λ_{em} = 526 nm). Results show the mean and SD of two replicates. Statistical analyses were done by T-test pairwise comparison: * p < 0.05, *** p < 0.001. C) Graphic representation of the possible structure of the Anti-miR21 in the DELOS-NV membranes when there is no pre-hybridization with the miR21 versus when it has been previously hybridized with the miR21. The positive charges in the DELOS-NV can entrap in their surface the single-stranded Anti-miR21 sequence preventing its binding to the miR21.*

7.4.1.3. Confirmation of the adequacy of ratio 20:30 nM Anti-miR21:OligoQ in presence of the DELOS-NV

Previous results (**Section 7.4.1.1**) demonstrated that the ratio 20:30 nM Anti-miR21:OligoQ (equivalent to 1:1.5 molar ratio) provided the maximum quenching of ATTO488 fluorescence (**Figure 7.6B**). Next, it was demonstrated the recovery of the fluorescence upon titration of the miR21 sequence into the Anti-miR21:OligoQ 20:30 nM hybridized sequences (**Figure 7.7B**). However, these experiments were carried out in the absence of DELOS-NV.

In this **Section**, the aim is to confirm that the 20:30 nM ratio of Anti-miR21:OligoQ is the most appropriate for the development of the DNA-grafted DELOS-NV biosensor. To achieve this, the recovery of fluorescence upon titration of miR21 into DELOS-NV functionalized with pre-hybridized Anti-miR21:OligoQ sequences has been evaluated (**Figure 7.9A**). As a control, different ratios Anti-miR21:OligoQ have been also tested. Titration experiments were performed as described in **Section 9.4.6.4**, in dPBS and waiting 5 minutes between injections. Since DELOS-NV could hinder the hybridization of complementary sequences, as explained in **Section 7.4.1.2**, the Anti-miR21 and OligoQ sequences were pre-hybridized before incorporating the DELOS-NV. Different molar ratios of Anti-miR21 to OligoQ were mixed and incubated for 10 minutes before adding the DELOS-NV. Subsequently, titration of miR21 was conducted into the pre-hybridized Anti-miR21:OligoQ sequences attached to the DELOS-NV (**Figure 7.9A**).

As shown in **Figure 7.9B**, the outcome of the titration experiment is consistent with the expected results. The higher the proportion of OligoQ, the lower the increase in fluorescent signal in response to the miR21 titration. This occurs because the miR21 competes with the excess of OligoQ sequences in the medium to bind to the Anti-miR21. As expected, the concentration of components in the medium affects the strand-displacement reaction equilibrium. A higher concentration of OligoQ leads to more encounters between the OligoQ and the Anti-miR21. These results further confirm that 20:30 nM Anti-miR21:OligoQ (equivalent to molar ratio 1:1.5 Anti-miR21:OligoQ) is the most appropriate for designing the DNA-grafted DELOS-NV biosensor to detect miR21.

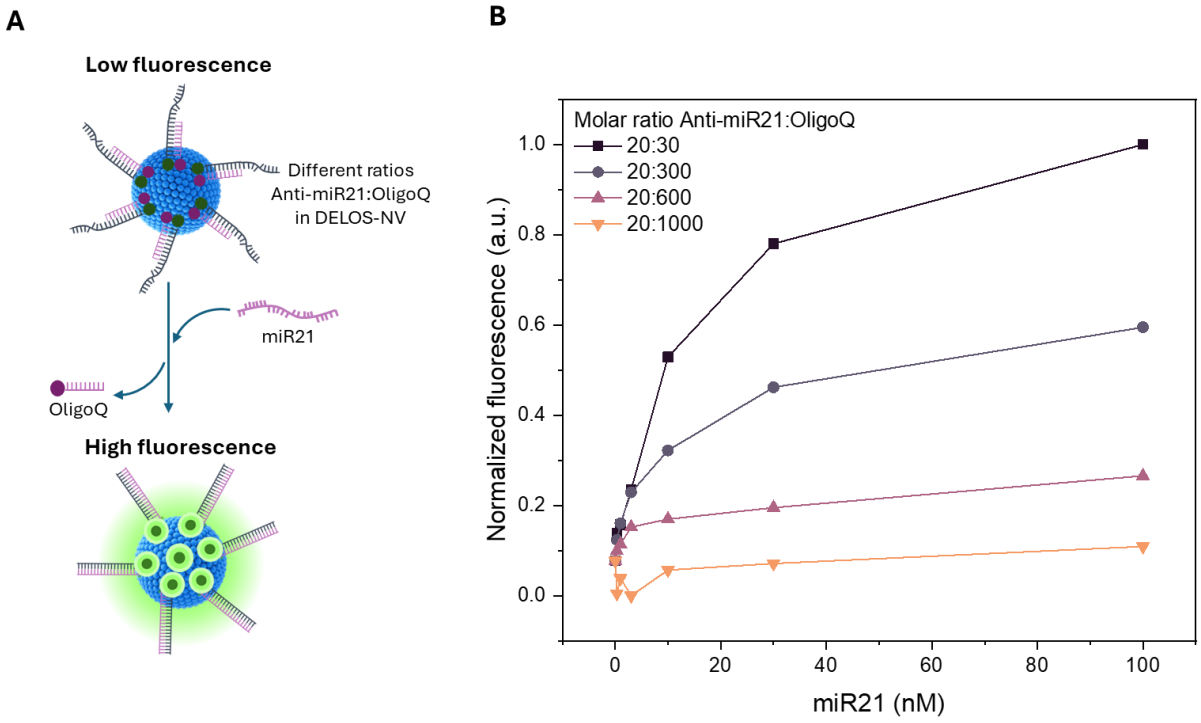


Figure 7.9. *miR21 titration into DELOS-NV grafted with different molar ratios Anti-miR21:OligoQ. The concentration of Anti-miR21 is 20 nM in all experiments and the OligoQ concentration varies between 30 and 1000 nM. A) Schematic representation of the hybridization reaction and expected fluorescence change in response to the miR21 titration. B) Experimental results showing the fluorescence change (λ_{ex} = 475 nm and λ_{em} = 526 nm) in response to the miR21 titration.*

7.4.1.4. Impact of the DELOS-NV concentration in the miR21 recognition

In this section, the objective was to study the effect of DELOS-NV concentration on miR21 recognition. Previously, it was observed that nanovesicles could impede the hybridization between complementary chains, likely because they entrap DNA sequences on their surface through electrostatic interactions between the positive charges of CPC, forming the nanovesicle membrane, and the negative charges of the DNA sequence. This limitation can be easily addressed by pre-hybridizing Anti-miR21 with its partially complementary OligoQ. However, it has not been tested yet the effect of nanovesicle concentration on miR21 recognition.

Therefore, in the present test, different samples were prepared containing equal concentrations of pre-hybridized Anti-miR21 and OligoQ sequences (20 nM and 30 nM, respectively) and increasing concentrations of DELOS-NV (from 0 mg/mL to 0.3 mg/mL membrane components -Chol + CPC-). Subsequently, an excess of miR21 was added to these samples (200 nM or 1000 nM), and the binding kinetics were analyzed by monitoring fluorescence increase over a 20-minute period (**Figure 7.10A**). In **Section 7.4.1.1** it was demonstrated that 30 nM miR21 was enough to completely recover the fluorescence; therefore, in this test, the concentration of miR21 will not be a limiting factor.

As shown in **Figure 7.10B**, the results obtained with both concentrations of miR21 are equivalent. These results could be expected since in both cases an excess of miR21 has been added to the samples (200 nM or 1000 nM miR21 versus the 20 nM Anti-miR21). The equivalent results obtained with both miR21 concentrations confirm the high robustness of the system. From these results was also found that the nanovesicles notably reduce the fluorescence maximum attained with the system. 0.3 mg/mL of DELOS-NV membrane components results in a loss of the recognition effect, while with the other two concentrations tested (0.03 and 0.015 mg/mL) the miR21 recognition is similar. A rational explanation for this outcome could be the entrapment of the miR21 molecules on the nanovesicles membranes through electrostatic interaction, thus preventing the strand-displacement reaction. Hence, from these results it was concluded that the most appropriate concentration of DELOS-NV to design the DNA-grafted DELOS-NV biosensor is 0.03 mg/mL of membrane components, since higher concentrations of DELOS-NV result in a loss of the recognition effect.

Therefore, this test permitted defining the concentration of DELOS-NV to be employed in the DNA-grafted DELOS-NV biosensor. In addition, the equivalent results obtained with both concentrations of miR21 demonstrate the robustness of the system.

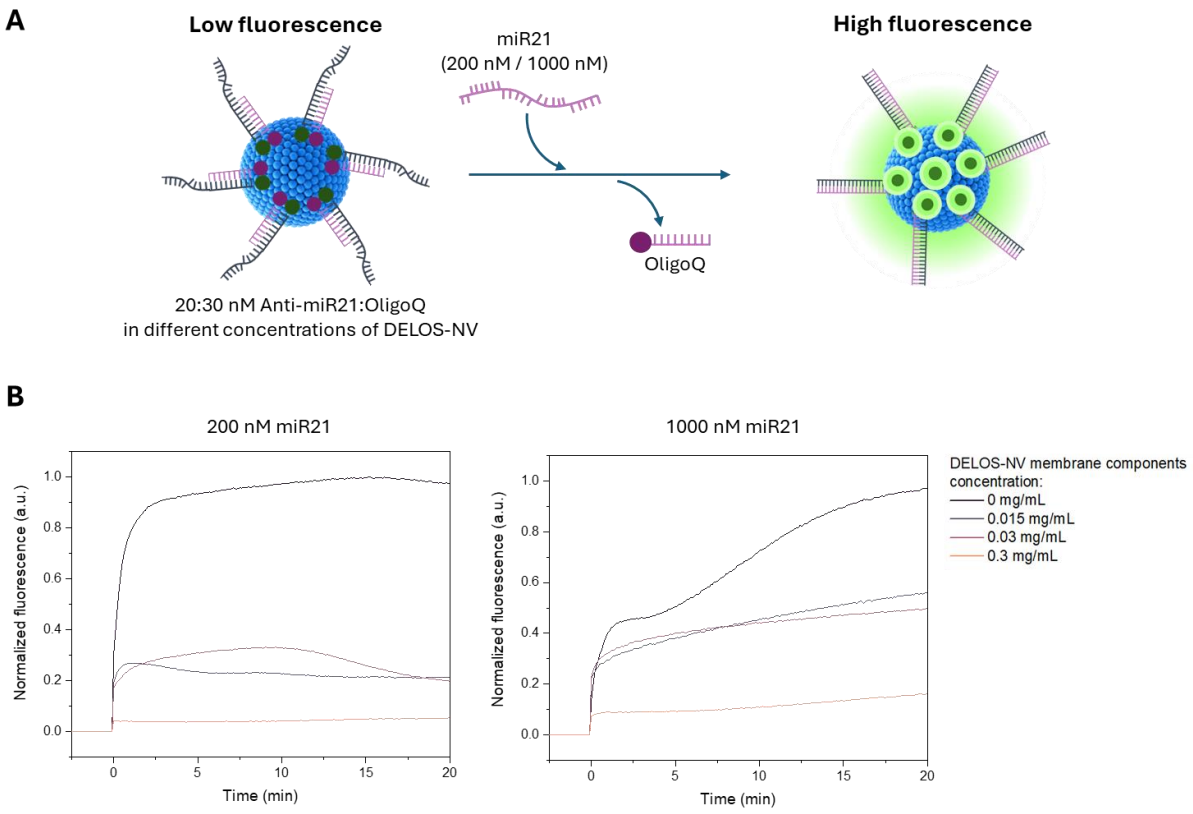


Figure 7.10. *miR21 binding to different concentration of DELOS-NV containing the pre-hybridized sequences Anti-miR21:OligoQ 1:1.5 (20 nM Anti-miR21 and 30 nM OligoQ, respectively). A) Schematic representations of the fluorescence change in response to the miR21 binding. B) 20-minute kinetic assay of the miR21 (200 nM or 1000 nM) binding to the Anti-miR21 (20 nM), pre-hybridized to the OligoQ (30 nM) and attached to different concentrations of DELOS-NV through the cholesteryl molecule (λ_{ex} = 475 nm and λ_{em} = 526 nm).*

7.4.2. DNA-grafted DELOS-NV biosensor production and miR21 binding assay

The previous set of tests enabled pinpointing the optimal conditions for preparing the DNA-grafted DELOS-NV biosensor. Consequently, in this section, the DNA-grafted DELOS-NV will be developed, integrating all the critical insights gleaned from the preliminary and control tests. The foundational principles established are as follows:

- The production order does affect the outcome: the Anti-miR21 and the OligoQ must be pre-hybridized before including the DELOS-NV on the system. Otherwise, the single-strand sequences get entrapped on the DELOS-NV surface and the hybridization is blocked.
- The most appropriate molar ratio Anti-miR21:OligoQ is 20:30 nM (equivalent to 1:1.5), which is almost an equimolar ratio. Lower ratios result in lower quenching of the ATTO488 fluorescence, while higher ratios result in an excess of non-bonded OligoQ that competes with the miR21 for hybridizing the Anti-miR21 sequences.
- The concentration of DELOS-NV has also an impact on miR21 recognition. High concentrations of DELOS-NV result in a lower recognition of the miR21, probably because

part of the negative-charged miR21 chains get entrapped on the positive charges of the DELOS-NV membrane. Therefore, when working with 20 nM Anti-miR21 hybridized to 30 nM OligoQ, a concentration of 0.03 mg/mL of DELOS-NV is adequate for the miR21 recognition.

Based on these premises, the DNA-grafted DELOS-NV were produced by first pre-hybridizing the 20 nM Anti-miR21 and the 30 nM OligoQ for 10 minutes and next adding the 0.03 mg/mL of nanovesicles (concentration correspondent to the membrane components sum -Chol + CPC-) and allowing the adsorption of the Anti-miR21 cholesteryl molecule into their membranes for another 10 minutes (**Figure 7.11**).

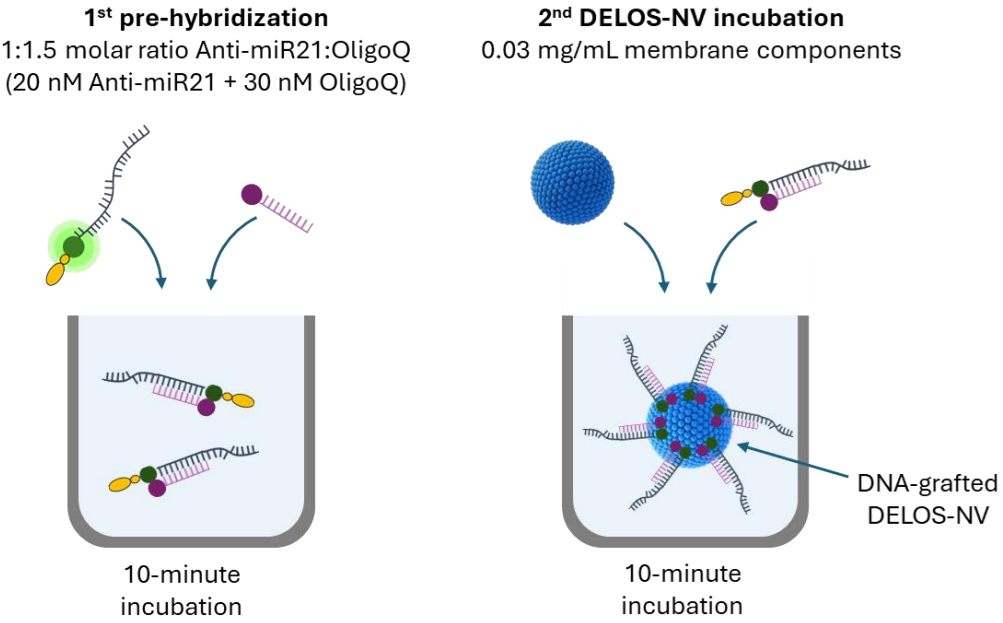


Figure 7.11. *Production of the DNA-grafted DELOS-NV. 20 nM Anti-miR21 and 30 nM OligoQ are pre-hybridized. Subsequently, the pre-hybridized sequences are incubated with the DELOS-NV (0.03 mg/mL membrane components) to form the DNA-grafted DELOS-NV biosensor.*

After production, and before testing the miR21 binding, this optimized system was physiochemically characterized. Cryo-TEM images were obtained (see **Section 9.3.4**) to study the morphology of the DNA-grafted DELOS-NV. The images in **Figure 7.12** show a high degree of interaction of the nanovesicles, caused by the presence of DNA, which probably binds hydrophobically through the cholesteryl to one nanovesicle membrane, and electrostatically to other nanovesicles. This high degree of interaction between DELOS-NV in the presence of miRNA was observed in previous studies of the Nanomol-Bio group working with nucleotides[7]. Despite the high degree of interaction, the nanovesicles' structure is maintained. They are spherical and unilamellar, and in most cases, they present a very small size, thus confirming that the SUV morphology is maintained in the DNA-grafted DELOS-NV. Moreover, the previous experience of Nanomol-Bio and Nanomol Technologies working with DELOS-NV and nucleotides suggests that this process is reversible and that miR21 can be recognized despite the high degree of interaction of the DELOS-NV.

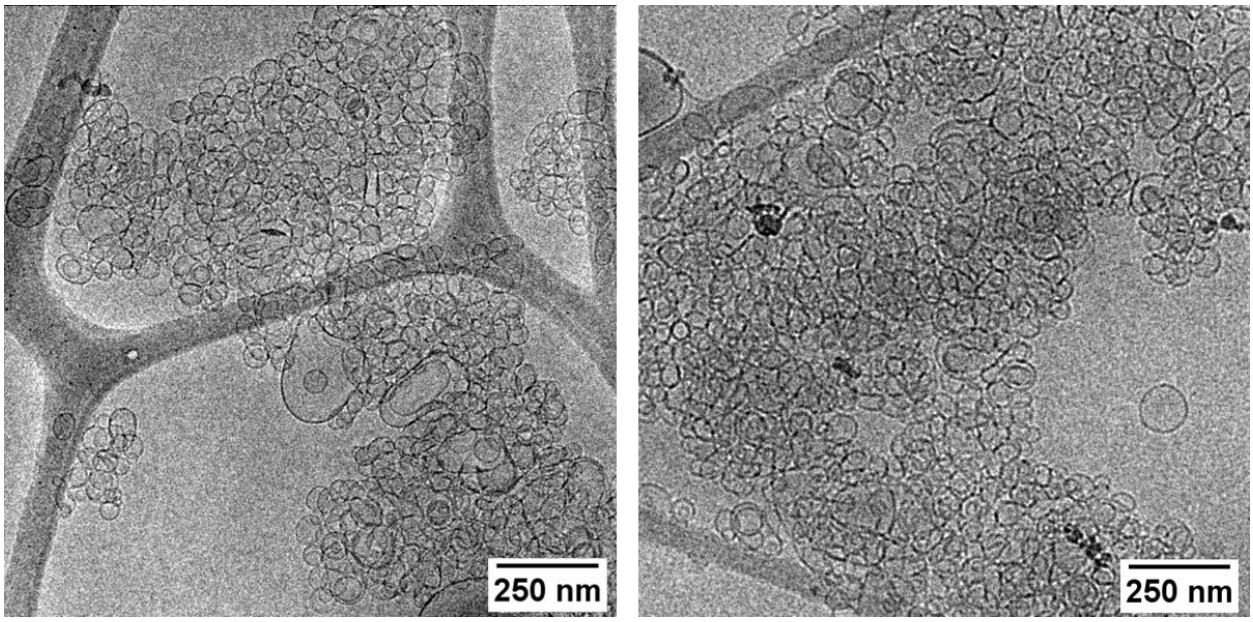


Figure 7.12. *Cryo-TEM images of the optimized DNA-grafted DELOS-NV biosensor developed in this thesis. The images correspond to two different shots of the same sample.*

After having confirmed the integrity of the nanovesicles in the developed system, this prototype was employed to conduct a miR21 binding assay. This is the most relevant experiment since it will demonstrate empirically if the developed biosensor works properly for miR21 recognition. In addition, it will provide information regarding the limit of detection (LoD) and limit of quantification (LoQ), very appreciable information in biosensor development.

To obtain the binding curve, miR21 was titrated into the optimized DNA-grafted DELOS-NV in dPBS. Injections were conducted every 5 minutes (see **Section 9.4.6.6** for details on the methodology). As previously mentioned, and considering the stated objective for this work, an increase of the fluorescence in response to the miR21 concentration increase was expected (see **Figure 7.4**). Eight replicates were performed to have representative data[h]. The results are shown as fluorescence intensity **(Figure 7.13A)**, and signal gain (%) (**Figure 7.13B**) calculated with **Equation 9.9**.

[h] *Andrea di Pede, Ph.D. student at Prof. Alessandro Porchetta's group, contributed to the obtainment of the replicates of the miR21 binding assay.*

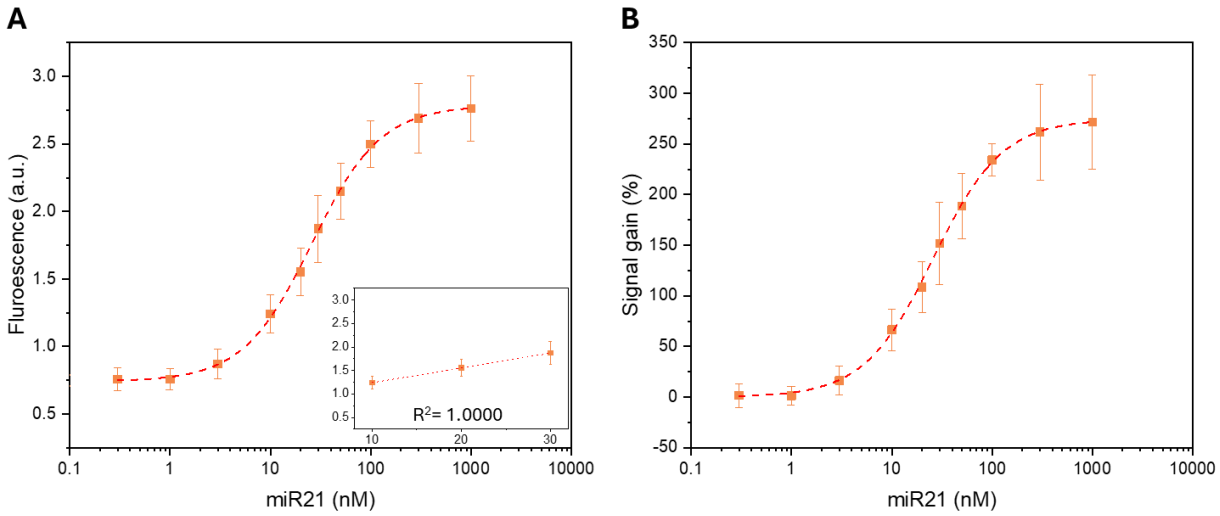


Figure 7.13. *The binding curve obtained by adding an increasing concentration of miR21 to a solution containing the DNA-grafted DELOS-NV. A) Fluorescence increase (λ_{ex} = 475 nm and λ_{em} = 526 nm), with the linear region represented and fitted in the inset (R^2= 1.0000) and B) Signal gain in percentage. All the experiments are performed in dPBS buffer at 25 ºC. The data corresponds to the average and SD of 8 replicates obtained on two different days. The curves were fitted with modified Hill equation (**Equation 9.10**) (red dashed line, R^2= 0.9992) in both cases, fluorescence (A) and Signal gain (B)).*

The binding curves shown in **Figure 7.13** were fitted using the modified Hill equation (**Equation 9.10**). Hill and Hill modified equations are mostly employed for dose-response curves in physiological and pharmacological studies[28,29], however, they have been used for a long time for the fitting of biosensors-target binding curves[8,30–32]. The modified Hill equation was preferred over the conventional because it correlates the outcome (fluorescence intensity in our case) with the ligand concentration, while the conventional correlates the fraction of occupied sites with the ligand[32].

Both fittings (fluorescence and signal gain binding curves), presented an R^2= 0.9992, thus indicating excellent fitting of the selected equation. From these fittings could be determined the dissociation constant (Kd) which is equivalent to the $K_{1/2}$ and was 25.9 nM in both fitted curves.

In addition to the Hill fitting, the linear region of the binding curve in **Figure 7.13A** was determined by visual inspection and by comparing the R^2 of the regression fitting between different concentration ranges. It was found that the response was linear in the range of 10 to 30 nM, with a regression showing an R^2 of 1.0000. The LoD and LoQ were calculated with equations **Equation 9.11** and **Equation 9.12** as explained in **Section 9.4.6.6**. A LoD of 5 nM and LoQ of 14 nM were obtained.

The LoD achieved with the developed system (LoD = 5 nM) is significantly lower than that of the previous approach developed between the Nanomol-Bio group, Nanomol Technologies S.L. and Prof. Alessandro Porchetta's group, which measured the signal using ratiometric FRET (LoD = 30-60 nM)[8] (**Figure 7.3**). Additionally, this novel approach is more intuitive for clinical applications, as it relies on direct quantification of fluorescence intensity rather than a ratiometric signal.

Therefore, this binding test has demonstrated the exceptional capacity of the developed biosensor to recognize miR21, achieving outstanding LoD and LoQ. The results have exceeded expectations,

showing that the DNA-grafted DELOS-NV biosensor is a significant improvement over the previous FRET-based approach[8]. As a next step, the specificity of the biosensor will be assessed.

7.4.3. Determination of the binding specificity for the developed DNA-grafted DELOS-NV biosensor

Having a very sensitive system is not enough to develop an effective biosensor. It is also important that the biosensor is highly specific in the recognition of the target molecule. To evaluate the specificity of the developed DNA-grafted DELOS-NV biosensor, a test was conducted where a non-specific miRNA was titrated into the DNA-grafted DELOS-NV (see **Section 9.4.6.7**). The non-specific miRNA selected was miR122 (5' – TGG AGT GTG ACA ATG GTG TTTG – 3') because it has a similar length and MW (5.564 KDa) to miR21 (see **Table 7.1**). At the same time, and for comparison purposes, a binding curve with the miR21 was also performed. In both tests, the experimental procedure was exactly the same, as well as the concentrations of miRNA titrated, and the unique difference was the miRNA employed (miR122 *vs* miR21). The results are shown in **Figure 7.14** and demonstrate the high specificity of the developed system. The signal gain for the miR122 at the end of the titration experiment is 11.7%, while for the miR21 is 160.3%.

Therefore, the results obtained in this **Section** demonstrate the high specificity of the developed biosensor. Together with the previous LoD and LoQ results, this highlights the optimized DNA-grafted DELOS-NV as a promising biosensor for miR21 identification.

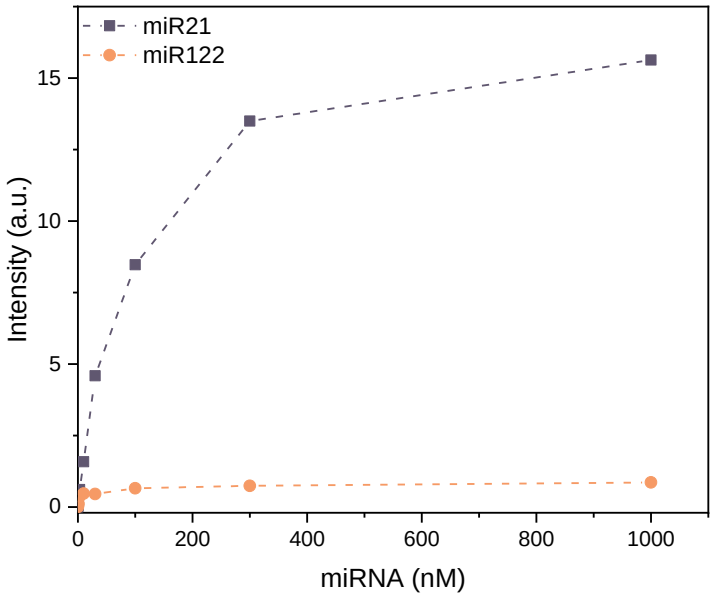


Figure 7.14. *Binding curves obtained by adding increasing concentration of the specific miR21 and non-specific miR122 targets to a solution of DNA-grafted DELOS-NV (20 nM Anti-miR21, 30 nM OligoQ and 0.03 mg/mL DELOS-NV membrane components).*

7.5. Summary of the chapter and perspectives

The previous chapter demonstrated the low permeability of FITC-BSA and insulin proteins entrapped in Chol:CPC DELOS-NV through the intestinal epithelium. This suggests that Chol:CPC DELOS-NV may be suitable for local applications in the gastrointestinal tract for certain molecules, minimizing the risk of systemic side effects.

Colorectal cancer is a prevalent gastrointestinal disease with high mortality in the US and Europe[17,18]. Early detection, primarily through endoscopy[23], is crucial, and surgical removal remains the most effective treatment[14]. However, conventional white light endoscopy struggles with early-stage detection, highlighting the need for advanced endoscopy methods to improve diagnosis and guide surgeries. In that context, the *in vivo* detection of miR21, a miRNA overexpressed in colorectal cancers, could contribute to these aspects during endoscopies. The most straightforward approach to detect miR21 would be using a complementary oligonucleotide. However, oligonucleotides are labile, and their *in vivo* application is challenging. DELOS-NV have demonstrated previously their ability to protect oligonucleotides from nucleases and enhance cellular penetration[7,8].

Within this framework, the objective of this **Chapter** was to leverage the possible local effect of Chol:CPC DELOS-NV by developing a biosensor for detecting miR21, which could potentially be employed for cancer diagnosis during endoscopies.

For this purpose, DNA-grafted DELOS-NV were designed and developed, using an Anti-miR21 with an ATTO488 fluorophore pre-hybridized to a partially complementary oligonucleotide sequence with a BHQ-1 quencher called OligoQ. These two sequences in the absence of the miR21 are hybridized, and the ATTO488 fluorescence is quenched. In the presence of the miR21, a strand-displacement reaction results in the hybridization of the miR21 to the Anti-miR21, releasing the OligoQ with the quencher. Hence, the distance between the ATTO488 and the quencher increases, thereby permitting the measurement of ATTO488 fluorescence upon its excitation.

During this **Chapter**, the first tests aimed to determine the optimal conditions to produce the DNA-grafted DELOS-NV. The most important premises determined from these studies are:

- It is necessary to pre-hybridize the Anti-miR21 sequence to the OligoQ before including the nanovesicles on the system. Otherwise, the nanovesicles trap the DNA, probably through electrostatic binding, preventing their hybridization and the recognition of the miR21.
- The optimal molar ratio Anti-miR21:OligoQ is 20:30 nM. A lower proportion of OligoQ sequences results in an incomplete quenching of the ATTO488 fluorescence, and a higher proportion of the OligoQ sequences results in lower recognition of the miR21 because both sequences compete on binding the Anti-miR21.
- The most appropriate concentration of DELOS-NV, understood as the concentration of membrane components (Chol + CPC) is 0.03 mg/mL, because higher concentrations result in lower signal gains in response to the miR21, probably because the miR21 is trapped by electrostatic charges in the nanovesicles membrane, preventing its hybridization with the Anti-miR21.

Following these statements, a novel DNA-grafted DELOS-NV biosensor system was developed and tested. The system recognized the miR21 with very high sensitivity and specificity as determined by

comparing the fluorescence increase in response to the miR21 and a non-specific miRNA (miR122). In addition, the LoD was significantly improved compared to the LoD achieved by Marianna Rosetti et al.[8] with the DELOS-NV-based biosensor developed in a previous collaboration between the Nanomol-Bio group, Nanomol Technologies S.L., and Alessandro Porchetta's group.

The tests carried out empirically demonstrate that the developed system has the potential as a novel biosensor for the diagnosis of colorectal cancer during endoscopies, through the recognition of miR21 with high sensitivity and specificity. This outstanding proof of concept requires further development to advance the formulation for *in vivo* detection of cancers. The next steps, outside the framework of this thesis, will consist of evaluating the *in vitro* detection in gastrointestinal cells. It is also worth mentioning that miR21 is overexpressed in many cancer types, highlighting the developed platform as a versatile tool with the potential for broad applicability in detecting various cancerous diseases.

7.6. References

1. P. Jolly, P. Estrela, M. Ladomery. Oligonucleotide-based systems: DNA, microRNAs, DNA/RNA aptamers. *Essays Biochem*. **2016**, 60 (1), 27–35.
2. E.S. Andersen, M. Dong, M.M. Nielsen, et al. Self-assembly of a nanoscale DNA box with a controllable lid. *Nature* **2009**, 459 (7243), 73–76.
3. T.C. Roberts, R. Langer, M.J.A. Wood. Advances in oligonucleotide drug delivery. *Nat. Rev. Drug Discov*. **2020**, 19 (10), 673–694.
4. L. Moumné, A.C. Marie, N. Crouvezier. Oligonucleotide therapeutics: From discovery and development to patentability. *Pharmaceutics* **2022**, 14 (2).
5. J. Kim, C. Hu, C.M. El Achkar, et al. Patient-customized oligonucleotide therapy for a rare genetic disease. *N. Engl. J. Med*. **2019**, 381 (17), 1644–1652.
6. N.B.Y. Tsui, E.K.O. Ng, Y.M.D. Lo. Stability of endogenous and added RNA in blood specimens , serum , and plasma. *Clin. Chem*. **2002**, 48 (10), 1647–1653.
7. A. Boloix, N. Feiner-Gracia, M. Köber, et al. Engineering pH-sensitive stable nanovesicles for delivery of microRNA therapeutics. *Small* **2022**, 18 (3), 2101959.
8. M. Rossetti, L. Stella, J. Morlà-Folch, et al. Engineering DNA-grafted Quatsomes as stable nucleic acid-responsive fluorescent nanovesicles. *Adv. Funct. Mater*. **2021**, 31 (46), 1–9.
9. B. Weinhold. Epigenetics: the science of change. *Environ. Health Perspect*. **2006**, 114 (3), 160–167.
10. L. Pavin. Unveiling the genetic symphony: Exploring the intricacies of gene expression. *Hum. Genet. Embriol*. **2023**, 14 (2).
11. G. Gentile, G. Morello, V. La Cognata, et al. Dysregulated miRNAs as biomarkers and therapeutical targets in neurodegenerative diseases. *J. Pers. Med*. **2022**, 12 (5).
12. F. Sessa, M. Salerno, M. Esposito, G. Cocimano, C. Pomara. miRNA Dysregulation in cardiovascular diseases: Current opinion and future perspectives. *Int. J. Mol. Sci*. **2023**, 24 (6).
13. S.M. Pauff, S.C. Miller. The role of microRNAs in colorectal cancer. *Bone* **2012**, 78 (2), 711–716.
14. A.M. Strubberg, B.B. Madison. MicroRNAs in the etiology of colorectal cancer: pathways and clinical implications. *Dis. Model. Mech*. **2017**, 10 (3), 197–214.
15. Y. Wu, Y. Song, Y. Xiong, et al. MicroRNA-21 (Mir-21) promotes cell growth and invasion by repressing tumor suppressor PTEN in colorectal cancer. *Cell. Physiol. Biochem*. **2017**, 43 (3), 945–958.
16. S.T. Crooke, J.L. Witztum, C.F. Bennett, B.F. Baker. RNA-targeted therapeutics. *Cell Metab*. **2018**, 27 (4), 714–739.
17. R.L. Siegel, N.S. Wagle, A. Cercek, R.A. Smith, A. Jemal. Colorectal cancer statistics, 2023. *CA. Cancer J. Clin*. **2023**, 73 (3), 233–254.

18. United european gastroenterology. Burden, economic impact and research gaps: Key findings from the Pan-European study on digestive diseases and cancers; **2023**.

19. C. You, L. Jin, Q.I. Xu, et al. Expression of miR-21 and miR-138 in colon cancer and its effect on cell proliferation and prognosis. *Oncol. Lett.* **2019**, 17 (2), 2271–2277.

20. J. Rhim, W. Baek, Y. Seo, J.H. Kim. From molecular mechanisms to therapeutics: Understanding microRNA-21 in cancer. *Cells* **2022**, 11 (18), 2791.

21. Y. Gao, M. Dai, H. Liu, W. He, S. Lin. Diagnostic value of circulating miR-21: An update meta-analysis in various cancers and validation in endometrial cancer. *Oncotarget* **2016**, 7 (42), 68894–68908.

22. Q. Liu, J. Fan, C. Zhou, et al. Quantitative detection of miRNA-21 expression in tumor cells and tissues based on molecular beacon. *Int. J. Anal. Chem.* **2018**, 3625823.

23. L. Rabeneck, L.F. Paszat, R. Saskin, T.A. Stukel. Association between colonoscopy rates and colorectal cancer mortality. *Am. J. Gastroenterol.* **2010**, 105 (7), 1627–1632.

24. A. Hoffman, R. Atreya, T. Rath, M.F. Neurath. Use of fluorescent dyes in endoscopy and diagnostic investigation. *Visc. Med.* **2020**, 36 (2), 95–102.

25. Y. Guo, B. Wei, S. Xiao, et al. Recent advances in molecular machines based on toehold-mediated strand displacement reaction. *Quant. Biol.* **2017**, 5 (1), 25–41.

26. Y. Bernard, T. Andrew J., M.J. Allen P., S. Friedrich C., N. Jennifer L. A DNA-fuelled molecular machine made of DNA. *Nature* **2000**, 406 (6796), 605–608.

27. A.K. Gaigalas, L. Li, O. Henderson, et al. The development of fluorescence intensity standards. *J. Res. Natl. Inst. Stand. Technol.* **2001**, 106 (2), 381–389.

28. H. Motulsky, A. Christopoulos. Fitting models to biological data using linear and nonlinear regression: A practical guide to curve fitting; **2004**.

29. R. Gesztelyi, J. Zsuga, A. Kemeny-Beke, et al. The Hill equation and the origin of quantitative pharmacology. *Arch. Hist. Exact Sci.* **2012**, 66, 427–438.

30. A.G. Rottinghaus, C. Xi, M.B. Amrofell, H. Yi, T.S. Moon. Engineering ligand-specific biosensors for aromatic amino acids and neurochemicals. *Cell Syst.* **2023**, 13 (3), 204–214.

31. I.A. Borisov, A. V Lobanov, A.N. Reshetilov, B.I. Kurganov. Quantitative analysis of the calibration dependences for biosensors. *Appl. Biochem. Microbiol.* **2000**, 36 (3), 215–220.

32. N. Aliakbarinodehi, P. Jolly, N. Bhalla, et al. Aptamer-based field-effect biosensor for tenofovir detection. *Nat. Sci. reports* **2017**, 7, 44409.



8 General conclusions

This thesis has focused on exploring the feasibility of using DELOS-NV as theragnostic nanocarriers for two novel administration routes not previously studied by the Nanomol-Bio group and Nanomol Technologies S.L.: the subcutaneous and oral administration routes. From the research conducted in this Ph.D. thesis, the following conclusions can be drawn:

1. **Reformulation of biocompatible DELOS-NV:**

DELOS-NV were rationally reformulated selecting only excipients from the United States Food and Drug Administration (FDA) Inactive Ingredients Database (IID) to pursue biocompatibility and regulated-oriented nanovesicles for the oral and subcutaneous administration routes. Two surfactants, cetylpyridinium chloride (CPC) and benzalkonium chloride (BKC), were compared in combination with cholesterol (Chol). A design of experiments (DoE) with a full factorial model was used to evaluate the impact of different formulation factors on specific critical quality attributes (CQA) of DELOS-NV. The obtained design space indicated a higher probability of meeting CQA specifications for DELOS-NV composed of CPC, leading to the selection of this surfactant for further development.

2. **Optimization of a DELOS-NV formulation for the subcutaneous drug delivery:**

In a subsequent DoE, CPC and Chol DELOS-NV dispersion was optimized by using a histidine 5 mM pH 7 buffer, as a more appropriate dispersant medium for subcutaneous administration. The impact of membrane components' concentration and the CPC:Chol molar ratio on the selected CQA was evaluated, resulting in an optimal formulation for subcutaneous administration when 5 mg/mL of Chol and CPC at an equimolar ratio were dispersed in a histidine 5 mM buffer, pH 7.

3. **Design of a DELOS-NV-loaded thermoreversible hydrogel as *in situ*-forming subcutaneous depot:**

The optimized DELOS-NV composed of Chol and CPC were gelled with varying concentrations (15-23% w/w) of Poloxamer 407 (Plx407) to create a hybrid subcutaneous *in situ*-forming depot to extend the release of the DELOS-NV and, consequently, of the drug entrapped. FRET fluorescence

measurements and cryogenic transmission electron microscopy (Cryo-TEM) images confirmed the integrity of the gelled Chol:CPC DELOS-NV. Rheological characterization identified 17% w/w Plx407 as the ideal concentration for an injectable hydrogel at 22 °C that solidifies at 37 °C. It was proved *in vitro* a consistent release pattern of the DELOS-NV over an 8-hour period, following a zero-order kinetics.

4. **Integration of a challenging-to-formulate "Beyond the Rule of 5" (bRo5) compound into the DELOS-NV-loaded thermoreversible hydrogel, as a preliminary proof-of-concept:**

A bRo5 compound with poor drug-like properties was successfully formulated into the Chol:CPC DELOS-NV-loaded 17% w/w Plx407 hydrogel. The compound was loaded into the DELOS-NV via the DELOS method and its concentration was adjusted through a concentration step using tangential flow filtration (TFF). The DELOS-NV formulation was successfully scaled up from a small laboratory-scale reactor to an intermediate laboratory-scale, demonstrating its scalability. This optimized nanoconjugate based on Chol:CPC DELOS-NV loading the bRo5 compound was gelled with 17% w/w Plx407. An *in vitro* release of the nanoconjugate from the hydrogel was achieved over 10 hours with promising zero-order kinetics, validating the hybrid platform as a potential subcutaneous delivery system for compounds with poor drug-like properties.

5. **Design of DELOS-NV nanoconjugates for intestinal drug delivery:**

Chol:CPC DELOS-NV loading Fluorescein Isothiocyanate – Bovine Serum Albumin (FITC-BSA) in Hank's Balanced Salt Solution (HBSS) buffer as dispersant medium, were designed through a DoE. HBSS medium was selected because this is the transport buffer in Caco-2 cell models for intestinal permeation assays. The effect that FITC-BSA and different formulation parameters had on specific DELOS-NV CQA was assessed and a design space was obtained. From the design space, different formulations were selected for the subsequent *in vitro* permeation assays. Through isothermal titration microcalorimetry (ITC) characterization, it was demonstrated the strong binding of FITC-BSA to the DELOS-NV, mainly through hydrophobic forces, ensuring no premature release of the protein before or during the permeation assays.

6. ***In vitro* intestinal permeation assays:**

The effect of the biocompatible Chol:CPC DELOS-NV in the intestinal epithelium has been assessed using Caco-2 cells *in vitro* models. The differentiation protocol was established, and the quality assays demonstrated appropriate differentiation of the Caco-2 cells into a mature intestinal epithelium. The permeation studies demonstrated that lucifer yellow integrated into Chol:CPC DELOS-NV permeated the Caco-2 monolayer at twice the rate of the free form, suggesting that DELOS-NV have potential for systemic delivery of certain molecules. In contrast, nanoconjugates based on Chol:CPC DELOS-NV with two different proteins -FITC-BSA and insulin- did not permeate the intestinal epithelium. In conclusions, Chol:CPC DELOS-NV might be appropriate for both, systemic and local delivery to the gastrointestinal tract, depending on the entrapped therapeutic molecule.

7. **Design of a potential biosensor for colorectal cancer diagnosis:**

A biosensor based on Chol:CPC DELOS-NV was developed for recognizing micro RNA 21 (miR21), which is overexpressed in colorectal cancers. An oligonucleotide sequence capable of recognizing

miR21 through a strand-displacement reaction and emitting fluorescence was grafted onto the DELOS-NV. Titration experiments established the optimal ratios for the DELOS-NV and oligonucleotide sequences for the biosensor development. In *in vitro* binding assays, the biosensor recognized the miR21 with very high sensitivity and specificity.

In conclusion, this thesis contributes to advancing the DELOS-NV as potential nanocarriers for both subcutaneous and oral administration routes, offering promising applications in extended drug release, local and/or systemic therapeutic effects depending on the administration route and the entrapped molecule, as well as potential for intestinal tract diagnostics.

9

9 Experimental Methods

9.1. Materials

9.1.1. Components employed in the DELOS-NV formulation preparation

5-Cholesten-3β-ol (Cholesterol (Chol) BioChemica, purity ≥ 95%) was obtained from PanReac AppliChem (Barcelona, Spain). The cetyltrimethylammonium bromide (CTAB BioUltra, purity ≥99.0%), the cetylpyridinium chloride (CPC, purity ≥ 98%) and the Benzalkonium chloride (BKC) were purchased from Sigma-Aldrich (Madrid, Spain). Ethanol (EtOH, High-Performance Liquid Chromatography -HPLC- grade) was obtained from PanReac AppliChem (Barcelona, Spain). Carbon dioxide (CO_2, purity ≥ 99.9%) and nitrogen (N_2, purity ≥ 99.9) were obtained from Carburos Metálicos (Barcelona, Spain).

The water used was pre-treated with the Milli-Q Reference A+ water purification system (Millipore Ibérica, Madrid, Spain). Buffer histidine was prepared using 0.005 M L-histidine (Purity ≥ 99%) from PanReac AppliChem (Barcelona, Spain). Hank's balanced salt solution (HBSS) powders were obtained from Sigma Aldrich (Madrid, Spain). HBSS solution was buffered by adding 4-(2-hydroxyethyl)-1-piperazineethanesulfonic acid (HEPES, 25 mM) and sodium bicarbonate $NaHCO_3$ (0.35 g/L) from Sigma Aldrich (Madrid, Spain).

All the chemicals were used without further purification.

9.1.2. Model molecules and fluorophores

Fluorophores: The 1,1'-dioctadecyl- 3,3,3',3'-tetramethyl-indocarbocyanine perchlorate (DiI) and 1,1'-dioctadecyl-3,3,3',3'-tetramethyl-indodicarbocyanine perchlorate (DiD) fluorophores were

purchased from Life Technologies (Carlsbad, CA, US). The lucifer yellow was acquired from Sigma-Aldrich (Madrid, Spain).

Beyond the Rule of 5 molecules (bRo5): The bRo5 active compounds were provided by the pharmaceutical company Boehringer Ingelheim.

Model proteins: The fluorescein isothiocyanate bovine serum albumin (FITC-BSA) and the human insulin were purchased from Sigma Aldrich (Madrid, Spain). Lyophilized rhEGF obtained from DNA recombinant technology was provided by Heber Biotec (La Habana, Cuba).

Oligonucleotides: All the oligonucleotides' sequences were purchased from Metabion International (Germany).

9.1.3. Hydrogelling agents

Poloxamer 407 (Plx407) was acquired from Merck (Darmstadt, Germany). Poly(lactide-co-glycolide)-block-poly(ethylene glycol)-block-poly(lactide-co-glycolide) (PLGA-PEG-PLGA) (Molecular weight: 1700-1500-1700; LA/GA ratio: 95:5) was acquired from Sigma Aldrich (Madrid, Spain).

9.1.4. Buffers, media, and reagents

In **Chapter 4** and **Chapter 5**, the release tests were performed in dPBS prepared with 0.14 M sodium chloride (NaCl, purity ≥ 99.5%) acquired from Thermo Fisher Scientific (Waltham, MA, US), 0.0027 M potassium chloride (KCl, purity ≥ 99.0%), 0.0081 M sodium hydrogen phosphate (Na_2HPO_4, purity ≥ 99.0%) and 0.0015 M sodium phosphate monobasic dihydrate ($NaH_2PO_4 \cdot 2H_2O$, purity ≥ 99.0%) acquired from Merck (Darmstadt, Germany).

In **Chapter 6**, cells were grown in Minimum essential medium (MEM) from Gibco (Pittsburgh, Pennsylvania, US), completed with 10% fetal bovine serum (FBS) and 1% penicillin/streptomycin solution (PEST) (10000 U/mL). All the components were purchased directly from the UAB's Cell Culture, Antibody Production and Cytometry service. The viability assays were conducted with the CellTiter 96® AQueous One Solution Cell Proliferation Assay (3-(4,5-dimethylthiazol-2-yl)-5-(3-carboxymethoxyphenyl)-2-(4-sulfophenyl)-2H-tetrazolium; MTS) from Promega, also purchased directly from the service. The permeation assays were conducted in HBSS transport media. HBSS powders, HEPES (25 mM) and $NaHCO_3$ (0.35 g/L) were obtained from Sigma Aldrich (Madrid, Spain).

In **Chapter 7** the oligonucleotide sequences were diluted upon reception in TRIS 0.1 M pH 8 buffer for their storage. Working dilutions of the oligonucleotides were subsequently made in dPBS buffer prepared with the same recipe as the one employed for the release test in **Chapter 4** and **Chapter 5**.

9.1.5. Other materials and reagents

In **Chapter 6**, the transwell filters employed for Caco-2 cells growth and permeation experiments were Corning Costar Transwell permeable supports, with a polycarbonate membrane, pore size 0.4

mm and diameter 12 mm (12-well plates), obtained from Sigma Aldrich (Madrid, Spain). Caco-2 cells were purchased directly from UAB's Cell Culture, Antibody Production and Cytometry service and were from the European Collection of Authenticated Cell Cultures (ECACC). CacoReady cells, already differentiated in filter supports, were acquired from Readycell S.L. (Spain). In addition, in **Chapter 6**, Hoechst and Cell Mask fluorophores were purchased directly to the Microscopy and X-ray Diffraction service from UAB and employed to stain the Caco-2 cells. Also, quantification of the insulin in the permeation assays was performed by an enzyme-linked immunosorbent assay (ELISA). The antibodies (Human/Canine/Porcine Insulin DuoSet ELISA, DY8056-05) and the reagents and plates for the assay (DuoSet ELISA Ancillary Reagent Kit 2, DY008B) were purchased from Biotechne (Minneapoli, MN, US).

Further, for the high-performance liquid chromatography (HPLC) analysis, in **Chapter 4** and **Chapter 6**, Optima® LC/MS Grade 2-Propanol > 99.9%, ammonium acetate > 99.5% and glacial acetic acid > 99.7% were obtained from Thermo Fisher Scientific (Waltham, MA, US). Ultra HPLC supergradient, ACS methanol > 99.9% was purchased from PanReac AppliChem (Barcelona, Spain). Formic acid > 98% was obtained from Merck (Darmstadt, Germany).

9.2. Preparation and post-process of DELOS nanovesicles

9.2.1. Production of DELOS nanovesicles by DELOS technology

9.2.1.1. Description of the technology and the equipment

To produce the DELOS-NV, DELOS technology was employed. This technology is based on compressed CO_2 and was developed by Nanomol-Bio group and Nanomol Technologies S.L. Depending on the desired batch size, two different configurations were used: the small laboratory-scale equipment (7.5 mL high-pressure vessel, batch size 25 – 75 mL) or the intermediate laboratory-scale equipment (25 mL or 50 mL high-pressure vessel, batch size 150 – 900 mL).

The small laboratory-scale equipment used to prepare DELOS-NV using DELOS technology is schematized in **Figure 9.1**. Briefly, the configuration consists of a 7.5 mL high-pressure vessel (R), for which the temperature is adjusted using an external heater (recirculating bath). CO_2 is pumped into the high-pressure vessel through a syringe pump (P) (model 260D, ISCO Inc., Lincoln, US) until reaching the working pressure, monitored with a pressure indicator (PI). Further, by using a depressurization valve, the expanded liquid solution contained in the vessel is depressurized into an aqueous phase placed in a collector (C) at atmospheric pressure. High pressure of nitrogen (N_2) (P_{N2} > P_{CO2}) is introduced directly from a pressurized reservoir to the vessel, to act as a plunger and push down the CO_2-expanded solution from the vessel, while maintaining constant pressure inside the equipment.

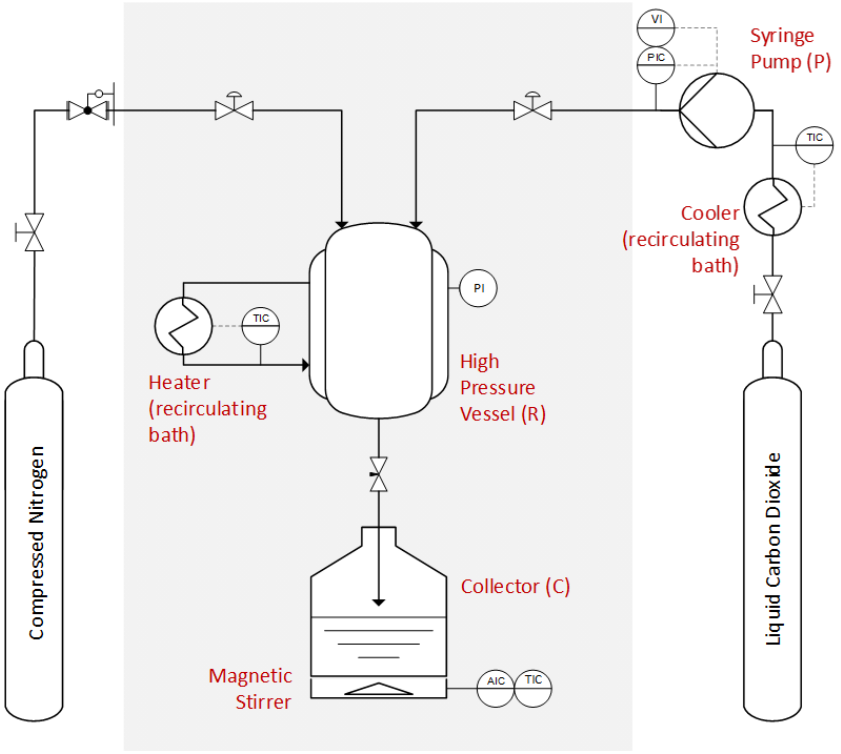


Figure 9.1. *Process diagram of the small laboratory-scale equipment (7.5 mL high-pressure vessel) set-up used for the preparation of nanovesicles by DELOS.*

The intermediate laboratory-scale equipment used to prepare DELOS-NV using DELOS technology is schematized in **Figure 9.2**. This setup closely resembles the small laboratory-scale equipment. It consists of 25 mL or 50 mL (independent and interchangeable) high-pressure vessels (R), for which the temperature is maintained using an external heater (recirculating bath), equivalent to the small laboratory-scale equipment. Key differences include the addition of a variable speed stirrer inside the high-pressure vessel, which can be adjusted and monitored by an agitator indicator and controller (AIC) to ensure homogeneity of the mixture in the volumetrically expanded phase. Additionally, the temperature and pressure inside the high-pressure vessel are monitored by a temperature indicator (TI) and a pressure indicator (PI). A safety valve is also included. The remaining components of the equipment, as well as the procedure involving CO_2 introduction to the vessel until reaching working pressure and the expanded organic solution, followed by depressurization over a collector (C) at atmospheric pressure, assisted by N_2 as a plunger, are identical to those of the small laboratory-scale equipment.

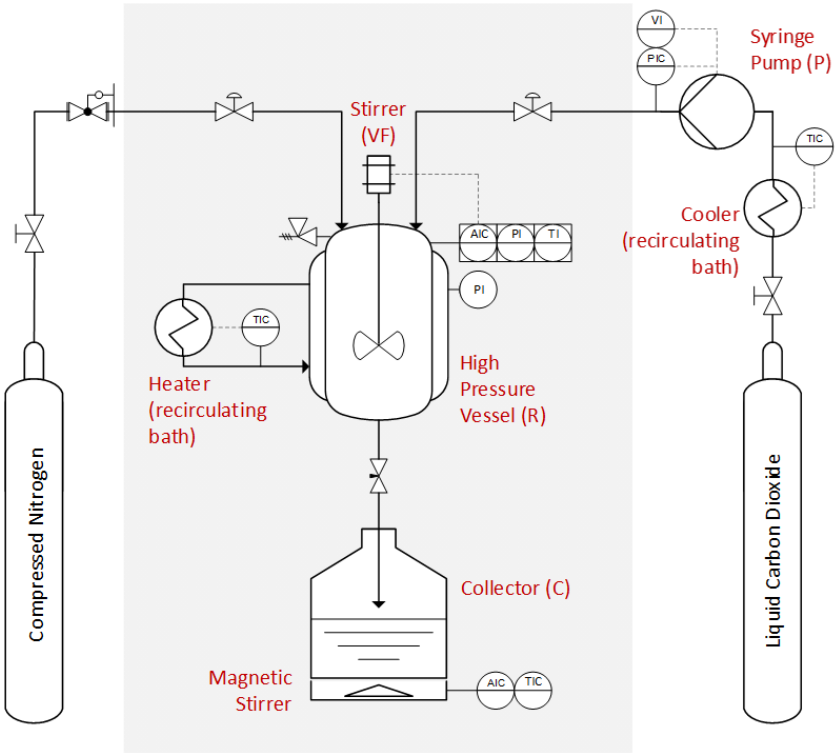


Figure 9.2. *Process diagram of the intermediate laboratory-scale equipment (25 mL or 50 mL high-pressure vessel) set-up used for the preparation of nanovesicles by DELOS.*

9.2.1.2. Procedure for DELOS-NV obtainment by DELOS technology

The procedure for the DELOS-NV obtainment by DELOS technology is equivalent for both, the small laboratory-scale and the intermediate laboratory-scale equipment. The generic procedure was explained in the **Introduction**, **Section 1.3.2.1.1**.

More in detail, during the development of this thesis, the different formulations were produced as follows:

The high-pressure vessel was loaded at atmospheric pressure and 40 °C with an organic solution of cholesterol and surfactant (BKC, CPC or CTAB) dissolved in EtOH. When applicable, hydrophobic payloads were also dissolved in the organic phase (DiI, DiD and bRo5 molecules). Afterward, CO_2 was introduced to the reactor at a working pressure of 85 bar to obtain a CO_2-expanded solution. The CO_2-expanded solution was kept for 45 min in the small laboratory-scale equipment, or 15 min under stirring (500 rpm) in the intermediate laboratory-scale equipment, to achieve complete homogenization and to attain thermal equilibration. Afterward, depressurization over an aqueous phase was conducted. The aqueous solutions employed in the present work were purified water, histidine 5 mM pH 7 buffer or HBSS pH 7.4 buffer. When required, hydrophilic payloads were also solubilized in the aqueous solutions prior to depressurization (lucifer yellow, insulin or FITC-BSA). A flow of nitrogen (N_2) at a working pressure of 100 bar was used to plunge the CO_2-expanded solution during depressurization.

The volumetric relation between the aqueous phase and the organic phase was 9:1 aqueous phase:organic phase, hence, the obtained formulations contained 10% v/v of EtOH. The colloidal suspensions were transferred to a container, hermetically sealed, and stored at 2-8 °C until further characterization.

Must be remarked that those formulations containing molecules sensitive to light (FITC-BSA, DiI, DiD and lucifer yellow) were protected by covering the storage recipient with foil. In addition, those formulations containing molecules sensitive to acidic pH (FITC-BSA) were produced in buffers with controlled pH.

9.2.2. Tangential flow filtration of the DELOS-NV suspension

Tangential flow filtration technique (TFF) permits purification, media exchange and/or concentration of suspensions.

In the present work, when required, TFF was employed a) to eliminate the remaining EtOH present in DELOS-NV suspensions after their production by DELOS technology; b) in loaded DELOS-NV, to eliminate the payloads non-integrated in the DELOS-NV; and c) to concentrate the DELOS-NV suspensions to achieve the target concentrations of the integrated payloads.

In TFF, the suspension flows tangentially across the surface of a filter membrane. This tangential flow helps to reduce fouling and clogging of the filter, allowing for continuous processing. The setup for TFF available at Nanomol Technologies S.L. is an ÄKTA flux system and is schematized in **Figure 9.3**. In detail, the sample to be filtrated is placed in a reservoir (C2), and a peristaltic pump (P2) recirculates it through the hollow fiber column. This is the feed flow and is represented in blue in the process diagram (**Figure 9.3A**). Afterwards, those elements smaller than the hollow fiber pores, such as water molecules or small actives non-integrated into the DELOS-NV, are eliminated into the permeate (**Figure 9.3B**), which is represented in orange in the process diagram. The retained suspension, which is called retentate and is represented in green, returns to the reservoir tank of the sample. To concentrate the sample, several recirculation cycles must be conducted until reaching the desired concentration. Conversely, if the sample is not meant to be concentrated, and the objective is buffer replacement or purification of the sample, the eliminated buffer is replaced by fresh one, which is transferred into the reservoir tank through another peristaltic pump (P1). This flow of fresh buffer, called transfer flow, is represented in purple in the process diagram. If the transfer flow is equal to the permeate flow, the volume of the suspension will remain constant at the end of the TFF process. It is considered that 5 to 6 cycles of TFF are enough to replace the hole buffer of a formulation with a fresh one and to purify the sample. Therefore, when 5 to 6 times the volume of the sample is recollected in the permeate, the process is finished.

In **Chapter 4**, TFF was employed to eliminate the ethanol in all samples (blank DELOS-NV and labeled DELOS-NV). In addition, for labeled DELOS-NV, the DiI and DiD non-integrated in the nanovesicles were eliminated by TFF. For this purpose, C04-E100-05-N hollow fiber columns with a 100 kDa molecular weight cut-off were employed. This size pore guarantees the preservation of the DELOS-NV while eliminating the solvent and the non-integrated fluorophores.

In **Chapter 5**, DELOS-NV incorporating bRo5 molecules were diafiltrated to eliminate the EtOH and non-integrated bRo5 molecules, and afterward, concentrated to reach the target concentration of bRo5 molecules in the formulation. For this purpose, C04-E100-05-N hollow fiber columns with a 100 kDa molecular weight cut-off were employed.

In **Chapter 6**, TFF was employed for EtOH elimination and sample purification. Non-integrated FITC-BSA, insulin and lucifer yellow molecules were eliminated. For FITC-BSA purification, D04-E300-10-N hollow fiber columns with a 300 kDa molecular weight cut-off were employed. For insulin and lucifer yellow purification, C04-E100-05-N hollow fiber columns were employed, with a 100 kDa molecular weight cut-off.

In **Chapter 7**, the nanovesicles employed for the biosensor development were diafiltrated by TFF to eliminate the EtOH with a C04-E100-05-N hollow fiber column with 100 kDa molecular weight cut-off.

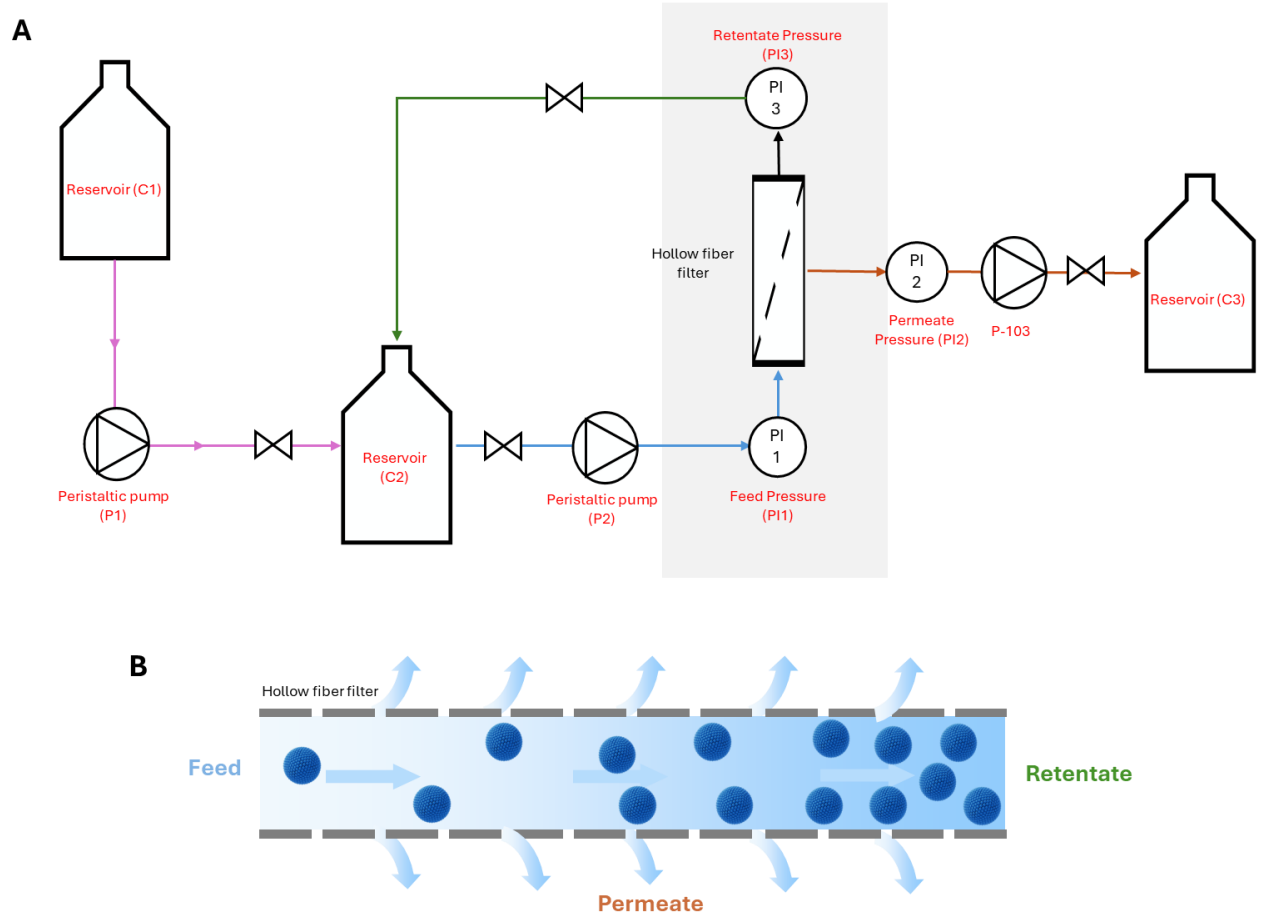


Figure 9.3. A) Process diagram of the ÄKTA flux TFF system. B) Representation of the flow through the hollow fiber column.

Formulations prepared by DELOS technology and tangential flow filtration

Table 9.1, **Table 9.2**, **Table 9.3** and **Table 9.4** summarize the compositions and processing of the different formulations produced in the present work except those prepared for DoE studies that are already included in the respective chapters.

Table 9.1. *DELOS-NV with* ***5 mg/mL of Chol + CPC at an equimolar ratio****; produced by DELOS* technology and diafiltrated using TFF in* ***Chapter 4****.*

Sample ID	*DELOS method:*		*TFF method:*		
	DELOS media	*Payload after DELOS*	*TFF*	*TFF media*	*Payload after TFF*
SC-Chol:CPC DELOS-NV	*Histidine 5 mM pH 7 + 10% EtOH*	*NA*	*NA*	*NA*	*NA*
TFF-Chol:CPC DELOS-NV	*Histidine 5 mM pH 7 + 10% EtOH*	*NA*	*Media exchange*	*Histidine 5 mM pH 7*	*NA*
DiD-DELOS-NV	*Histidine 5 mM pH 7 + 10% EtOH*	*DiD 45 µM*	*Media exchange*	*Histidine 5 mM pH 7*	*DiD 45 µM*
DiI/DiD-DELOS-NV	*Histidine 5 mM pH 7 + 10% EtOH*	*DiI/DiD 45/45 µM*	*Media exchange*	*Histidine 5 mM pH 7*	*DiI/DiD 45/45 µM*

**Chol:CPC DELOS-NV were produced in the intermediate DELOS equipment. DiD-DELOS-NV and DiI/DiD DELOS-NV in the small DELOS equipment.*

Table 9.2. *DELOS-NV with* ***6 mg/mL Chol + CPC at an equimolar ratio****; produced by DELOS* technology and diafiltrated using TFF in* ***Chapter 5****.*

Sample ID	*DELOS method:*		*TFF method:*		
	DELOS media	*Payload after DELOS*	*TFF*	*TFF media*	*Payload after TFF*
Control DELOS-NV	*Histidine 5 mM pH 7 + 10% EtOH*	*NA*	*Media exchange + 2.4 times conc.*	*Histidine 5 mM pH 7*	*NA*
bRo5.1-DELOS-NV	*Histidine 5 mM pH 7 + 10% EtOH*	*bRo5.1 1 mg/mL*	*Media exchange + 2.4 times conc.*	*Histidine 5 mM pH 7*	*bRo5.1 1.23 mg/mL*
bRo5.2-DELOS-NV	*Histidine 5 mM pH 7 + 10% EtOH*	*bRo5.2 1 mg/mL*	*Media exchange + 2.4 times conc.*	*Histidine 5 mM pH 7*	*bRo5.2 1.56 mg/mL*
bRo5.3-DELOS-NV	*Histidine 5 mM pH 7 + 10% EtOH*	*bRo5.3 1 mg/mL*	*NA*	*NA*	*NA*
bRo5.4-DELOS-NV	*Histidine 5 mM pH 7 + 10% EtOH*	*bRo5.4 1 mg/mL*	*NA*	*NA*	*NA*
bRo5.5-DELOS-NV	*Histidine 5 mM pH 7 + 10% EtOH*	*bRo5.5 1 mg/mL*	*NA*	*NA*	*NA*
bRo5.1-DELOS-NV replicate 2	*Histidine 5 mM pH 7 + 10% EtOH*	*bRo5.1 1 mg/mL*	*Media exchange + 2.4 times conc.*	*Histidine 5 mM pH 7*	*bRo5.1 1.42 mg/mL*
bRo5.2-DELOS-NV replicate 2	*Histidine 5 mM pH 7 + 10% EtOH*	*bRo5.2 1 mg/mL*	*Media exchange + 2.4 times conc.*	*Histidine 5 mM pH 7*	*bRo5.2 1.06 mg/mL*

Scaled-bRo5.1-DELOS-NV	*Histidine 5 mM pH 7 + 10% EtOH*	*bRo5.1 0.5 mg/mL*	*Media exchange + 2.4 times conc.*	*Histidine 5 mM pH 7*	*bRo5.1 4.52 mg/mL*

**All formulations except Scaled-bRo5.1-DELOS-NV were produced in the small DELOS equipment. Scaled-bRo5.1-DELOS-NV were produced in the intermediate DELOS equipment.*

Table 9.3. *DELOS-NV produced by DELOS* technology and diafiltrated using TFF in* ***Chapter 6****. Note that these samples were further diluted for the permeation assays in Caco-2 cells as described in* ***Chapter 6****.*

Sample ID	*DELOS method:*					*TFF method:*		
	Surfactant employed	*Membrane components concentration (mg/mL)*	*Surf.:Chol molar ratio*	*Payload after DELOS*	*DELOS media*	*TFF*	*TFF media*[2]	*Payload after TFF*
ITC-Chol:CTAB DELOS-NV	*CTAB*	*5.5 mg/mL*	*1:1*	*NA*	*Histidine 5 mM pH 7 + 10% EtOH*	*Media exchange*	*Histidine 5 mM pH 7*	*NA*
ITC-Chol:CPC DELOS-NV	*CPC*	*3 mg/mL*	*1:1*	*NA*	*HBSS pH 7.4 + 10% EtOH*	*Media exchange*	*HBSS pH 7.4*	*NA*
Abs1-DELOS-NV	*CPC*	*1 mg/mL*	*1:1*	*FITC-BSA 0.01 mg/mL*	*HBSS pH 7.4 + 10% EtOH*	*Media exchange*	*HBSS pH 7.4*	*FITC-BSA ≈ 0.01 mg/mL*
Abs2-DELOS-NV	*CPC*	*1 mg/mL*	*2:1*	*FITC-BSA 0.01 mg/mL*	*HBSS pH 7.4 + 10% EtOH*	*Media exchange*	*HBSS pH 7.4*	*FITC-BSA ≈ 0.01 mg/mL*
Abs3-DELOS-NV	*CPC*	*5 mg/mL*	*1:1*	*FITC-BSA 0.01 mg/mL*	*HBSS pH 7.4 + 10% EtOH*	*Media exchange*	*HBSS pH 7.4*	*FITC-BSA ≈ 0.01 mg/mL*
Abs4-DELOS-NV	*CPC*	*5 mg/mL*	*2:1*	*FITC-BSA 0.01 mg/mL*	*HBSS pH 7.4 + 10% EtOH*	*Media exchange*	*HBSS pH 7.4*	*FITC-BSA ≈ 0.01 mg/mL*
Ins- DELOS-NV	*CPC*	*1 mg/mL*	*1:1*	*Insulin 0.1 mg/mL*	*HBSS pH 7.4 + 10% EtOH*	*Media exchange*	*HBSS pH 7.4*	*Insulin ≈ 0.1 mg/mL*
LY- DELOS-NV	*CPC*	*5 mg/mL*	*1:1*	*Lucifer yellow 0.4 mg/mL*	*HBSS pH 7.4 + 10% EtOH*	*Media exchange*	*HBSS pH 7.4*	*Lucifer yellow 0.2 mg/mL*

**All DELOS-NV except LY-DELOS-NV were produced in the intermediate DELOS equipment. LY-DELOS-NV were produced in the small DELOS equipment.*

*Table 9.4. DELOS-NV with **1 mg/mL Chol + CPC at an equimolar ratio**; produced by DELOS* technology and TFF in **Chapter 7**. These DNA-DELOS-NV were produced in the intermediate DELOS equipment as blank nanovesicles (without payload) and conjugated with DNA at posteriori by incubation.*

Sample ID	DELOS method:		TFF method:		
	DELOS media	Payload after DELOS	TFF	TFF media	Payload after TFF
DNA-DELOS-NV	dPBS pH 7.4 + 10% EtOH	NA	Media exchange	dPBS pH 7.4	NA

9.2.3. Formulation of DELOS-NV into polymer matrix

In **Chapter 4** and **Chapter 5**, to prepare the enriched hydrogels with DELOS-NV, Plx407 was added to DELOS-NV dispersions at 4 °C to obtain DELOS-NV-loaded hydrogels with a final concentration of 15, 17, 20 and 23% w/w of polymer. The samples were left overnight at 5 ± 3 °C for hydrating the polymer and the day after, magnetic stirring was applied in a bath at the same temperature until the sample was clear and had no particles in dispersion (**Figure 9.4**).

The same procedure was applied for Chol:CPC DELOS-NV, DiD-DELOS-NV, DiI/DiD-DELOS-NV and bRo5.1-DELOS-NV (**Table 9.1** and **Table 9.2**) loaded into the hydrogels. Blanks without DELOS-NV of Plx407 in histidine buffer at pH 7 were also prepared following the same procedure (blank hydrogels).

In **Chapter 4**, the polymer PLGA-PEG-PLGA (Moleular weight: 1700-1500-1700; LA/GA ratio: 95:5), was also employed for the obtainment of TFF-Chol:CPC DELOS-NV-loaded hydrogels. When working with this polymer, the polymer was weighed before the DELOS-NV. Afterward, the TFF-Chol:CPC DELOS-NV suspension was added over the polymer to obtain the 25 % w/v PLGA-PEG-PLGA hydrogel. The mixture was kept in the fridge for 3 days prior to its homogenization with magnetic stirring in a bath at 4 °C.

All the obtained formulations (see **Table 9.5**) were stored at 5 ± 3 °C until their analysis.

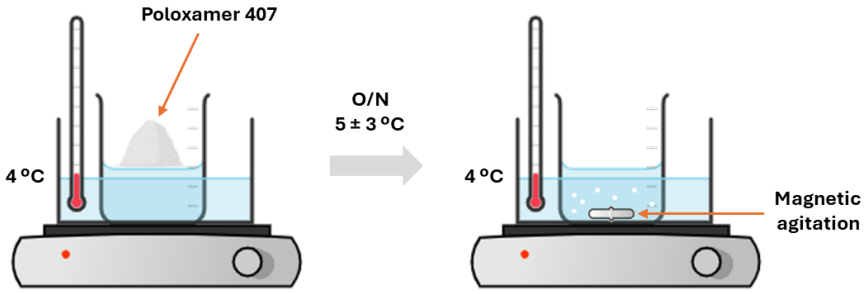


Figure 9.4. Schematic representation of the Poloxamer 407 hydrogels preparation. The polymer is directly weighed over the DELOS-NV suspensions or buffer for blank hydrogels.

Table 9.5. *Hydrogels of poloxamer 407 (Plx407) produced in* ***Chapter 4*** *and* ***Chapter 5****.*

Sample ID	***Polymer***	***Polymer concentration***	***DELOS-NV incorporation***
Chapter 4			
Blank 15% w/w Plx407	*Plx407*	*15% w/w*	*NA*
Blank 17% w/w Plx407	*Plx407*	*17% w/w*	*NA*
Blank 20% w/w Plx407	*Plx407*	*20% w/w*	*NA*
Blank 23% w/w Plx407	*Plx407*	*23% w/w*	*NA*
TFF-Chol:CPC DELOS-NV-loaded 15% w/w Plx407	*Plx407*	*15% w/w*	*TFF-Chol:CPC DELOS-NV*
TFF-Chol:CPC DELOS-NV-loaded 17% w/w Plx407	*Plx407*	*17% w/w*	*TFF-Chol:CPC DELOS-NV*
TFF-Chol:CPC DELOS-NV-loaded 20% w/w Plx407	*Plx407*	*20% w/w*	*TFF-Chol:CPC DELOS-NV*
TFF-Chol:CPC DELOS-NV-loaded 23% w/w Plx407	*Plx407*	*23% w/w*	*TFF-Chol:CPC DELOS-NV*
DiI/DiD-DELOS-NV-loaded 15% w/w Plx407	*Plx407*	*15% w/w*	*DiI/DiD-DELOS-NV*
DiI/DiD-DELOS-NV-loaded 17% w/w Plx407	*Plx407*	*17% w/w*	*DiI/DiD-DELOS-NV*
DiI/DiD-DELOS-NV-loaded 20% w/w Plx407	*Plx407*	*20% w/w*	*DiI/DiD-DELOS-NV*
DiD-DELOS-NV-loaded 15% w/w Plx407	*Plx407*	*15% w/w*	*DiD-DELOS-NV*
DiD-DELOS-NV-loaded 17% w/w Plx407	*Plx407*	*17% w/w*	*DiD-DELOS-NV*
TFF-Chol:CPC DELOS-NV-loaded PLGA-PEG-PLGA	*PLGA-PEG-PLGA*	*25% w/v*	*TFF-Chol:CPC DELOS-NV*
Chapter 5			
bRo5.1-DELOS-NV-loaded 17% w/w Plx407	*Plx407*	*17% w/w*	*bRo5.1-DELOS-NV*

9.3. DELOS-NV suspensions and hydrogels physicochemical characterization

9.3.1. Particle hydrodynamic diameter, size polydispersity index and apparent zeta potential assessment

The DELOS-NV particles' size as intensity-weighted hydrodynamic diameter, the size polydispersity index (PdI) and the apparent zeta potential (Z-potential) were determined at 25 °C using a Zetasizer Ultra (Malvern Instruments, Worcestershire, UK) with non-invasive backscatter optics, equipped with helium-neon laser at 633 nm and configurated with a detector set at 173º for hydrodynamic diameter and PdI measurements, and 13º for Z-potential measurements. The hydrodynamic diameter and size PdI were determined by dynamic light scattering (DLS). When measuring DLS of labeled DELOS-NV (DiD-DELOS-NV, DiI/DiD-DELOS-NV or LY-DELOS-NV), a fluorescent filter was applied; otherwise, no filter was utilized. The electrophoretic light scattering (ELS) was employed for the estimation of the apparent Z-potential. A 20-mV voltage was used for samples in buffers. Otherwise, an automatic voltage was used.

Suspensions of DELOS-NV concentrated more than 10-fold by TFF were diluted 1:10 to adjust concentration for the DLS and ELS analysis. Otherwise, the measurements were performed directly

without any previous modification or dilution. 1 mL of each suspension or dilution was transferred into disposable polystyrene cuvettes for DLS measurements or disposable folded capillary cells for Z-potential measurements.

Data was recorded using the ZS Xplorer software (Malvern Panalytical, UK). The hydrodynamic diameter data was based on the intensity size distribution and corresponds to the zeta average ± SD of three consecutive measurements. The use of scattered intensity is the most recommendable data when using DLS, since it comes from the original data provided by the analyzer, without further processing or involved assumptions for calculating particle size. The apparent Z-potential data was based on Smoluchowski model and corresponds to the Z-potential average ± SD of three consecutive measurements.

9.3.2. pH measurements of DELOS-NV

The determination of pH was measured using a pH meter pH 50+ DHS (XS instruments, Italy). Samples were left outside the fridge for at least 15 minutes at room temperature before performing the measurement. The electrodes were cleaned with water between measurements.

9.3.3. Quantification of the DELOS-NV membrane components by HPLC

The concentration of Chol and CPC components from the blank Chol:CPC DELOS-NV suspensions (**Table 9.1** and **Table 9.3**) was evaluated by Arnau Güell, Analytical Development Scientist at Nanomol Technologies S.L., using an Acquity Arc ultra-HPLC (Waters) coupled to a PDA 2998 detector. Each component was quantified by using its own specific analytical method.

Chol was quantified by using an XBridge BEH C18 column (2.5 µm 3.0 x 75 mm, Waters) in an isocratic mode of 90% of mobile phase A (volume ratio 5:95 water:methanol) and 10% of mobile phase B (0.1% formic acid in 2-propanol) at a flow rate of 1.0 mL/min for 4 min. The column and sample temperatures were fixed at 30 °C and 15 °C, respectively. The Chol detection wavelength was 206 nm.

CPC was quantified by using an InfinityLab Poroshell 120 EC-C18 column (4 µm 4.6 x 100 mm, Agilent) in a gradient mode using mobile phase A (50 mM ammonium acetate at pH 3.6) and mobile phase B (1% glacial acetic acid in methanol) at a flow rate of 1.0 mL/min for a total of 20 min. The column and sample temperatures were fixed at 35 °C and 15 °C, respectively. The CPC detection wavelength was 260 nm.

The obtained data was automatically processed by using the Empower 3 software (Waters).

The concentration of Chol and CTAB in the Chol:CTAB DELOS-NV, employed in **Chapter 6** (**Table 9.3**), was evaluated by Dr. Lidia Ferrer, R&D Director at Nanomol Technologies S.L., in the Chemical Analysis Service from the UAB as self-service. The analysis was performed in an HPLC (1100 series, Agilent Technologies (US)) equipped with an Evaporative Light Scattering Detector, ELSD (1260 infinity ELSD, Agilent Technologies (US)).

Chol separation was done using a C18 Symmetry® (5 µm; 4.6 × 150 mm) column (Waters Cromatografía S.A.) with an ELSD nebulization temperature of 40 °C and evaporative temperature of 80 °C. A gradient mode was employed using mobile phase A (5:95 water:methanol) and mobile phase B (0.1% formic acid in 2-propanol) at a flow rate of 1.0 mL/min for 20 min. The column and samples were maintained at room temperature.

CTAB was quantified using an InfinityLab Poroshell 120 EC-C18 (4 µm; 4.6 x 100 mm) column (Agilent Technologies) with an ELSD nebulization temperature of 40 °C and evaporative temperature of 90 °C. A gradient mode was employed using mobile phase A (50 mM ammonium acetate at pH 3.6) and mobile phase B (1% glacial acetic acid in methanol), at a flow rate of 1.0 mL/min for 20 min. The column temperature was fixed at 35 °C, while the samples were maintained at room temperature.

The obtained data was manually processed by using the OpenLab software (Agilent Technologies).

9.3.4. Morphological characterization by cryogenic transmission electron microscopy

The morphology of the systems was studied using cryogenic transmission electron microscopy (Cryo-TEM), after sample plunge freezing. Cryo-TEM allows the direct investigation of colloidal systems, such as DELOS-NV, in the vitrified, frozen-hydrated state, so their structure is quite well preserved, and very close to their native state (**Figure 9.5**). During all the procedure, it is necessary to work at cryogenic temperatures, reached using liquid nitrogen (N_2), to avoid damaging the sample by phase transition of the vitrified water into crystalline ice.

The Cryo-TEM images were obtained by the superior technician Martí de Cabo Jaume at the Microscopy and X-ray Diffraction service from UAB using a JEOL JEM-2011 transmission electron microscope (JEOL Ltd., Tokyo, Japan) operating at 200 kV. Vitrified samples were prepared using a controlled environment vitrification system (CEVS) Leica EMCPC (Leica Microsystems, Germany).

In the case of the DELOS-NV dispersions, 4 µL of the sample were directly placed on a copper grid coated with a perforated polymer film. Conversely, DELOS-NV incorporated into Plx407 or PLGA-PEG-PLGA hydrogels were diluted 1:5 in water, to adjust the viscosity for an adequate fixation and preservation of the hydrogel sample in the grid. Afterward, the excess of the sample was removed by blotting with filter paper (Whatman® grade 1) for 2.5 s, obtaining a thin film of 10 – 500 nm. Immediately after film preparation, the grid was plunged into liquid ethane held at a temperature just above its freezing point (−179.15 °C). The vitrified sample was then transferred to the microscope for analysis using a cryogenic-transfer holding (Gatan 626, Gatan, Pleasanton, US). To prevent sample perturbation and the formation of ice crystals, the specimens were kept cold (−196.15 °C) during both the transfer and viewing procedures. Images were recorded on a Gatan RIO 16 camera using Digital Micrograph 3.50.3584.0 (Gatan Inc., Pleasanton, CA, US). No image processing was applied except for contrast enhancement.

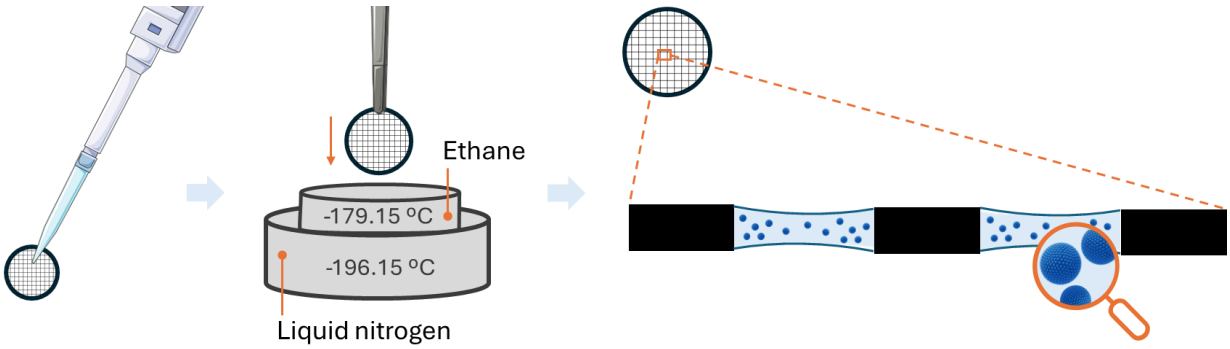


Figure 9.5. *Vitrification of the DELOS nanovesicles suspensions for Cryo-TEM imaging.*

9.3.5. Small-angle X-ray scattering

Small-angle X-ray scattering (SAXS) is a non-invasive and nondestructive technique that can provide unique structural information on colloidal systems with the advantage of measuring the average properties of the bulk samples, which can otherwise be obviated by using only microscopic techniques such as Cryo-TEM.

From a fundamental point of view, the interaction of radiation with inhomogeneities in matter can cause a small deviation of the radiation from its incident direction, called small angle scattering and can take place for a wide variety of radiation, such as X-rays (SAXS) (**Figure 9.6**). This static light scattering technique is sensitive to the electron density contrast, so that the larger the difference in electron density, the larger the scattering contribution. So basically, SAXS measures the time average intensity of the scattered X-rays as a function of the scattering angle and consequently, the measured intensity curve bears information on the radius of gyration, mean size, size distribution, shape, among other parameters.

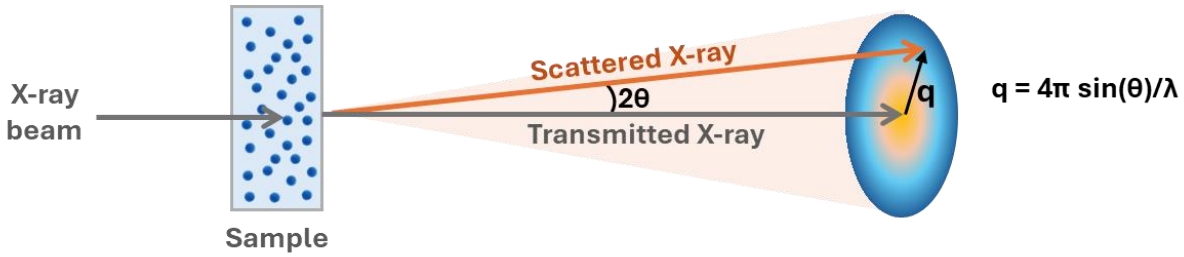


Figure 9.6. *Representative image of the SAXS measurement. The modulus of the scattering vector is defined as q, the scattering angle as 2θ and the wavelength of the X-ray beam as λ.*

Two different types of samples were analyzed by SAXS in **Chapter 4**, the Chol:CPC DELOS-NV suspension (**Table 9.1**) and also the different concentrations of Plx407 hydrogels containing the Chol:CPC-DELOS-NV (**Table 9.5**; Chol:CPC DELOS-NV-loaded 15% w/w Plx407, Chol:CPC DELOS-NV-loaded 17% w/w Plx407, Chol:CPC DELOS-NV-loaded 20% w/w Plx407 and Chol:CPC DELOS-NV-loaded 23% w/w Plx407).

The SAXS measurements were carried out at NCD-SWEET beamline at the ALBA Synchrotron, Spain, by Dr. Cristián Huck Iriart. The incident beam energy was set at 15 keV with a distance between the samples and detector of 3.6 m (Pilatus 1M detector, pixel size of 172μm), under those conditions, the scattering vector modulus q ($q = 4\pi \sin(\theta)/\lambda$, where 2θ is the scattering angle and λ is the incoming wavelength) was in the range from 0.067 to 4.8 nm^{-1}. The measurements were performed at 22 °C. The liquid and gel samples were placed in sample holders with Kapton® windows.

The SAXS data for the DELOS-NV sample was analyzed by Dr. Cristián Huck Iriart and Prof. Jan Skov Pedersen. It was analyzed by the model of polydisperse spherical vesicles[1], in which the cross-section structure consists of three layers, i.e. a central layer for describing the hydrocarbon region with an excess electron density lower than the buffer surrounded by two layers with positive excess electron density for describing the headgroup regions. It turned out that significantly better fits were obtained when the cross-section profile was asymmetric with different excess scattering lengths of the two headgroup layers. In agreement with previous models[1], the layers were described by Gaussian functions, $Gauss(r,\sigma) = exp\ (-r^2/(2\,\sigma^2))$, to have a smooth variation of the electron density as a function of the distance r from the center (**Equation 9.1**):

$$\Delta\rho(r) = Sc_{ph1}Gauss\big(r - R - R_{ph}, \sigma_{ph}\big) + Sc_{hc}Gauss(r - R, \sigma_{hc}) + Sc_{ph2}Gauss\big(r - R + R_{ph}, \sigma_{ph}\big)$$

Equation 9.1. *Where the subscript ph refers to headgroups, hc to hydrocarbon, and R is the distance from the center to the middle of the bilayer.*

For the asymmetric electron density profile, the two Gaussians representing the headgroups have independent amplitudes ($Sc_{ph1} \neq Sc_{ph2}$). The Gaussian representing the hydrocarbon core had a fixed scale $Sc_{hc} = -1$.

For the actual calculation of the form factor $P(q,R)$, a general expression for centrosymmetric structures was used[2] (**Equation 9.2**):

$$P(q) = \frac{\left[4\pi \int \Delta\rho(r) \frac{sin(qr)}{qr} r^2 dr\right]^2}{[4\pi \int \Delta\rho(r) r^2 dr]^2}$$

Equation 9.2. *General expression for centrosymmetric structures to calculate P(q,R).*

Thus, the form factor was calculated numerically from the electron density of the bilayer cross-section according to the sum of Gaussians. The distance between the centers of the two headgroup Gaussians was set to sum of half width half maximum of headgroup and hydrocarbon Gaussian, $R_{ph} = \sqrt{2\ln 2}\left(\sigma_{ph} + \sigma_{hc}\right)$, whereas the sigma value was kept as a fit parameter to diminish artifacts from non-linear parameter correlation. Furthermore, the sigma value of the Gaussian that models the central hydrocarbon layer was set to $2\sqrt{2\ln 2}\,\sigma_{hc} = 12$ Å . Thus, the variation in the cross-section was obtained from the sigma value for the headgroup. In this model, the external diameter of the vesicle is given as $D = 2\left[R' + \sigma_{hc} + 2\sigma_{ph}\right]$. In practice, the integration in the form factor equation was performed using 100 steps in the range from -3s of the inner Gaussian to +3s of the outer Gaussian. Finally, the polydispersity of the overall size of the vesicles was taken into account in terms of a Gaussian distribution, and instrumental smearing mode was included using a pinhole resolution function[3].

9.3.6. Loading and entrapment efficiency of actives and model molecules in DELOS-NV

To calculate the loading and entrapment efficiency (EE%) of the active molecules or model compounds integrated into DELOS-NV, it is first necessary to eliminate non-integrated molecules from the samples through purification steps such as diafiltration by TFF.

Loading refers to the concentration of the molecule integrated into the DELOS-NV, typically expressed in mg/mL or μM. The EE% represents the percentage of integrated molecules relative to the total amount initially added during the DELOS process. EE% is calculated using the following **Equation 9.3**:

$$EE\% = \frac{Molecule\ integrated}{Molecule\ integrated + \ \ Molecule\ not\ integrated}\ x100$$

Equation 9.3. *EE% equation.*

In this equation:

- The **numerator** (Molecules integrated) is the amount of active or model molecules that remain in the formulation after purification steps such as diafiltration (e.g., using TFF) or filtration through syringe filters. This quantity can be determined by measuring the concentration, absorbance, or fluorescence intensity.
- The **denominator** is the total amount of active or model molecules added during the DELOS process. This can be either the theoretical concentration added, or the actual quantity measured immediately after the DELOS process as concentration, absorbance or fluorescence intensity.

The specific values used for these calculations will be specified in each case within the results chapters.

For the purification step:

- Hydrophilic molecules are eliminated through TFF (see **Section 9.2.2**). When the media is exchanged, those molecules solubilized in the media are eliminated. Therefore, in **Chapter 6**, the lucifer yellow, the FITC-BSA and the insulin were eliminated by this technique. Note that LY-DELOS-NV were first filtrated with a PES 0.45 μm syringe filter to eliminate some lucifer yellow precipitates present in the sample.
- Hydrophobic molecules are also separated by TFF (see **Section 9.2.2**). These molecules are not soluble in aqueous media, however, there is a remanent 10% EtOH in the DELOS-NV suspensions after the DELOS method. In addition, in the case of the bRo5 molecules, that had been loaded into the DELOS-NV for the first time in the present thesis, the colloidal suspensions diafiltrated by TFF were further filtrated with a 0.22 nm PES syringe filter to eliminate any possible aggregate of bRo5 molecules non-integrated in the nanovesicles that could be present in the suspension.

The quantification of the molecules in the formulations prior and after the purification step is conducted by two different techniques according to the molecules' properties: Ultraviolet-visible (UV-Vis, see **Section 9.3.7**) or fluorescence spectroscopy (see **Section 9.3.8**).

UV-Vis spectroscopy was used in **Chapter 5** to determine the amount of bRo5 molecules entrapped within DELOS-NV. To prepare the samples for analysis, the bRo5-DELOS-NV nanoconjugates were diluted in 90% EtOH to dissolve the membrane components and prevent them from interfering with the UV-Vis measurements. Additionally, a calibration curve was established to determine the concentration of bRo5 molecules. This calibration curve was constructed using a dispersant medium composed of 90% EtOH and 10% histidine 5 mM pH 7, ensuring consistency with the conditions used in the sample analysis.

UV-Vis spectroscopy was also utilized in **Chapter 6** to calculate the EE% of FITC-BSA in DELOS-NV. The DELOS-NV containing FITC-BSA were diluted in 80% EtOH to dissolve the membrane components and avoid interference in UV-Vis analysis. In this specific case, the UV-Vis absorbance intensity was not converted into concentration, and the EE% was directly calculated by dividing the UV-Vis absorbance of BSA-DELOS-NV diafiltrated using TFF between the absorbance of the BSA-DELOS-NV non-diafiltrated.

In the same **Chapter** 6, the EE% of the lucifer yellow was also assessed by UV-Vis. In this specific case, the LY-DELOS-NV samples were measured directly (lucifer yellow is insoluble in EtOH). To calculate the concentration of lucifer yellow into the LY-DELOS-NV, a calibration curve for lucifer yellow was constructed. The medium employed in the calibration curve consisted of the identical buffer medium present in the LY-DELOS-NV batches (90% histidine + 10% EtOH). Next, the absorption of the LY-DELOS-NV after filtration with a PES 0.45 µm syringe filter and after filtration and diafiltration by TFF was measured. The concentration of the diafiltrated sample was divided by the concentration of the filtrated sample to calculate the EE%.

On the other hand, fluorescence spectroscopy was employed to assess the EE% of the insulin within DELOS-NV by using the intrinsic tyrosine autofluorescence of the protein. The maximum peak of the tyrosine is at 305 nm and, in samples containing DELOS-NV, it is partially overlapped by the DELOS-NV scattering. To solve this limitation, the Ins-DELOS-NV were diluted in 90% EtOH and left overnight to ensure complete stabilization of the fluorescence prior to the measurements, as inspired by the work of I. Bekard et. al[4]. The emission spectra were collected the day after at 280-500 nm after excitation at 276 nm.

As mentioned earlier, in some cases, the EE% of the payloads within the DELOS-NV was sufficient, making it unnecessary to perform calibration curves. However, in other instances, a calibration curve was needed to accurately determine the exact concentration of the payload entrapped in the DELOS-NV. This was necessary either because a specific target concentration had to be achieved (e.g. bRo5-DELOS-NV), or because the EE% could not be calculated from the absorbance intensities of the samples before and after diafiltration using TFF due to precipitation in the samples right after DELOS (e.g., LY-DELOS-NV).

9.3.7. Ultraviolet-visible spectroscopy

UV-Vis spectroscopy is a technique used to analyze the absorption of ultraviolet and visible light by molecules. In UV-Vis spectroscopy, a beam of ultraviolet (UV) or visible light passes through a sample, and the amount of light absorbed by the sample at various wavelengths is measured. The amount of light absorbed depends on the concentration of the sample and can be employed to quantify it.

Absorption spectra were recorded using a Varian Cary 5000 UV-Vis-NIR spectrophotometer (Agilent Technologies, Santa Clara, CA, US). In particular, spectra were acquired by placing samples in a quartz SUPRASIL high precision cell (Hellma Analyti cs, Müllheim, Germany) with 1 cm pathlength at room temperature (25 °C). The measurements were carried out in the wavelength interval 700 to 200 nm.

When measuring the absorbance of DELOS-NV labeled with fluorophores, appropriate dilutions were made to achieve absorption values between 0.1 and 0.3, ensuring a linear relationship between absorbance and concentration. For DELOS-NV samples containing other molecules, the absorbance was adjusted to fall between 0.1 and 1, unless linearity above 1 had been confirmed through a calibration curve, with the same goal in mind.

9.3.8. Fluorescence spectroscopy

Fluorescence spectroscopy is a technique used to analyze the fluorescence emitted by a sample when it is excited by light of a specific wavelength.

Fluorescence emission and excitation spectra were collected with a Varian Cary Eclipse (Agilent Technologies, Santa Clara, US) fluorescence spectrophotometer, at the UAB's Laboratory of Luminescence and Spectroscopy of Biomolecules service. For fluorescence spectra recording, samples (20-50 µL) were placed in a 1 cm quartz SUPRASIL® precision cell (Hellma Analytics, Müllheim, Germany).

Exceptionally, fluorescence measurements in **Chapter 7** (see **Section 9.4.6**) were carried out in a Jasco FP-8050 spectrofluorometer (Jasco, Pennsylvania, US) in Prof. Alessandro Porchetta's laboratory.

9.3.9. Stability of DELOS-NV in Poloxamer 407 hydrogels by Förster resonance energy transfer efficiency evaluation

In **Chapter 4,** to evaluate the stability of DELOS-NV when formulated into Plx407 hydrogels, the Förster resonance energy transfer (FRET) efficiency in DiI/DiD-DELOS-NV in suspension and integrated into Plx407 was measured. FRET is an energy transfer phenomenon that occurs between a pair of fluorochromes in which the emission of one, called the donor, overlaps the excitation spectra of the other, called the acceptor. This only occurs when they are closer than 5 nm. Therefore, the efficiency of this energy transfer is expected to be higher in well-formed nanovesicles than in broken nanovesicles, since if the nanovesicles dissociate the distance between fluorochromes would increase[5,6] (see **Section 4.3.5** in **Chapter 4** for a detailed explanation).

To analyze the stability of the DELOS-NV in the hydrogels, DiI/DiD-DELOS-NV were loaded with 45 μM DiI and 45 μM DiD as described in **Section 9.2.1** and **Section 9.2.2**. As a control, NV containing only DiD (45 μM) were also produced. See formulation details in **Table 9.1**.

First, UV-Vis was employed to characterize the DiD-DELOS-NV and the DiI/DiD-DELOS-NV spectra, to know the structuration of the fluorophores on the samples (see **Section 9.3.7**).

Afterward, fluorescence spectroscopy was employed to evaluate the FRET efficiency in DiI/DiD-DELOS-NV in suspension and integrated into Plx407 (see **Section 9.3.8**). FRET emission spectra were collected at 500-800 nm after excitation at 490 nm for DiI/DiD-DELOS-NV and DiD-DELOS-NV as controls. In addition, the emission spectra (λ_{ex} = 590 and λ_{em} = 600-800 nm) and the excitation spectra (λ_{em} = 710 and λ_{ex} = 400-700) were also collected for DiI/DiD-DELOS-NV and DiD-DELOS-NV, as an extra control. In all the cases, samples were diluted 10 times in water.

The FRET efficiency was calculated with **Equation 9.4**[6]. Measurements were performed in triplicate.

$$Efficiency\ FRET\ (E_{FRET}, \%) = \frac{Intensity\ DiD}{Intensity\ DiI + Intensity\ DiD}$$

Equation 9.4. *FRET efficiency ($E_{FRET,}$ %) calculation.*

9.3.10. Stability tests at 40 °C

In **Chapter 5**, to test the stability at 40 ± 3 °C of the formulations developed, an aliquot of the formulations was stored for 1 month in the oven. Afterwards, the hydrodynamic diameter, average size PdI and apparent Z-potential were measured as described in **Section 9.3.1** and values were compared with the aliquots stored at 5 ± 3 °C.

9.3.11. Isothermal titration microcalorimetry

ITC measures the heat that is either released (exothermic reaction) or absorbed (endothermic reaction) when a ligand interacts with a macromolecule. The determination of this heat gives necessary insight into the mechanism of an interaction. ITC is the only technique that measures this heat change from which detailed thermodynamic information about the binding process -affinity constant, *Ka;* enthalpy change, *ΔH;* and stoichiometry, *n*- can be determined.

The ITC instrument uses the power compensation technique as a detection method. A reference cell and a sample cell are placed in an adiabatic jacket (see **Figure 9.7A**). The reference cell is filled with buffer (or water) and the sample cell with a molecule under investigation diluted in the same solvent. Both cells are heated in such a way that the temperature is almost constant between them and increases very slowly. The instrument is also equipped with a syringe device that holds the ligand. This device titrates the ligand into the sample cell and, also, acts as a stirrer so the binding equilibrium can be reached very quickly. In each ligand injection, a chemical reaction, a molecular reorganization, or a sum of events spontaneously occurs in the sample cell accompanied by a heat "*q"* exothermic or endothermic that is sensed by the control system. The control system adjusts the electrical power supplied to the heaters of the sample cell to maintain the two cells at the same

temperature. For example, in exothermic reactions, the heaters will stop heating the sample cell until the temperature of the reference cell has caught up with the temperature of the sample cell. The ITC records the rate of heating (or heating stop) of the sample cell over the time required to bring the sample and reference cells back to a common temperature. Therefore, when the sum of heat changes in an injection is exothermic, the peak recorded is negative and when the sum of heat changes in an injection is endothermic, the recorded peak is positive[7,8]. **Figure 9.7B** shows a reference thermogram of a single exothermic interaction. The intensity of the peaks is highest at the beginning because many ligands are binding to their receptors. As the receptor binding sites become saturated over time, fewer binding events occur, leading to a decrease in peak intensity.

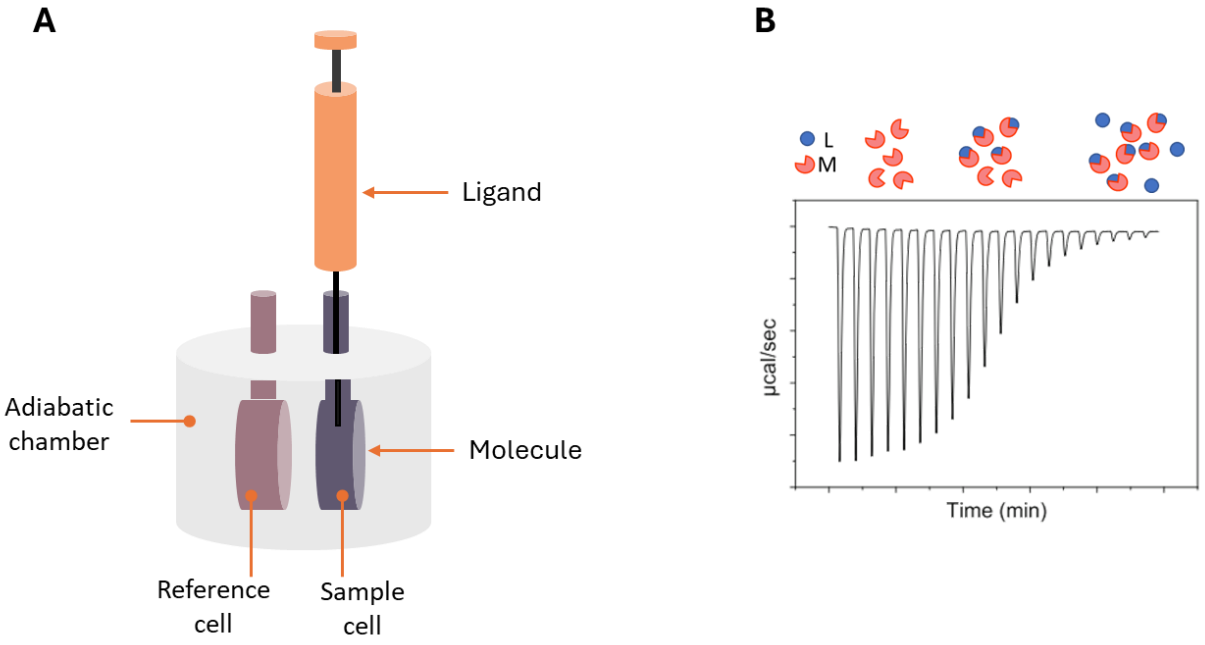


Figure 9.7. A) Schematic representation of the ITC system. The arrows indicate where are placed the compounds in the study. B) Representative thermogram of an exothermic binding interaction.

The thermodynamic characterizations were conducted on a Malvern MicroCal VP-ITC (Malvern Instruments, Worcestershire, UK) at 25 °C.

Two different systems were studied: the binding between ITC-Chol:CTAB DELOS-NV and the rhEGF in histidine 5 mM buffer at pH 7, and the binding between ITC-Chol:CPC-DELOS-NV and the FITC-BSA in HBSS buffer at pH 7.4 (See composition of the DELOS-NV in **Table 9.3**). In both cases, the DELOS-NV were produced by DELOS technology (see **Section 9.2.1**) and diafiltrated by TFF (see **Section 9.2.2**) to eliminate the EtOH. The ligands (rhEGF and FITC-BSA) were prepared in the same media as the DELOS-NV.

Different concentrations of the ligands (rhEGF/FITC-BSA) were placed on the 290 µL syringe and titrated into the sample cell (1448 µL) containing different concentrations of the diafiltrated DELOS-NV (ITC-Chol:CTAB or ITC-Chol:CPC DELOS-NV) as a sequence of 57 injections of 2 µL each. The duration of each injection was 10 s, and the time delay between injections 300 s, to allow equilibration between successive injections. The stirring velocity was fixed at 307 rpm throughout the

experiment, to ensure thorough mixing of the titrant and the DELOS-NV during the injections. Data acquisition was achieved with Origin VP Viewer software. Blanks of the ligand titrated over the same buffer medium were also performed. By use of the AFFINIMETER software [www.AFFINImeter.com], raw data was integrated peak by peak and normalized to get a plot of observed enthalpy change per mole of injectant (ΔH) against ligand/DELOS-NV molar ratio.

In the case of the rhEGF binding study, the resulting data were fitted in a global analysis employing a stoichiometric binding model conformed of two different equilibriums in order to obtain the binding ratio of proteins per DELOS-NV, the affinity constant (K_a) and the thermodynamic parameters (Enthalpy change (ΔH), Free energy of Gibb's change (Δ*G*) and Entropy change (ΔS) associated to the rhEGF binding to ITC-Chol:CTAB DELOS-NV. For all the calculations, an estimated molecular weight of 1.44×10^7 g mol^{-1} was used for the ITC-Chol:CTAB DELOS-NV.

In the case of the FITC-BSA binding study, a global analysis was performed using the independent sites approach for obtaining the same information. The molecular weight of ITC-Chol:CPC DELOS-NV was assumed to be equivalent to that of ITC-Chol:CTAB DELOS-NV (1.44×10^7 g mol^{-1}).

9.3.12. Rheological characterization of the hydrogels

Rheology is the science that studies the flow behavior of viscoelastic materials. By viscoelastic materials, it is understood any material that does not behave as a complete liquid or solid. The rheological characterization of the Plx407 hydrogels was performed using a Kinexus Pro+® (Netzsch, Germany). The geometry employed was a stainless-steel parallel plate (diameter 40 mm) at a 1 mm gap between plates.

Chol:CPC DELOS-NV-loaded hydrogels or blank hydrogels (**Table 9.5**) were poured on the rheometer lower plate at a given temperature, trimmed, covered with a thermal cover, and rested 10 min before each analysis. Three replicates of each hydrogel formulation were produced and characterized with the rheometer.

9.3.12.1. Shear Viscosity Measurements

Flow measurements were performed at 4 °C (store temperature), 22 °C (room temperature) and 37 °C (body temperature). Each measurement was performed with a three-step method. First a shear rate ramp from 0.1 to 500 s^{-1} followed by 60 seconds of a steady shear rate at 500 s^{-1} and a shear rate ramp from 500 to 0.1 s^{-1}. Viscosity and shear stress were measured at each point and plotted.

9.3.12.2. Oscillatory Measurements

The shear oscillatory measurements were conducted at 10 Pa and 1 Hz, as optimized with preliminary amplitude and frequency sweeps, respectively. A temperature ramp from 4 °C to 40 °C at a rate of 1 °C/min was performed and the storage -or elastic- modulus (G'), the loss -or viscous- modulus (G''), and the phase angle (δ) across the temperature ramp were investigated. The gelation temperature ($T_{sol\text{-}gel}$), the temperature at which the Plx407 solution becomes a gel, was determined as the temperature at which both modulus (G' and G'') crossover.

9.3.13. Determination of the gelation time

For the determination of the gelation time a mechanical test was conducted according to the method of Mura et al.[9], slightly modified. 2 mL of the TFF-Chol:CPC DELOS-NV-loaded hydrogels and blank hydrogels stored at 4 °C were placed in 3 ml glass beakers and put under magnetic stirring (500 rpm) in a water bath at 22 °C for 30 min to stabilize their temperature. Next, the vials were transferred to a 37 °C water bath, maintaining the same agitation. The gelation temperature was determined in triplicate as the time required for the bar magnet to stop moving due to gelation at 37 °C.

9.3.14. Optical microscopy of DELOS-NV in hydrogel dosage form

Optical microscopy was used to control the stability of the DELOS-NV in hydrogel dosage forms. To test them, a drop of the hydrogel samples was placed in a glass slide and covered with a coverslip. Then, the microscopic examination was carried out at room temperature with a Morphologi G3S (Malvern Panalytical, UK) automatic microscope using a 20x magnification in search of microscopic particles that could indicate nanovesicles breakage.

9.4. In vitro assays

9.4.1. In vitro injectability and thixotropy of DELOS-NV-loaded hydrogel

In **Chapter 4**, the injectability of the DiD-DELOS-NV-loaded 17% w/w Plx407 hydrogel (**Table 9.5**) was directly evaluated with a simple injection through a 1 mL syringe coupled to a 25 G needle. The injection was performed directly into dPBS, at pH 7.4 and pre-warmed to 37 °C and permitted evaluation of the flowability through the syringe and the thixotropic behavior of the hydrogel.

9.4.2. In vitro hydrogel dissolution test

The hydrogel dissolution profile and the *in vitro* release profile of the DELOS-NV/nanoconjugates from the 17% w/w Plx407 hydrogel formulation were obtained simultaneously, by adapting Lee et al. method[10]. Vials with an inner diameter of 15 mm and 60 mm height, containing 1.5 mL of the corresponding hydrogel (i.e., DiD-DELOS-NV-loaded 17% w/w Plx407 hydrogel or bRo5.1-DELOS-NV-loaded 17% w/w Plx407 hydrogel) were placed in an incubator with orbital agitation at 37 °C and 30 rpm. 45 minutes later, after a complete liquid-to-gel transition, 4.5 mL of dPBS (pH 7.4) pre-warmed to 37 °C were carefully layered over the hydrogel surface (**Figure 9.8**). Every hour, the entire release medium was removed by decantation, and the weight of the vial and remaining hydrogel was recorded. The percentage of hydrogel weight loss was calculated by dividing the hydrogel weight recorded at the different time points by the initial hydrogel weight. The dissolution test was performed in triplicates.

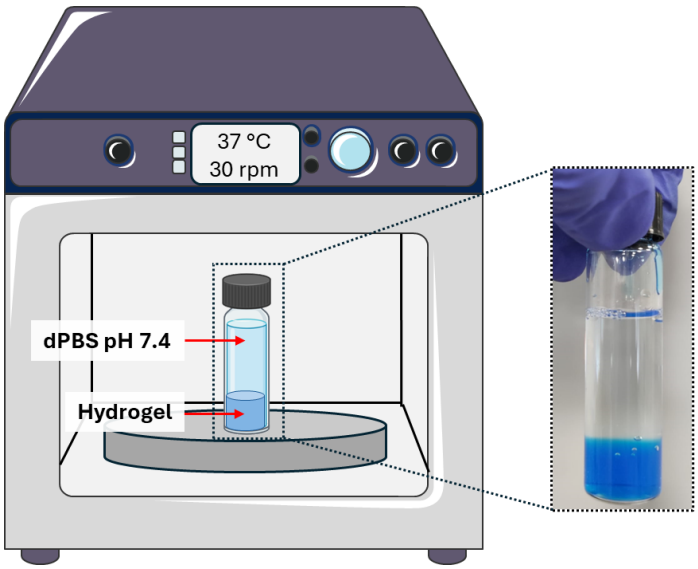


Figure 9.8. *Schematic representation of the in vitro dissolution test setup for the hydrogels, accompanied by a representative image showing the appearance of the dissolution samples with DiD-DELOS-NV-loaded 17% w/w Plx407.*

9.4.3. In vitro DELOS-NV release from hydrogels

In vitro release behavior from the Plx407 hydrogels (i.e. DID-DELOS-NV-loaded 17% w/w Plx407 hydrogel; bRo5.1-DELOS-NV-loaded 17% w/w Plx407 hydrogel) was monitored using a membrane-less diffusion method, according to the procedure described in the hydrogel dissolution test. The release profiles of the DiD-DELOS-NV and the bRo5.1-DELOS-NV were determined by UV-Vis spectroscopy as described in **Section 9.3.7**. Absorbance intensities (λ = 647 for DiD-DELOS-NV; λ = 330 nm for bRo5.1-DELOS-NV) were converted into concentration by employing calibration curves. Calibration curves were generated by diluting DiD-DELOS-NV or bRo5.1-DELOS-NV to various concentrations in the same buffer used in the release (dPBS, pH 7.4). The accumulated release was then calculated at different time points.

As a control for the DiD-DELOS-NV-loaded 17% w/w Plx407 release test, an equivalent release with the DiD freely dispersed in the hydrogel without DELOS-NV was performed. Due to its hydrophobic nature, the DiD (45 uM) was solubilized in a volume ratio of 1:2:97 EtOH: Benzyl alcohol:Water. Next, the solution was gelled with 17% w/w Plx407 and the *in vitro* release was conducted.

The release data was fitted to different models (i.e., the Korsmeyer-Peppas model and zero-order model) to mathematically describe the release mechanism and kinetics (see **Section 4.3.9** in **Chapter 4** for details in model fitting).

All release tests were conducted in triplicate.

9.4.4. In vitro viability assays in Caco-2 cells

The viability assays were performed employing the CellTiter 96® AQueous One Solution Cell Proliferation Assay ((3-(4,5-dimethylthiazol-2-yl)-5-(3-carboxymethoxyphenyl)-2-(4-sulfophenyl)-2H-tetrazolium); MTS) from Promega Biotech Ibérica S.L. (Spain). MTS is reduced by the cells' dehydrogenases and converted into a colored formazan dye (**Figure 9.9**). Therefore, the stronger the formazan color, the more viable the cells are. This technique is read by quantifying the absorbance at 490 nm in a plate lector.

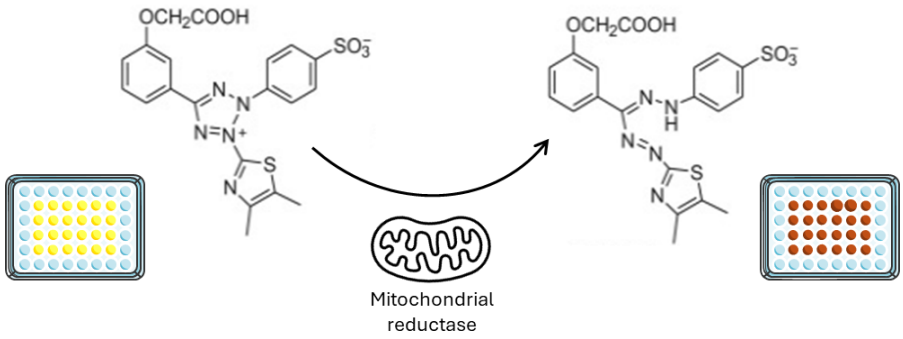


Figure 9.9. *Representation of the MTS reduction into colored brown formazan.*

For the viability assays, Caco-2 cells were cultured in a 96 well-plate. First, the cells were counted in a Neubauer chamber by previously staining their nucleus with Trypan blue. Next, they were diluted in culture medium (Minimum essential medium (MEM) from Gibco, completed with 10% fetal bovine serum (FBS) and 1% penicillin/streptomycin solution (PEST) (10000 U/mL)) to have 45 cells/µL. 200 µL of the cell's suspension were transferred to the assay wells (9000 cells/well). The wells in the contour of the plate were not employed for the assay and were filled only with the culture medium to compensate for possible evaporation phenomena during the cell culture. Cells were incubated for 9 days at 37 °C and 5% CO_2. Every other day the culture medium was exchanged for a fresh one.

On the 9th day, viability assays were carried out. The cell culture media was eliminated and replaced with 100 µL of the corresponding DELOS-NV formulations: Abs1-, Abs2-, Abs3-, Abs4-DELOS-NV, Ins-DELOS-NV or LY-DELOS-NV (see **Table 9.3**) at different concentrations (from 1 mg/mL to 0.0001 mg/mL). The culture medium was employed as 100% viability and DMSO 50% as positive control. In addition, the HBSS, which is the transport medium employed for the permeation assays and the medium of the colloidal suspensions of nanovesicles, was also assessed to detect possible effects on cell viability.

After 4 hours of incubation at 37 °C and 5% CO_2 the solutions were eliminated and replaced with 120 µL of 1:6 MTS:HBSS. The plate was incubated again for the MTS to be reduced by the cells' mitochondrial dehydrogenase enzymes. Next, the absorbance of the reduced MTS at 490 nm was measured at different time points in a Perkin-Elmer Victor 3V fluorescence multiwell plate reader, in the Cell Culture, Antibody Production and Cytometry service from UAB. The absorbance at 620 nm was also measured to subtract background contributed by excess cell debris, fingerprints and other nonspecific absorbance.

9.4.5. In vitro permeation assays in Caco-2 cells

The permeation assays were carried out in Caco-2 cells grown in transwell plates. The permeable transwell plates allow Caco-2 cells to differentiate into polarized monolayers that mimic the intestinal epithelium (See schematic representation of the Caco-2 monolayers in **Figure 6.23** in **Chapter 6**).

First, permeation assays were conducted in cells grown in the Cell Culture, Antibody Production and Cytometry service from UAB, while the last permeation assays were conducted on CacoReady cells bought from ReadyCell S.L.

9.4.5.1. Caco-2 monolayer culture and differentiation

The culture and differentiation of the Caco-2 cells were done in Corning Costar Transwell permeable supports, with a polycarbonate membrane, pore size of 0.4 mm and diameter of 12 mm (12-well plates). Hubatsch et al. protocol[11] was followed with small adaptations. The cells were cultured on the transwells 21 to 29 days prior to the permeation assay. To do so, cells were counted with the Neubauer chamber as explained in **Section 9.4.4**. Next, 0.5 mL of cells suspension were dispensed on the apical side of each transwell pre-wetted with 0.1 mL of MEM-PEST for about 2 min (60000 cells/transwell). On the basal side, 1.5 mL of MEM-PEST without cells was also added. The plates were incubated for 21 to 29 days at 37 °C and 5% CO_2 and the culture medium of the basal and apical side was exchanged for fresh one on Mondays, Wednesdays, and Fridays.

In CacoReady models, cells are provided on the 14th day of culture and differentiation. Therefore, these models only require the shipment medium to be liquefied and replaced with culture medium on the Friday before the permeation assays.

9.4.5.2. Quality tests of the monolayer integrity

After complete differentiation of the Caco-2 cells and before the permeation assays, quality checks of the integrity of the cell monolayer were done:

- Confocal images observing the nucleus of the cells stained with Hoechst to determine if al nuclei are placed in the same Z height (see **Section 9.4.5.4** for staining details). If cells are grown in several layers, the nuclei of the cells would be observed at different Z heights.
- Measurement of the transepithelial resistance (TEER) of the monolayer with a Millicell-ERS2 Volt-Ohm Meter. To do so, the manufacturer's instructions were followed. First, the electrodes were sterilized by submerging them in 70% ethanol for 30 minutes. Next, they were equilibrated for 30 minutes in the HBSS buffer. The plates with the Caco-2 cells were rinsed twice with HBSS (1.5 mL on the basal side and 0.5 mL on the apical side) and let stabilize for 30 minutes too. The resistance (Ω) was measured after the stabilization time by submerging the shorter electrode in the apical side of the transwell and the longer electrode through the lateral hole of the transwell, into the medium of the basal well. From the values obtained, the resistance values of a filter without Caco-2 cells were subtracted. TEER values are the result

of multiplying the resistance value by the cell growth area (cm^2). Only those monolayers with TEER values around 1000 Ω cm^2 or higher were considered well-formed.

- Permeation test of the lucifer yellow through Caco-2 monolayers. This molecule is a hydrophilic paracellular marker with very low permeability through Caco-2 monolayers that is usually employed to test the integrity of Caco-2 tight junctions. To ensure that the tight junctions of the monolayer are correctly formed, permeation of the lucifer yellow should be less than 5 % after 1 hour of permeation assay. Comparison between the permeation through a Caco-2 monolayer and a transwell without cells is important to corroborate that transwells are not obstructed. The permeation assay of the lucifer yellow (0.1 mg/mL) was done in parallel with the permeation assay of the nanovesicles formulations as described below in **Section 9.4.5.3**. To avoid confusion, it is important to remark that lucifer yellow, a part of being employed as a control, was also integrated in DELOS-NV and used as a model molecule to test the effect of DELOS-NV in its permeation.

9.4.5.3. Permeation assays in Caco-2 cells

Prior to the assay, the formulations (i.e., Abs1-, Abs2-, Abs3-, Abs4-, Ins- and LY-DELOS-NV) were diluted in HBSS to a 0.1 mg/mL concentration of membrane components as determined by the viability assays. The same dilution was applied to the controls -corresponding to the same molecules integrated in the DELOS-NV but free in the medium-. Next, all the samples were filtered with a 0.22 µm PES filter.

Before the permeation assays, the cell monolayers were washed three times with HBSS pH 7.4 and the TEER values were measured as explained in **Section 9.4.5.2**. Next, the HBSS on both sides of the cell monolayers was removed by aspiration. To measure the permeation of the model molecules from the apical-to-basal side, 0.5 mL of each formulation were added to the apical side, and 1.5 mL of HBSS buffer were added to the basal side. Three transwells were used in each transport experiment. In addition, one transwell was employed to verify the integrity of the tight junctions by testing the permeation of the lucifer yellow solution.

Immediately after sample addition (time 0), a 100 µL aliquot was withdrawn from the apical side to facilitate mass balance calculations at the experiment's conclusion. The plate containing the transwells was then incubated at 37 °C with 5% CO_2 for 4 hours. Upon completion of the experiment, all samples from both the basal and apical sides were collected to assess the permeation of the model molecules and perform mass balance calculations.

9.4.5.4. Staining and confocal imaging

The staining procedure consisted of cleaning the plate twice with HBSS to ensure the elimination of any residues of the donor sample not internalized in the cells. Next, the filter supports of the transwells were cut with a scalpel and transferred to wells containing 1.5 µL of Hoechst and 1.5 µL of Cells mask per 1 mL of HBSS buffer. After 20 min of incubation, the staining solution was eliminated, and the filters were cleaned twice with HBSS. Finally, the cells were fixed with PFA 4% for 20 minutes. The fixed cells were stored in an HBSS buffer until their analysis, the day after, by confocal.

Confocal images were acquired with a Zeiss LSM 980 confocal microscope (Carl Zeiss GmbH, Jena, Germany). Sequential excitation of the target compound (FITC-BSA), Cell Mask (cells' membranes), and Hoechst (nuclei) was carried out. The FITC-BSA was excited at 488 nm, the cell mask at 639 nm and Hoechst at 405 nm. Detection was performed with GaAsP- and multialkali-PMT detectors device at specific ranges as follows: FITC-BSA was detected within the range 500 – 562 nm, cell mask within 659-735 and Hoechst within 408 – 500 nm range.

9.4.5.5. FITC-BSA quantification by fluorescence in a spectrofluorometer

Quantification of the FITC-BSA was conducted in a spectrofluorometer as described in **Section 9.3.8**. No dilutions were done on the samples obtained from the release study. Excitation of the FITC-BSA was performed at 485 nm and the spectra recorded from 500 to 600 nm.

9.4.5.6. Lucifer yellow quantification by fluorescence in a multiwell plate reader

Lucifer yellow was used for two purposes: to assess the integrity of the cell monolayer in Caco-2 experiments and as a model molecule in permeation assays with DELOS-NV.

Lucifer yellow was quantified using a Perkin-Elmer Victor 3V fluorescence multiwell plate reader from the Cell Culture, Antibody Production and Cytometry service from UAB. 200 µL of each sample were transferred to a 96-well black Optiplate microplate and analyzed with the spectrofluorometer, using an excitation wavelength of 485 nm and an emission wavelength of 535 nm. The 485 nm excitation wavelength was chosen as it was the closest available fluorescence filter on the plate reader.

Samples included the solutions or suspensions added to the donor chamber (lucifer yellow alone or LY-DELOS-NV) and those obtained after 4 hours of incubation from both the apical and basolateral chambers. Fluorescence from the HBSS buffer (blank) was also measured.

A calibration curve was generated by measuring sequential dilutions of lucifer yellow in HBSS pH 7.4 to convert the fluorescence readings into concentration values.

The percentage of permeated lucifer yellow was calculated using **Equation 9.5**:

$$\%\ Permeability = \frac{C^{B}_{txh} - C_{blank}}{\frac{(C^{A}_{t0h}\ x\ Va)}{(Va + Vb)} - C_{blank}} x\ 100$$

Equation 9.5. *Percentage of permeated lucifer yellow: In this equation,* $\boldsymbol{C^{B}_{txh}}$ *refers to the concentration of lucifer yellow in the basal side at a specific time point tx.* $\boldsymbol{C^{A}_{t0h}}$ *is the initial concentration of lucifer yellow added to the apical side at the start of the experiment.* $\boldsymbol{Va}$ *represents the volume of the apical side, while* $\boldsymbol{Vb}$ *is the volume of the basal side.* $\boldsymbol{C_{blank}}$ *corresponds to the blank sample (without lucifer yellow), which has been converted to a concentration using the calibration curve.*

9.4.5.7. Enzyme-linked immunosorbent assay (ELISA) quantification of the insulin

The quantification of the insulin from the permeation assay samples was conducted by a solid-phase sandwich enzyme-linked immunosorbent assay (ELISA). Solid-phase immunoassays are quantitative immunological techniques employing a solid phase where the antibodies have been attached. In a sandwich ELISA the mechanism of detection is entrapping between two layers of antibodies (capture and detection antibody) the target molecule (see **Figure 9.10**). The ELISA employed was a colorimetric assay in which the 3,3',5,5'-tetramethylbenzidine (TMB) substrate is used for detection. This substrate, when in contact with the horseradish peroxidase enzyme is reduced into a colored substance which is subsequently read in a microplate spectrofluorometer.

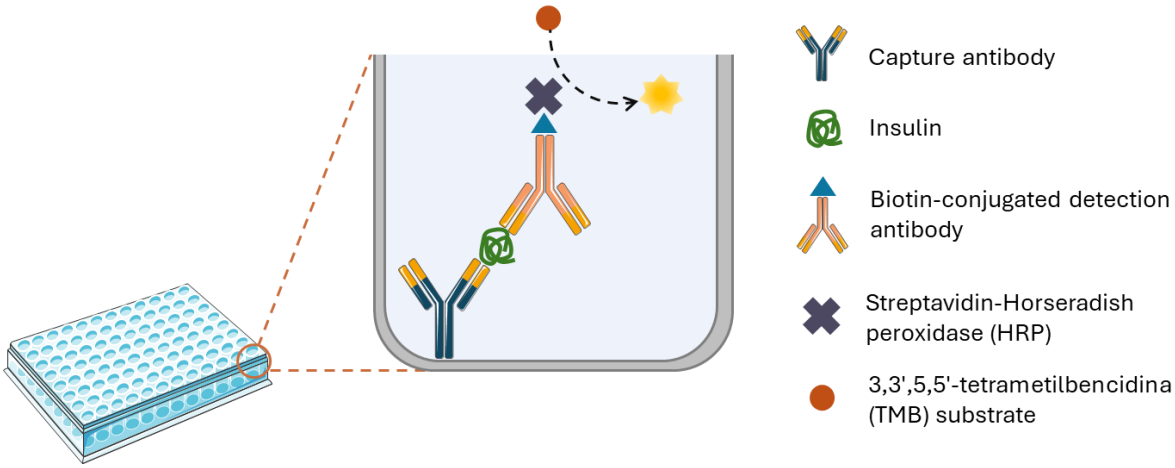


Figure 9.10. *Solid-phase sandwich ELISA employed for the detection of human insulin.*

The ELISA assay for insulin detection was conducted by Dr, Antoni Iborra from the Cell Culture, Antibody Production and Cytometry service. To set up the procedure, preliminary assays were conducted to assess the most appropriate dilutions for the concentrations of insulin expected in the samples from the absorption experiments. Next, the ELISA was conducted the day after the absorption assay, following the procedure described by the manufacturer. A calibration curve was performed by measuring known concentrations of the insulin patron.

The calibration curve was fitted to a 4 parameters logistic (4PL) function. From the calibration curve could also be determined the limit of detection (LoD) with the **Equation 9.6** :

$$LoD = 3.3x\frac{\sigma_{\text{residual}}}{S}$$

Equation 9.6. *The limit of detection (LoD) equation employed to calculate the LoD of the 4PL equation in the ELISA assays, where $\sigma_{residual}$ is the standard deviation of the residuals of the linear fit and S is the slope of the regression.*

After the assay, the optical density of each well was measured immediately, using the Perkin-Elmer Victor 3V multiwell plate reader set to 450 nm. To correct for optical imperfections in the plate, readings at 550 nm were subtracted from the readings at 450 nm. Next, the fluorescence results were converted to the concentration of insulin with the 4PL equation.

The tests were performed twice to confirm the results obtained.

9.4.6. In vitro DNA assays

9.4.6.1. DNA stock solutions and determination of the DNA concentration

The solid oligonucleotide sequences purchased at Metabion International were resuspended in TRIS 0.1 M pH 8 buffer to a 100 μM stock solution. Aliquots from the stock solution were prepared and stored at -25 °C.

Prior to the experiments, the required aliquots were thawed, vortexed for thorough mixing, spun down and annealed for 2 minutes at 90 °C. These steps ensure that the DNA sequences are not forming aggregates in the highly concentrated stock solutions. Next, dilutions to a working concentration of 10 μM were performed and the real concentration in the working solution was assessed by transferring 2 μL to a Tecan Infinite M-200 Pro with NanoQuant Plate (Tecan Trading AG, Switzerland). This step was repeated daily before conducting experiments to ensure precision in preparing DNA dilutions and to identify any issues with the DNA, such as degradation or aggregation.

The equipment reads the absorbance of the DNA, which has its maximum absorbance at λ = 260 nm. Using the Beer-Lambert equation, the concentration of oligonucleotide in the sample could be calculated (**Equation 9.7**).

$$Concentration\ Oligonucleotide = \frac{(A_{260nm}\ sample - A_{260nm}\ buffer)}{\varepsilon_{260} * l}$$

Equation 9.7. *Beer-Lambert equation, where ($A_{260\,nm} - A_{260\,nm}$) is the absorbance of the sample at 260 nm minus the absorbance of the blank (the buffer) at the same wavelength, ε is the molar extinction coefficient specific to each sequence and l is the length of the optical path, that was 0.05 cm.*

The molar extinction coefficient of the oligonucleotide sequences was calculated by isolating it in the Beer-Lambert equation, using the optical density at 260 nm (OD260) and the mols of nucleotides reported by Metabion International (**Equation 9.8**). The OD260 is the absorbance at 260 nm wavelength absorbed by an oligonucleotide resuspended in 1 mL of water and read in a 1 cm length quartz cuvette.

$$\varepsilon_{260} = \frac{OD_{260}}{(\text{mol oligonucleotide}/0.001L) * 1\ cm}$$

Equation 9.8. *Beer-Lambert equation to determine the molar extinction coefficient (ε) from the optical density at 260 nm (OD_{260}) and the amount of oligonucleotides in mol.*

Once determined the exact concentration in the working solutions the *in vitro* experiments were conducted as described below.

9.4.6.2. Titration of the DNA sequences free in medium, without DELOS-NV

To test the effectiveness of the designed DNA sequences to be employed in the DNA-grafted DELOS-NV biosensor development, two initial titration experiments, without DELOS-NV, were performed.

In the first experiment, the short oligonucleotide containing the BHQ (named OligoQ), was titrated into a solution of 20 nM anti-miR21 sequence containing the cholesteryl and the ATTO488 (named

Anti-miR21) in dPBS pH 7.4. Injections were performed every 5 minutes. Fluorescence measurements were carried out after each injection in a spectrofluorometer (see **Section 9.3.8**), by exciting the sample at λ_{ex} = 475 nm and recording the spectra in 500 - 650 nm. The fluorescence intensity at λ_{em}= 526 nm was represented versus the concentration of OligoQ. Replicates of each titration injection were conducted.

Next, in a second titration experiment without DELOS-NV, the miR21 in dPBS pH 7.4 was titrated into a solution of 30 nM OligoQ and 20 nM Anti-miR21 in the same buffer. To do so, the solution with the OligoQ and the Anti-miR21 was prepared in dPBS and incubated for 10 minutes to ensure hybridization. Afterwards, the miR21 was titrated into the solution and fluorescence measurements were carried out after each injection. The injections were performed every 5 minutes, and the fluorescence was measured with the same conditions mentioned previously (λ_{ex} = 475 nm and λ_{em} = 500 - 650 nm). The fluorescence intensity at λ_{em}= 526 nm was represented versus the concentration of miR21. Two replicates were conducted.

9.4.6.3. Titration experiment to evaluate the Anti-miR21 fluorescence in different scenarios

For these experiments, the concentration of Anti-miR21 employed in the different tests was fixed to 20 nM, the concentration of miR21 was fixed to 200 nM and the concentration of DELOS-NV, was fixed to 0.3 mg/mL membrane components (Chol + CPC). The fluorescence of the ATTO488 fluorophore contained in the Anti-miR21 was measured in the following conditions:

1. Single-strand Anti-miR21.
2. Anti-miR21 hybridized with miR21.
3. DELOS-NV functionalized with the single-strand Anti-miR21.
4. DELOS-NV functionalized with the single-strand Anti-miR21 and miR21. First, the Anti-miR21 was added to a solution of 0.03 mg/mL DELOS-NV. The mixture was incubated for 10 minutes and next, the miR21 was titrated into the same solution.
5. DELOS-NV functionalized with the Anti-miR21 and miR21 pre-hybridized. In this test, the exact amount of components as in the previous test was assessed, however, pre-hybridization between the Anti-miR21 and the miR21 was carried out. The two sequences were incubated for 10 minutes to ensure hybridization before the inclusion of the DELOS-NV.

Fluorescence measurements were performed in a spectrofluorometer (**Section 9.3.8**), by exciting the sample at λ_{ex} = 475 nm and recording the spectra in 500 - 650 nm. The fluorescence intensity at λ_{em}= 526 nm was represented for each scenario. Two replicates of each scenario were performed.

9.4.6.4. Titration experiment to test the impact of the Anti-miR21 and OligoQ molar ratio in presence of DELOS-NV

For these experiments, different ratios Anti-miR21 and OligoQ were prepared. After 10 minutes of Anti-miR21 and OligoQ pre-hybridization, DELOS-NV were added to the formulation (0.03 mg/mL of membrane components). Next, titration of the miR21 into these solutions was performed. Injections of miR21 were done every 5 minutes. Fluorescence after each injection was acquired in a

spectrofluorometer (**Section 9.3.8**), by exciting the sample at λ_{ex} = 475 nm and recording the spectra in 500 - 650 nm. The fluorescence intensity at λ_{em}= 526 nm was represented versus the concentration of miR21.

9.4.6.5. Kinetic assay: Impact of the DELOS-NV concentration in the miR21 recognition

In this experiment, a single concentration of miR21 was injected over different concentrations of DELOS-NV (0, 0.015, 0.03 and 0.3 mg/mL of membrane components) containing 20 nM Anti-miR21 pre-hybridized with 30 nM OligoQ. First, the Anti-miR21 and the OligoQ were pre-hybridized for 10 minutes. After, the pre-hybridized sequences were incubated with the DELOS-NV for 10 minutes more. The experiment was repeated twice, injecting 200 nM miR21 and 1000 nM miR21. The kinetics of the reaction were evaluated by measuring the fluorescence increase over a period of 20 minutes with the spectrofluorometer (**Section 9.3.8**) in kinetics mode assay. The sample was excited at λ_{ex}= 475 nm and the fluorescence recorded at λ_{em} = 526 nm.

9.4.6.6. Binding assay miR21 to the DNA-grafted DELOS-NV biosensor

DNA-grafted DELOS-NV were produced by pre-hybridizing 20 nM Anti-miR21 and 30 nM OligoQ for 10 minutes in dPBS. Next, the hybridized sequences were incubated for another 10 minutes with 0.03 mg/mL of DELOS-NV to allow the adsorption of the cholesteryl molecule into the nanovesicles membrane.

The binding curves were obtained by titrating increasing amounts of miR21 (from 0.3 to 1000 nM) over the DNA-grafted DELOS-NV. Eight replicates were performed. The fluorescence after each injection was measured in a spectrofluorometer (**Section 9.3.8**), by exciting the sample at λ_{ex}= 475 nm and recording the spectra at 500 - 650 nm. The fluorescence intensity at λ_{em}= 526 nm (average of the eight replicates + SD) was represented versus the concentration of miR21. In addition, the fluorescence intensity (a.u.) increase was transformed into a signal gain (%) with the following **Equation 9.9**.

$$Signal\ gain\ (\%) = \frac{(FI_{[T]} - FI_{start})}{FI_{start}} x100$$

Equation 9.9. *Signal gain calculated as a percentage, where $FI_{[T]}$ refers to the fluorescence intensity at different miR21 concentrations and FI_{start} to the fluorescence intensity at the beginning of the experiment.*

The binding curves were fitted to a modified Hill equation (**Equation 9.10**):

$$FI(T) = FI_{start} + (FI_{end} - FI_{start}) x \frac{[T]^{nH}}{[T]^{nH} + K_{1/2}^{nH}}$$

Equation 9.10. *Modified Hill equation sigmoidal equation, where FI_{start} refers to the fluorescence intensity at the beginning of the experiment (or signal gain at the beginning of the experiment); FI_{end} to the fluorescence intensity at the end of the experiment (or signal gain at the beginning of the experiment); [T] is the concentration of miR21; $K_{1/2}$ is the observed equilibrium concentration at half-maximum FI gain (or signal gain) and nH is the Hill's coefficient.*

From the binding curve, the linear region was determined and fitted to a regression curve to obtain the slope. The limit of detection (LoD) and limit of quantification (LoQ) were calculated with **Equation 9.11** and **Equation 9.12**:

$$LoD = 3.3x\frac{\sigma_{\text{blank}}}{S}$$

Equation 9.11. *LoD equation employed to determine the LoD of the biosensor developed, where σ_{blank} is the standard deviation of the fluorescence in the absence of the target and S is the slope of the regression.*

$$LoQ = 10x\frac{\sigma_{\text{blank}}}{S}$$

Equation 9.12. *LoQ equation employed to determine the LoQ of the biosensor developed, where σ_{blank} is the standard deviation of the fluorescence in the absence of the target and S is the slope of the regression.*

9.4.6.7. Binding assay of non-specific miRNA to the DNA-grafted DELOS-NV biosensor

The miR21 and a non-specific DNA sequence, the mi122, were titrated over the DNA-grafted DELOS-NV composed of 20 nM Anti-miR21 pre-hybridized with 30 nM OligoQ for 10 minutes, and after, incubated with the DELOS-NV (0.03 mg/mL of membrane components) for another 10 minutes. The fluorescence after each injection was measured in a spectrofluorometer, by exciting the sample at λ_{ex}= 475 nm and recording the spectra in 500 - 650 nm. The fluorescence intensity at λ_{em}= 526 nm was represented versus the concentration of miR21 and miR122.

9.5. Design of experiments and statistical analysis

Design of Experiments (DoE): Modde 12 Pro software (Umetrics, Sweden) was employed for the definition of the experimental runs according to the different models selected (i.e., full factorial two-level with or without center point). Next, data fitting and calculation of statistical parameters were performed by multiple linear regression (MLR) model with the same software. The applicability of the models was assessed by the Q2 and R2 parameters provided by the Modde 12 Pro software. The obtainment of the design space was also conducted with the Design Space Explorer option from the Optimizer module of the same software.

Statistical analysis: When applicable, the differences among groups were evaluated by Student's t-test. The statistical analysis was performed in Microsoft Excel software (Microsoft Corp, Redmond, WA). A *P*-value below 0.05 was considered statistically significant. In figures, the symbols indicating statistical significance are: * $p < 0.05$, ** $p < 0.01$, and *** $p < 0.001$.

All data are reported as mean ± standard deviation of the mean (SD).

9.6. References

1. J. Tomsen-Melero, S. Passemard, N. García-Aranda, et al. Impact of chemical composition on the nanostructure and biological activity of α-galactosidase-loaded nanovesicles for Fabry disease treatment. *ACS Appl. Mater. Interfaces* **2021**, 13 (7), 7825–7838.
2. J.S. Pedersen. Analysis of small-angle scattering data from colloids and polymer solutions: Modeling and least-squares fitting. *Adv. Colloid Interface Sci.* **1997**, 70 (1–3), 171–210.
3. J.S. Pedersen, D. Posselt, K. Mortensen. Analytical treatment of the resolution function for small-angle scattering. *J. Appl. Crystallogr.* **1990**, 23 (4), 321–333.
4. I.B. Bekard, D.E. Dunstan. Tyrosine autofluorescence as a measure of bovine insulin fibrillation. *Biophys. J.* **2009**, 97 (9), 2521–2531.
5. X. Sun, G. Wang, H. Zhang, et al. The blood clearance kinetics and pathway of polymeric micelles in cancer drug delivery. *ACS Nano* **2018**, 12 (6), 6179–6192.
6. L. Ballell-Hosa, E. González-Mira, H. Santana, et al. DELOS nanovesicles-based hydrogels: An advanced formulation for topical use. *Pharmaceutics* **2022**, 14 (1), 1–20.
7. M.J. Blandamer, P.M. Cullisa, J.B.F.N. Engbertsb. Titration microcalorimetry. *J. Chem. Soc. Faraday Trans.* **1998**, 94 (16), 2261–2267.
8. L. Damian. Isothermal titration calorimetry for studying protein-ligand interactions. In *Protein-Ligand Interactions: Methods and Applications*; **2013**; Vol. 1008, pp 103–118.
9. P. Mura, N. Mennini, C. Nativi, B. Richichi. In situ mucoadhesive-thermosensitive liposomal gel as a novel vehicle for nasal extended delivery of opiorphin. *Eur. J. Pharm. Biopharm.* **2018**, 122, 54–61.
10. S.Y. Lee, S.I. Jeon, S.B. Sim, Y. Byun, C.H. Ahn. A supramolecular host-guest interaction-mediated injectable hydrogel system with enhanced stability and sustained protein release. *Acta Biomater.* **2021**, 131, 286–301.
11. I. Hubatsch, E.G.E. Ragnarsson, P. Artursson. Determination of drug permeability and prediction of drug absorption in Caco-2 monolayers. *Nat. Protoc.* **2007**, 2 (9), 2111–2119.

Scientific Contributions

Patents

L. Ferrer-Tasies, **C. Castellar-Álvarez**, E. González-Mira, N. Ventosa, L. Ballell-Hosa, A. Córdoba, S. Sala, and Y. Ronda-Lopez. DELOS nanovesicles embedded in thermoreversible hydrogels as *in situ*-forming subcutaneous depots. – *Submitted*

Publications

L. Ferrer-Tasies, H. Santana, I. Cabrera-Puig, E. González-Mira, L. Ballell-Hosa, **C. Castellar-Álvarez**, A. Córdoba, J. Merlo-Mas, H. Gerónimo, G. Chinea, V. Falcón, E. Moreno-Calvo, J. Skov-Pedersen, J. Romero, C. Navarro-Requena, C. Valdés, M. Limonta, J. Berlanga, S. Sala, E. Martínez, J. Veciana and N. Ventosa. Recombinant human epidermal growth factor/quatsome nanoconjugates: a robust topical delivery system for complex wound healing. *Adv. Ther.* 2021, 4 (6), 2000260

C. Castellar-Álvarez, L. Ballell-Hosa, Y. Ronda-Lopez, A. Gimó-Santamaria, A. Güell-Bara, C. Huck-Iriart, J. Skov-Pedersen, A. Córdoba, S. Sala, N. Ventosa, E. González-Mira and L. Ferrer-Tasies. Extended release of DELOS nanovesicles from thermoreversible *in situ*-forming subcutaneous depots. – *Submitted*